Spring 2022

ELECTROCATALYTIC PROCESSES FOR ENERGY STORAGE & CONVERSION

APURV SAXENA
Missouri University of Science and Technology

Department: Chemistry

ELECTROCATALYTIC PROCESSES FOR ENERGY STORAGE & CONVERSION

by

APURV SAXENA

A DISSERTATION

Presented to the Graduate Faculty of the

MISSOURI UNIVERSITY OF SCIENCE AND TECHNOLOGY

In Partial Fulfillment of the Requirements for the Degree

DOCTOR OF PHILOSOPHY

in

CHEMISTRY

2022

Approved by:

Manashi Nath, Advisor
Shubhender Kapila
Philip Whitefield
Jeffery Winiarz
Julia Medvedeva

PUBLICATION DISSERTATION OPTION

This dissertation consists of the following five articles, formatted in the style used by the Missouri University of Science and Technology:

Paper I, found on pages 39-81, 'Selective Electroreduction of CO_2 to Carbon-rich Products by Simple Binary Copper Selenide Electrocatalyst' has been published in Journal of Materials Chemistry A, 2021, **9**, 7150–7161.

Paper II, found on pages 82-121, 'Nickel Selenide as Efficient Electrocatalyst for Selective Reduction of Carbon Dioxide to Carbon-rich Products' has been submitted to Catalysis Science and Technology, and is under review.

Paper III, found on pages 122-157, 'Cobalt Telluride Electrocatalyst for Selective electroreduction of CO_2 to Value-added Chemicals' has been submitted to Materials for Renewable and Sustainable Energy, and is under review.

Paper IV, found on pages 158–192, 'Copper Cobalt Selenide as Efficient Electrocatalyst for Selective Reduction of CO_2 to Carbon-rich Products' is being prepared for submission to ACS Aplied Energy Materials.

Paper V, found on pages 193–219 'Progress of Transition Metal Chalcogenides as Efficient Electrocatalysts for Energy Conversion' has been published in Current Opinion in Electrochemistry (2022) 100993.

ABSTRACT

The continuous excessive usage of fossil fuels has resulted in its fast depletion leading to an escalating energy crisis as well as several environmental issues leading to increased research towards sustainable energy conversion. Electrocatalysts play crucial role in the development of numerous novel energy conversion devices including fuel cells and solar fuel generators.

High-efficiency and cost-effective catalysts are required for large-scale implementation of these new devices. Over the last few years transition metal chalcogenides have emerged as highly efficient electrocatalysts for several electrochemical devices such as water splitting, carbon dioxide electroreduction and, solar energy converters. These transition metal chalcogenides exhibit high electrochemical tunability, abundant active sites and superior electrical conductivity. Hence, they have been actively explored for various electrocatalytic activities.

This report details the research on the Carbon dioxide electroreduction and water splitting using metal chalcogenides as electrocatalyst also elaborating on the connection of the composition and the catalytic activity. At first, the aim was to develop catalysts which show desired activity and stability over extended periods. In addition, the catalyst should be economically viable so that it can be produced and applied on an industrial scale. Herein, I have provided comprehensive report of transition-metal chalcogenide electrocatalysts for hydrogen evolution, oxygen evolution, and carbon dioxide reduction and illustrated structure-property correlation that increases their catalytic activity.

ACKNOWLEDGMENTS

I would like to express my heartful thanks to my advisor, Prof. Manashi Nath, for the opportunity she provided to work in her lab. It has been a great honor to work with her and with the group, and for her continuous guidance throughout my stay at Missouri S&T. I would also like to thank my committee members, Prof. Philip Whitefield, Prof. Shubhender Kapila, Prof. Julia Medvedeva, and Prof. Jeff Winiarz, for their perceptive suggestions during my study and research. Dr. Eric W. Bohannan and Brian Porter for exceptional assistance in X-Ray diffraction and X-Ray Photoelectron spectroscopy measurements. Thanks go to all the faculty and staff at the Chemistry department as well for their efforts to create an efficient and friendly working environment. I would like to thank all my friends and my lab mates. I would like to thank, Dr. Jahangir Masud, for teaching me the basics of electrochemistry and sharing his valuable inputs during my Ph.D. Finally, I would like to deeply thank my wife, Mrs. Deeksha Mathur, for her unconditional love and encouragement. I owe her a lot and she has been a constant support to me throughout this journey.

TABLE OF CONTENTS

Page

PUBLICATION DISSERTATION OPTION iii

ABSTRACT iv

ACKNOWLEDGMENTS v

LIST OF ILLUSTRATIONS xii

LIST OF TABLES xvi

SECTION

1. INTRODUCTION 1

1.1. GLOBAL WARMING: MOTIVATION FOR CO_2 RECYCLING AND WATER SPLITTING 1

1.2. CARBON DIOXIDE ELECTROREDUCTION 3

1.2.1. Importance of CO_2 Electroreduction 3

1.2.2. Literature Review: Carbon Dioxide Reduction Reaction (CO2RR) 6

1.2.2.1. Transition metal chalcogenides for CO_2 electroreduction 7

1.2.2.2. Copper and other transition metal catalysts. 9

1.2.2.3. Copper chalcogenides and other transition metals with d^5-d^{10} electrons. 9

1.2.2.4. Transition metal with d^1-d^3 electrons 11

1.2.3. Challenges: Scalability 11

1.2.4. Experimental Methods. 12

1.2.4.1. Electrochemical cell setup. 13

1.2.4.2. Electrode preparation. 14

1.2.4.3. Electrochemical reaction procedure.....14

1.2.4.4. Electrolysis method.....15

1.2.4.5. Electrochemical surface area determination. 15

1.2.4.6. Membrane selection. 16

1.2.4.7. Gas chromatography: gas phase product quantification 17

1.2.4.8. NMR liquid phase product quantification. 17

1.2.4.9. Faradaic efficiency.....18

1.3. WATER SPLITTING 18

1.3.1. Types of Water Electrolysis. 19

1.3.2. Thermodynamics of Water Splitting. 21

1.3.3. Efficiency Parameters..... 22

1.3.3.1. Overpotential (η).....22

1.3.3.2. Stability.....23

1.3.3.3. Tafel slope and exchange current density (J_0). 23

1.4. LITERATURE REVIEW: WATER SPLITTING..... 24

1.4.1. TMC for Water Splitting. 25

1.4.2. Binary TMCs. 26

1.4.3. Multinary TMCs. 27

1.5. CONCLUSION AND FUTURE OUTLOOK 36

PAPER

I. SELECTIVE ELECTROREDUCTION OF CO_2 TO CARBON-RICH PRODUCTS BY SIMPLE BINARY COPPER SELENIDE ELECTROCATALYST..... 39

ABSTRACT 39

1. INTRODUCTION 40

2. EXPERIMENTAL METHODS 45

2.1. MATERIAL 45

2.2. SOLVOTHERMAL SYNTHESIS OF CU_2SE 45

2.3. PREPARATION OF ELECTRODES……...46

2.4. PREPARATION OF ELECTROLYTE 46

3. METHODS OF CHARACTERIZATION 46

3.1. POWDER X-RAY DIFFRACTION 46

3.2. SCANNING ELECTRON MICROSCOPY (SEM) 47

3.3. X-RAY PHOTOELECTRON SPECTROSCOPY (XPS) 47

3.4. ELECTROCHEMICAL CHARACTERIZATION AND ELECTROCATALYTIC STUDIES PREPARATION OF ELECTROLYTE 48

3.5. TAFEL PLOTS 48

4. RESULTS AND DISCUSSION 49

4.1. STRUCTURE AND MORPHOLOGY OF CU_2SE 49

4.2. ELECTROCHEMICAL PERFORMANCE AND CO2RR CATALYTIC ACTIVITIES 50

4.3. EXPLORING CO ADSORPTION ENERGIES ON CATALYST SURFACES……...61

5. CONCLUSIONS 66

SUPPORTING INFORMATION 67

REFERENCES 76

II. NICKEL SELENIDE AS EFFICIENT ELECTROCATALYST FOR SELECTIVE REDUCTION OF CARBON DIOXIDE TO CARBON-RICH PRODUCTS 82

ABSTRACT 82

1. INTRODUCTION 83

2. MATERIALS AND METHODS 87

2.1. SYNTHESIS OF $NISE_2$ 87

2.2. PREPARATION OF ELECTRODE 87

3. RESULTS AND DISCUSSION 87

3.1. ELECTROCHEMICAL CATALYTIC ACTIVITY OF $NISE_2$ FOR CO2RR-OER 101

4. CONCLUSION 109

SUPPORTING INFORMATION 111

REFERENCES 117

III. COBALT TELLURIDE ELECTROCATALYST FOR SELECTIVE ELECTROREDUCTION OF CO_2 TO VALUE-ADDED CHEMICALS 122

ABSTRACT 122

1. INTRODUCTION 123

1.1. BACKGROUND 123

2. EXPERIMENTAL PROCEDURE 126

2.1. MATERIALS 126

2.2. SYNTHESIS OF COTE 127

2.3. CHARACTERIZATION 127

2.4. ELECTROCHEMICAL MEASUREMENTS 128

3. RESULTS 129

3.1. ELECTROCATALYTIC CO2RR PERFORMANCE OF COTE CATALYST 131

3.1.1. Tafel Plot 132

3.2. CO2RR PRODUCTS IDENTIFICATION AND QUANTIFICATION 134

3.2.1. Electrochemical Capacitance Measurements. 140

3.2.2. Electrochemical Impedance Spectroscopy Measurements. 142

4. CONCLUSIONS 145

4.1. CONCLUSIONS AND FUTURE WORK 145

SUPPORTING INFORMATION 147

REFERENCES 150

IV. COPPER COBALT SELENIDE AS EFFICIENT ELECTROCATALYST FOR SELECTIVE REDUCTION OF CO_2 TO CARBON-RICH PRODUCTS 158

1. INTRODUCTION 158

2. EXPERIMENTAL AND COMPUTATIONAL METHODS 161

2.1. SYNTHESIS OF $CUCO_2SE_4$ AND ELECTRODE PREPARATION 161

2.2. CHARACTERIZATION OF CATALYST 162

2.2.1. Powder X-ray Diffraction. 162

2.2.2. Electrochemical Activity for CO_2 Conversion. 162

2.3. DENSITY FUNCTIONAL THEORY CALCULATIONS 163

3. RESULTS AND DISCUSSION 164

3.1. CHARACTERIZATION 164

3.2. ELECTROCATALYTIC PERFORMANCE FOR CO2RR 167

3.3. ELECTROCHEMICAL PERFORMANCE OF $CUCO_2SE_4$ FOR ALCOHOL OXIDATION REACTION (AOR) 176

3.4. ELECTROCHEMICAL CATALYTIC ACTIVITY OF $CUCO_2SE_4$ FOR CO2RR-AOR COMBINED REACTION ($CUCO_2SE_4$/CF|| $CUCO_2SE_4$/CF) 180

4. CONCLUSION 186

REFERENCES 187

V. PROGRESS OF TRANSITION METAL CHALCOGENIDES AS EFFICIENT ELECTROCATALYSTS FOR ENERGY CONVERSION 193

ABSTRACT 193

1. INTRODUCTION 194

2. TRANSITION METAL CHALCOGENIDES FOR CO_2 ELECTROREDUCTION 196

2.1. COPPER AND OTHER TRANSITION METAL CATALYSTS 197

2.2. TRANSITION METAL CHALCOGENIDES 198

2.2.1. Copper Chalcogenides and Other Transition Metals with d^5-d^{10} Electrons. 198

2.3. TRANSITION METAL WITH D1-D3 ELECTRONS 200

3. PERSPECTIVE AND FUTURE OUTLOOK 200

REFERENCES 204

SECTION

2. CONCLUSIONS 220

BIBLIOGRAPHY 221

VITA 237

LIST OF ILLUSTRATIONS

SECTION Page

Figure 1.1. Effect of CO_2 emissions on different environmental areas..... 2

Figure 1.2. Market price of select CO_2 recycling products as a function of energy content.. 13

Figure 1.3. Sustainable pathways for hydrogen generation from solar energy 20

Figure 1.4. Electrochemical water splitting. 22

Figure 1.5. OER and HER polarization curves and it's parts 26

Figure 1.6. Trend of OER catalytic activity within the entire Fe–Co–Cu trigonal phase space……...……..29

Figure 1.7. Comparison of OER activity of various metal chalcogenides at current density of 10 mA cm^{-2}..... 30

Figure 1.8. Experimental and theoretical studies..... 37

PAPER I

Figure 1. PXRD pattern of hydrothermally synthesized Cu_2Se compared with the standard Cu_2Se reference pattern (PDF # 00-006-0680)..... 47

Figure 2. SEM images of the Cu_2Se nanoparticles at (a) low and (b) high magnification showing formation of nanocubes and surface roughness, respectively. (c) EDS analysis of the catalyst confirming presence of Cu and Se in 2:1 relative atomic ratio. (d) Cu 2p and (e) Se 3d XPS spectra of as-synthesized Cu_2Se 51

Figure 3. Cyclic voltammograms measured for Cu_2Se catalyst in 0.3 M $NaHCO_3$ at continuous N_2 purging at different scan rates from 2.5 to 40 mV s^{-1}..... 52

Figure 4. Electrochemical performance of $NiSe_2$. 55

Figure 5. Identification and quantification of CO2RR products..... 57

Figure 6. Bar plot depicting relative faradaic efficiency of liquid as well as gas products at different applied potentials 58

Figure 7. Polarization curve with cathodic CO2RR and anodic OER with Cu_2Se@CFP as both cathodic and anodic electrocatalyst..... 60

Figure 8. Comparison of calculated CO adsorption energy on known catalyst materials with Cu_2Se. 63

PAPER II

Figure 1. PXRD pattern of hydrothermally synthesized $NiSe_2$ compared with the standard $NiSe_2$ reference pattern (PDF # 01-088-1711). 88

Figure 2. SEM images of the $NiSe_2$ nanoparticles at (a) low and (b) high magnification showing formation of nanostructures and surface roughness, respectively. (c) EDS analysis of the catalyst confirming presence of Ni and Se in 1:2 relative atomic ratio. (d) Ni 2p and (e) Se 3d XPS spectra of as-synthesized $NiSe_2$ 90

Figure 3. Electrocatalytic activity of $NiSe_2$ towards CO2RR..... 92

Figure 4. CO2RR products quantification. 93

Figure 5. Bar plots depicting relative faradaic efficiency of cumulative liquid and gas phase CO_2 reduction products at different applied potentials quantified through NMR and GC-MS. 95

Figure 6. Polarization curve with cathodic CO2RR and anodic OER with $NiSe_2$@CFP as both cathodic and anodic electrocatalyst.. 97

Figure 7. Cyclic voltammograms measured for $NiSe_2$ catalyst in 0.3 M $NaHCO_3$ under continuous N_2 purging at different scan rates from 2.5 to 40 mV s^{-1}.. 98

Figure 8. CO2RR performances of $NiSe_2$ catalyst..... 104

Figure 9. EIS Nyquist plots of $NiSe_2$@CFP in CO_2-saturated 0.3 M $NaHCO_3$ electrolyte (pH 6.8) from 0 V vs RHE to -1.3 V vs RHE. 106

Figure 10. CO adsorption energy on $NiSe_2$ (111) surface compared with other known CO2RR reduction catalysts.. 108

PAPER III

Figure 1. Characterization..... 130

Figure 2. XPS spectra of (a) Co 2p and (b) Te 3d in CoTe. 130

Figure 3. Electrocatalytic activity 132

Figure 4. Product quantification……..135

Figure 5. Bar plots depicting relative faradaic efficiency of cumulative liquid and gas phase CO_2 reduction products at different applied potentials quantified through NMR and GC-TCD. 137

Figure 6. CV scans of CoTe@CC from scan rate 5 to 200 mV/s.. 141

Figure 7. CO2RR performances of CoTe catalyst.. 142

Figure 8. EIS Nyquist plots of CoTe@CFP in CO_2-saturated 0.3 M $NaHCO_3$ electrolyte (pH 6.8) from 0 V vs RHE to -1.1 V vs RHE. 143

Figure 9. Comprehensive comparison of products obtained through electrocatalytic CO2RR with CoTe and other catalysts as assembled from various reports published from different research groups. 145

PAPER IV

Figure 1. PXRD pattern of hydrothermally synthesized $CuCo_2Se_4$ compared with the standard $CuCo_2Se_4$ reference pattern (PDF# 04-019-0997) 165

Figure 2. SEM images of the $CuCo_2Se_4$ nanoparticles at (a) high and (b) low magnification showing formation of nanostructures and surface roughness, respectively. (c) Cu 2p and (d) Co 2p and (e) Se 3d XPS spectra of as-synthesized $CuCo_2Se_4$. 166

Figure 3. (a) LSVs measured in 0.3 M $NaHCO_3$ at a scan rate of 10 mV s^{-1} in presence and absence of CO_2 with different electrodes. (b) Tafel plots measured in 0.3 M $NaHCO_3$ 167

Figure 4. (a) NMR spectra identifying CO_2 reduction products in reaction aliquots collected at different potentials. (b) Plots illustrating relative concentrations of liquid products quantified from NMR at different stationary applied potentials. 172

Figure 5. Bar plots depicting relative faradaic efficiency of cumulative liquid and gas phase CO_2 reduction products at different applied potentials quantified through NMR and GC-TCD. 174

Figure 6. CO2RR performances of $CuCo_2Se_4$ catalyst 175

Figure 7. Cyclic voltammograms measured for $CuCo_2Se_4$ catalyst in 0.3 M $NaHCO_3$ under continuous Ar purging at different scan rates from 5 to 200 mV s^{-1}. 177

Figure 8. EIS Nyquist plots of $CuCo_2Se_4$@CFP in CO_2-saturated 0.3 M $NaHCO_3$ electrolyte (pH 6.8) from 0 V vs RHE to -1.3 V vs RHE..... 178

Figure 9. Electrocatalytic performances of $CuCo_2Se_4$/CFP..... 179

Figure 10. Faradaic efficiencies of Formic acid and Carbon monoxide and Acetic acid varying with different metallic surfaces and reported catalysts ……....181

Figure 11. Total density of states (TDOS) of bulk $CuCo_2Se_4$ compared with CO attached on Co and Cu atoms…….184

Figure 12. Partial density of states (PDOS) and it's parts.……...……...…….185

PAPER V

Figure 1. Schematic Illustration of the TMC electrocatalysts…….195

Figure 2. Experimental and theoretical studies……...…….201

LIST OF TABLES

SECTION Page

Table 1.1. Reaction Potentials for Carbon Dioxide Reduction half reactions. 5

Table 1.2. Production rates at different power outputs for an ideal electrolysis reactor of CO_2 electroreduction..... 12

Table 1.3. The comparison of OER and HER overpotentials with overall water splitting performance of selected bifunctional nonnoble transition binary and multinary metal chalcogenides. 31

PAPER I

Table 1. Fitting parameters obtained from Nyquist plots at various potentials..... 105

PAPER III

Table 1. Fitting parameters obtained from Nyquist plots at various potentials 144

PAPER IV

Table 1. Fitting parameters obtained from Nyquist plots at various potentials 176

1. INTRODUCTION

1.1. GLOBAL WARMING: MOTIVATION FOR CO_2 RECYCLING AND WATER SPLITTING

As the world's population and industrialization is increasing the surge in energy demand of fossil fuels has affected the earth's climate to a great extent. Carbon dioxide level has reached to a very high level.[1] Due to the limited fossil fuel reserves, pressure to maintain environmental balance and limitation of conventional renewable resources, it is challenging to find alternative resource of energy. Today world requires 17 TWh of power generation and more than 80% comes from the fossil fuels.[2] As observed by US EIA, Energy demand all over the world is predicted to increase from 549 quadrillion BTU to 815 quadrillion BTU by 2050. From total US energy requirement, 80 % is met by fossil fuels.[3] Using renewable and economical energy sources rather than fossil fuel reserves will be crucial for making the environment clean and will ensure availability in future. There has been progress in use of renewable resources too. Renewable energy sources has increased by in US.[4,5] As biomass is of less cost, widely available and is renewable, biomass has lot of potential to replace non-renewable resources both at laboratory and industrial scale. Nature produces approximately 200 billion metric tons of biomass through plants and vegetation at one tenth price of crude oil production.[6,7] Biomass contain different types of carbohydrates which can be converted into value added compounds.

Rate of CO2 emission increase has doubled from 1990-1999 to 2000-2014.8 These new levels pose a great threat towards the climate. It can lead to an increase in global temperature by 2^0 C which can lead to rise in the sea levels as a result of melting of polar ice.[10]

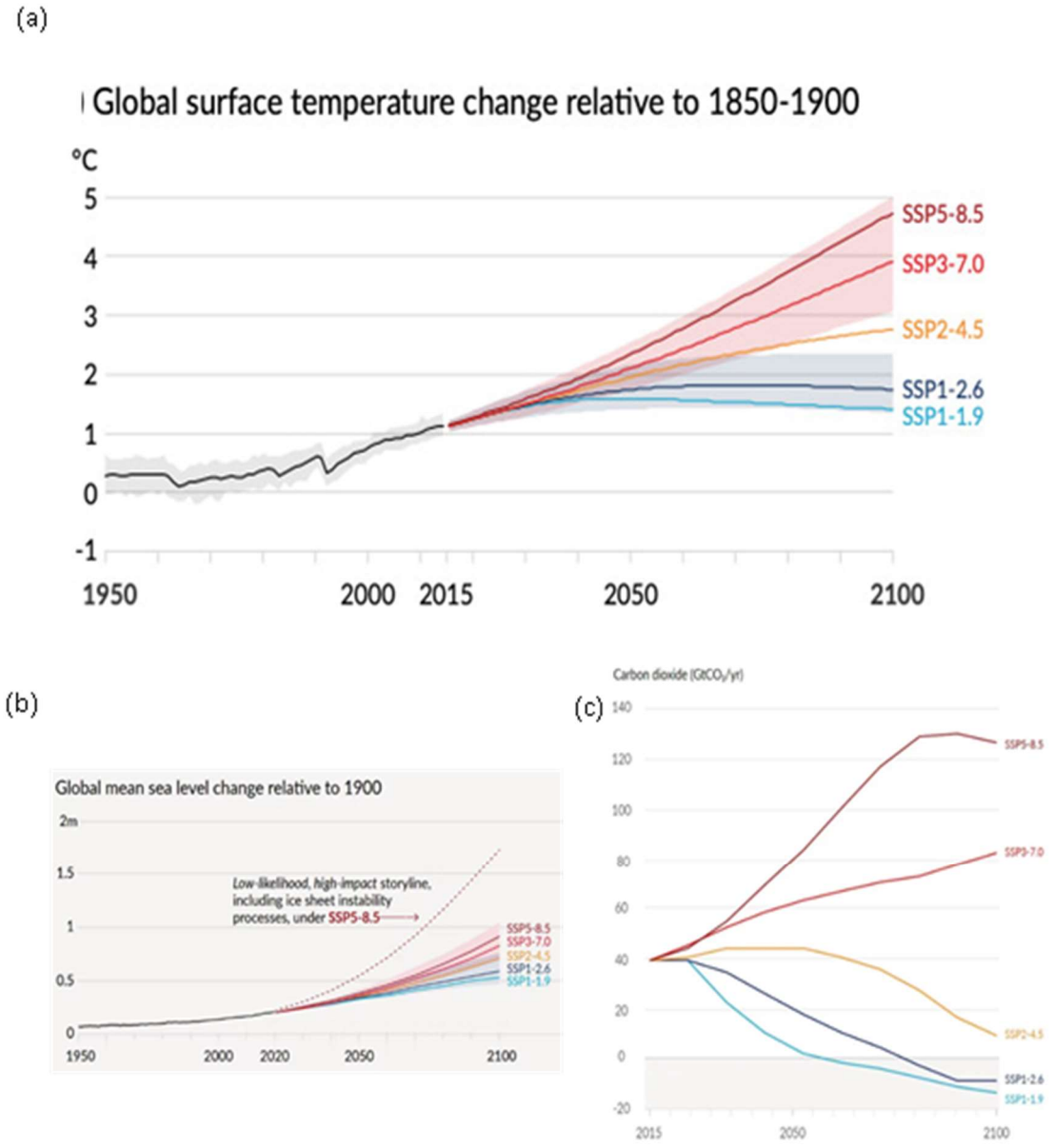

Figure 1.1. Effect of CO_2 emissions on different environmental areas a) Change in global surface temperature over time, b) Change in mean sea level over time, c) emissions of anthropogenic CO_2 emission over time.[9]

Also, CO_2 dissolves in water to form H_2CO_3 (carbonic acid). This acid can decrease the pH of the sea water which can result in the bleaching of the coral reefs and dissolution

of carbonates like $CaCO_3$.[11] As these changes continue to take place due to increased level of the CO_2, unexpected outcomes will arise.

Solar Energy, wind energy and hydro energy are the main sources of renewable energy.[12,13] Downside of these energy sources is the intermittent supply of energy so we need some energy storage solutions so that we can tap into productive hours of energy generation.[14] One of the solutions is the use of electrochemical processes to convert the electricity into fuels which act as a chemical storage (like hydrogen and other fuels) using the abundant sources like Water (H_2O), Carbon Dioxide (CO_2). We can store intermittent electricity generated from any renewable sources via these processes.[14,15]

This work is focused on discovering different catalyst which can make these electrochemical processes efficient and understanding the underlying mechanisms involved.

Focus of this work is on electrochemical processes like:

1. Carbon dioxide reduction reaction: which can give us fuels like methanol, ethanol and other chemicals like formic acid and acetic acid.
2. Water Splitting: that gives us hydrogen.

1.2. CARBON DIOXIDE ELECTROREDUCTION

The reduction of CO_2 into value added chemicals using renewable energy such as wind or solar power could soon replace the use of fossil fuels. This section describes the importance of CO_2 electroreduction, dicusses the current state of research and limitations.

1.2.1. Importance of CO_2 Electroreduction. Carbon Dioxide electroreduction can serve as an alternative pathway for producing fuels and value-added chemicals.

Products like carbon monoxide, formic acid, acetic acid, methanol, ethanol etc. have been observed in different studies. Electrochemical reduction of CO_2 provides a path to convert energy from renewable energy sources which have intermittent supply to a limitless supply which is fuel. When there is a surge in electrical energy output which is generated from wind and solar energy, it can be stored in form of chemical energy later to be used in low output hours. Fuels produced through CO_2 reduction can replace the fuels extracted from fossil materials petroleum. We want to make the carbon zero cycle where the carbon dioxide is converted back to fuels which can be used for further energy generation. This CO_2 electrochemical reaction consists of two half-cell reactions:

- Carbon dioxide electrochemical reduction $CO_2 + e^- \rightarrow$ Hydrocarbons,
- Oxygen evolution reaction $OH^- + e^- \rightarrow O_2$.

These half-cell reactions are kinetically sluggish and have high activation energy requirements. To successfully and efficiently do CO_2 electrochemical reduction both of these processes need to have less energy barrier which can be done using electrocatalysts. Potential which need to be applied in addition to the thermodynamic requirements is called overpotential and is the indicator of Kinetic energy barrier. So the need is to decrease the overpotential by designing catalyst which can decrease the overpotential leading to better economics of CO2RR. In the dissertation, I have resolved the issue of kinetic sluggishness for both half reactions CO2RR and OER. I have also developed a full cell where I have used the catalyst as both anode and cathode and demonstrated the better OER and CO2RR activity.

Table 1.1. Reaction Potentials for Carbon Dioxide Reduction half reactions. Adapted from Dongwei et. al.[24]

Thermodynamic electrochemical half-reactions	**Electrode potentials (V vs. SHE)**
$CO_2(g) + 4H^+ \rightarrow C(s) + 2H_2O(I)$	0.210
$CO_2(g) + 2H_2O(1) + 4e^- \rightarrow C(s) + 4OH^-$	-0.627
$CO_2(g) + 2H^+ + 2e^- \rightarrow HCOOH\ (1)$	-0.250
$CO_2(g) + 2H_2O(I) + 2e^- \rightarrow HCOOH\ (aq) + OH"$	-1.078
$CO_2(g) + 2H^+ + 2e^- \rightarrow CO + H_2O(I)$	-0.106
$CO_2(g) + H_2O(1) + 2e^- \rightarrow CO + 2OH^-$	-0.934
$CO_2(g) + 4H^+ + 4e^- \rightarrow CH_2O\ (1) + H_2O\ (1)$	-0.070
$CO_2(g) + 3H_2O(I) + 4e^- \rightarrow CH_2O(I) + 4OH^-$	-0.898
$CO_2(g) + 6H^+ + 6e^- \rightarrow CH_3OH\ (1) + H_2O(I)$	0.016
$CO_2(g) + 5H_2O(1) + 6e^- \rightarrow CH_3OH(1) + 6OH^-$	-0.812
$CO_2(g) + 8H^+ + 8e^- \rightarrow CH_4(g) + 2H_2O(I)$	0.169
$CO_2(g) + 6H_2O(1) + 8e^- \rightarrow CH_4(g) + 8OH^-$	-0.659
$2CO_2\ (g) + 2H^+ + 2e^- \rightarrow H_2C_2O_4(aq)$	-0.500
$2CO_2\ (g) + 2e^- \rightarrow C_2O_4^{2-}\ (aq)$	-0.590
$2CO_2\ (g) + 12H^+ + 12e^- \rightarrow CH_2CH_2(g) + 4H_2O(1)$	0.064
$2CO_2\ (g) + 8H_2O(I) + 12e^- \rightarrow CH_2CH_2(g) + 8OH^-$	-0.764
$2CO_2\ (g) + 12H^+ + 12e^- \rightarrow CH_3CH_2OH(I) + 3H_2O(1)$	0.084
$2CO_2\ (g) + 9H_2O(l) + 12e^- \rightarrow CH_3CH_2OH\ (1) + 12OH^-$	-0.744

All these half-cell reactions (Table 1.1) demonstrate the thermodynamic energy requirements of the possible reaction which can undergo during CO2RR. As demonstrated in Table 1.1, CO_2 is thermodynamically stable which make the activation of carbon dioxide difficult. Energy input is required to pass the energy barrier and Electrical Energy should be used if potential is applied across electrodes (anode and cathode) for reduction of CO_2

electrochemically at cathode.[16,17]. Two type of electrolysis cells can be used to reduce carbon dioxide:

1. Solid oxide electrolysis: - high temperatures (750-900°C), high current densities. Generally CO is the observed product.[16]
2. Aqueous CO_2 electrolysis: - low temperature (25-100°C). economical, less infrastructure. Products are various hydrocarbons, alcohols, formic acid etc., from CO_2 reduction.[18–22]

The major competing reaction of CO_2 Electroreduction is the Hydrogen evolution reaction (HER) in the water. This is due to the fact that dissolved CO_2 is very much less than the concentration of H^+.[23] Also due to the low kinetic barriers for HER in comparison to CO_2 electroreduction, Hydrogen is generally the primary product during an electrolysis at the cathode during CO_2 electroreduction in water. Based on the mechanism of CO_2 electroreduction will proceed on different catalysts, with possibility of different products. For generating value added chemicals, many electron transfer steps are required of single carbon or many carbon products (carbon- carbon bond formation). All these requirements and possibilities proves that it is difficult to find CO2RR catalyst of desired activity.

1.2.2. Literature Review: Carbon Dioxide Reduction Reaction (CO2RR). First work in this area was by Yoshiro Hori beginning in the 1980s, this study did the CO_2 electroreduction on metals which are on the right side of manganese in the periodic table.[25,26] It was observed that the metals on the right of the copper in the periodic table produced CO and HCOOH but metals in the left of copper were found to be produce H_2. Metals of group 11 (Cu, Ag, Au was observed to be becoming more selective towards CO going from Cu to Au. Metals to the left of copper were found to produce mostly H_2, metals to the right

of Cu were found to produce mostly CO or $HCOO^-$, and group 11 metals were found to be the most active becoming more selective for CO as you move from Cu to Ag, to Au. Copper was observed to give many products after CO_2 electrochemical reduction which varies form C2 products like ethanol to C1 products like CH_4, CO and $HCOO^-$.

Although these products are of great use ranging to fuels to chemical feedstocks, Copper does not show selectivity and performs on very large overpotential which is not possible to apply on industrial scale. There has been research done for modification of the reactivity and selectivity of Cu but there has not been a major success till now.[20,27–29] As these things limit the applications of Cu, we need to discover new catalysts which are selective towards value added chemicals, which have low overpotentials in doing so and have high partial current densities.

According to the study done by Hori et. al., metals having partially filled d-orbitals (left of copper) have strong σ-bonds with CO which allows the back bonding of electrons towards the π-acceptor orbitals of CO which makes M-CO stable complex. This indicates that metals like Nickel should reduce CO_2 to CO at lower overpotential but it also leading to poisoning of metals and CO is not able to desorb from the surface. Hence these metals are poor catalysts for CO_2 reduction in their metallic form. Metals in periodic table to the right of copper have comparatively weaker interaction with CO and hence are not able to reduce CO_2 at lower overpotentials.

1.2.2.1. Transition metal chalcogenides for CO_2 electroreduction. Research on electrocatalytic conversion of CO_2 has evolved over past few years with respect to developing catalyst composition with special emphasis on achieving selectivity for the reduction products.[30–34] In the following section we will discuss first about Cu- and other

transition metal based catalyst and then focus on transition metal chalcogenides. We will highlight new CO2RR catalysts which will provide fundamental understanding of catalytic processes to achieve product selectivity, that can be helpful for development of efficient CO2RR catalysts in future. From early on transition metal-based electrocatalysts have been proven to be efficient candidates for CO2RR in commercial devices.[35] They have the ability to convert CO_2 into variety of hydrocarbons with good faradaic efficiency. While CO_2 conversion is of utmost importance to reduce atmospheric levels of this greenhouse gas, production of carbon monoxide, i.e., CO as the reduction product does not really mitigate the problem, since CO is a toxic gas. The produced CO, hence, needs to be further processed to other carbonaceous product with higher fuel value. Ongoing research is directed towards improving selectivity for value-added carbon-rich products. It was hypothesized that adsorption energy of intermediate *CO on the transition metal site played a critical role in influencing product composition and selectivity.[30] Specifically, catalysts with smaller adsorption *CO adsorption energy led to preferential formation of CO and formic acid as the reduction products (Figure. 1.7(a)). Catalysts with significantly larger *CO adsorption energy, on the other hand, exhibited surface poisoning with CO. Hence, recent efforts have been guided towards designing catalyst compositions that will have *CO adsorption energy in the moderate range as shown in Figure. 1.7(a). Since metal-to-ligand back bonding plays a major role in deciding binding of intermediate *CO to the transition metal site, optimizing *CO adsorption energy has been attempted by modulating d-electron density near the transition metal site through investigating different transition metals and changing anion coordination. The following sections compile various CO2RR catalysts that has been reported based on their d-electron density and highlights the

correlation of *CO adsorption energy with product selectivity as has been studied in chalcogenide-based catalysts.

1.2.2.2. Copper and other transition metal catalysts. Copper was found to have enhanced activity towards CO2RR in producing at least 16 different C1–C3 hydrocarbon/oxygenate products which is better than other metals but the selectivity was not attained towards a specific product.[36] Use of other transition metals such as Au,[37,38–41] Ag, [36,42,43] Pd,[44] Co,[45,34] Zn,[34,46,47] led to formation of CO as the major product of CO_2 reduction. Similarly, other metal catalysts like Pb,48 In,49 Sn,4450 and Bi,51,52 also led to predominantly to formation of CO. Polycrystalline Ag is known for producing CO with Faradaic efficiency (FE) of 22.4% at −0.8 VRHE.[34] DFT based studies revealed that most of these metal catalysts had a weak binding energy towards CO, which led to weaker adsorption and formation of CO as major product. Therefore, there was a need to modify transition metals like Cu and other metals to get better selectivity for C2+ products.

1.2.2.3. Copper chalcogenides and other transition metals with d^5-d^{10} electrons. It has been proposed that chalcogenide anions increased lattice covalency owing to their decreased electronegativity, which led to enrichment of d-electron density near the transition metal site.[53] Hence, it was expected that chalcogenides will show better *CO adsorption energy leading to better selectivity of C2 products.[30,5446] Indeed DFT calculation revealed that Cu-selenides showed better *CO adsorption energy compared to the base metal and its oxide as shown in Figure. 1.7(a). Experimental studies also confirms that chalcogens favors the formation of C2 products and deters the formation of C1 products because of decrease in surface concentration of CO.[3446] Investigation of various Cu-based catalysts such as Cu, Cu-oxide, Cu-sulfide and Cu-selenide catalysts, revealed that

selectivity towards certain carbon products increased with Cu-chalcogenides compared to Cu. This fact can be proven by comparing polycrystalline Cu,[5546] and CuS having HCOOH product with FE= 80% at −0.8 V RHE[46], 3D- Cu_2S showing improved performance with a FE=87.3% at −0.9 VRHE,[56] while, Cu_2Se nanocubes,[30] and $Cu_{1.63}Se$ nanowires,[57] $Cu_{1.8}Se$ nanowires,[34] showed a high C2 product selectivity. In case of other transition metals also chalcogenides showed improved activity and selectivity.

FeS_2/NiS showed very good performance in reduction of CO_2 to form CH_3OH with overpotential of 280 mV and Faradaic efficiency of 64%.[58] Using molecular engineering, iron porphyrin was synthesized which showed good activity achieving 98% Faradaic efficiency for CO production.[34] Cobalt Phthalocyanine with pyridyl moieties as axial ligands achieved 70% FE towards CO production.[37] This study showed that upon axial coordination to CoPc, catalytic activity towards CO2RR improved due to energy level rise of d_z^2 orbital.[59] When Ag was modified by sulfur to form Ag_2S, selectivity improved to 92.0% at very low overpotential (−0.754 V).[3760] Zn has shown limited activity towards CO2RR.[61] Zn nanosheets exhibit Faradaic efficiency of 70.9% when producing CO from CO_2 electrochemical reduction. Upon modification with sulfur to make ZnS/Zn, the FE increased to 94.2%.[62] ZnTe is also an efficient catalyst to photochemically convert CO_2.[63] Similarly Cd also changes selectivity from formic acid to CO when it is converted to CdS.[64] CdS showed good stability of 40+ hours and 95% FE towards CO during CO2RR.[34] Sn is also known to be an active metal towards CO2RR often modulated by surface structure. Modifications like change in particle size,[65]oxide layer thickness,[66] morphology,[67] and electrolyte's pH have improved the activity, selectivity, energetic efficiency, and robustness of tin-based catalysts.[68,69] In a study, tin oxide (SnOx) layer was found to be

active because CO_2- intermediate adheres better to the catalyst surface, and oxide layer suppresses the competing hydrogen evolution reaction.[70,71] The catalytic efficiency was improved further by converting SnO_x to $SnSe_2$ which balances the binding strength of $CO_2^{\bullet-}$ intermediates and also improves conductivity as compared to oxide layer.[72] The electronic conductivity of metal selenides was found to be better due to higher electronegativity of oxygen than selenium. This also leads to the fast charge transfer during catalytic activity.[72] Hence, $SnSe_2$ showed high current density (12.0 mA cm^{-2}) and high FE (88.4%) at very low potential (−0.76 V vs RHE) for CO2RR.[72]

1.2.2.4. Transition metal with d^1-d^3 electrons. Liu et al. showed that ultrathin $MoTe_2$ layers can reduce CO_2 to CH_4 with faradaic efficiency of 83 % with extended stability of 45 hours. Ultrathin layers lead to highly efficient mass transport due to layered structure which makes active sites available and improves CO_2 electrochemical reduction.[73] To improve conductivity and number of active sites two-dimensional (2D) $MoSe_2$ doped transition metals (Fe, Co, Ni and Cu) were explored using density functional theory (DFT) calculations. Cu doped $MoSe_2$ was found to potentially have great activity for methane production.[74] WSe_2 nanoflakes show activity towards CO2RR at very low overpotential of 0.054 V forming CO as main product (FE=24%).[37]

1.2.3. Challenges: Scalability. The implementation of CO_2 electrochemical reduction to produce chemicals on industrial scale depends on the economics of the main factor contributing to the cost of the process is cost of electricity. Decrease in the cost of electricity and discovery of catalyst which uses less electrical energy to reduce CO_2 are the main solutions of reducing the cost of implementing CO2RR. Production rate should also be comparable to petroleum if we want to replace them. As shown in Table 1.2, product

formation rate will be correlated with power input. high production rates could be possible with an optimized device.

The application of CO_2 electrochemical reduction in industrial processes mainly depends on the economics of the process. Main factor which influences the feasibility of this process is cost of electricity. Improving the energy input in the reaction by achieving lower overpotential we can decrease the amount of electricity consumed. Figure 1.2 signifies the change in prices if electrical energy requirement is reduced which can be done by lowering overpotential. Also, if we want to make this technology as an alternative for the fossil fuels, we need to take scalability into consideration. The formation rate needs to be high to make practical CO2RR application. Processes like electrolytic aluminum refining etc. are perfect example of the requirement needed for practical applications.

1.2.4. Experimental Methods. This section describes the experimental procedures

Table 1.2. Production rates at different power outputs for an ideal electrolysis reactor of CO_2 electroreduction

Production Rate (kg/hr)	100 W	1 kW	10 kW	100 kW	1 MW	10 MW	100 MW
Formic acid	0.046	0.46	4.64	46.4	464	4640	46400
Carbon monoxide	0.027	0.27	2.71	27.1	271	2710	27100
Methanol	0.011	0.11	1.11	11.1	111	1110	11100
Methane	0.004	0.04	0.45	4.5	45.1	451	4510
Acetic acid	0.014	0.14	1.44	14.4	144	1440	14400
Ethylene glycol	0.014	0.14	1.42	14.2	142	1420	14200
Acetaldehyde	0.009	0.09	0.92	9.2	92.3	923	9230
Ethanol	0.008	0.08	0.82	8.2	82.3	823	8230
Ethylene	0.005	0.05	0.50	5.0	49.8	498	4980
Acetone	0.007	0.07	0.69	6.9	68.8	688	6880
1-Propanol	0.008	0.08	0.77	7.7	76.9	769	7690

for measuring the activity of electrocatalysts for CO_2 electrochemical reduction and analytical techniques for quantification of the reduction products.

1.2.4.1. Electrochemical cell setup. There has been no established experimental setup for CO2RR and various electrolyzers. Electrolyzers used for the CO2RR are of two types one is H cell and other is flow cell. In both designs, dissolved CO_2 makes contact with the catalyst on working electrode. In H cell, carbon dioxide diffuses from hydrodynamic boundary layer of $NaHCO_3$ solution. H-shaped cell are generally used for lab based CO2RR reactions. This cell has one anodic compartment and cathodic compartment separated by anion-exchange polymer membrane Nafion. Menbrane in between the compartments makes ion exchange feasible prohibiting the products

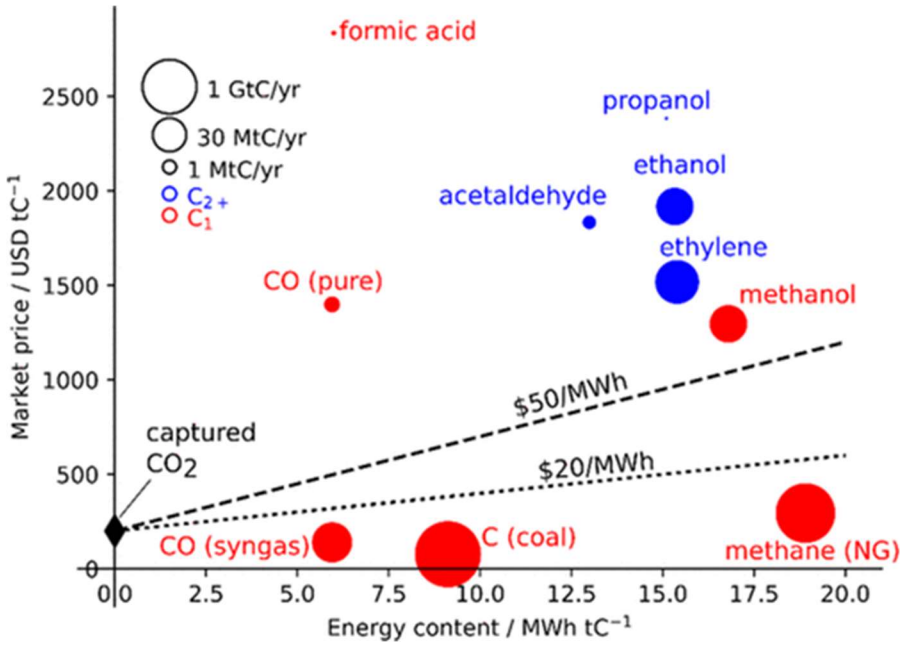

Figure 1.2. Market price of select CO_2 recycling products as a function of energy content. Lines represent minimum energy and CO_2 costs.

generated in the anodic compartment from oxidizing at cathodic compartment. Three electrode setups consisting of one working electrode, one counter electrode and on reference electrode was used for experiments carried out.

1.2.4.2. Electrode preparation. To observe the activity of hydrothermally synthesized catalyst, working electrode was made using the homogeneous catalyst ink. To prepare ink, 5 mg of the catalyst was added to 250 µL of Nafion solution and homogenized by sonication. Nafion solution had 125 µL of 1% nafion solution added to 125 µL of 50% isopropyl alcohol (IPA) in water. On substrate, 5 µL of the homogenized ink was drop casted on a confined area (0.07 cm^{-2}). The drop-casted film on substrate was then dried overnight at room temperature.

1.2.4.3. Electrochemical reaction procedure. In N_2-saturated 1M KOH solution (pH 13.6), polarization curves were recorded at scan rate of 10 mVs^{-1} to observe the water splitting activity of the catalyst. Electrochemical cell used in this study consisted of three electrode system. A standard Ag|AgCl electrode saturated with 4M KCL was used as reference electrode, carbon rod was used as counter electrode and catalyst modified substrate served as working electrode. Calibration of Ag|AgCl reference electrode was done using the open circuit potential (OCP, -1.99 V) with the Pt wire in H_2-saturated H_2SO_4 solution and converted to RHE according to the Equation (1):

$$E_{RHE} = E_{Ag|AgCl} + 0.059\ \text{pH} + E^0_{Ag|AgCl} \quad (1)$$

where E_{RHE} is the converted potential vs RHE, $E_{Ag|AgCl}$ is the experimentally measured potential vs Ag|AgCl reference electrode, and $E^0_{Ag|AgCl}$ is the standard thermodynamic potential of Ag|AgCl reference electrode at 25 °C (0.199 V).

The stability of the catalyst was measured using chronoamperometric studies. The current-time curve was generally recorded for more than 12 hours on the working electrode while maintaining constant the Potential value generally corresponding to i = 10 mA/cm^2. Measuring stability of the catalyst is very important as it depicts the possibility of material being used commercially.

1.2.4.4. Electrolysis method. Once the cell was assembled and CO_2 was purging the electrochemistry began. A CV was taken at 50 mV/s before the CA (chronoamperometry) section of each electrolysis experiment to ensure the reduction of any surface metal oxide present. In cases where the potential of the CA was more negative than the potential where oxide reduction occurred, then CVs were taken out to the voltage of the CA. When the CA was collected at a voltage less negative than needed to ensure surface oxide reduction, then the CV was taken to a more negative voltage than the CA. The initial CV was followed by 1 hr of CA at a set potential with the value of Ru updated every 3 mins by running a quick impedance measurement. It was necessary to update the value of Ru, particularly at the more negative potential values because the value would decrease over the course of experiment (for more on voltage measurement, see Section 2.6). After an hour of CA, another CV with the same voltage range and scan rate was collected as the original CV. For the most part, CVs collected before and after the CA experiment matched well. In cases where a slight decrease in the absolute value of the current was observed during the CA, the CV also showed a decrease in current. Section 5.6 discusses the effect of skipping the initial CV in this procedure.

1.2.4.5. Electrochemical surface area determination. Enhanced electrocatalytic activity can typically be assigned to intrinsic factors which includes facile catalyst

activation through intermediate adsorption and enhanced charge transport, as well as extrinsic factors such as catalyst morphology and surface roughness which influences electrolyte and analyte access to the catalytically active sites. The extrinsic factors affecting CO2RR electrocatalytic activity of catalyst is investigated by estimating the electrochemically active surface area (ECSA) by following previously reported experimental procedure.[75] The ECSA was calculated by plotting electrochemical double layer capacitance in the non-Faradaic region as a function of scan rate and then comparing specific capacitance ($\boldsymbol{C_S}$) to the double layer capacitance observed. The electrochemical double layer capacitance ($\boldsymbol{C_{DL}}$) was calculated following Equation (2):

$$i_{DL} = C_{DL} \times \nu \tag{2}$$

where i_{DL} represents the current observed while ν is the scan rate. C_{DL} is calculated slope of the i vs ν plot. The ratio of C_{DL} and C_S was used to calculate ECSA as shown in Equation (3):

$$ECSA = C_{DL}/C_S \tag{3}$$

Carbon rod was used as counter electrode and Ag|AgCl was used as reference electrode. Cyclic voltammetry (CV) is generally done at various scan speeds

1.2.4.6. Membrane selection. Membrane selection can a crucial decision in the electrochemical setup. There have been observations in studiesref where leaching of the contaminants has been observed. Only Nafion membranes when used leached very trace level of common solvents. Nafion solvents were soaked for very long time to remove any contaminants. Also, blank NMR measurements were done before the experiments to remove the possibility of any contamination from the membranes.

1.2.4.7. Gas chromatography: gas phase product quantification. Gas chromatography is the most reliable and easy to use analytical technique for identifying components in mixtures. Gas chromatography separates the chemical entities of a mixture of hydrocarbons, detects them to confirm their presence or absence and also quantifies the individual components for this technique to work, the components should be volatile and thermally stable.

The main components of a GC are Column and detector. Separation of the mixture which consists of gaseous products is done by column and the signal from the detector indicates the identity of the gas. Interaction of the gases with stationary phase of column separates them into individual gases. Retention time was calculated as the interval between the introduction of a sample into the column and the detection of separated components by the detector. To detect and quantify the gases from the reaction, standards with known concentration were injected into the GC-TCD. These measurements were done at different concentrations for every gas. Retention time and the area under curve of standards were used to draw a calibration curve. This curve then leads to the unknown concentration of the reaction product.

1.2.4.8. NMR liquid phase product quantification. Proton NMR was used for the detection and quantification of liquid products. Proton NMR shows the be havior of hydrogen nuclei within the molecules of a substance are placed in a strong magnetic field, for identifying the identity and structure of product molecules. In midst of different analytical techniques, NMR is not generally preferred for quantification of compounds as different T1 causes slight difference in peak areas due to change in number of scan and concentration of solution. We increased the reliability of the measurements by keeping the

no. of scans, same acquisition parameters and the concentration similar. Even with these drawbacks, NMR is the best technique to identify and quantify the liquid products. To use other analytical techniques, electrolyte ions need to be absent. This makes the process of sample preparation very difficult and leads sometimes to contamination. As the solvent is water, the NMR spectrum is dominated by the water peak. To resolve this, we used water suppression program present in topspin which educed the peak of water. NMR samples of the reaction mixture was prepared by mixing 200 µL D_2O and 500 µL reaction mixture. 10 mM dimethyl sulfoxide (DMSO) was also mixed in this mixture for quantification using NMR because of its non-volatile property which made the storage DMSO solution possible without change in concentration. Amount of the products were calculated by using the calibration curve of DMSO and comparing it with the area of the product peak. Long term storage should be avoided as DMSO is prone to oxidation.

1.2.4.9. Faradaic efficiency. The faradaic efficiency is the ratio of the charge passed for generating certain product and the total charge consumed for generation of products. The FE or selectivity foreach product in CO2RR is calculated according to the following Equation (4):

$$FE\% = \frac{\mathrm{Qx}}{\mathrm{Qtotal}} \times 100\% = \frac{\eta ZF}{it} \times 100\% \quad (4)$$

1.3. WATER SPLITTING

Hydrogen is a fuel having very high calorific value (energy density per mass = 0.0899 kg/Nm^3).[76] It also doesn't have any carbon and produce water (H_2O) after combustion. It has uses ranging from being used for heat to industry refining processes to provide electricity via fuel cells. Currently, most of the hydrogen production (96%) is

through the process steam methane reforming.[77] Very small fraction of hydrogen production (4%) is from water decomposition.[78,79] Even though steam methane reforming it is cheaper than the other production methods produces large amount of CO_2 in process.[80,81]

Implementation of hydrogen production through renewable processes depends on the cost effectiveness of catalysts and development of energy efficient processes. Water splitting coupled with renewable energy sources like wind energy is likely to be the major source of H_2 production.

Water splitting produces hydrogen without any impurity which does not happen with other methods of production which serves the requirement oh ultra-high purity hydrogen which is needed in specific industries (like electronic components manufacturing). Production cost of hydrogen from water splitting can go at low of \$3.23 kg^{-1} if electricity from renewable resource is used.[82] This price is good for ultra-high purity hydrogen needed in specific industries but if applied in common industry it is still costlier than hydrogen produced from steam methane reforming (\$2.67 kg^{-1}).[83]

1.3.1. Types of Water Electrolysis. When voltage is applied at anode, cathode, oxygen and hydrogen is produced. This process proceeds very slowly when the water is pure as ion concentration is only 10^{-7} M of both $[H^+]$ and $[OH^-]$. Salts or similar compounds are added to increase the ion concentration for more conductivity of electrolyte. Water splitting can be distinguished into three types:

1. Membrane (PEM) water electrolysis: PEM electrolysis is very promising because it generates Ver high purity hydrogen and efficiency is also high at normal tempteratures.[84] Drawback with PEM electrolysis is strong acidic environment in not

lot of materials can sustain for longer periods and that is why very limited options of electrodes.[85] Materials which can be used are noble metals as they do not corrode and have suitable work function. These noble metals are very costly and are not abundant on earth.

2. Solid Oxide Electrolyte (SOE) water electrolysis: SOE electrolyzer consumes less energy than conventional low-temperature water electrolyzer, because of the improved reaction thermodynamic and kinetic working at high temperatures. Unfortunately, high temperatures are also connected with severe corrosion issues.[86]

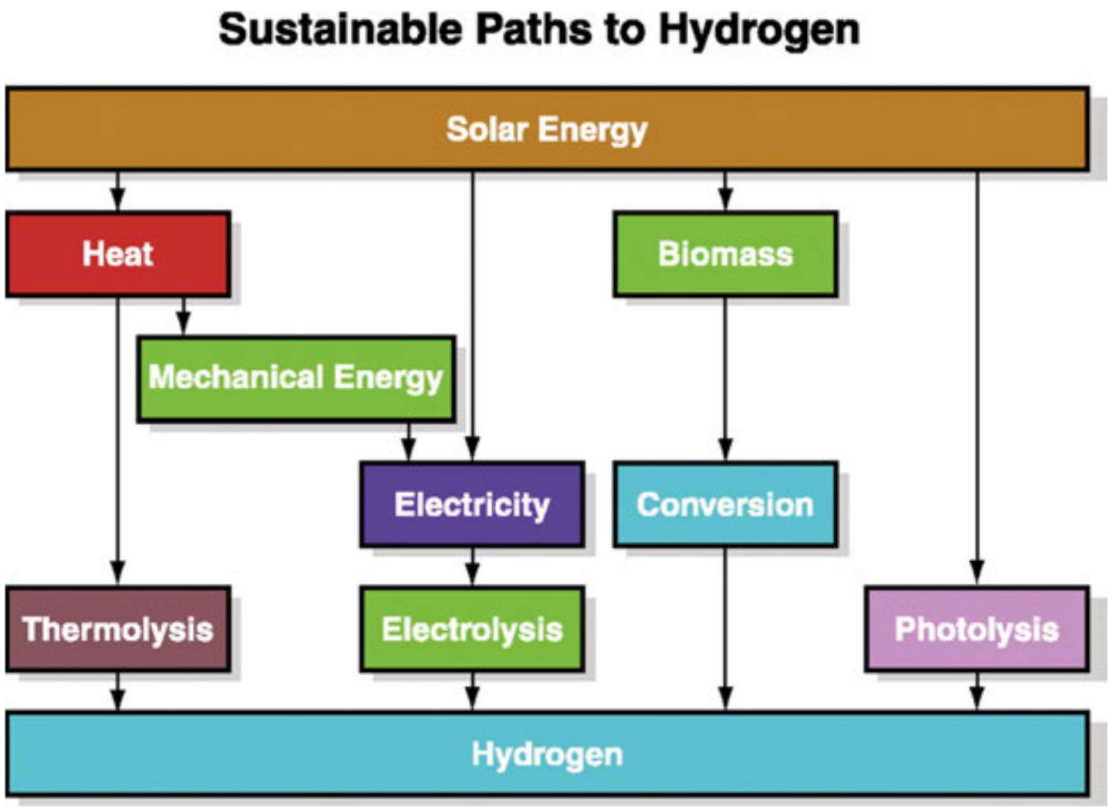

Figure 1.3. Sustainable pathways for hydrogen generation from solar energy[81]

3. Alkaline Water Electrolysis: This process has been around from long time and has been used for H_2 production.[87,88] In the setup, electrolyte used are KOH and NaOH in high concentration in water. This electrolysis is very promising because of its simple setup, better stability, and low environmental sabotage. It can perform better than PEM if thinner separators are used[89]. Lot of transition metals and transition metal compounds have shown exceptional performance. They have better corrosion resistance in alkaline electrolytes as they form passivating layer. They are used in industry as electrocatalyst and in laboratories for further development of water electrolysis.

1.3.2. Thermodynamics of Water Splitting. Water electrolysis consists of reaction of two half reactions:

- Oxygen evolution reaction, OER, happening at anode
- Hydrogen evolution reaction, HER, happening at cathode

Minimum potential which should be applied to split water is known as thermodynamic potential derived from the change in gibbs free energy of reaction.

Cathode reaction (HER):

$$4e^- + 4H_2O \rightarrow 4OH^- + 2H_2 \qquad Ec_o = 0 \text{ V vs RHE}$$

Anode reaction (OER)

$$4OH^- \rightarrow 4e^- + 2H_2O + O_2 \qquad Ea_o = 1.23 \text{ V vs RHE}$$

Overall reaction

$$2H_2O \rightarrow 2H_2 + O_2 \qquad E_o = Ea_o - Ec_o = 1.23 \text{ V}$$

But this reaction is uphill reaction i.e. it's a reaction with sluggish reaction kinetics and requires additional energy/potential to happen denoted by overpotential (η). Actual voltage required for water electrolysis is using Equation (5):

$$E_{total} = 1.23\,V + \eta_a + |\eta_c| + iR \quad (5)$$

where thermodynamic potential = 1.23 V at 298.15 K and 1atm, η_a and $|\eta_c|$ denote the anodic and cathodic overpotentials at a certain current density and *iR* - voltage drop in the electrochemical setup, determined by Ohm's law.

1.3.3. Efficiency Parameters. This section outlines the parameters used to measure the activity of catalysr by using data obtained from different electrochemical experiments.

1.3.3.1. Overpotential (η). Most important indicator of the electrocatalyst performance is overpotential (η) at specific current density. Applied potential should be equal to the reaction potential at equilibrium in the ideal situation.

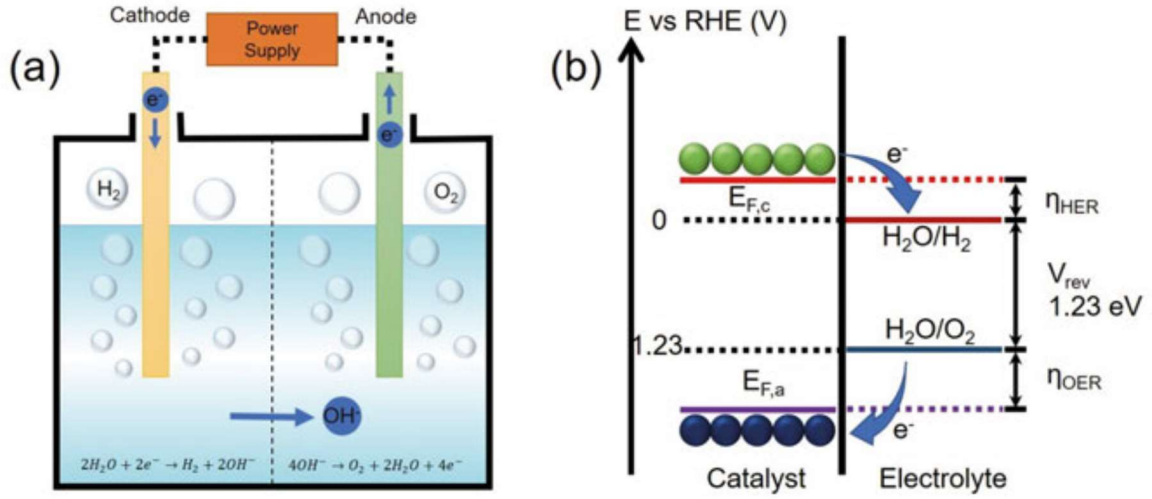

Figure 1.4. Electrochemical water splitting (a) Alkaline water splitting (b) the energy levels involved in water splitting with the overpotentials of the HER and OER indicated.

But applied potential is more than the equilibrium potential for a specific reaction because of presence of reaction energy barrier. Overpotential is the difference of applied potential and equilibrium potential.

$$\eta = E - E_{rev} \quad (6)$$

If we consider the solar energy to produce hydrogen, standard value to compare the electrocatalyst's efficiency is 10 mA cm^{-2} as for the PV systems giving voltage for water splitting is approximately 10 mA cm^{-2}.

1.3.3.2. Stability. To test the performance of the catalyst for industrial application stability is a very important factor. It can be tested using chronoamperometric test operating at a constant potential. If a catalyst doesn't show any major change in activity or current density for the period of more than 12h in chronoamperometric test at selected potential, then the catalyst is considered as highly efficient catalyst.

1.3.3.3. Tafel slope and exchange current density (J_0). Kinettics of the electrochemical water splitting can be described by the Butler-Volmer Equation (7).

$$J = J_0[\frac{\exp(\alpha_a \times n \times F \times \eta_a)}{R \times T} - \frac{\exp(\alpha_c \times n \times F \times |\eta_c|)}{R \times T}] \quad (7)$$

Here

J_0 = the exchange current density

α= the transfer coefficient of the anode or the cathode ($\alpha_a+\alpha_c=1$, usually, $\alpha_a=\alpha_c=0.5$)

F = faradays constant

T = absolute temperature

n = number of transferred electrons

OER (Oxygen Evolution Reaction) process involves four electrons while HER (Hydrogen Evolution Reaction) involves two electrons which make OER kinetically sluggish process. When we plot the polarization curves of electrocatalytic process, we can obtain the Tafel plot by plotting Log J vs overpotential which is derived by Butler-Volmer equation. For comparing the catalytic activities of different catalysts, Tafel plot is very important parameter. For the catalyst to have good activity, it should have good charge transfer which is depicted by small Tafel slope. Smaller Tafel Slope signifies fast reaction kinetics but it should be noted that Tafel slope is a quantitative characterization of reaction kinetics because it is based on assumptions taken like symmetry factor, surface coverage is constant in each catalyst.[90–92] . J_0 can be calculated by Equation (8):

$$\frac{d}{d\eta}\log|J| = 2.303\ RT/\alpha nF \qquad (8)$$

η is over potential, J is current density, n is number of electrons and T is temperature. Also, J_0 can also be calculated by equation above and if we see it with Tafel plot we can get good idea about the intrinsic bonding/charge transferring interactions between electrocatalyst and reactant.

1.4. LITERATURE REVIEW: WATER SPLITTING

The family of transition metal chalcogenides has attracted tremendous attention in the materials community due to its promising future in sensors, energy conversion and energy storage among other applications.[93–97] In addition, transition metal based electrocatalysts for electrochemical energy conversion has attracted significant attention during last several years owing to their high activity, low cost and tunability. Among these electrocatalytic water splitting which includes hydrogen evolution and oxygen evolution

reactions (HER and OER, respectively) has been the focus of major research activity.[93,98] The challenge for practical implementation of water splitting technology, however, depends on identification of suitable and stable catalysts which can lower reaction energy barrier and increase Faraday efficiency for both reactions.

Traditionally, Pt metal is most active as HER catalyst, whereas oxides of iridium (Ir), and ruthenium (Ru), exhibit higher OER performance. However, high price and low stability of these precious metal-based catalysts make commercialization difficult. Transition metal-based chalcogenides (TMCs) have recently shown unprecedented high efficiency for HER and OER in wide range of pH. [93]

1.4.1. TMC for Water Splitting. The two major half-reactions, HER and OER, are responsible for total water splitting to create pure H_2 and O_2. Although thermodynamic water splitting voltage is 1.23 V, a much larger potential is required due to energy loss in the electrochemical system necessitating use of suitable electrocatalysts.[99] Several TMCs have recently demonstrated promising performance for HER and OER, surpassing noble metal-based catalysts.[93,100,101] The TMCs typically exhibit low intrinsic electrical resistivity and rapid charge transfer owing to their electron rich transition metal centers, highly covalent network, and electrochemical tunability. These TMCs are primarily comprised of selenides and tellurides of cobalt, nickel, iron, and copper, in binary and multinary compounds. By modifying the intrinsic and extrinsic structures and compositions of TMCs, a variety of compounds containing different transition metals and chalcogens can be synthesized. In the following sections, binary and multinary (ternary, quaternary, and more complex) chalcogenides have been discussed with respect to electrocatalytic water splitting.

1.4.2. Binary TMCs. Binary metal chalcogenides, more commonly referred to as TMCs, contains one type of transition metal and one type of chalcogen. The most well-known example among them is nickel based binary metal chalcogenides (NixSey) which has been widely studied for water splitting. A variety of stoichiometric (Nise, $NiSe_2$, Ni_3Se_2, Ni_3Se_4) and non-stoichiometric ($Ni_{0.85}Se$) nickel selenides has been investigated for OER and HER.[100] Xu et al., have also compared OER catalytic performance of various Ni-based materials (NiO, NiSe, Ni_3Se_2, and Ni),[102] and have observed that Ni_3Se_2 had the best OER electrocatalytic activity due to the synergistic impact of intrinsic metal states and better surface recombination of anions in metal matrix.

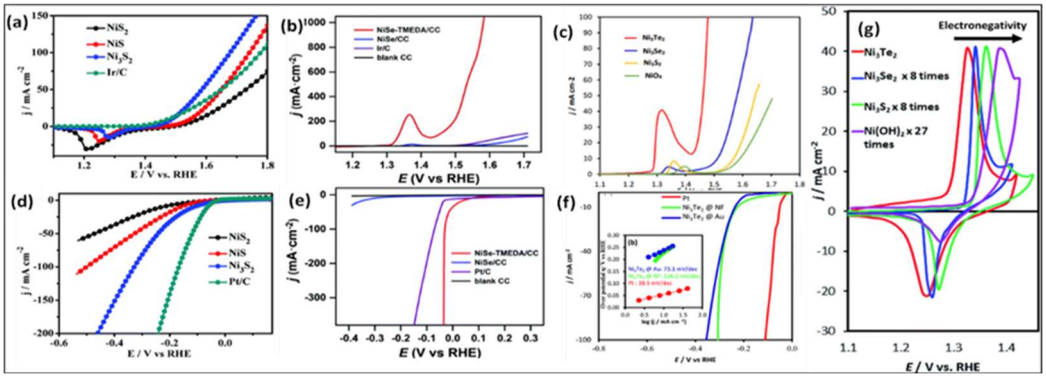

Figure 1.5. OER and HER polarization curves and it's parts (a, d) Nickel sulphide, [117] (b, e) Nickel selenide, [118]. (c) Comparison of OER polarization curves for NiO_X, Ni_3S_2, Ni_3Se_2 and Ni_3Te_2 in 1.0 M KOH depicting effect of anion electronegativity on OER activity.53 (f) HER polarization curves of Ni_3Te_2 in 1.0 M KOH. (g) Comparison of $Ni^{2+} \rightarrow Ni^{3+}$ oxidation peaks in Ni_3Te_2, Ni_3Se_2, Ni_3S_2 and $Ni(OH)_2$ confirming effect of anion electronegativity on active site generation.[53]

Umanga et al. proposed that the major cause for high catalytic activity for Ni-chalcogenides was due to increased covalency of the chalcogenide anions, which increases electrochemical activity of the transition metal center.[53] This hypothesis was confirmed by

investigating OER activity of Ni_3Te_2 and comparing it with Ni_3E_2 (E = S, Se, Te) and NiOx. Ni_3Te_2 showed an overpotential of 180 and 212 mV at 10 mA cm^{-2} for OER and HER, respectively, exhibiting one of the lowest overpotential for OER. This study further confirmed that decreasing electronegativity of the chalcogenide anions [Te (2.1) vs Se (2.55), O (3.44)], led to increased catalytic efficiency attributed to enhanced degree of covalency in nickel tellurides.[53] Figure 1.6 (a-g) represents the effect of change in chalcogenide anions on OER and HER activity for Ni based material which show an order of Ni_3Te_2 > Ni_3Se_2 > Ni_3S_2 toward the OER and NiSe > Ni_3S_2 > Ni_3Te_2 toward the HER. The effect of electronegativity in improving OER catalytic activity was also confirmed in Co-based composition, whereby, it was observed that $CoTe_2$ showed significantly improved catalytic efficiency compared to Co-oxides and selenide.[93] Density functional theory (DFT) calculations provided further insight into the structure-property correlation of these chalcogenides, wherein the -OH adsorption energy was identified as a key descriptor for OER activity.[93] The tellurides and selenides were observed to exhibit optimal -OH adsorption energy leading to most efficient catalytic activity. Apart from the nickel based chalcogenides, other metal binary metal chalcogenides such as $FeSe_2$[103], $CoSe_2$[104], $CoTe_2$[93], CuSe [105] have aroused interest for bifunctional HER and OER activity.

1.4.3. Multinary TMCs. Since the electron density around the catalytically active transition metal center plays a critical role in defining catalytic activity, it was impervious to tune that electron density through structural and compositional modifications. While changing anions in the chalcogenide series leads to change in lattice electronegativity, doping in the transition metal site can lead to more subtle change in electron density around the catalytic center through d-d transitions and advent of metal-metal bonding. Hence,

mixed-transition-metal based electrocatalysts have emerged as new pH-universal electrocatalysts for water-splitting which has also been characterized by their enhanced electrical conductivity, synergistic impact of bimetallic compositions, and structural stability. Several multinary TMC composites with tunable compositions were investigated in addition to cobalt and nickel chalcogenides. These composites typically outperformed their monometallic counterparts in terms of catalytic performance as has been exemplified through several examples.106,107 As an example, superior conductivity and reactive properties of Ni–Co bimetallic selenides has been identified as viable electrocatalysts for OER.[107] $NiCoSe_2$@PCM showed outstanding catalytic activity as a bifunctional electrocatalyst, with overpotentials of 116 mV and 140 mV at 10 mA cm^{-2} for HER and OER, respectively.107 NiFe hybrid selenides have recently been proposed as interesting OER and HER bifunctional catalysts that pave the path for the development of ternary metal chalcogenides. Xianbiao et al. suggested a self-standing $Ni_{0.75}Fe_{0.25}Se_2$@NF electrocatalyst that demonstrated remarkable OER and HER activity with overpotentials of 210 mV and 117 mV, respectively, to achieve current density of 10 mA cm^{-2}.[108] Cao et al. synthesized a bimetallic spinel-structured $CuCo_2Se_4$ electrocatalyst that requires a low overpotential of 320 mV to obtain a current density of 50 mA cm^{-2} for OER and 125 mV to achieve a current density of 10 mA cm^{-2} for HER.[98] Combinatorial electrodeposition was also utilized to examine quaternary mixed metal selenide compositions by exploring the ternary phase diagrams of Fe-Cu-Co-Se systems as shown in Figure 1.7.[109–111] In this work quaternary composition such as $(Fe_{0.48}Co_{0.38}Cu_{0.14})Se$ showed the superior OER catalytic performance with overpotential of 256 mV respectively [Figure 1.6(h-j)].[109–111]

These experiments demonstrated that transition metal doping enhanced the number of actual catalytically active sites and expedited the rate-determining steps by manipulating the OH–adsorption kinetics on the catalyst surface by changing the local electron density surrounding the catalytic site.[112] Further, Leiming et al. synthesized mixed metal telluride

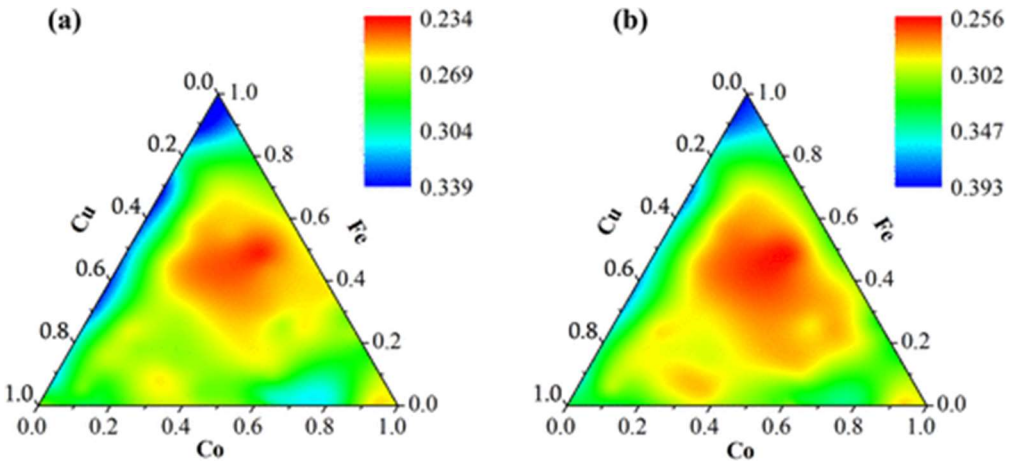

Figure 1.6. Trend of OER catalytic activity within the entire Fe–Co–Cu trigonal phase space. Mapping of overpotential η (in units of V) (a) at the onset of OER activity and (b) at a current density of 10 mA cm^{-2}.

$NiCo_2Te_4$/PTCDA which showed the superior activity in both OER and HER in neutral pH with overpotential of 120 and 60 mV respectively. Effect of doping of different transition metals like Co, Cu and V into NiSe matrix for water splitting activity was recently demonstrated by Xiaoqiang et al.[113] The catalytic performance of these M–NiSe/NF materials is M-dependent, and it follows the order V–NiSe > Co–NiSe > Cu–NiSe > NiSe toward the OER and Cu–NiSe > Co–NiSe > NiSe > V–NiSe toward the HER. Doping of NiSe with different transition metals is an example of intrinsic effect. An intrinsic doping consisting of doping in the transition metal site, leads to scrambling of the active sites and

modulation of electron density around the active site leading to change in catalytic activity.[109] Although this review is focused on alkaline water electrolysis, it must be noted that water splitting has also been conducted in acidic electrolyte to be more compatible with fuel cell systems. Accordingly electrocatalysts for acid water electrolysis has received substantial attention because of its high reaction efficiency, high current density, low overpotential, and compact design.[114–116] However, the functional and compositional instability of the chalcogenide based electrocatalysts in acidic medium over extended period of time limits their practical application.

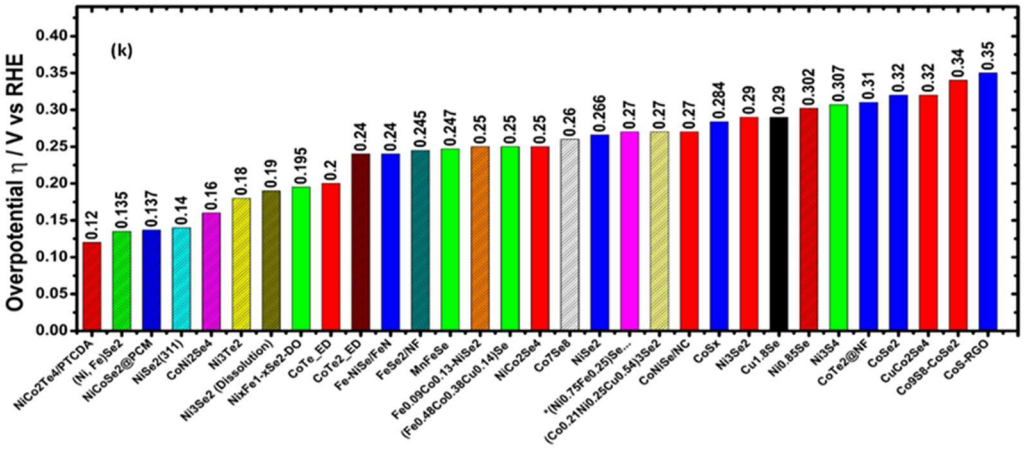

Figure. 1.7 Comparison of OER activity of various metal chalcogenides at current density of 10 mA cm^{-2}. [53,64,119–128,93,129–136,98,103,106,107,109–111]

The overpotentials of the various metal chalcogenides catalysts with high OER activity reported by different research groups has been benchmarked in terms of the overpotential at 10 mA cm^{-2} and shown in Figure 1.8. Analysis of this benchmarking figure confirms certain trends: (i) decreasing electronegativity in the chalcogenide series leads to decreasing overpotential with tellurides forming the most efficient OER electrocatalysts;

(ii) transition metal doping enhances electrocatalytic activity for OER making ternary and quaternary chalcogenides as better catalysts than the binaries in the same series. However, for such aliovalent substitution, doping with transition metals with fewer d-electrons is found to be more beneficial. This outlook can now be applied for better catalyst design incorporating less electronegative anions along with aliovalent. substitution in the catalytically active site. Table 1.3 represents the progress in binary and multinary metal chalcogenides as bifunctional electrocatalysts for overall water splitting.

Table 1.3. The comparison of OER and HER overpotentials with overall water splitting performance of selected bifunctional nonnoble transition binary and multinary metal chalcogenides.

Binary TMC'S	**Electrolytes**	**OER_η @ 10 mA cm^{-2} (mV *vs* RHE)**	**HER_η @ 10 mA cm^{-2} (mV *vs* RHE)**	**Overall Voltage @10mA cm^{-1} (V)**	**Reference**
$FeSe_2$/NF	1 M KOH	245	178	1.73	[103]
p-$CoSe_2$/CC	1M KOH	243	138	1.62	[104]
$CoTe_2$-ED	1M KOH	240	350	-	[93]
CuSe/NF	1M KOH	297	162	1.68	[105]
Ni_3Te_2	1M KOH	180	212	1.66	[53]
CoTe-NF	1M KOH	241	90	1.45	[137]
Ni_3S_2	1M KOH	400	306	2.0	[138]
$Ni_{0.85}Se$/RGO	1M KOH	320 @30	169	1.64	[139]

Table 1.3. The comparison of OER and HER overpotentials with overall water splitting performance of selected bifunctional nonnoble transition binary and multinary metal chalcogenides. (Cont.)

$CoSe_2$-NC	1M KOH	360	234	1.47@20 mA cm^{-2}	[140]
$Ni_{0.85}Se$	1M NaOH	302	200	1.73	[129]
$NiSe_2$	1M KOH	266	132	1.547	[126]
$CoTe_2$@NF	1M KOH	310	111	1.605	[130]
$Co_{0.85}Se$	1M KOH	232	129	1.60	[141]
$NiSe_2$/Ni	1M KOH	235	166	1.64	[142]
$CoSe_2$	OER_1M KOH HER_0.5 M H_2SO_4	325	167	-	[132]
$NiS_{0.5}Se_{0.5}$	1M KOH	257	70	1.55	[143]
Co_9S_8-$CoSe_2$	OER_1M KOH HER_0.5 M H_2SO_4	340	61	1.66	[133]
CoSx	1M KOH	284	102	1.64	[127]
CoS-RGO	1M KOH	350	111	1.77	[134]

Table 1.3. The comparison of OER and HER overpotentials with overall water splitting performance of selected bifunctional nonnoble transition binary and multinary metal chalcogenides. (Cont.)

Multinary TMC'S	**Electrolytes**	**OER_η @ 10 mA cm^{-2} (mV *vs* RHE)**	**HER_η @ 10 mA cm^{-2} (mV *vs* RHE)**	**Overall Voltage@10 mAcm^{-1} (V)**	**Reference**
$NiCoSe_2$@PCM	OER_1M KOH HER_0.5 M H_2SO_4	137	116	1.73	[107]
$Ni_{0.75}Fe_{0.25}Se_2$@NF	1M KOH	210	117	1.61	[108]
$CuCo_2Se_4$	1M KOH	350@50 mA cm^{-2}	125	1.782 V@50 mA cm^{-2}	[98]
$NiCo_2Te_4$/PTCDA	1 M PBS	120	60	1.55	[106]
$NiCo_2Se_4$	1M KOH	245	122	1.58	[136]
CoNiSe/NC	1M KOH	270	100	1.65	[136]
CoFe–Se–P	OER_0.1M KOH HER_0.5 M H_2SO_4	210	172.5	1.59	[144]

Table 1.3. The comparison of OER and HER overpotentials with overall water splitting performance of selected bifunctional nonnoble transition binary and multinary metal chalcogenides. (Cont.)

$NiCoSe_{2-x}$/NC	1M KOH	215	89	1.53	[145]
MnCoSe	1M KOH	243	60	1.66@50 mA cm^{-2}	[146]
FeNiSSe	OER_1M KOH HER_1 M H_2SO_4	213	91.2	1.56	[147]
(Ni, Fe)Se_2	1M KOH	135	145	1.58	[119]
$Fe_{0.09}Co_{0.13}$-$NiSe_2$	1M KOH	251	92	1.52	[124]
Mo-$CoSe_2$ NS@NF	1M KOH	234	89	1.54	[148]
$ZnCo_2S_4$/NF	1M KOH	278	185	1.66	[149]
$Fe_{0.08}Ni_{0.77}Se$/C NT_3	1M KOH	204	108	1.53	[150]
P-$(Ni,Fe)_3S_2$/NF	1M KOH	196	98	1.54	[151]
$FeCo_2S_4$– $NiCo_2S_4$/Ti	1M KOH	230	150	1.51	[152]
Fe-MoS_2/NF	OER_1M KOH HER_0.5 M H_2SO_4	230@20 mA cm^{-2}	153	1.52	[153]

Table 1.3. The comparison of OER and HER overpotentials with overall water splitting performance of selected bifunctional nonnoble transition binary and multinary metal chalcogenides (Cont.)

H–Fe–CoMoS	1M KOH	282	137	1.6@20 mA cm^{-2}	[154]
GO/Cu_2ZnSnS_4	OER_1M KOH HER_0.5 M H_2SO_4	130	47	-	[155]
Cr-$CoxS_8$		313@100 mA cm^{-2}	120	1.45	[156]
Ni–Fe-S	1M KOH	292	140	1.46	[157]
$CoNiSe_2$/NF	1M KOH	370	170	1.591	[158]
CDs/$NiCo_2S_4$ /Ni_3S_2/NF	1M KOH	116	127	1.5	[159]
$CuCo_2S_4$	1M KOH	310@100 mA cm^{-2}	65	1.65@20 mA cm^{-2}	[160]
$FeCo_2S_4$/NF	1M KOH	270@50 mA cm^{-2}	132	1.56	[161]
($Ni_{0.33}Co_{0.67}$) S_2 NWs	OER_1M KOH HER_0.5 M H_2SO_4	295@100 mA cm^{-2}	156@100 mA cm^{-2}	1.57	[162]
$NiCo_2S_4$	1M KOH	200@40 mA cm^{-2}	190	1.57	[163]
NCT-$NiCo_2S_4$	1M KOH	330@100 mA cm^{-2}	295@100 mA cm^{-2}	1.6	[164]

1.5. CONCLUSION AND FUTURE OUTLOOK

Transition metal chalcogenides have gained considerable attraction in the last few years as electrocatalysts for various electrochemical energy conversion processes owing to their tunable electrochemical properties, structural richness, enhanced charge transfer ability, and possibility of tuning electron density at the catalytic center through doing and vacancy ordering. In this review we have highlighted their high activity for electrocatalytic water splitting and CO_2 electroreduction. Various binary and multinary metal chalcogenides catalysts have been reported for OER with significantly improved catalytic performance compared to the state-of-the-art precious metal-based oxides as shown in Figure 1.8. In particular, these catalysts exhibited low η overpotentials primarily due to facile catalyst activation through enhanced electrochemical tunability of the transition metal center, which is facilitated by the lower electronegativity and higher covalency of the chalcogenide anions. These semiconducting TMCs also have a high potential for use in solar water splitting due to their ideal band gap and acceptable band edge positions that align well with both water reduction and oxidation potentials. when illuminated in acidic solutions utilizing n-type single crystals.[114–116] Coupling these transition metal chalcogenide electrocatalysts with efficient photoabsorbers to create a hybrid module will lead to significant advances in solar water splitting, by combining low overpotential and functional stability of the electrocatalysts with efficient solar energy capture. Interestingly, the transition metal chalcogenides function as highly efficient electrocatalysts for CO_2 electroreduction, producing carbon-rich products with high selectivity. Such capability makes these TMS highly applicable for CO_2 utilization which has become an issue of prime interest to reduce carbon footprint of industrial processes.

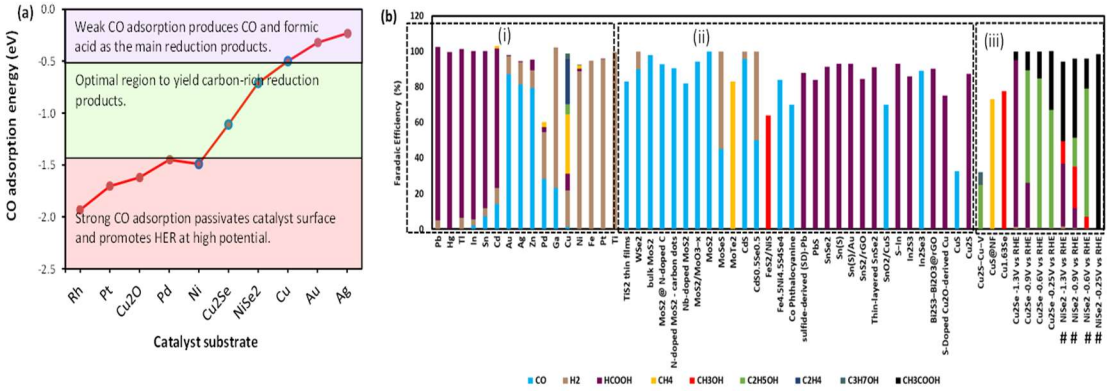

Figure 1.8. Experimental and theoretical studies (a) Comparison of the *CO adsorption energy calculated on various catalyst surfaces estimated from DFT calculations. (b) Benchmarking of CO2RR activity of various metal chalcogenide electrocatalysts highlighting the various reduction products formed, [31,58,172,73,165–171,37,34.]

In this report, we have discussed the fundamental issues related to formation of carbon-rich product from CO_2 electroreduction and its relationship with the underlying chemical reactions on the catalyst surface. By comparing the product formation on various catalyst surfaces it was observed that *CO dwell time on the surface can be used as an appropriate descriptor for tuning the product composition. The *CO dwell time depends on the CO adsorption energy on the catalytic site. Comparison of the CO adsorption energy on various catalyst surfaces showed that weak adsorption energy (leading to less *CO dwell time) resulted in C1 products, whereas very high adsorption energy leads to indefinite stay of *CO on the surface and catalyst poisoning as seen in Ni, Pd and Pt. This observation offers insight into designing an optimal catalyst surface where the CO adsorption energy should be in the middle range as shown in Figure 1.7(a) to yield predominantly C2+ products. Tuning anion electronegativity and changing the transition metal center can lead

to such optimal *CO adsorption energy as is shown in the benchmark Figure 1.7(c). The section marked as (i) and (ii) in Figure 1.7(c) shows catalysts producing mainly C1 products and H_2, wherein, (i) represents the base metals, while (ii) contains the binary and ternary compounds. This can be attributed to lower *CO adsorption energy. Section (iii) represents catalysts that can produce C2+ products. Hence, future outlook for effective CO_2 reduction electrocatalysts with high selectivity for carbon-rich product involves designing the catalyst surface that can facilitate metal-ligand (CO) back-bonding by aligning the metal d-orbitals with the ligand (CO) π^* orbitals, leading to better CO dwell time on the surface and optimal *CO adsorption energy. Such catalysts can have significant effect on CO_2 utilization by forming value-added chemicals and fuels from waste CO_2.

Several of these TMCs have shown efficient catalytic activity for both anodic and cathodic processes such as OER-HER and OER-CO2RR, respectively, making them suitable as bifunctional electrocatalyst. Among these, the OER-CO2RR bifunctional activity is useful, since such electrocatalytic cell (as shown in Figure 1.7 (b)), can essentially reduce atmospheric CO_2 to value-added carbon-rich products while enriching O_2 in the atmosphere.[7] Such electrochemical setup has also been used to carry out more economical oxidation processes such as methanol oxidation, ethanol oxidation, urea oxidation etc.[173,174] It will be interesting to explore such electrocatalytic activity for TMCs. Such bifunctional activity can be lucrative for practical industrial applications since it has minimum energy expense and the total cell potential for this Methanol oxidation/OER-CO2RR electrolytic cell is lower than combination of individual processes.

PAPER

I. SELECTIVE ELECTROREDUCTION OF CO_2 TO CARBON-RICH PRODUCTS BY SIMPLE BINARY COPPER SELENIDE ELECTROCATALYST

Apurv Saxena[a], Wipula Liyanage[a], Jahangir Masud[b], Shubender Kapila[a], Manashi Nath[a]*

Deparment of Chemistry, Missouri University of Science and Technology, Rolla, MO 65409

ABSTRACT

In this article solvothermally synthesized copper selenide nanostructures have been resported as highly efficient electrocatalysts for carbon dioxide reduction under ambient conditions with high selectivity for carbon rich C2 products at low applied potential. On addition to electrochemical measurements, density functional theory calculations were also performed to investigate adsorption energy of the key intermediate carbon monoxide on the catalyst surface. The authors proposed that CO adsorption energy on the surface can be a critical component to determine extent of CO_2 reduction on the surface, whereby a low CO adsorption energy was expecetd to yiled primarily C1 products while very large adsorption energy leads to catalyst posioning. In this article the authors have shown that by carefully designing catalyst surface to optimize CO adosrption energy and dwell time, selenide based electrocatalysts can indeed show more efficient CO_2 reduction compared to the base metal, leading to carbon-rich products. This is one of the first reports where Cu_2Se surface has been studied in detail with experimental as well as DFT studies for CO_2 reduction. Interestingly, the reduction products showed dependence on applied potential

forming exclusively formic acid at high applied potential (1.2 V and higher vs RHE) while ethanol and acetic acid were produced in high yield at potentials lower than 0.8 V vs RHE. The applied potential required for CO_2 with copper selenide was as low as 100 mV vs RHE and is one of the lowest reported till date. The CO_2 reduction products were analyzed through NMR and GC TCD spectroscopy which showed ethanol and acetic acid production in excess of 80% Faradaic efficiency at low applied potential.

1. INTRODUCTION

While fossil fuel combustion continues to supply power to meet majority of global energy needs, the Achilles heel of the entire process is the production of copious quantities of carbon dioxide, CO_2 as a natural by-product. CO_2 representing the highest oxidation state of carbon, is a linear molecule containing sp-hybridized carbon doubly bonded to two O atoms. CO_2 is thermodynamically stable product and hence keeps enriching the atmosphere with increasing concentration. The natural escape route for atmospheric CO_2 is provided through sequestration by forest cover on the earth's surface, which over the past several decades has been depleted significantly making way for industrial landscape. While the effect of atmospheric CO_2 on global warming is a controversial topic in the current socio-political scenario, undisputed fact is that atmospheric carbon dioxide concentration is at an all-time high and is projected to rise in the next several years with a steeper slope.[1,2] Intergovernmental Panel on Climate Change (IPCC) in its 2018 report has indicated a strong risk of crisis as early as 2040 due to rising CO_2 levels in the atmosphere, which includes worsening food shortages and wildfires, and a mass die-off of coral reefs.[3-

[7] Currently CO_2 level in the atmosphere exceeds 400 ppm,[2] and CO_2 sequestration and storage will simply not be enough to combat this problem.[8] Hence a clever solution is direly needed whereby this huge amount of atmospheric CO_2 can be converted back to valuable chemical products thereby, closing the loop. However, CO_2 reduction reaction, (CO2RR) is a kinetically slow, energy intensive uphill reaction which necessitates the use of suitable catalysts that can lower the activation barrier and bring CO_2 out of the potential well. CO_2 is an extremely stable molecule with a high bond strength (~532 kJ/mol) and needs a high electrical potential to be activated in an electrochemical environment. Hence electrocatalysts which lowers this activation barrier, plays a predominant role for CO2RR and are considered to be the backbone of the entire process.[9-12] Although tremendous amount of research has been done for catalytic CO2RR,[13-22] catalyst design still presents a significant challenge in terms of product selectivity, lowering constraints of operating conditions (such as high voltage, pressure and temperature), and lastly economic feasibility.

Over the last several decades, significant amount of research has been conducted on converting CO_2 to other carbonaceous products through homogeneous[13-16] as well as heterogeneous catalysis.[17-22] Among the various catalysts reported for CO2RR, a major chunk includes precious metal based catalysts, such as Pt, Pd,[23] Ru, Au,[24] Ag[25] and their alloys. Recently, intensive research has led to identification of several non-precious transition metal based CO2RR catalysts based on Cu and Ni.[26-29] While this is definitely exciting from a practical point of view, the hindrance lies in range and selectivity of reduction products obtained. Typically, range of CO2RR products are categorized as C1 or C2 products depending on the formation and extent of C-C linkage. In most cases CO2RR

with Cu- and Ni-based catalysts leads to a mixture of predominantly C1 reduction products primarily composed of carbon monoxide (CO), formate ion and formic acid, with trace amounts of formaldehyde or methanol.[28-30] While the lack of selectivity is a serious issue, the more detrimental fact is that CO, a toxic gas, is not a desirable product to be released in the atmosphere and hence must be reduced/processed further (typically through syn gas conversion) making the whole process tedious, cumbersome and less efficient. Rather, direct electroreduction of CO_2 to alcohols or other value-added hydrocarbons with higher carbon content (C2 or higher) is more desirable.

Among the various transition metals studied for CO2RR, Cu has attracted most attention due to the range of reduction products formed under ambient conditions as well as feasible electroreduction of CO_2 at low applied potential.[31] Bulk Cu as well as Cu nanoparticles has been shown to primarily produce CO and CH_4. Hori et al.[32] reported extensive study of CO_2 electroreduction using Cu electrodes and described the product distribution at different applied potentials. C1-C3 products were produced when the CO2RR was carried out in presence of Cu.[31] It has been claimed that size of Cu nanoparticles also has an effect on CO_2 reduction products.[33] Even morphology and surface roughness of Cu can effect Faradaic efficiency and selectivity of the reduction products.[34] Cu films oxidized on the surface gives some C2 products.[35] Cu nanocrystals produces formic acid (HCO_2H) at -0.5V (vs RHE) with Faradaic efficiency of 28%.[36] Cu fibers and Cu nanowires also showed selectivity at different applied potential. Variation of crystal dimensions also led to selectivity for different products. Fe porphyrin on CNTs showed CO2RR activity producing CO at 0.5 V overpotential.[37] It was observed that doping can also influence the electrocatalytic properties with respect to CO2RR. For example,

products of CO_2 reduction with boron doped diamond vary in amount as a function of boron content and maximum Faradaic efficiency (75%) for producing formic acid was obtained with boron content of 0.1%. The Faradaic efficiency decreased with increasing boron content.[38] Multiphase systems like Cu on TiO_2, Ag on TiO_2 or $In(OH)_3$ were also observed to be photocatalytically active for CO2RR with a 97% conversion to CH4 under normal solar illumination.[39] Cu_2O has also been reported as a electrocatalyst for CO2RR.[40] In addition, WSe_2 and $MoSe_2$ has also shown good activity for CO2RR.[41] Although Cu has proved to be a cheap and energy efficient electrocatalyst for the CO_2 reduction, the lack of product selectivity at room temperature under ambient conditions has been less than ideal, leaving plenty of room for improvement in catalyst performances.[42] Although Faradaic efficiency of CO2RR products formed from metal-based electrocatalysts (Cu, Ni, Au, Ag, and Pd) are reasonable, they suffer from several major drawbacks, the most concerning being poisoning of the catalyst surface with CO and other reaction intermediates, and deactivation of the catalysts within a small time. These metallic electrocatalysts also have very low Faradaic efficiency for C2 or higher carbon-rich products.[43-45] Surface modification of the metal catalysts by forming oxide layers could reduce the catalyst poisoning and deactivation problems slightly. However, with Cu_2O electrode, the Faradaic efficiency of the hydrocarbon products were also reduced compared to Cu, and CO became one of the major products again. Hence, while Cu_2O showed sustained catalytic activity for CO_2 reduction compared to Cu, lower Faradaic efficiency and lesser product selectivity, leads to the feasibility of Cu_2O as practical CO2RR electrocatalyst as being severely challenging.[46] In a study by Ramirez and coworkers, experimental and theoretical study of chalcogen modified copper for CO_2 electroreduction was performed which resulted in

selective electroreduction of CO_2 into formate. This study concluded that formate generation happens because of presence of basic sites where CO_2 was secured preventing its dissociation toward CO.[47,48]

Previously it has been reported that reducing anion electronegativity around the catalytically active transition metal site leads to better modulation of electrochemical redox of the catalytic site leading to lowering of the activation energy for electrocatalytic activity. Hence, we propose that Cu-based chalcogenides will show better electrocatalytic activity for CO2RR at lower applied potential compared to oxides and the base metal. Moreover, we further propose that reducing anion electronegativity will also lead to enrichment of electron density around the transition metal center, which will influence binding energy of CO intermediate on the surface, which becomes crucial for preferential formation of C1 and C2 reduction products. Specifically, we have proposed that optimal CO adsorption energy on the catalyst site is required to maximize dwell time of CO intermediate on the surface, enough for further reduction to form carbon-rich products, while weak CO adsorption energy leads to ready desorption of C1 products (CO and formic acid). High CO adsorption energy, on the other hand, leads to catalyst surface poisoning. We have applied this concept to design selenide based electrocatalyst surface as optimal catalyst for CO2RR producing carbon-rich products.

In this article we have reported the highly efficient electrocatalytic activity of copper selenide (Cu_2Se) nanostructures obtained via solvothermal method. Cu_2Se nanoparticles exhibited enhanced CO2RR activity at low applied potential ranging from -0.1 to -1.3 V vs RHE with high product selectivity, high Faradaic efficiency, and functional stability for prolonged period of time. At very low negative potentials, C2 products like

ethanol and acetic acid were obtained selectively, whereas at high negative potentials, C1 product such as formic acid was obtained almost exclusively. Interestingly, no CO was detected in the product composition. We have also performed density functional theory (DFT) calculations to estimate CO binding energy on the catalyst surface and correlate that with typical CO2RR products obtained with various catalyst systems (Cu_2Se, Cu_2O, Cu etc.) and validate our hypothesis regarding CO adsorption energy and preferential formation of C1/C2 products.

2. EXPERIMENTAL METHODS

2.1. MATERIAL

Cuprous oxide (Cu_2O, 99%), selenium, hydrazine (99.5%) and $NaHCO_3$ (99.7%) were purchased from Sigma-Aldrich and used without purification. Deionized water was used to prepare all solutions and to rinse samples and glassware.

2.2. SOLVOTHERMAL SYNTHESIS OF CU_2SE

1.0 mmol Cu_2O was mixed in 5.0 ml of H_2O and stirred for 15 minutes. Then 1.0 mmol Se powder was added to the reaction mixture and stirred for another 30 minutes. 2.0 ml of hydrazine ($N_2H_4.H_2O$) was added dropwise to the mixture with continuous stirring for 10 minutes. The resulting solution was transferred to a polytetrafluoroethylene (PTFE) lined stainless-steel autoclave. The autoclave was sealed and maintained at 185 °C for 24 h, then cooled naturally to room temperature. The product formed was washed and centrifuged for several times with DI water and then with mixture of ethanol and water to

remove impurities and unreacted precursors. Lastly, the product was dried in a vacuum oven at 35°C for 24 h.

2.3. PREPARATION OF ELECTRODES

To check the activity of copper selenide powder, the working electrodes were prepared by drop-casting catalyst ink on carbon fiber paper (CFP). Typically, a catalyst ink was prepared by dispersing 5 mg of catalyst (copper selenide) powder in 250 µL Nafion solution (50 µL of 1% Nafion solution in 50 µL of 50% IPA in water). After 30 minutes of ultrasonication, 50 µL of the dispersion was drop casted on a confined area (2 cm^2) on carbon fiber paper substrate. The drop-casted Cu_2Se@CFP film was then dried at room temperature and further heated at 130 °C for 30 minutes in an oven.

2.4. PREPARATION OF ELECTROLYTE

$NaHCO_3$ aqueous solution was used as electrolyte for CO2RR. 0.3M $NaHCO_3$ electrolyte solution was prepared from stock solutions of higher concentration in DI water, which were then diluted to the target molarity.

3. METHODS OF CHARACTERIZATION

3.1. POWDER X-RAY DIFFRACTION

The crystalline phase of as-synthesized catalyst powder was identified through powder X-ray diffraction (pxrd) with Philips X-Pert utilizing CuKα (1.5418Ǻ) radiation. Pxrd pattern was collected from the pristine product with no further treatments.

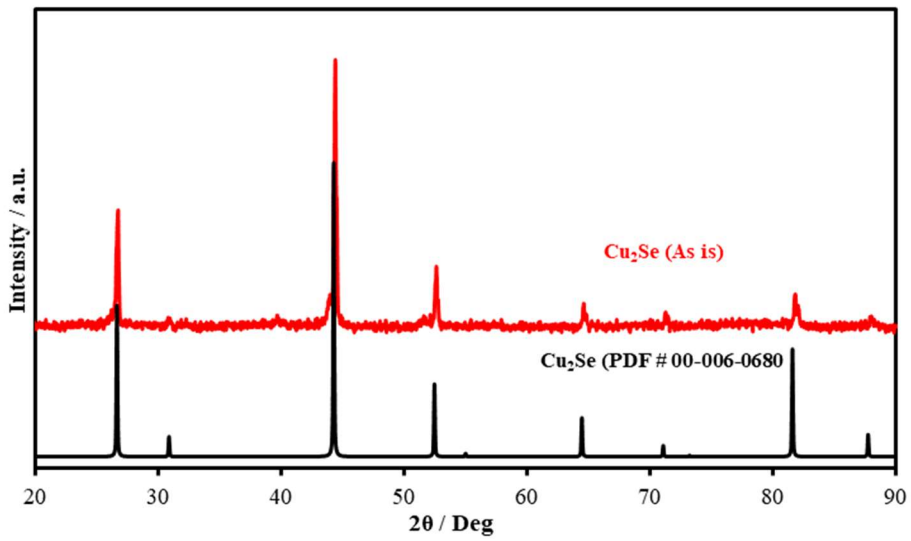

Figure 1. PXRD pattern of hydrothermally synthesized Cu_2Se compared with the standard Cu_2Se reference pattern (PDF # 00-006-0680).

3.2. SCANNING ELECTRON MICROSCOPY (SEM)

SEM images of the Cu_2Se-modified electrode surfaces was obtained using a FEI Helios NanoLab 600 FIB/FESEM at an acceleration voltage of 10 kV and a working distance of 4.8 mm. Energy dispersive spectroscopy (EDS) along with line scan analysis was also obtained from the SEM microscope.

3.3. X-RAY PHOTOELECTRON SPECTROSCOPY (XPS)

The oxidation states of the elements in copper selenide samples were investigated by X-ray photoelectron spectroscopy (XPS) using the KRATOS AXIS X-ray Photoelectron Spectrometer with monochromatic Al X-ray source. All XPS measurements

of the catalyst surface were collected as-is without sputtering. C1s signal at 284.5 eV was used as a reference to calibrate all the XPS binding energies.

3.4. ELECTROCHEMICAL CHARACTERIZATION AND ELECTROCATALYTIC STUDIES PREPARATION OF ELECTROLYTE

Electrochemical H-cell was used in this study consisting of separate cathode and anode compartments with a volume of 30 ml each, separated by an anion exchange Nafion (115) membrane. The linear sweep voltammetry (LSV) was performed in N_2-saturated, and CO_2 saturated 0.3 M $NaHCO_3$ electrolyte with a scan rate of 10 $mV.s^{-1}$. In this study carbon rod was used as counter electrode, Cu_2Se@CFP and Ag|AgCl|KCl(sat.) were used as working and reference electrodes, respectively. The Ag|AgCl reference electrode was calibrated using open circuit potential (OCP, −0.199 V) measured with a Pt wire in H_2-saturated H_2SO_4 solution. The potential measured in Ag|AgCl was converted to reversible hydrogen electrode (RHE) using the Equation (1):

$$E_{RHE} = E_{Ag|AgCl} + 0.059\,\text{pH} + E^{0}_{Ag|AgCl} \quad (1)$$

where E_{RHE} is the converted potential vs RHE, $E_{Ag|AgCl}$ is the experimentally obtained potential, $E°_{Ag|AgCl}$ is the standard potential of Ag|AgCl (0.199 V), and the pH of CO_2 saturated 0.3 M $NaHCO_3$ was measured to be 6.8. 0.3M $NaHCO_3$ in cathode compartment was saturated with CO_2 through continuous purging at the rate of 10 sccm using mass controller during the experiments.

3.5. TAFEL PLOTS

For explaining the kinetics of a reaction and electrocatalytic activity, Tafel slope is an important parameter. and Tafel equation can be expressed as follows:

$$\eta = \alpha + (2.3\ RT)\ \log j\ /\alpha nF \quad (2)$$

where η is the overpotential, α is the transfer coefficient, n is the number of electrons involved in the reaction, F is the Faraday constant, j is the current density, and the slope is given by 2.3RT/ αnF.

The Tafel equation as shown in equation (2) is a fundamental equation which acquires from the kinetically controlled region of CO2RR and relates the overpotential Z with current density j where the Tafel slope is given by 2.3RT/anF. To calculate Tafel slopes, LSV plots were obtained with a slow scan speed (10 mV s^{-1}) in non-stirred solution.

4. RESULTS AND DISCUSSION

4.1. STRUCTURE AND MORPHOLOGY OF CU_2SE

Composition and phase of the hydrothermally synthesized product was ascertained with XPS and pxrd, respectively. The pxrd pattern as shown in Figure 1 confirmed that the as-synthesized product was primarily composed of crystalline Cu_2Se and the diffraction lines could be well-matched with that of standard Cu_2Se phase (PDF# 00-006-0680).

Morphology of the product was studied through SEM which showed that the hydrothermally synthesized Cu_2Se formed nanocubes (Figures 2a and 2b) with sizes in the range of 100 nm – 1 μm and exhibiting considerable surface roughness. These granular nanocubes were comprised of Cu and Se with a relative atomic ratio of approximately 2:1, respectively, as shown in Figure 2c. The EDS measurements were typically performed on different regions of catalyst surface to confirm uniformity of composition. While EDS confirmed the presence of Cu and Se uniformly throughout the sample, it also confirmed

absence of even trace amounts of oxygen, confirming that the sample composition was indeed pure Cu_2Se. The composition of the catalyst was also confirmed through XPS studies. Figure 2d represents the deconvoluted Cu 2p XPS peak for as-synthesized Cu_2Se catalyst where the peaks at 932.8 and 953.1 eV for Cu^{1+} $2p_{3/2}$ and $2p_{1/2}$ peaks and 934.1 and 954.8 eV for Cu^{2+} $2p_{3/2}$ and $2p_{1/2}$ peaks, confirmed the presence of Cu in +1/+2 mixed oxidation states.[49] The coexistence of +1 and +2 mixed valence states for Cu has been reported previously in Cu_2Se.[40] The deconvoluted Se 3d XPS spectra (Figure 2e) showed peaks at 54.5 and 55.3eV corresponding to Se $3d_{5/2}$ and Se $3d_{3/2}$, respectively, in accordance with previously reported spectra for Cu_2Se.[49] The oxidation state of Se was estimated to be Se^{2-} by comparison with previously reported literature.[49] The relative ratio of Cu^{2+} and Cu^{+} was also estimated from the deconvoluted XPS spectra as shown in Figure 2 using area under the peaks. A Cu^{2+}: Cu^{+} ratio of 1.07 was obtained for the pristine catalyst. These XPS results along with pxrd confirmed that the predominant phase of these solvothermally synthesized catalyst powder was Cu_2Se. Comparison of XPS spectra collected before and after long-term electrolysis shows that Cu and Se XPS peaks do not change positions indicating no change in oxidation states and/or coordination geometry. The Cu^{+}: Cu^{2+} ratio after prolonged CO2RR activity shows minimal change (Cu^{2+}:Cu^{+}=1.07) compared to pristine sample. Selenium oxidation state remains -2, same as before activity.

4.2. ELECTROCHEMICAL PERFORMANCE AND CO2RR CATALYTIC ACTIVITIES

The solvothermally synthesized Cu_2Se powder was assembled onto a CFP electrode following method as described in the methods section. A typical catalyst loading of 1.25 $mg.cm^{-2}$ was used for most electrochemical measurements reported in this manuscript.

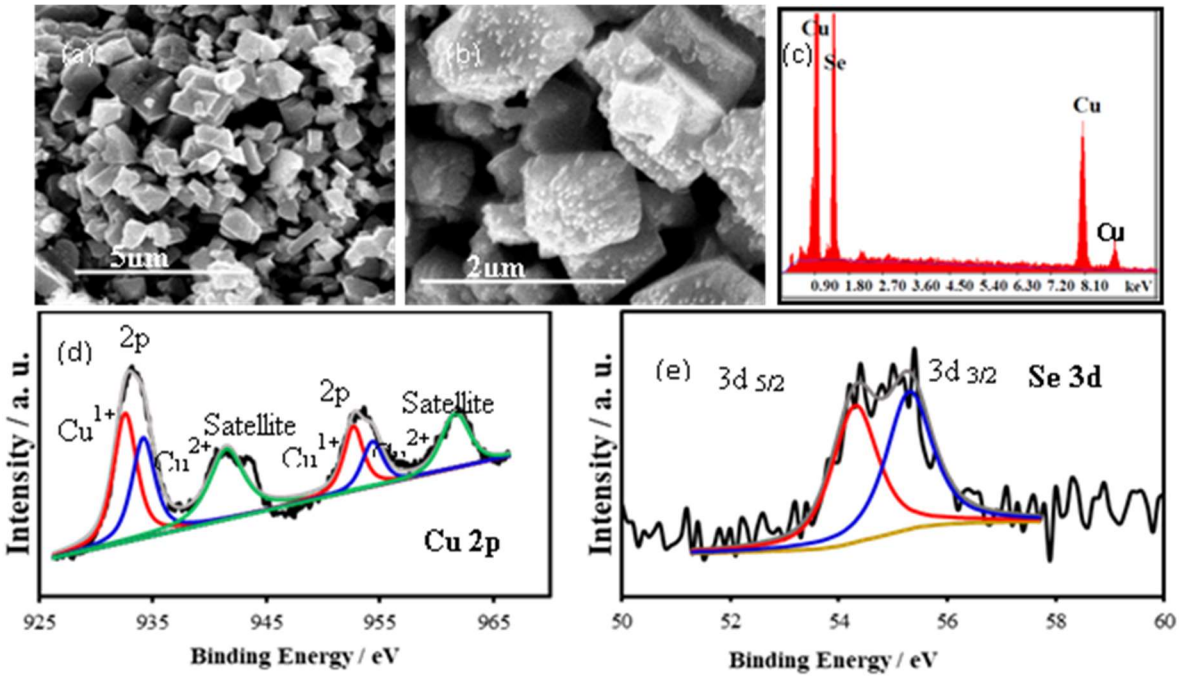

Figure 2. SEM images of the Cu_2Se nanoparticles at (a) low and (b) high magnification showing formation of nanocubes and surface roughness, respectively. (c) EDS analysis of the catalyst confirming presence of Cu and Se in 2:1 relative atomic ratio. (d) Cu 2p and (e) Se 3d XPS spectra of as-synthesized Cu_2Se.

Carbon fiber paper (CFP) was used as the substrate. Catalyst ink was dropcasted on the the carbon fiber paper was prepared by dispersing the catalyst powder in 1% Nafion solution in ethanol. Then this electrode is left to dry overnight in the fumehood. This electrode is used as working electrode in 3 electrode setup. Electrolyte is purged vigorously for 30 minutes before starting the experiments so that electrolyte gets saturated by carbon dioxide gas. To investigate the electrocatalytic property of Cu_2Se towards CO_2 reduction, electrochemical studies were performed in 0.3 M $NaHCO_3$ solution (pH = 6.8) with continuous purging of CO_2 gas at room temperature under ambient pressure. Linear scan voltammetry was used for checking activity of the catalyst. The electrochemically active surface area (ECSA) of the catalyst composite was calculated from electrochemical double

layer capacitance as a function of scan rate measured in the non-Faradaic region (Figure 3) and comparing this capacitance with the specific capacitance (C_S) obtained from the literature.49 The double layer capacitance (C_{DL}) was estimated by using equation (3) wherein, i_{DL} is the measured current and ν is the scan rate.

$$i_{DL} = C_{DL} \times \nu \quad (3)$$

$$ECSA = C_{DL}/C_S \quad (4)$$

C_{DL} estimated from the i vs ν plot as shown in inset of Figure 3 gave a value of 0.49 mF. ECSA estimated as the ratio between C_{DL} and CS (equation. 4), was calculated to be 12.25 cm^2 using a C_S value of 40μF cm^{-2}, typical of the electrolyte as reported in previous literature.49 The roughness factor (RF) of the electrode composite estimated from the ratio between ECSA and geometric area, was estimated to be 153.12. A high ECSA and

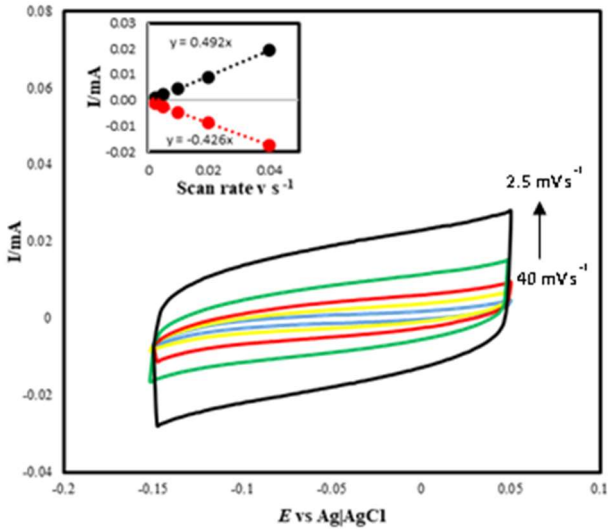

Figure 3. Cyclic voltammograms measured for Cu_2Se catalyst in 0.3 M $NaHCO_3$ at continuous N_2 purging at different scan rates from 2.5 to 40 mV s^{-1}. Inset shows plot of anodic and cathodic current measured at 0.044 V vs Ag|Agcl as function of scan rate.

roughness factor typically signifies a rough catalyst surface which facilitates electrolyte access to the catalytically active sites and hence is expected to enhance electrocatalytic activity.

The CO2RR activity of Cu_2Se modified CFP electrode was checked by measuring the current-voltage polarization curves in 0.3M $NaHCO_3$ solution in presence and absence of dissolved CO_2 introduced in the solution by purging. Similar measurements were also performed with blank CFP electrode to study the effect of substrate only as shown in Figure 4a. It was observed that blank CFP did not show much current response in absence of CO_2. Purging the solution with CO_2 changed the polarization curve for the CFP very slightly. The Cu_2Se@CFP electrode on the other hand, showed a significant change in the polarization curve in presence of dissolved CO_2 in the bicarbonate-based electrolyte as can be seen in the Figure 4a. A significant reduction current was observed between 0.2 and −0.4 V vs RHE for Cu_2Se@CFP electrode in presence of CO_2 similar to those reported previously for other CO2RR systems such as Pd layers deposited on Pt(Pd−Pt)9. This reduction current can be due to either direct carbon dioxide reduction on the electrode surface or indirect reduction of bicarbonate anion (HCO_3^-) to formate/formic acid. It has been reported previously that as pH decreases near the electrode surface with decreasing potential due to continuous hydrogen evolution,[24] in situ conversion of CO_2 to HCO_3^- occurs. However, such spontaneous conversion occurs at high concentration of nascent hydrogen and consequently at higher applied potential. From the linear sweep voltammetry (LSV) studies as shown in Figure 4, it was confirmed that although CFP was minimally responsive towards CO2RR, the Cu_2Se-modified CFP has high catalytic activity towards CO2RR and can exhibit high current density in excess of 50 $mA.cm^{-2}$ at low applied

potential. Kinetics of CO_2 electrochemical reduction on Cu_2Se@CFP was also studied through Tafel plots as shown in Figure 4b. The Tafel slope was estimated to be 126.8mV dec^{-1} for the CO_2 electroreduction on Cu_2Se@CFP electrode which is much smaller than the Tafel slope of only CFP substrate indicating that electron transfer from the Cu_2Se modified electrode surface is much faster. It should be also noted that the Tafel slope of CO2RR (126.8mV dec^{-1}) on Cu_2Se is different than that of protonation (134.2 mV dec^{-1}) which was calculated from polarization curve of Cu_2Se@CFP electrode without CO_2 purging. Tafel slopes typically provide insight regarding reaction kinetics as well as information about the rate determining step. The Tafel slope obtained for Cu_2Se catalyst was comparable to other CO2RR electrocatalyst systems.[50,51] To analyze the composition of different products being formed through CO2RR on Cu_2Se@CFP electrodes, CO_2 electroreduction were performed at different applied potentials (-1.3 V, -1.2 V, -0.9 V, -0.6 V, -0.25 V, -0.1 V vs RHE) held constant for 1 h in 0.3M $NaHCO_3$ under constant purging with CO_2 gas at low flow rate (20 sccm).

The gaseous products from CO_2 reduction were examined with gas chromatography equipped with thermal conductivity detector (GC-TCD) (Figure S1), while the liquid products were quantified by 1H NMR spectroscopy (Table S1). It was observed that the CO2RR products chemistry was dependent on the applied potential and exhibited a significant product selectivity as can be seen in the NMR plots (Figure 5a) collected at different applied potential. Interestingly, it was observed that at low applied potential the reduction products consisted of exclusively higher carbon-content compositions such as ethanol and acetic acid. As applied potential was increased, the amount of these carbon-rich products (ethanol, acetic acid) increased in yield, while above -0.6 V (vs RHE) minute

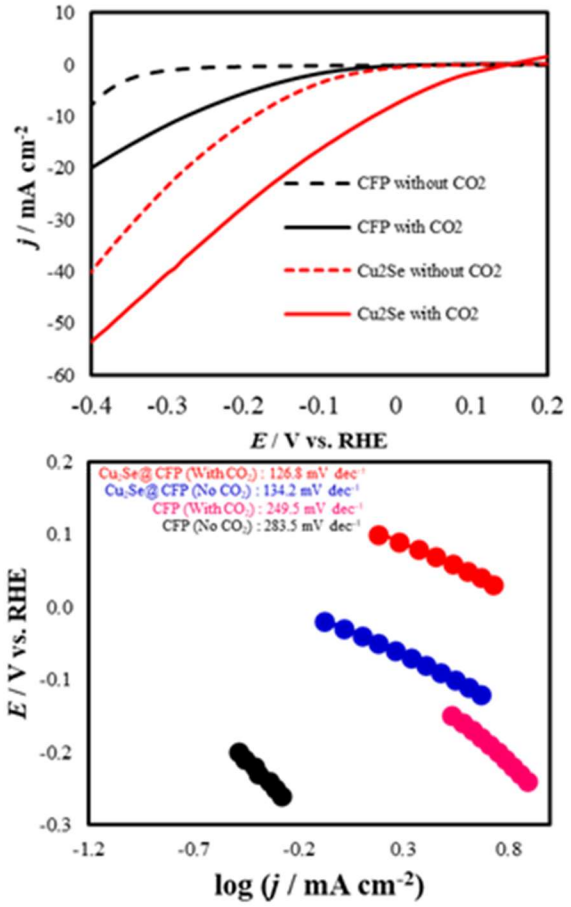

Figure 4. Electrochemical performance of $NiSe_2$ (a) LSVs measured in 0.3M $NaHCO_3$ at a scan rate of 10 mV s^{-1} in presence and absence of CO_2 with different electrodes. (b) Tafel plots measured in 0.3 M $NaHCO_3$.

quantities of C1 product such as formic acid could be detected along with ethanol and acetic acid. As the applied potential was increased even further, amount of formic acid production increased along with decrease in the relative quantities of ethanol and acetic acid. At significantly higher applied potential (-1.2 V vs RHE) the product formed was exclusively formic acid as detected through NMR (Figure 5a). The relative product yields at different potentials was estimated by quantifying the NMR plots as mentioned in

supporting information (Table S2). Figure 5b shows the product selectivity at different applied potential. It was observed that at lower applied potential C2 products formed more preferably while the C1 products formed exclusively at higher applied potential. Such product selectivity is extremely important for practical implementation of catalytic CO2RR as a viable technology. More importantly, formation of higher carbon-rich fuels such as ethanol with high selectivity at low applied potential and consequently with lesser energy expenditure, will also have significant implication in practical application of these CO2RR reactions. The gaseous products formed at different applied potential was also investigated by collecting the head space gas after 1 h of CO2RR. Interestingly no carbon monoxide (CO) was detected while there was minimal production of H_2 at high applied potential. Production of H_2 increased considerably at higher applied potential (-0.9 V vs RHE and above). HER is known to compete with CO2RR and it has been a challenge to design catalyst surfaces that will suppress HER while favoring CO2RR. For Cu_2Se-modified electrodes, since CO2RR can occur at much lower applied potential than required for HER, production of hydrogen is inhibited, while hydrocarbon production is enhanced at low potentials. The total Faradaic efficiency for CO2RR was calculated by considering both liquid and gas phase products quantified through GC-TCD and NMR analysis performed on the same experimental set-up and taking into account all the products that were detected. Typically, electron mole fraction required for each product formation was used along with the product mole fraction estimated from GC-TCD (gaseous products) or NMR spectra (liquid products) and total charge consumed for each period of time, to calculate Faradaic efficiency. The total product percentage at any specific potential was obtained by adding the product quantification data from GC-TCD of all reduction products detected (through

combined GC-TCD and NMR analysis) at each applied potential. It was observed that while H_2 was generated at high negative potential, there was no production of CO within detectable range of GC-TCD.

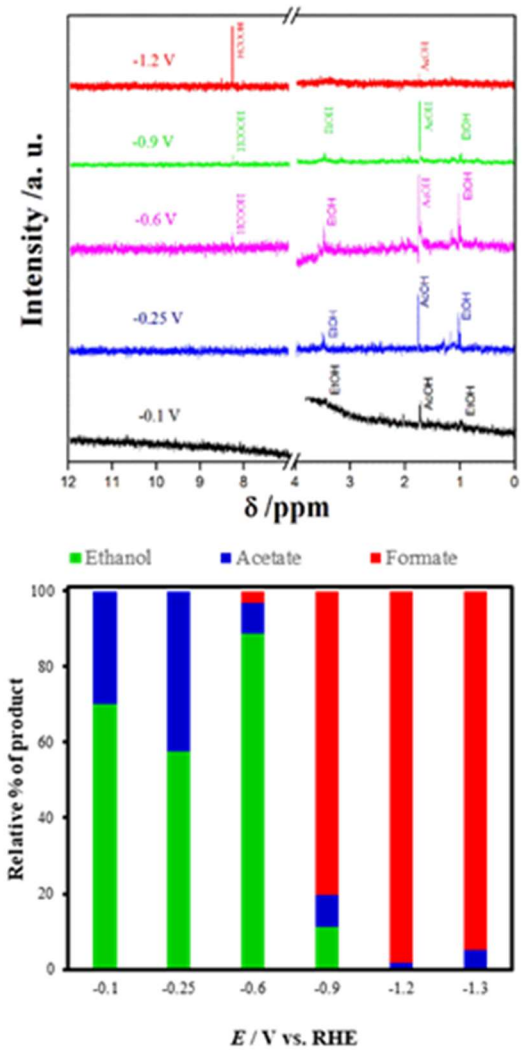

Figure 5. Identification and quantification of CO2RR products (a) NMR spectra identifying reduction products in reaction aliquots collected at different potentials. (b) Bar plot depicting relative concentrations of liquid products quantified from NMR at different stationary applied potentials.

Hydrocarbons such as methane, ethane etc. were also absent from the products possibly due to les availability of reactive hydrogen at such low applied potentials. As mentioned above Faradaic efficiency for CO_2 reduction was calculated by considering the total charge consumed and quantifying products detected in NMR and GC-TCD.

An optimal condition was observed for C1 products at an applied potential of −1.2 V vs RHE wherein formic acid was produced with 98.33% product selectivity after 1 h of electrolysis with high Faradaic efficiency. For potentials higher than −1.2 V vs RHE, the maximum faradaic efficiency (for formic acid) decreased to 94 % (−1.3 V vs RHE), which also showed deactivation over time (Table S4).

For lower applied potentials (−0.9, −0.6, and −0.25 V vs RHE) C1 products showed decrease in Faradaic efficiency (25.26 %, 0.5 %, and 0 %, for formic acid at -0.9, -0.6, and -0.25 V, respectively) while relative yield of C2 products increased.

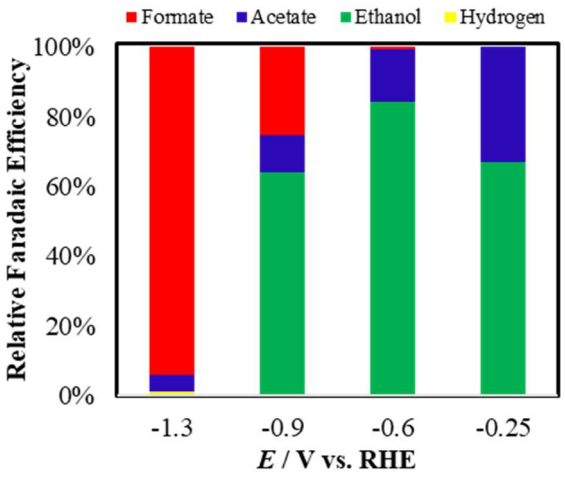

Figure 6. Bar plot depicting relative faradaic efficiency of liquid as well as gas products at different applied potentials

.

Details of estimation of the Faradaic efficiency for each reduction product at various applied potentials has been provided in supporting information (Tables S2, S3).

At -0.6 V, Faradaic efficiency in excess of 84 % was observed for ethanol. It must be noted here that such high Faradaic efficiency for C2 product such as ethanol has been observed very rarely. Hence the novelty of this simple binary copper selenide based electrocatalyst lies in its ability to produce carbon rich fuels with high selectivity and Faradaic efficiency at low energy expense. Moreover, this Cu_2Se-based catalyst also exhibits high current density exceeding 50 $mA.cm^{-2}$ at moderately low applied potential.

The stability of Cu_2Se electrocatalyst for long-term CO2RR activity was also investigated by carrying out the electrochemical carbon dioxide reduction under constant applied potential for extended period of time, typically 12, 24 or 100 h. These are typically referred to as chronoamperometry measurement where potential is kept constant for extended period of time while current density is measured. Typical chronoamperometry plots measured at different applied potentials has been shown in Figures S2a (12 h at -0.1 V, -0.6 V, and -0.9 V vs RHE), S3 (24h at -0.9 V vs RHE) and S4 (100 h at -0.6 V vs RHE). As can be seen from these plots, the reduction current density did not any change for extended period of time indicating the catalyst was functionally stable under conditions of continuous CO2RR under an applied potential. The product composition analyzed by NMR after chronoamperometry studies showed similar relative percentages as shown in Figure 5. The catalyst composition after long-term electrolysis under an applied potential was also investigated through pxrd and XPS analysis. Pxrd pattern of the catalyst film after 24 h of CO2RR at -0.9 V was superimposable with that of pristine Cu_2Se as shown in Figure S2b, indicating that there was no change in the crystalline phase of the catalyst. XPS analysis of

the catalyst film after chronoamperometry studies has been shown in Figure S2c -f, which shows Cu 2p and Se 3d peaks which are exactly superimposable with that of the pristine catalyst, with no change in peak positions indicating no change in oxidation states and/or coordination geometry. The Cu^{2+}:Cu^{+} ratio estimated from the deconvoluted XPS spectra was obtained as 1.07, similar to the pristine catalyst composition. Hence, pxrd and XPS analysis confirmed that the catalyst was also compositionally stable after extended period of catalytic activity. It must be noted here that Cu_2Se has also been reported recently as an efficient electrocatalyst for oxygen evolution reaction (OER) in alkaline medium with an onset potential of 1.42 V (vs RHE) and overpotential of 310 mV at 10 $mA.cm^{-2}$.[49]

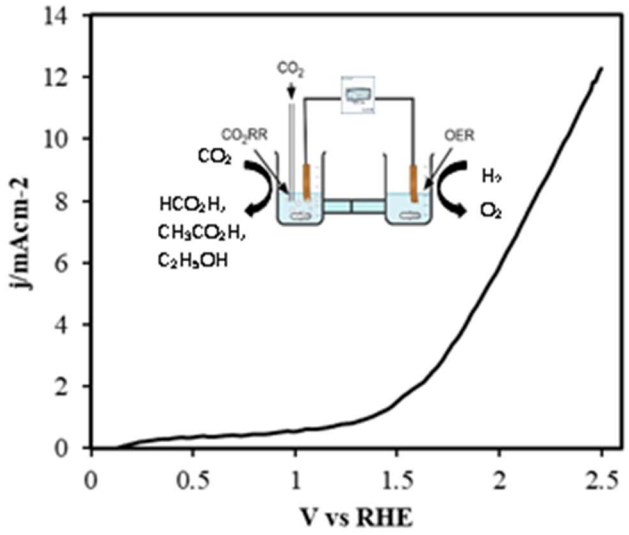

Figure 7. Polarization curve with cathodic CO2RR and anodic OER with Cu_2Se@CFP as both cathodic and anodic electrocatalyst. Inset shows schematic of the electrochemical setup for combined CO2RR and OER.

Hence Cu_2Se can be ideally used as a bifunctional catalyst that can reduce atmospheric CO_2 while simultaneously enriching the air with oxygen produced through

water electrolysis. The bifunctionality of this catalyst was probed by constructing an electrochemical H-cell containing alkaline electrolyte (1M KOH) in the anodic chamber and bicarbonate solution in the cathodic chamber. The two electrolyte chambers were separated by Nafion membrane, and it was confirmed that there was no enrichment of OH^- in the cathodic chamber. CO_2 was purged in the cathodic chamber. Inset in Figure 7 shows schematic representation of the electrochemical cell along with the LSV plot obtained from the CO2RR-OER combined experiment. Potential was scanned in the anodic direction whereby O_2 evolution was observed in the anode concurrent with the rise in oxidation current. The reduction products in catholyte were analyzed by collecting the aliquot from cathode chamber after 12 hours of continuous CO_2RR-OER at 2 V. NMR analysis of the catholyte showed that they contained primarily formic acid, acetic acid, and ethanol analogous to product composition observed previously in Figure 5.

4.3. EXPLORING CO ADSORPTION ENERGIES ON CATALYST SURFACES

The excellent activity of Cu_2Se was also investigated using density functional theory (DFT) to further understand enhanced performance of the catalyst and selectivity towards carbon-enriched reduction products. Details of the DFT calculation has been provided in the supporting information. Previously it has been shown that amongst numerous pathways to electrochemically reduce CO_2 to various hydrocarbon products on the catalyst surface, one of the key intermediates is CO.[52] Reduction of CO_2 to CO is a two electron transfer process as schematically illustrated in Figure S5 in supporting information. First, a proton-electron pair (H^+/e^-) is transferred to the CO_2 adsorbed on the catalyst-electrode which is then reduced to a carboxyl intermediate *COOH (where *

denotes adsorbed species on the catalyst surface). Then a second H^+/e^- pair participate in further reduction of *COOH to *CO and H_2O.[52] Although the conversion of *COOH to *CO takes place readily, the conversion of CO_2 to *COOH was found to be limited by the weak binding of COOH to the catalyst surface.[53] This elementary reaction step of CO_2 adsorption on Cu_2Se surface was simulated as shown in Figure S5(b), and it was observed that *COOH intermediate can form a stable configuration with the formation of Cu-C and Cu-O bonds with adjacent Cu atoms on the surface of Cu_2Se which is similar to stable *COOH configurations previously reported by other researchers.[53,54] Hence, favorable binding of *COOH on Cu_2Se accelerates the formation of *CO intermediate on catalyst surface. A primary hypothesis is being proposed in this manuscript regarding catalyst design to promote preferential formation of carbon-rich (C2 and C3) reduction product. It can be expected that *CO dwell time on the catalyst surface is a key parameter for preferential formation of C1 or C2/C3 reduction products. The *CO dwell time can be directly related to the CO adsorption energy on the catalyst site. If *CO is weakly bound to the catalyst surface, it can desorb readily forming carbon monoxide (CO) as the major product.[52] Hence, a moderately higher *CO adsorption energy is essential for retaining *CO on the catalyst surface long enough for facilitating continuous reduction of *CO to higher hydrocarbons such as methanol and ethanol. We proposed that the CO adsorption on the catalytically active site can be optimized by increasing ligand to metal back-bonding possibilities.

In this case, increasing the oxidation state of Cu from 0 (Cu metal) to +1/+2 is expected to favor ligand to metal back bonding due to availability of partially filled d-

orbitals at comparable energy level. Moreover, decreasing electronegativity of the anions also facilitates such ligand-to-metal backbonding by increasing electron density around the

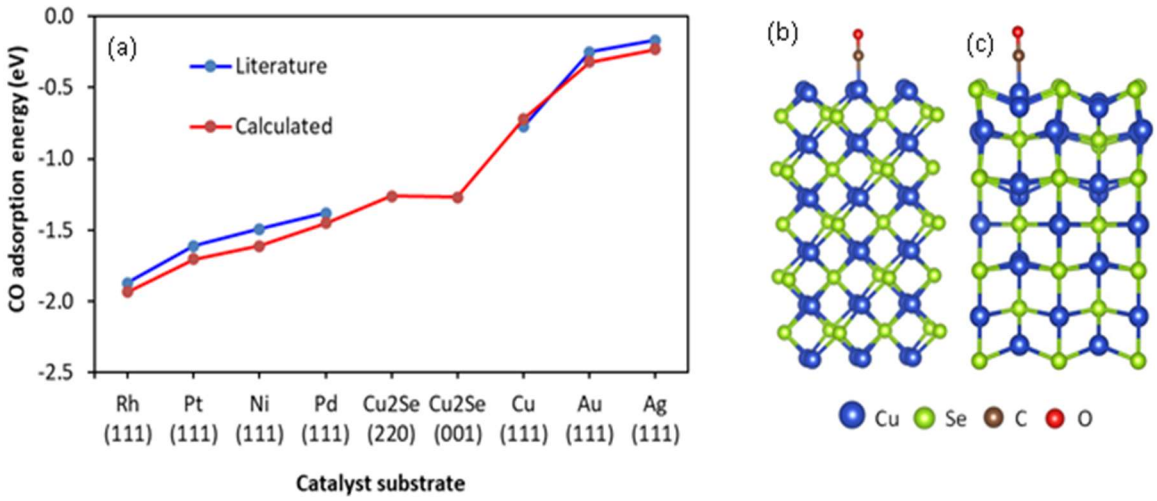

Figure 8. Comparison of calculated CO adsorption energy on known catalyst materials with Cu_2Se. (a) CO adsorption on Cu_2Se was calculated on (001) surface and (220) surface while for the metals it was calculated on (111) surfaces. Reported values were selected from data that has used the same functional as the present study for calculation of adsorption energies.[52,53] Adsorption configurations used for calculation of (b) CO on (001) surface (c) CO on (220) surfaces.

transition metal centers. Hence, it was hypothesized that Cu_2Se will show larger CO adsorption energy compared to Cu. It was also hypothesized that smaller *CO adsorption energy on specific catalyst surface will lead to preferential formation of C_1 products (CO and HCO_2H) while larger *CO adsorption energy will lead to more C2 products. However, it was also realized that very large *CO adsorption energy can potentially passivate the catalyst surface and will lead to catalyst poisoning. A series of DFT calculations were carried out for comparing the CO adsorption energy on various known catalyst surfaces along with Cu_2Se and the results are shown in Figure 8. It was observed that metals such

as Ag and Au show low CO adsorption energy and they almost exclusively produce CO as has been reported previously by various research groups.[55,56] On the other hand, catalysts such as Pt, Pd and Ni showed high CO binding energy. It is well-known that these catalysts also have a high binding energy for *H and starts hydrogen evolution reaction instead of reduction of CO_2 in aqueous medium and the catalyst is deactivated due to CO passivation by the small amounts of CO produced during continuous electroreduction of CO_2.[57] Cu metal showed a moderately larger CO adsorption energy compared to other noble metals such as Au and Ag, as shown in Figure 8. It has been reported previously that Cu is capable of producing a wide range of hydrocarbons with considerable Faradic efficiency which nicely corroborates with higher CO adsorption energy indicating longer *CO dwell time on the surface.[57] Interestingly, Cu_2Se has a moderately strong CO adsorption energy which is slightly higher than that of Cu (higher the negative value, higher the binding energy), which is favorable for further reduction of CO to carbon-rich hydrocarbon products such as ethanol and acetic acid. In addition, CO binding energy on Cu_2Se was also lower than that of the passivation level observed with other metal catalysts keeping Cu_2Se in an ideal position for CO_2 reduction. CO adsorption energy was calculated on various lattice planes of Cu_2Se and interestingly it was observed that CO adsorption energy showed minimal lattice plane dependence showing a value of -1.26 eV, for both (220) and (001) lattice planes, at ~11% surface coverage. We propose the presence of Se influences the electrocatalytic activity in multiple ways: (i) Indirect effect on electron density on catalytically active Cu center that increases CO dwell time. This has been also confirmed by the DFT studies which shows higher CO adsorption energy on Cu_2Se surface compared to bare Cu. (ii) Presence of less electronegative Se also increases electrochemical activity

of Cu thereby decreasing overpotential. Such effect of enhanced electrocatalytic activity as a function of decreasing anion electronegativity has also been observed previously.[58] (iii) Presence of Se also lead to more adsorption of hydrogen in the vicinity through Lewis acid-base interaction that can lead to formation of more hydrocarbon based reduction products.

As illustrated in Figure S6, atom projected local density of states (DOS) was also calculated on surface Cu atoms before and after binding with CO for getting further insight regarding changes of electronic structure of the surface-active sites as a function of intermediate binding. It can be seen from Figure S6 that an overall stabilization of Cu 3d orbitals has taken place by moving to lower energy upon binding with CO molecules. Adsorption of CO on transition metals occur through two mechanisms contributing to the coordination bond: CO to metal σ donation through HOMO (highest occupied molecular orbitals) located on C; and metal (*d*-) to CO (π*) back donation. In Figure S6, Cu 3*d* to CO π* back donation can be identified from the contribution of CO pDOS as a low intensity peak near -3.7 eV energy range, which is comparable to previously reported results.[59] While it is imperative to do a thorough DFT study involving all the mechanistic steps of the reaction pathway and also using other possible lattice surfaces of Cu_2Se to fully understand the role of catalyst for the selective formation of specific reduction products, present DFT results indicate that Cu_2Se catalyst surface has beneficial properties for electroreduction of CO_2 to carbon-rich products by facilitating intermediate CO adsorption, which agrees with our experimental observations.

5. CONCLUSIONS

Copper selenide nanostructures synthesized through one-pot solvothermal synthesis were found to be highly active for electrocatalytic carbon dioxide reduction under a range of applied potential. The reduction products showed selectivity between C1 and C2 products depending on the applied potential. At high applied potential (-1.3 V) the product was identified as exclusively formic acid with a Faradaic efficiency of 94.2%. At more anodic potential (<-1.2 V) preferential formation of C2 products such as acetic acid and ethanol were observed. A maximum Faradaic efficiency for ethanol production was observed at a low applied potential of -0.6 V vs RHE. It must be noted that these are among the lowest applied potential at which C2 products have been obtained with high relative yield. The reduction products were characterized through NMR and GC-TCD spectroscopies by performing time-dependent measurements. It was also observed that H_2 was produced at high cathodic potential (>-1.2 V) indicating that Cu_2Se has reduced HER catalytic activity. This is significant since HER poses as a commendable competitor and inhibits CO2RR on the catalyst surface. Interestingly it was observed that no detectable amount of CO was formed as the reduction potential even at high negative potential. The electrocatalyst surface was further studied through DFT calculations specifically to estimate CO adsorption energy on the catalyst site, which showed moderate adsorption energy which suggests longer dwell time of the adsorbed CO on the catalyst surface leading to preferential reduction to C2 products. As mentioned above, this Cu_2Se catalyst surface can effectively reduce CO_2 to ethanol and acetic acid with high Faradaic efficiency at one of the lowest applied potentials reported till date. This result along with the correlation of

catalytic activity with CO adsorption energy will lead to optimal catalyst design for forming carbon-rich high-value products through CO_2 reduction.

SUPPORTING INFORMATION

1. NMR SPECTROSCOPY

Liquid products formed during CO_2 electrochemical reduction were analyzed with ^{1}H-NMR. Aliquots were collected at regular intervals as mentioned in the manuscript and 2 µL DMSO (internal standard) and 200 µL D_2O was added to 0.5 ml electrolyte. The NMR experiments were performed on a Bruker 400 MHz NMR spectrometer, using a presaturation sequence to suppress the water signal. NMR spectra of reaction mixture was measured before starting any electrochemical reaction to make sure that there was no impurity in the solution which can lead to false results.

Table S1. Chemical shifts and assignments of peaks from different possible products observed in 1H-NMR spectra after CO_2 reduction.

Observed NMR Values			Products		Standard NMR Values[47]
Chemical Shift	1H Splitting	J coupling	Probed Nucleus	Name	Chemical Shift
8.35			$CHOO^-$	Formate	8.35
3.64	q	7.08	$CH3CH_2OH$	Ethanol	3.64
1.8	s		$CH_3C(=O)\ O^-$	Acetate	1.8

2. QUANTIFICATION OF THE PRODUCTS

Liquid products were quantified from NMR spectra by calibrating it with respect to the internal standard and quantifying the identified products. Gaseous products of CO_2 reduction were collected and transferred to GC using gas-tight syringe. The GC was equipped with thermal conductivity detector (GC- TCD) and Molecular Sieve 5A capillary column. Helium (99.999%) was used as the carrier gas. The GC columns led directly to a TCD detector to quantify hydrogen and carbon monoxide. At ambient conditions, CO_2 was continuously purged through a cathode compartment flow cell at a rate of 20 sccm while a constant potential was applied for designated time. The cell effluent was sampled using 100 µL syringe. The Faradaic efficiency (FEs) was calculated by measuring the current and using mole percentages quantified through GC-TCD as well as NMR analysis as follows:

2.1. FARADAIC EFFICIENCY (%) CALCULATION OF PRODUCTS

No. of moles of product = C

Total current = I (A)

No. of electrons(moles) required to form certain product = $C \times n$

N = No. of electrons required to obtain 1 molecule of product.

Charge consumed in forming certain product $C_e = C \times F \times n$ where F = Faraday constant, 96485 C mol^{-1}. The number of electrons required to form a molecule of Ethanol, Acetate, Formate and H_2 are 12, 8, 2 and 2, respectively. Total charge consumed can be

determined using Faraday's laws of electrolysis: $C_T = I \times t$. Faradaic efficiency of the product = $\frac{C_e}{C_T} \times 100\%$

Following worksheet shows typical calculation of Faradaic efficiency at specific potentials (-0.6 V and -0.9 V vs RHE):

2.2. CALCULATION OF THE FE OF PRODUCTS AT -0.6 V VS RHE

Current Density mA/cm^2 (1h) = 4 mA/cm^2

Surface Area of the electrode = 2 cm^2

Total current(A) = $\frac{(current\ density \times surface\ area\ of\ the\ electrode)}{1000}$ = 0.008A

Total charge consumed $C_T = I \times t$ = 0.008 x 3600 = 28.80 C

Table S2. Calculated Faradaic Efficiency along with product concentration obtained at -0.6 V vs RHE.

Products	No. of moles of product(mol)	*n* (number of electrons required to form specific product)	C_e (Charge required to form certain product) (C)	$F = \frac{C_e}{C_T} * 100$
Hydrogen	2.68E-07	2	0.51	0.18
Ethanol	2.10433E-05	12	24.36	84.00
Acetate	5.72789E-06	8	4.42	15.34
Formate	7.55558E-07	2	0.14	0.48

2.3. CALCULATION OF THE FE OF PRODUCTS AT -0.9V VS RHE

Current Density mA/cm^2 (1h) = 5.5 mA/cm^2

Table S3. Calculated Faradaic Efficiency along with product concentration obtained at -0.9 V vs RHE.

Products	No. of moles of product(mol)	N (number of electrons required to form specific product)	Ce (Charge required to form certain product) (C)	$F = \frac{C_e}{C_T} * 100$
Hydrogen	1.28E-06	2	0.25	0.64
Ethanol	2.14789E-05	12	24.86	63.58
Acetate	5.3476E-06	8	4.12	10.53

Surface Area of the electrode = 2 cm^2

Total current(A) = $\frac{(current\ density \times surface\ area\ of\ the\ electrode)}{1000}$ =0.01086A

Total charge consumed $C_T = I \times t$ = 0.01086 x 3600 = 39.10 C

Table S4. Faradaic efficiency of the liquid and gas phase products estimated from NMR and GC-TCD respectively at different applied potential with Cu_2Se

Product	Faradaic Efficiency (%)			
	-0.25 V	- 0.6 V	- 0.9 V	- 1.3 V
H_2	0	0.17	0.63	1.12
Formic Acid	0.4	0.50	25.26	94.2
Acetic Acid	33	15.25	10.54	4.67
Ethanol	66.6	84.06	63.55	0
Formate	5.12389E-05	2	9.88	25.25

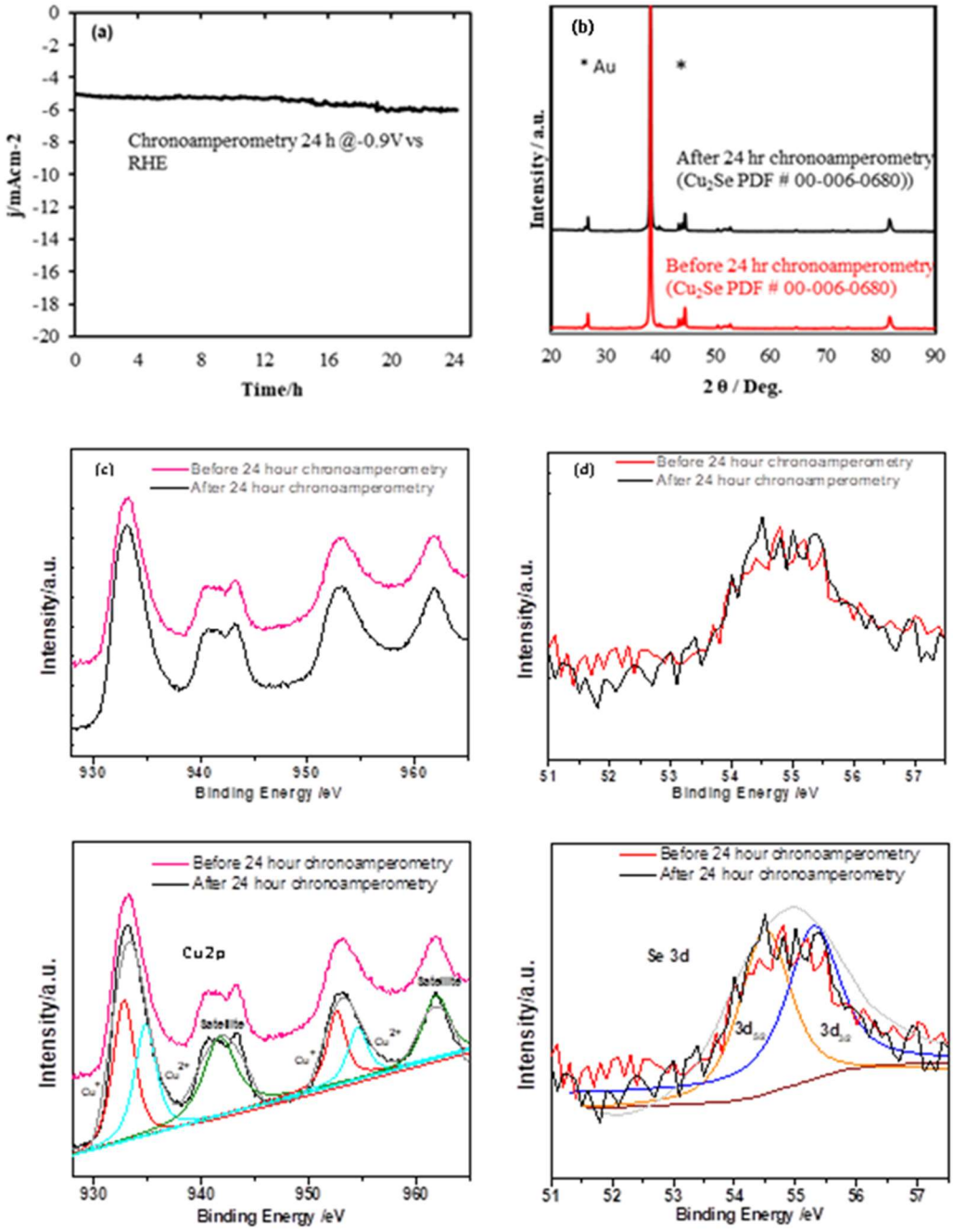

Figure S1. (a) 24 h of chronoamperometry study at applied potential = -0.9V vs RHE (b) Pxrd spectra of Cu_2Se before and after 24 h of chronoamperometry (c) Cu 2p XPS signal before and after chronoamperometry for 24 h. (d) XPS spectra of Se 3d before and after chronoamperometry study(e) & (f) Deconvoluted Spectra

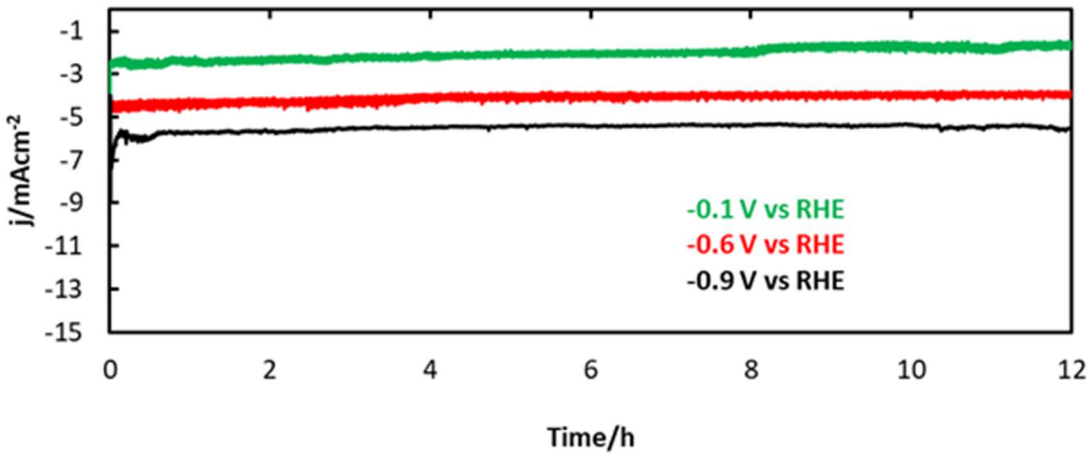

Figure S2. Chronoamperometric stability study for Cu_2Se nanocomposite under continuous CO_2 purging for 12 h held at constant potential (-0.1 V vs RHE, -0.6 V vs RHE, -0.9 V vs RHE)

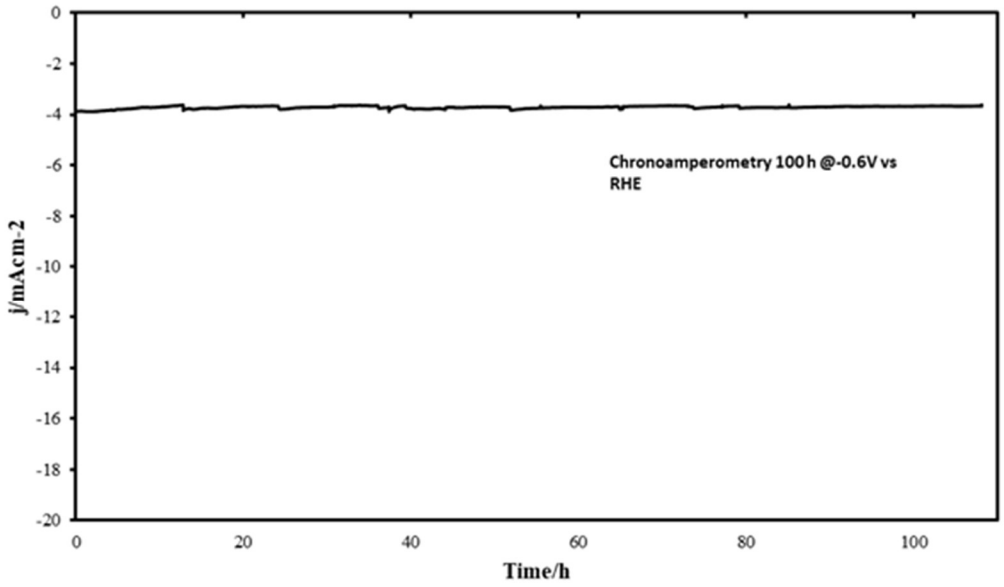

Figure S3. Chronoamperometric stability study for Cu_2Se nanocomposite under continuous CO_2 purging for 100 h held at constant potential (-0.6 V vs RHE)

3. COMPUTATIONAL SETUP

The fully periodic plane-wave density functional theory (DFT) calculations were carried out as implemented in Vienna Ab-initio Simulation Package (VASP)[1] with the exchange-correlation functional Perdew−Burke−Ernzerhof (PBE)[2] within the generalized gradient approximation (GGA)[3] implemented with the Projector Augmented Wave function (PAW) method[4] to investigate adsorption energy of CO molecules on the surface of catalyst materials. An energy cutoff limit of 500 eV was applied with the convergence criteria for electronic self-consistent iterations set at 1.0×10^{-6} eV, and the ionic relaxation was carried out by conjugate gradient algorithm until atomic forces of the system were smaller than 0.01eV without any constrains. The Methfessel−Paxton smearing with a value of smearing parameter σ of 0.2 eV was applied to the orbital occupation. The calculations employed 11x11x3 k-point Monkhorst−Pack[5] mesh for Cu and other transition metals along with a 11x8x3 grid for Cu_2Se (220) surface and 11x11x5 grid for Cu_2Se (001) surface for sampling the Brillouin zone. For each species, surface models with a unit cell of 2x2x2 and 2x3x3 with a vacuum region of 15 Å along z-direction were used.

During the calculation of CO adsorption energy, first the free surfaces were relaxed to obtain the energy of the clean surface, E_{clean}, and then CO ions were placed on top of active sites of the catalyst at a distance of ~ 1.80 Å, which is very close to the equilibrium distance of CO on transition metal sites, and let the system to relax to calculate, Esys., the total formation energy of the system. The adsorption energy of CO, E_{ad}, was calculated as $E_{ad} = E_{sys} - E_{clean} - E_{CO}$, in which E_{CO} is the energy of free CO.

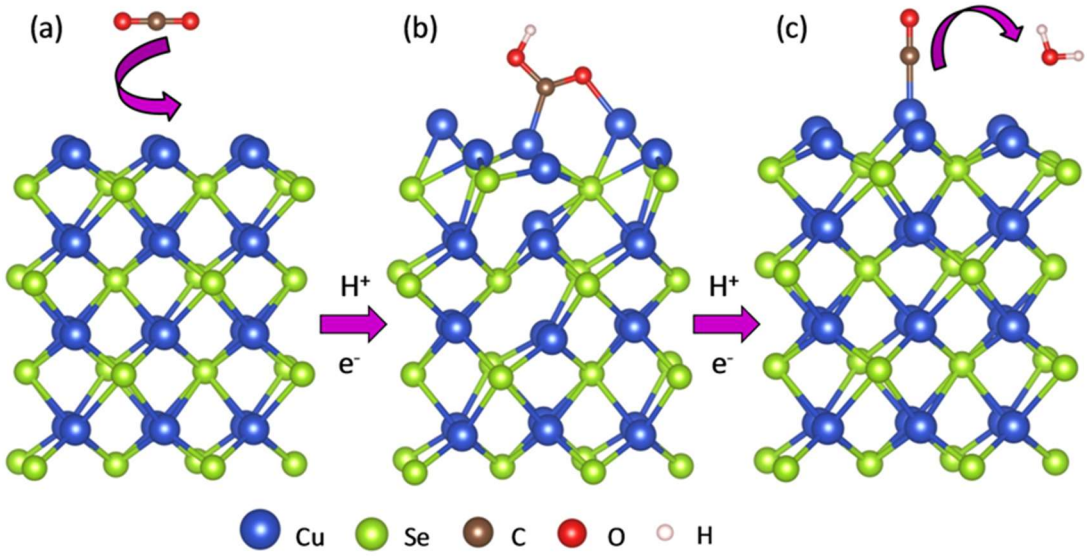

Figure S4. Schematic representation of the elementary reaction steps for the formation of CO on Cu_2Se (001) surface. The simulated *COOH intermediate in (b) shows the formation of a stable configuration on Cu_2Se surface by attaching through C and O atoms to neighboring Cu atoms on the catalyst surface.

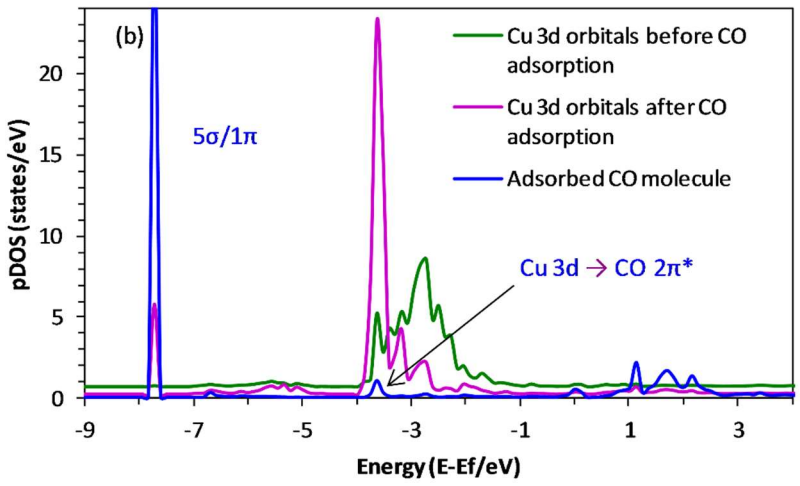

Figure S5. Atom projected partial density of states of the 3d orbitals of a Cu atom on Cu_2Se (001) surface before and after binding with CO molecule.

REFERENCES

1. Gattuso, J. P.; Magnan, A.; Bille, R.; Cheung, W. W. L.; Howes, E. L.; Joos, F.; Allemand, D.; Bopp, L.; Cooley, S. R.; Eakin, C. M.; Hoegh-Guldberg, O.; Kelly, R. P.; Portner, H.-O.; Rogers, A. D.; Baxter, J. M.; Laffoley, D.; Osborn, D.; Rankovic, A.; Rochette, J.; Sumaila, U. R.; Treyer, S.; Turley, C. Contrasting futures for ocean and society from different anthropogenic CO_2 emission scenarios Science, 2015, 349, aac4722 (1-10).

2. Le Quéré, C.; Andrew, R. M.; Friedlingstein, P.; Sitch, S.; Pongratz, J.; Manning, A. C.; Korsbakken, J. I.; Peters, G. P.; Canadell, J. G.; Jackson, R. B., Global carbon budget 2017. Earth System Science Data Discussions 2017, 1-79.

3. Solomon, S.; Plattner, G.-K.; Knutti, R.; Friedlingstein, P. Irreversible climate change due to carbon dioxide emission, Proc. Natl. Acad. Sci. 2009, 106, 1704-1709.

4. Mikkelsen, M.; Jorgensen, M.; Krebs, F. C. The tetraton challenge: A review of fixation and transformation of carbon dioxide Energy Environ. Sci. 2010, 3, 43-81.

5. Bushuyev, O. S.; De Luna, P.; Dinh, C. T.; Tao, L.; Saur, G.; Lagemaat, J.; Kelley, S. O.; Sargent, E. H. What should we make with CO_2 and how can we make it? Joule, 2018, 2, 825-832.

6. Zhu, D. D.; Liu, J. L.; Qiao, S. Z., Recent advances in inorganic heterogeneous electrocatalysts for reduction of carbon dioxide. Advanced materials 2016, 28 (18), 3423-3452.

7. Qiao, J.; Liu, Y.; Hong, F.; Zhang, J., A review of catalysts for the electroreduction of carbon dioxide to produce low-carbon fuels. Chemical Society Reviews 2014, 43 (2), 631-675.

8. Choi, S.; Drese, J. H.; Jones, C. W., Adsorbent Materials for Carbon Dioxide Capture from Large Anthropogenic Point Sources. ChemSusChem 2009, 2 (9), 796-854

9. Nitopi, S.; Bertheussen, E.; Scott, S. B.; Liu, X.; Engstfeld, A. K.; Horch, S.; Seger, B.; Stephens, I. E. L.; Chan, K.; Hahn, C.; Norskov, J. S.; Jaramillo, T. F.; Chorkendorf, I. Progress and perspectives of electrochemical CO_2 reduction on Copper in aqueous electrolyte Chem. Rev. 2019, 119, 7610-7672.

10. Qiao, J.; Liu, Y.; Hong, F.; Zhang, J. A review of catalysts for the electroreduction of carbon dioxide to produce low-carbon fuels. Chem. Soc. Rev. 2014, 43, 631–675.

11. Li, Y.; Chan, S. H.; Sun, Q. Heterogeneous catalytic conversion of CO_2: a comprehensive theoretical review, Nanoscale 2015, 7, 8663– 8683.

12. Zhang, R.-Z.; Wu, B.-Y.; Li, Q.; Lu, L.-L.; Shi, W.; Cheng, P. Design strategies and mechanism studies of CO_2 electroreduction catalysts based on coordination chemistry, Coord. Chem. Rev. 2020, 422, 213436 (1-28)

13. Azcarate, I.; Costentin, C.; Robert, M.; Savéant, J.-M. Through-space charge interaction substituent effects in molecular catalysis leading to the design of the most efficient catalyst of CO_2-to-CO electrochemical conversion. J. Am. Chem. Soc. 2016, 138, 16639– 16644.

14. Francke, R.; Schille, B.; Roemelt, M. Homogeneously catalyzed electroreduction of carbon dioxide – Methods, mechanisms, and catalysts Chem. Rev., 2018, 118, 4631-4701.

15. Benson, E. E.; Kubiak, C. P.; Sathrum, A. J.; Smieja, J. M. Electrocatalytic and homogeneous approaches to conversion of CO_2 to liquid fuels. Chem. Soc. Rev. 2009, 38, 89–99.

16. Rountree, E. S.; McCarthy, B. D.; Eisenhart, T. T.; Dempsey, J. L. Evaluation of homogeneous electrocatalysts by cyclic voltammetry Inorg. Chem. 2014, 53, 9983–10002.

17. Liu, X.; Xiao, J.; Peng, H.; Hong, X.; Chan, K.; Norskov, J. K. Understanding trends in electrochemical carbon dioxide reduction rates, Nature Commun. 2017, 8, article number 15438 (1-7)

18. Wuttig, A., Yaguchi, M., Motobayashi, K., Osawa, M. & Surendranath, Y. Inhibited proton transfer enhances Au-catalyzed CO_2-to-fuels selectivity. Proc. Natl Acad. Sci. USA 2016, 113, E4585–E4593.

19. Appel, A. M. Bercaw, J. E.; Bocarsly, A, B.; Dobbek, H.; DuBois, D. L.; Dupuis, M.; Ferry, J. G.; Fujita, E.; Hille, R.; Kenis, P. J. A.; Kerfeld, C. A.; Morris, R. H.; Peden, C. H. F.; Portis, A. R.; Ragsdale, S. W.; Rauchfuss, T. B.; Reek, J. N. H. Seefeldt, L. C.; Thauer, R. K.; Waldrop, G. L. Frontiers, opportunities, and challenges in biochemical and chemical catalysis of CO_2 fixation Chem. Rev. 2013, 113, 6621–6658.

20. Malik, K.; Singh, S.; Basu, S.; Verma, A. Electrochemical reduction of CO_2 for synthesis of green fuel, WIREs Energy Environ 2017, 6:e244. doi: 10.1002/wene.244 (1-17).

21. Ogura K. Electrochemical reduction of carbon dioxide to ethylene: mechanistic approach. J CO_2 Utilization 2013, 1, 43–49.

22. Hori, Y.; Kikuchi, K.; Suzuki, S. Production of CO and CH4 in electrochemical reduction of CO_2 at metal electrodes in aqueous hydrogencarbonate solution Chem. Lett. 1985, 14, 1695–1698.

23. Yang, H.-P.; Qin, S.; Wang, H.; Lu, J.-X., Organically doped palladium: a highly efficient catalyst for electroreduction of CO_2 to methanol. Green Chemistry 2015, 17 (12), 5144-5148.

24. Chen, Y.; Li, C. W.; Kanan, M. W., Aqueous CO_2 reduction at very low overpotential on oxide-derived Au nanoparticles. Journal of the American Chemical Society 2012, 134 (49), 19969-19972.

25. Jiang, K.; Kharel, P.; Peng, Y.; Gangishetty, M. K.; Lin, H.-Y. G.; Stavitski, E.; Attenkofer, K.; Wang, H., Silver Nanoparticles with Surface-Bonded Oxygen for Highly Selective CO_2 Reduction. ACS Sustainable Chemistry & Engineering 2017, 5 (10), 8529-8534.

26. Hori, Y.; Kikuchi, K.; Suzuki, S. Production of CO and CH4 in electrochemical reduction of CO_2 at metal electrodes in aqueous hydrogencarbonate solution Chem. Lett. 1985, 14, 1695–1698.

27. Kudo, A.; Nakagawa, S.; Tsuneto, A.; Sakata, T. Electrochemical reduction of high pressure CO_2 on Ni electrodes J. Electrochem. Soc. 1993, 140, 1541–1545.

28. Reske, R.; Duca, M.; Oezaslan, M.; Schouten, K. J. P.; Koper, M. T. M.; Strasser, P. Controlling catalytic selectivities during CO_2 electroreduction on thin Cu metal overlayers. J. Phys. Chem. Lett. 2013, 4, 2410–2413.

29. Rasul, S.; Anjum, D. H.; Jedidi, A.; Minenkov, Y.; Cavallo, L.; Takanabe, K. A highly selective copper–indium bimetallic electrocatalyst for the electrochemical reduction of aqueous CO_2 to CO. Angew. Chem. Int. Ed. 2014, 54, 2146–2150.

30. Ohya, S; Kaneco, S.; Katsumata, H.; Suzuki, T.; Ohta, K. Electrochemical reduction of CO_2 in methanol with aid of CuO and Cu_2O Catal. Today 2009, 148, 329–334.

31. Kuhl, K. P.; Cave, E. R.; Abram, D. N.; Jaramillo, T. F., New insights into the electrochemical reduction of carbon dioxide on metallic copper surfaces. Energy & Environmental Science 2012, 5 (5), 7050-7059.

32. Hori, Y.; Wakebe, H.; Tsukamoto, T.; Koga, O., Electrocatalytic process of CO selectivity in electrochemical reduction of CO_2 at metal electrodes in aqueous media. Electrochimica Acta 1994, 39 (11-12), 1833-1839.

33. Reske, R.; Mistry, H.; Behafarid, F.; Roldan Cuenya, B.; Strasser, P., Particle size effects in the catalytic electroreduction of CO_2 on Cu nanoparticles. Journal of the American Chemical Society 2014, 136 (19), 6978-6986.

34. Tang, W.; Peterson, A. A.; Varela, A. S.; Jovanov, Z. P.; Bech, L.; Durand, W. J.; Dahl, S.; Nørskov, J. K.; Chorkendorff, I., The importance of surface morphology in controlling the selectivity of polycrystalline copper for CO_2 electroreduction. Physical Chemistry Chemical Physics 2012, 14 (1), 76-81.

35. Kas, R.; Kortlever, R.; Milbrat, A.; Koper, M. T.; Mul, G.; Baltrusaitis, J., Electrochemical CO_2 reduction on Cu_2O-derived copper nanoparticles: controlling the catalytic selectivity of hydrocarbons. Physical Chemistry Chemical Physics 2014, 16 (24), 12194-12201.

36. Whipple, D. T.; Kenis, P. J., Prospects of CO_2 utilization via direct heterogeneous electrochemical reduction. The Journal of Physical Chemistry Letters 2010, 1 (24), 3451-3458.

37. Maurin, A.; Robert, M., Noncovalent immobilization of a molecular iron-based electrocatalyst on carbon electrodes for selective, efficient CO_2-to-CO conversion in water. Journal of the American Chemical Society 2016, 138 (8), 2492-2495.

38. Xu, J.; Natsui, K.; Naoi, S.; Nakata, K.; Einaga, Y., Effect of doping level on the electrochemical reduction of CO_2 on boron-doped diamond electrodes. Diamond and Related Materials 2018, 86, 167-172.

39. Neaţu, S. t.; Maciá-Agulló, J. A.; Concepción, P.; Garcia, H., Gold–copper nanoalloys supported on TiO_2 as photocatalysts for CO_2 reduction by water. Journal of the American Chemical Society 2014, 136 (45), 15969-15976.

40. Albo, J.; Sáez, A.; Solla-Gullón, J.; Montiel, V.; Irabien, A., Production of methanol from CO_2 electroreduction at Cu_2O and Cu_2O/ZnO-based electrodes in aqueous solution. Applied Catalysis B: Environmental 2015, 176, 709-717.

41. Asadi, M.; Kim, K.; Liu, C.; Addepalli, A. V.; Abbasi, P.; Yasaei, P.; Phillips, P.; Behranginia, A.; Cerrato, J. M.; Haasch, R., Nanostructured transition metal dichalcogenide electrocatalysts for CO_2 reduction in ionic liquid. Science 2016, 353 (6298), 467-470.

42. Ahn, S. T.; Abu-Baker, I.; Palmore, G. T. R., Electroreduction of CO_2 on polycrystalline copper: Effect of temperature on product selectivity. Catalysis Today 2017, 288, 24-29.

43. Hori, Y.; Takahashi, I.; Koga, O.; Hoshi, N., Selective formation of C2 compounds from electrochemical reduction of CO_2 at a series of copper single crystal electrodes. The Journal of Physical Chemistry B 2002, 106 (1), 15-17.

44. Chen, Y.; Kanan, M. W., Tin oxide dependence of the CO_2 reduction efficiency on tin electrodes and enhanced activity for tin/tin oxide thin-film catalysts. Journal of the American Chemical Society 2012, 134 (4), 1986-1989.

45. Jitaru, M.; Lowy, D.; Toma, M.; Toma, B.; Oniciu, L., Electrochemical reduction of carbon dioxide on flat metallic cathodes. Journal of Applied Electrochemistry 1997, 27 (8), 875-889.

46. Albo, J.; Sáez, A.; Solla-Gullón, J.; Montiel, V.; Irabien, A., Production of methanol from CO_2 electroreduction at Cu_2O and Cu_2O/ZnO-based electrodes in aqueous solution. Applied Catalysis B: Environmental 2015, 176, 709-717.

47. R. García-Muelas, F. Dattila, T. Shinagawa, A. J. Martín, J. Pérez-Ramírez and N. López, Origin of the Selective Electroreduction of Carbon Dioxide to Formate by Chalcogen Modified Copper, J. Phys. Chem. Lett., 2018, 9, 24, 7153–7159.

48. Shinagaya, T.; Larrazabai, G. O.; Martin, A. J.; Krumeich, F.; Perez-Ramirez, J. *ACS Catalysis* **2018**, *8*, 827-844.

49. J. Masud, W. P. R. Liyanage, X. Cao, A. Saxena and M. Nath, Copper Selenides as High-Efficiency Electrocatalysts for Oxygen Evolution Reaction, *ACS Appl. Energy Mater. 2018, 1, 8, 4075–4083*.

50. Zhu, Q., Sun, X., Yang, D. et al. Carbon dioxide electroreduction to C2 products over copper-cuprous oxide derived from electrosynthesized copper complex. Nat Commun 10, 3851 (2019)

51. Z. Chen, K. Mou, S. Yao and L. Liu, Highly selective electrochemical reduction of CO_2 to formate on metal-free nitrogen-doped PC61BM, J. Mater. Chem. A, J. Mater. Chem. A, 2018,6, 11236-11243, DOI:10.1039/c8ta03328e..

52. Sun, Z., Ma, T., Tao, H., Fan, Q., & Han, B. (2017). Fundamentals and challenges of electrochemical CO_2 reduction using two-dimensional materials. Chem, 3(4), 560-587.

53. Hansen, H. A., Varley, J. B., Peterson, A. A., & Nørskov, J. K. (2013). Understanding trends in the electrocatalytic activity of metals and enzymes for CO_2 reduction to CO. The journal of physical chemistry letters, 4(3), 388-392.

54. Yang, D., Zhu, Q., Chen, C., Liu, H., Liu, Z., Zhao, Z. & Han, B. (2019). Selective electroreduction of carbon dioxide to methanol on copper selenide nanocatalysts. Nature communications, 10(1), 1-9.

55. Rosen, J., Hutchings, G. S., Lu, Q., Rivera, S., Zhou, Y., Vlachos, D. G., & Jiao, F. (2015). Mechanistic insights into the electrochemical reduction of CO_2 to CO on nanostructured Ag surfaces. Acs Catalysis, 5(7), 4293-4299.

56. Back, S., Yeom, M. S., & Jung, Y. (2015). Active sites of Au and Ag nanoparticle catalysts for CO_2 electroreduction to CO. ACS Catalysis, 5(9), 5089-5096.

57. U. De Silva, J. Masud, N. Zhang, Y. Hong, W. P. R. Liyanage, M. Asle Zaeem and M. Nath, Nickel telluride as a bifunctional electrocatalyst for efficient water splitting in alkaline medium, *J. Mater. Chem. A*, 2018,**6**, 7608-7622

58. Chatterjee, S., Griego, C., Hart, J. L., Li, Y., Taheri, M. L., Keith, J., & Snyder, J. D. (2019). Free standing nanoporous palladium alloys as CO poisoning tolerant electrocatalysts for the electrochemical reduction of CO_2 to formate. ACS Catalysis, 9(6), 5290-5301.

II. NICKEL SELENIDE AS EFFICIENT ELECTROCATALYST FOR SELECTIVE REDUCTION OF CARBON DIOXIDE TO CARBON-RICH PRODUCTS

Apurv Saxena[a], Wipula Liyanage[a], Shuben Kapila[a], Manashi Nath[a]*

Deparment of Chemistry, Missouri University of Science and Technology, Rolla, MO 65409

ABSTRACT

Identifying new catalyst composition for carbon dioxide electroreduction to high value products has been at the center of attraction over the last several years. In this article, nickel selenide, $NiSe_2$ has been identified as a high efficiency electrocatalyst for CO_2 electroreduction at neutral pH. Interestingly, $NiSe_2$ shows high selectivity towards specific reduction products forming carbon rich C2 products like ethanol and acetic acid exclusively at lower applied potential, while C1 products formic acid and carbon monoxide formed preferentially at higher applied potential. The hydrothermally synthesized $NiSe_2$ sample also shows high activity for oxygen evolution through electrocatalytic water splitting in alkaline medium, effectively making it a bifunctional catalyst which can lower the concentration of atmospheric pollutant CO_2 while at the same time enrich the air with O_2. The $NiSe_2$ catalyst surface has been studied through density functional theory calculations which show that the adsorption energy of intermediate CO on the $NiSe_2$ surface is optimal for extensive reduction through formation of C-C bonds, but not strong enough for surface passivation, and leading to high selectivity. Such high efficiency of the

catalyst can be a result of increased covalency of the selenide anion along with high d-electron density of the Ni center.

1. INTRODUCTION

The continuous consumption of fossil fuels to support todays fast paced economic and social growth has led to serious energy crisis and environmental problems. Atmospheric levels of CO_2 have reached an all-time high of 415 ppm which along with the global warming has also caused several catastrophic consequences including effects on human health, extinction of species leading to ecological imbalance, and food shortage. While researchers are trying to reduce our dependence on fossil fuels by identifying alternative sources of clean energy which will also curb further production of carbon dioxide, there is still a need to reduce the existing vast amount of CO_2 already present. Sequestration and storage can mitigate that problem to a small extent, however, utilization of CO_2 to produce fuels and other valuable chemicals can significantly reduce atmospheric CO_2 levels and close the carbon-cycle loop efficiently. Another imminent necessity is to utilize the copious quantities of CO_2 being produced from various industrial sectors and generate value-added end-products thereby reducing carbon footprint. Carbon dioxide electroreduction (CO2RR) is an effective technique to convert atmospheric CO_2 to valuable products and has been researched widely over the past several decades.[175] Carbon dioxide electroreduction is facilitated by the use of catalysts and the primary challenge is to identify catalyst composition that can convert CO_2 to carbon-rich high-value products with high faradaic efficiency and high selectivity towards specific products. Among these, product

selectivity towards high value products plays a significant role in defining catalyst efficiency as well as practical useability. The high value products of particular importance include formic acid, acetic acid, ethanol, and methanol. As recent research activities have led to discovery of several catalyst compositions, however, optimizing CO2RR while reducing hydrogen evolution reaction from electrocatalytic reduction of water remains a great challenge. Hence, identifying catalysts which can promote CO2RR and suppress the competing HER will be an important step in this field.

Recent research has identified several catalyst compositions for efficient CO2RR. However, among these copper based compositions have showed predominance as effective catalysts leading to a wide range of products.[176,177] Several researchers have reported CO2RR with metallic Cu as well as copper oxide catalysts.[18] Apart from Cu, other metals like Sn and Pb has been also explored as catalysts by different research groups.[178] Similarly, mixed metal alloys such as Cu-Ni and Cu_3Pd have been utilized for CO2RR which have been shown to produce methanol.[6,7] In-Sn alloy catalyst on the other hand, produces formic acid from CO2RR.[181] Nitrogen doped nanodiamonds over silicon rod array have also been proven as efficient electrocatalyst in converting CO_2 to acetic acid with the onset potential of −0.36 V (vs RHE).[182] NiO/MWCNT composite, on the other hand, produces syn gas upon CO2RR.[183] Apart from metals, metallic alloys, and oxides, chalcogenides have also been recently explored as electrocatalysts for CO2RR.[184] Recently Cu_2Se has been identified as efficient CO2RR electrocatalyst with high efficiency.[57,177] Interestingly Cu_2Se shows high selectivity towards carbon-rich products for low applied potentials, with more than 70% Faradaic efficiency for formation of ethanol.[177] Graphene supported NiO/Ni nanoparticles are also explored as efficient photocatalyst for CO_2

reduction with H_2. Under continuous flow, 50 mg of NiO/Ni-G photocatalyst produced CH_4 at rate 244.8 μL h^{-1} with a residence time of 3.1 s. [185]

Catalyst design plays an important role in defining efficiency especially with respect to product selectivity. As we have proposed earlier, formation of carbon-rich products is enhanced by longer dwell time of adsorbed carbon monoxide (-CO) formed as an intermediate on the catalyst surface, which provides more opportunities for further reduction. Another parameter than enhances CO_2 electroreduction is the improved conductivity of the catalyst surfaces which enhances electron transfer especially at lower applied potential which can reduce rate of competing HER. The first parameter can be optimized by selecting transition metal centers that can potentially increase metal-to-ligand back bonding with the intermediate surface-adsorbed CO thereby increasing CO^- adsorption energy on the surface. We propose that transition metals with more than half-filled d-orbitals can effectively optimize such back bonding leading to moderate CO dwell times that will lead to further reduction while not poisoning the catalyst surface. Conductivity and efficient charge transfer on the catalyst surface on the other hand, can be improved by increasing covalency of the lattice anions which leads to decreasing bandgap as has been shown earlier through density functional theory (DFT) studies.[94] We propose that effective application of such catalyst design principles by optimizing charge transfer and intermediate CO^- retention on the catalyst surface will lead to efficient CO2RR catalysts that can lead to preferential formation of carbon-rich reduction products with high selectivity at lower applied potentials.

In this article, we have investigated the efficient electroreduction of CO_2 selectively to C1 and C2 products such as formic acid, methanol, ethanol, and acetic acid on

hydrothermally synthesized nanoporous $NiSe_2$ electrocatalyst surfaces. High product selectivity could be achieved by varying the applied potential where C1 products formed at higher applied potential while C2 products formed predominantly at lower applied potentials. More importantly, it was observed that the product composition could be made to be exclusively acetic acid by maintaining lower applied potential. Acetic acid is an important industrial chemical[186] and selective production of this through waste CO_2 utilization can be viewed as another novelty of this research. DFT calculations were also performed to estimate the intermediate CO^- adsorption energy on the catalyst surface which was observed to be moderately strong suggesting longer CO^- dwell time on the catalytic site without poisoning effect. It must be noted here that most of the existing CO2RR catalysts are based on Cu, and Ni-based system has been studied very rarely for CO2RR. This is the first report of Ni-chalcogenides as active catalyst for CO_2 reduction. Moreover, $NiSe_2$ also exhibits formation of carbon-rich products with high Faradaic efficiency at low applied potential which increases novelty of this catalyst system. High product selectivity at low energy expense also makes this $NiSe_2$-based catalyst highly applicable for CO_2 reduction at points of generation as well as stored gas. Previously $NiSe_2$ was explored as a good electrocatalyst for oxygen evolution reaction (OER).[120] Hence this catalyst was applied as bifunctional catalyst that could reduce atmospheric CO_2 to value-added chemicals, and at the same time enrich the atmosphere with O_2 produced through water electrolysis, thereby providing opportunities for environmental remediation.

2. MATERIALS AND METHODS

2.1. SYNTHESIS OF $NISE_2$

Hydrothermal method was used to synthesize $NiSe_2$ following a previously reported procedure.[120] In 15mL deionized water, 10 mmols of $NiCl_2.6H_2O$ and 20 mmols of SeO_2 were mixed by stirring on a magnetic stirrer for 15 minutes. Then 0.2 ml (0.6 mols) of hydrazine monohydrate was added with further stirring for 15 minutes. This solution was then transferred to 23 ml Teflon-lined stainless steel autoclave and heated at 145°C for 24 hours. The autoclave was cooled to room temperature under ambient conditions, and the product was collected through filtration. After washing several times with DI water and ethanol, the solid product was dried overnight in an oven maintained at 35°C.

2.2. PREPARATION OF ELECTRODE

4 mg of the powder $NiSe_2$ was dispersed in 200 μL of 1% Nafion in ethanol. The mixture was sonicated for 30 mins to produce a homogeneous catalyst ink. 20 μL of the catalyst ink was drop casted on to the Carbon Fiber Paper (CFP) at room temperature to prepare the $NiSe_2$-modified electrode. Finally, the as- prepared electrode was allowed to dry at room temperature for 8 hrs. Catalyst loading on the working electrode was calculated to be 1.25 mg cm^{-2} for most of the electrochemical experiments done in this study.

3. RESULTS AND DISCUSSION

The composition of the product was confirmed through powder X-ray diffraction (PXRD). As can be seen in the PXRD pattern shown in Figure 1, diffraction peaks from

the as synthesized product could be matched with the standard $NiSe_2$ phase (PDF# 01-088-1711) confirming phase purity and crystallinity of the as-synthesized product. Significant broadening of the diffraction peaks was observed suggesting presence of nanostructured grains. Using Scherrer equation, average size of the crystalline domain was estimated to be 27.43 nm.

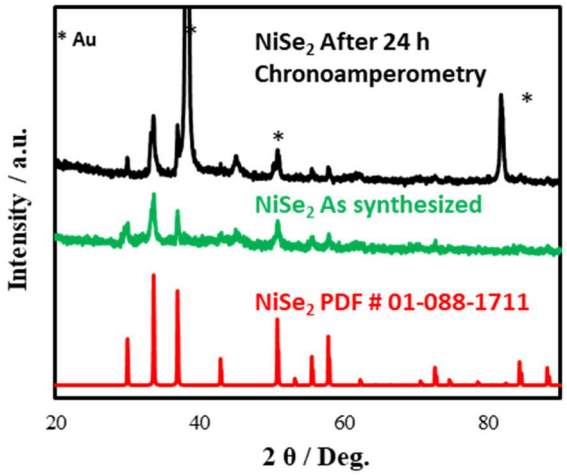

Figure 1. PXRD pattern of hydrothermally synthesized $NiSe_2$ compared with the standard $NiSe_2$ reference pattern (PDF # 01-088-1711).

This stability was confirmed later by doing chronoamperometric stability studies. (Figure S2). We believe that the affinity of nickel to form Ni-CO complex is the driving factor for C2 product formation.

Catalyst morphology was observed through SEM which showed that the hydrothermally frormed $NiSe_2$ formed nanostructured grains as shown in Figures 2a and b, with sizes ranging from 100 nm – 800 nm and exhibiting considerable surface roughness. The composition of granular nanostructures was confirmed through EDS (Figure 2c) which

confirmed the existence of Ni and Se in the film with an approximate ratio of 1:2 and validated the composition as $NiSe_2$. The EDS measurements were usually made on different points of the catalyst surface to confirm uniformity of composition. While EDS confirmed the presence of Ni and Se consistently all through the example, it also affirmed absence of even trace amounts of oxygen, affirming that the sample composition was pure $NiSe_2$. Elemental composition of the hydrothermally synthesized product was further confirmed through X-ray photoelectron spectroscopy (XPS) measured from pristine surfaces without any sputtering. Calibration was performed using C 1s peak (284.6 eV) and fitting by the Gaussian fitting method.[187] The high-resolution XPS spectra showed peaks corresponding to Ni 2p and Se 3d as shown in Figure 2 (d) and (e). The Ni 2p XPS peaks consists of two spin-orbit doublets and two shake-up satellites at binding energies 855.6 eV and 873.6 eV, respectively corresponding to Ni $2p_{3/2}$ and Ni $2p_{1/2}$ of Ni^{2+}.[187] Very weak intensity peaks at 853.7 eV and 871.8 eV corresponding to Ni $2p_{3/2}$ and Ni $2p_{1/2}$ from Ni^{3+} were also observed indicating presence of mixed oxidation states.[187] Se XPS peaks were obtained at binding energies of 55.0 eV and 59.0 eV corresponding to Se $3d_{3/2}$ and Se $3d_{5/2}$ (Figure 2e).[187] It must be noted here that no peaks of Ni- and/or Se-oxide were observed indicating compositional purity of the catalyst surface.

The electrochemical activity of $NiSe_2$ was measured by using a 3-electrode system where $NiSe_2$-modified CFP electrode was used as the working electrode, while Ag|AgCl and graphite rod was used as the reference and counter electrodes, respectively. A H-cell was used for all electrochemical studies where the cathodic and anodic chambers were separated by an anion exchange membrane (Nafion 115). The catholyte and anolyte consisted of 30 ml of 0.3 M $NaHCO_3$ and 1 M KOH, respectively. The Ag|AgCl reference

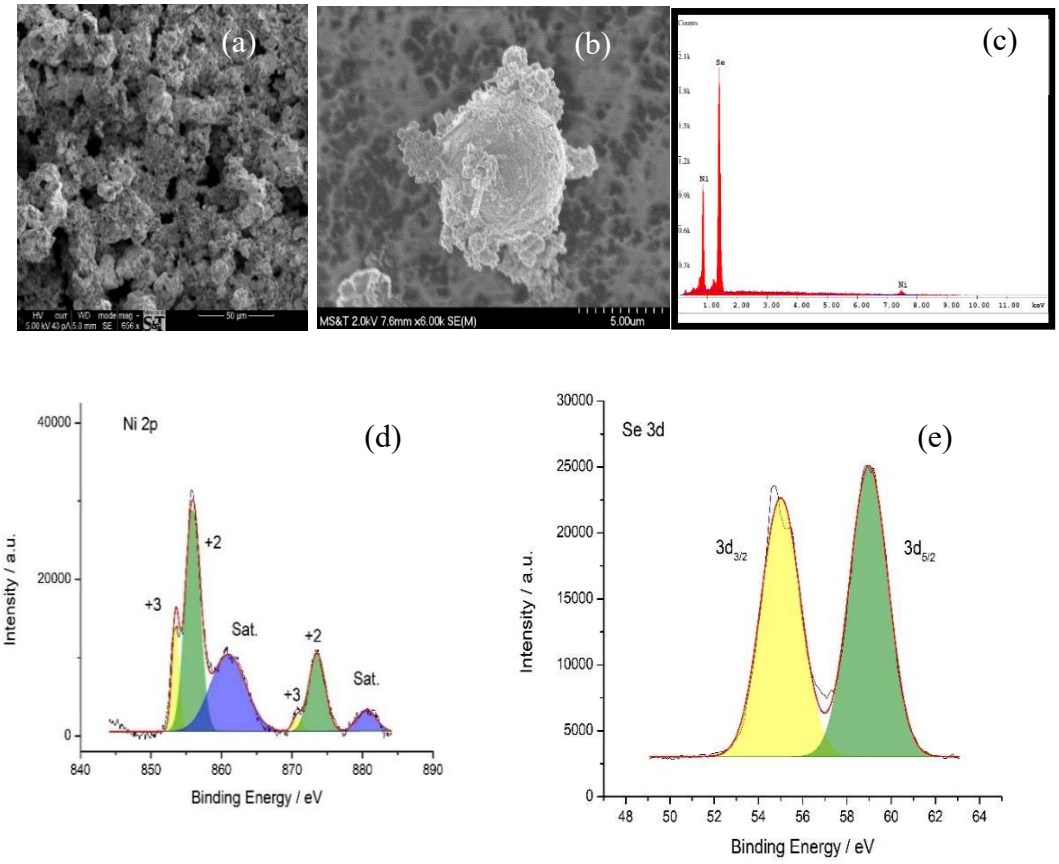

Figure 2. SEM images of the $NiSe_2$ nanoparticles at (a) low and (b) high magnification showing formation of nanostructures and surface roughness, respectively. (c) EDS analysis of the catalyst confirming presence of Ni and Se in 1:2 relative atomic ratio. (d) Ni 2p and (e) Se 3d XPS spectra of as-synthesized $NiSe_2$.

electrode was calibrated with a Pt wire in H_2-saturated H_2SO_4 and an open circuit potential was obtained as −0.199 V. The potential reportedin Ag|AgCl was changed to reversible hydrogen electrode (RHE) using the Equation (1):

$$E_{RHE} = E_{Ag|Agcl} + 0.059\text{pH} + E^0_{Ag|AgCl} \quad (1)$$

where E_{RHE} is the transformed potential vs RHE. $E_{Ag|AgCl}$ is the experimentally obtained potential. $E^0_{Ag|AgCl}$ is the standard potential of Ag|AgCl (0.199 V). The pH of CO_2 saturated 0.3 M $NaHCO_3$ was calcutated to be 6.8.

To test the electrochemical activity of the catalyst towards CO_2 electroreduction, linear sweep voltammetry (LSV) was performed at a scan rate of 10 $mV.s^{-1}$ in Ar- and CO_2-saturated 0.3 M $NaHCO_3$ electrolyte solutions. It was observed that $NiSe_2$@CFP showed higher cathodic current in the polarization curve in CO_2 saturated electrolyte compared to the Ar-saturated electrolyte which proves that CO_2 electroreduction overcomes the competing HER process as can be seen in the Figure 3a. Similar measurements were also performed with blank CFP electrode to study the effect of substrate only, as shown in Figure 3a. Interestingly, it was observed that the cathodic current of blank CFP in CO_2 saturated electrolyte was similar to that in the Ar-saturated electrolyte suggesting that it had no activity towards CO_2 electroreduction under these operational conditions.The LSV studies as shown in Figure 3a further confirms that although CFP (substrate) showed no activity towards CO2RR, the $NiSe_2$ coated CFP substrate has high catalytic activity towards CO2RR exhibiting high current density reaching up to 35 $mA.cm^{-2}$ at low applied potential. The kinetics of a reaction and electrocatalytic activity, was estimated from the Tafel slope using the Tafel equation as shown in Equation (2):

$$\eta = \alpha + (2.3RT) \log j / \alpha nF \quad (2)$$

where η represents the overpotential, n is the number of electrons involved in the reaction, α represents the transfer coefficient, F represents the Faraday constant, j is symbol of the current density, and the slope is calculated by 2.3RT/ αnF. The Tafel equation as

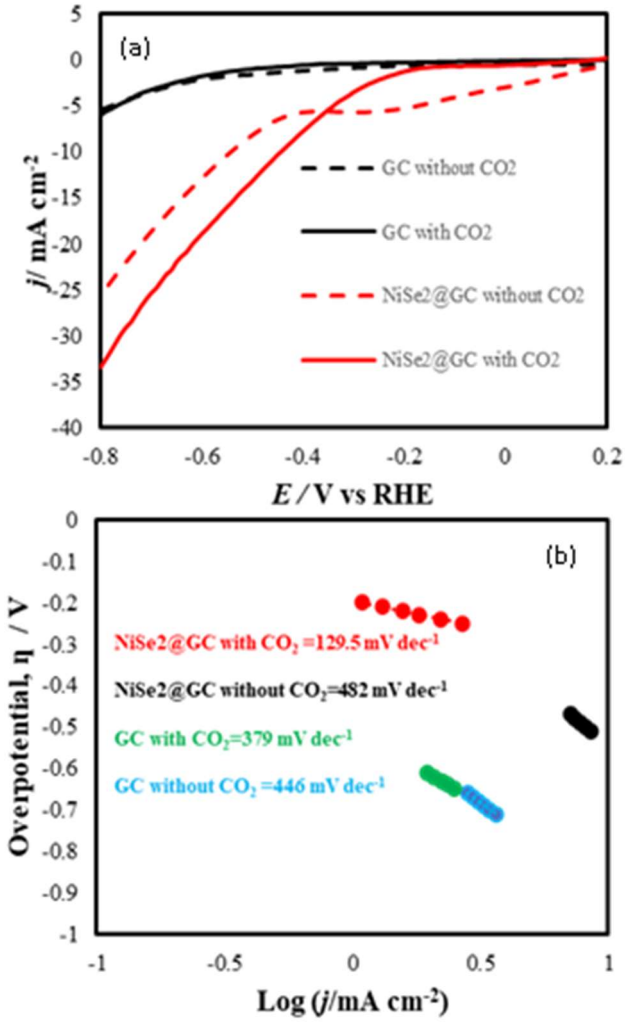

Figure 3. Electrocatalytic activity of $NiSe_2$ towards CO2RR(a) LSVs measured in 0.3 M $NaHCO_3$ at a scan rate of 10 mV s^{-1} in presence and absence of CO_2 with $NiSe_2$ modified GC and bare GC electrodes. (b) Tafel plots measured in 0.3 M $NaHCO_3$.

represented in equation (2) is an important equation which is acquired from the kinetically controlled region of CO2RR and explains the relationship of overpotential η with the current density j. LSV plots were obtained in a non-stirred solution with a slow scan speed (10 mV s-1) for measuring Tafel slopes. The plots were derived from the partial current

density and overpotential (the difference in value between the applied potential and the thermodynamic potential).

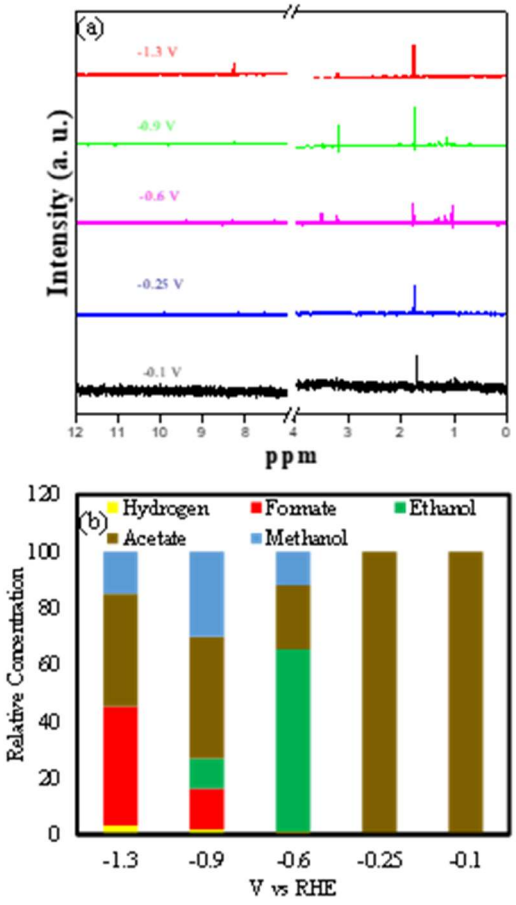

Figure 4. CO2RR products quantification (a) NMR spectra identifying CO_2 reduction products in reaction aliquots collected at different potentials. (b) Plots illustrating relative concentrations of liquid products and gaseous products quantified from NMR and GC TCD at different reduction potentials.

Tafel slope of $NiSe_2$ was estimated to be 129.5 mV dec^{-1} in presence of CO_2 while in absence of CO_2 it showed a much higher Tafel slope. The very low Tafel slope indicates faster kinetics for the reduction of CO_2 in a bicarbonate electrolyte. The Tafel slope for

$NiSe_2$ is near to the theoretical value of 118 mV dec^{-1}, which is expected for the chemical rate-determining step (RDS) of initial single-electron transfer step for formation of adsorbed radical intermediate ($CO_2^{\bullet-}$) on the catalyst surface.[26,188] Low Tafel slope values indicating faster intermediate adsorption kinetics at lower applied potential can corroborate well with formation of CO_2 reduction products at lower applied potential including selective formation of carboxylic acids such as acetic acid. The standard reduction potential of CO_2 to acetic acid is 290 mV.[189] The low Tafel slope (129.5 mV dec−1) measured at low overpotential of 290 mV indicates faster kinetics for acetic acid generation illustrating high selectivity and efficiency of the catalyst. However, given the complexity of CO2RR on the catalyst surface and multitude of steps, more studies are needed to correctly ascertain the proper RDS as well as accurate mechanism for CO2RR on the surface of $NiSe_2$. The Tafel slope for $NiSe_2$@CFP was observed to be smaller than that of bare CFP which confirms the fast transfer of electrons from the $NiSe_2$ modified electrode surface. To check the product composition formed from CO2RR at $NiSe_2$ modified electrode and evaluate catalyst performance, CO_2 electroreduction studies were performed at different applied potentials (-1.3 V, -1.2 V, -0.9 V, -0.6 V, -0.25 V, -0.1 V vs RHE) in 0.3 M $NaHCO_3$ aqueous solution. The products were collected from the cathodic chamber after 1 h of chronoamperometry at fixed applied potential while the catholyte was subjected to constant purging with CO_2 gas at low flow rate (20 sccm). The liquid-state product identification and quantification were performed through ^1H NMR analysis at different applied potentials.

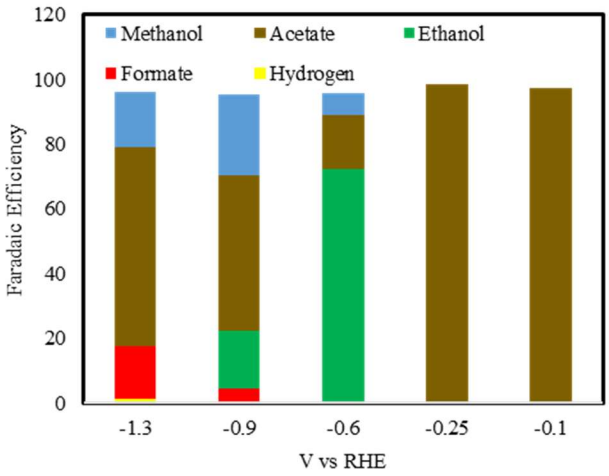

Figure 5. Bar plots depicting relative faradaic efficiency of cumulative liquid and gas phase CO_2 reduction products at different applied potentials quantified through NMR and GC-MS.

Products in gaseous state were identified and quantified by gas chromatography equipped with thermal conductivity detector (GC-TCD). From NMR plots as shown in Figure 4a, it was observed that the product composition was very dependent on the applied potential and showed selectivity towards specific products at each potential. More interestingly, reduction products generated at low applied potentials were carbon rich compounds like acetic acid and ethanol. It must be noted here that the product composition was exclusively acetic acid for over 150 mV potential range. Acetic acid is an industrially important chemical, and the selectivity towards its production at lower applied potential highlights the novelty of this catalyst. Specifically, this catalyst paves the way for high-selectivity direct acetic acid synthesis from CO_2 replacing the conventional multi-step industrial process which typically begins with synthesis of syngas and ends with the generation of methanol followed by its carbonylation.[190] Moreover, the product

composition remained predominantly C2 compounds all the way till -0.6 V vs RHE, which increases novelty of this catalyst even further since most CO2RR catalyst reported previously produces C1 products such as formic acid or CO at similar applied potential. Formation of such carbon-rich products at higher potentials also leads to high production rate due to application of high negative potential. Formic acid was detected in the product composition in addition to carbon rich products at -1.3 V (vs RHE). Hydrogen evolution reaction (HER) occurring at the cathode chamber in aqueous electrolyte is a competitor for CO2RR and has been observed to occur simultaneously. Previous studies has reported that when pH decreases in the vicinity of the electrode surface potential decreases due to continuous hydrogen evolution,[191] in situ conversion of CO_2 to HCO_3^- occurs. However, this spontaneous change happens at higher concentration of nascent hydrogen which also leads to formation of formic acid at higher applied potential. The product composition and relative product yield at different applied potentials was quantified using NMR and the selectivity of C1 and C2 product formation at different applied potentials is shown in Figure 4b. At lower applied potential C2 products (acetic acid and ethanol) are formed exclusively whereas higher applied potentials support the formation of C1 (formic acid) along with some C2 products. This result makes $NiSe_2$ very promising as CO2RR catalyst since for application of any CO_2 conversion technology in industrial setup, selectivity is a critical factor. More importantly, the formation of value-added C2 products with less energy expenditure and high selectivity can have practical application in industry. GC-TCD was used to detect and quantify gaseous products. The head-space gas was collected after 1 hr of CO2RR experiment at fixed potential (-0.1 V, -0.25 V, -0.6 V, -0.9 V vs RHE) and was injected into the GC-TCD column.

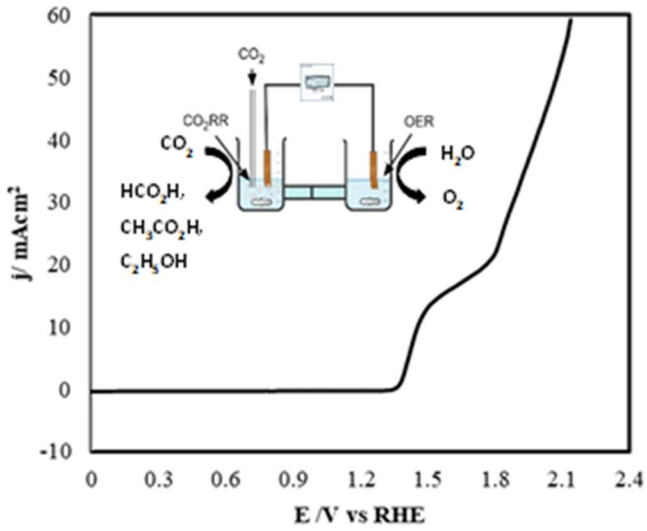

Figure 6. Polarization curve with cathodic CO2RR and anodic OER with $NiSe_2$@CFP as both cathodic and anodic electrocatalyst. Inset shows schematic of the electrochemical setup for combined CO2RR and OER.

Only H_2 was detected as a gaseous product at higher applied potential (> –0.6 V) and no other gaseous product like CO or CH_4 commonly observed with previously reported catalysts,[183,185,199,200,191–198] were detected. Amount of hydrogen gas produced was dependent on the applied potential and increased with increasing cathodic potential (FE = 0 %, 0 %, 0.29%, 0.89 %, 1.69 % at -0.1, -0.25, -0.6, -0.9 and -1.3 V, respectively). HER has been known to be a competing reaction of CO2RR and the challenge is to design catalyst surfaces which can subdue Hydrogen Evolution reaction while reinforcing CO2RR. Hence the observation that even at higher applied potential $NiSe_2$ produces only minor amount of H_2, while predominantly forming hydrocarbons, is very promising for electrocatalytic CO2RR. This can be due to the fact that on $NiSe_2$ surface CO_2 reduction

occurs at much lower applied potential, while HER requires a much higher overpotential as has been reported earlier.[201]

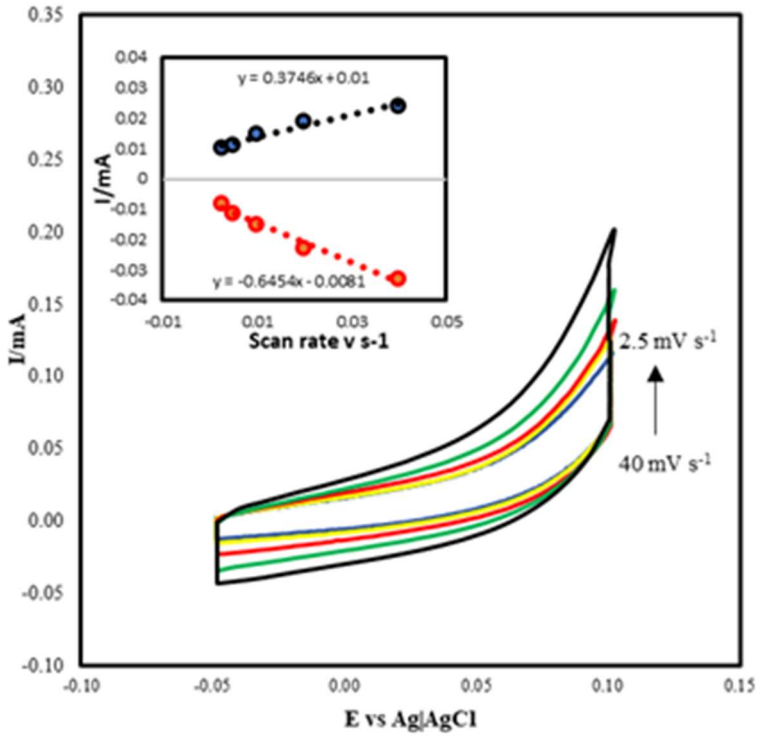

Figure 7. Cyclic voltammograms measured for $NiSe_2$ catalyst in 0.3 M $NaHCO_3$ under continuous N_2 purging at different scan rates from 2.5 to 40 mV s^{-1}. Inset shows plot of anodic and cathodic current measured at 0.04 V vs Ag|AgCl as function of scan rate.

The observed product selectivity also suggests that at lower applied potential intermediate adsorption and kinetics of CO2RR on the catalyst surface is more favorable than rate of water reduction. Moreover, absence of CO in the product composition and production of C2 products selectively, makes $NiSe_2$ catalyst very unique as almost all the nickel-based catalyst are known to produce CO as their main product.[192]

Quantification of gaseous and liquid products was done using combined GC-TCD and NMR measurements, which was further used to calculate individual and total faradaic efficiency (FE) for all the CO_2 reduction products that were identified. The Faradaic efficiency for each product was calculated following previously reported standard method[177] where, the electron mole fraction for formation of specific product were considered along with total charge consumed during the electrochemical conversion and mole fractions of products (gaseous and liquid) formed. The absolute quantity of each product was estimated from GC-TCD (gas) and NMR (liquid) experiments. Also, by quantifying the products at any specific potential using GC-TCD and NMR experiments, relative percentage of different products formed was obtained at different potentials.

Faradaic efficiency for all the gaseous as well as liquid products detected using GC-TCD and NMR analysis simultaneously in fixed potential CO2RR experiments has been shown in Figure 5. It was observed that at lower applied potential there was a high selectivity for formation of C2 products such as ethanol and acetic acid as has been explained above from NMR data. Specifically, at the lowest applied potential of 100 mV vs RHE, there was exclusive formation of acetic after 1 h of electrolysis with 100% FE. When the applied potential was increased to more negative potential from -0.1 V, new product ethanol was obtained till -0.9 V vs RHE. With the emergence of new products, faradaic efficiency of acetic acid decreased with increasing cathodic potential. Specifically, the Faradaic efficiency for acetic varied from 54.8%, 61.4%, 18.9%, 100% and 100%, respectively at -1.3, −0.9, −0.6, 0.25, and −0.1 V vs RHE. On the other hand, Faradaic efficiency for ethanol formation varied from 22.4% and 80.8% respectively at−0.9, and -0.6 V vs RHE. Since carbon-rich products such as ethanol and acetic acid have high

industrial value and can also be used as fuels, their exclusive formation at low energy expense can have large implications for practical CO_2 utilization. More importantly, achieving faradaic efficiency of 80.8 % for ethanol at such low applied potential has not been commonly observed in any catalyst systems. Methanol which is a C1 product was first observed at -0.6V reaching its maximum FE at -0.9V. From the figure we can also observe the absence of CO and presence of H_2 in the chromatogram obtained from measurements done on GC-TCD. Alkane products such as methane and ethane were also not observed during the measurement which can be due to: (i) suppression of HER at such low potential as nascent hydrogen produced during HER can be helpful in producing hydrocarbons. (ii) suppression of CO formation which inhibits its further reduction to C1 hydrocarbons such CH4. These results show the uniqueness of this electrocatalyst which is able to selectively produce carbon rich fuels with high faradaic efficiency at low energy input. Moreover, this CO2RR electrocatalyst is also capable of producing high current density of 35 mA cm^{-2} at moderately low applied potential.

Stability of the catalyst for CO2RR was checked through chronoamperometry studies where CO_2 was reduced at constant applied potential for 24 hours. The chronoamperometry figures obtained at various applied potentials ranging from -0.1 to -0.9 V vs RHE showed that the reduction current density corresponding to CO2RR was maintained constant for over 12 h as shown in Figure S1 (supporting information). The catalyst composition after CO2RR activity was confirmed through PXRD measurements which showed that there was no change in the crystallinity or composition of the catalyst before and after CO2RR activity (Figure 1).

Phase stability of $NiSe_2$ under operational conditions for CO2RR can be also explained through Pourbaix diagrams which are electrochemical phase diagrams as a function of pH depicting compositional stability of metal and its compounds in the aqueous phase. These phase maps help in assessing the electrochemical stabilities of $NiSe_2$ under various applied potential. Ni Pourbaix diagrams calculated from density-functional theory (DFT) makes $\Delta_f G$ values (free energy of formation) more consistent with direct electrochemical experiments. It was reported previously that the Ni metallic phase forms below -0.75 V vs RHE in the Pourbaix diagram[202] making $NiSe_2$ very stable catalyst on the applied potential range for CO2RR. Specifically, the conversion of Nickel (II) to Nickel (0) requires excess energy/potential in operational pH for CO2RR (i.e., pH = 7.2–8.9).[202] The corrosion rate for Ni^{2+} was also observed to be minimal at neutral pH below 1 V vs RHE. Hence, from the Pourbaix digram it can be confirmed that there is minimal catalyst reduction and degradation at neutral pH under operational condition for CO2RR, illustrating fuinctional and compositional stability of $NiSe_2$. The preferential reduction that occurs on the surface of $NiSe_2$ under these operational conditions is analyte reduction, i.e. CO2RR and HER.

3.1. ELECTROCHEMICAL CATALYTIC ACTIVITY OF $NISE_2$ FOR CO2RR-OER

It must be mentioned here that $NiSe_2$ has been previously reported as a promising catalyst in alkaline medium for oxygen evolution reaction (OER) [120,200] with an onset potential of 1.36 V (vs RHE) and overpotential of 290 mV at 10 $mA.cm^{-2}$. Hence, the application of $NiSe_2$ was applied as a bifunctional OER-CO2RR catalyst wherein, the $NiSe_2$@CFP was used both as cathodic catalyst to electrochemically reduce CO_2 in the

cathodic chamber and also as anodic catalyst for generation of oxygen through water splitting in the anodic chamber. This experiment was done in a H-shaped electrochemical cell where the cathodic and anodic chambers were separated by Nafion membrane. The catholyte was 0.3 M $NaHCO_3$ solution where CO_2 was continuously purged while the anolyte consisted of 1 M KOH. The pH of both the chambers were continuously monitored to confirm that there was no transport of OH^- remains across the membrane and catholyte and anolyte maintained their neutral and alkaline nature, respectively. Figure 6 shows the polarization curve obtained for such CO2RR-OER experiment while a schematic representation of the experimental setup has been shown as an inset in the figure. It was observed that the CO2RR-OER electrolytic cell exhibited a cell potential of ~1.8 V at 20 $mA.cm^{-2}$ indicating high efficiency of the process. The catholyte composition detected through NMR showed presence of ethanol and acetic acid similar to that as has been shown in Figure 4, confirming the occurrence of CO2RR similar to the constant potential experiment. Such bifunctional activity emphasizes the novelty of this catalyst since it can not only reduce the concentration of atmospheric pollutant CO_2, but also enrich the air with O_2. This will have tremendous impact in practical applicability of such catalysts especially in situations where there is a high concentration of CO_2 and access to clean oxygen is needed on-demand.

Enhanced electrocatalytic activity can typically be assigned to intrinsic factors which includes facile catalyst activation through intermediate adsorption and enhanced charge transport, as well as extrinsic factors such as catalyst morphology and surface roughness which influences electrolyte and analyte access to the catalytically active sites. The extrinsic factors affecting CO2RR electrocatalytic activity of $NiSe_2$ was investigated

by estimating the electrochemically active surface area (ECSA) by following previously reported experimental procedure.[75] The ECSA was calculated by plotting electrochemical double layer capacitance in the non-Faradaic region as a function of scan rate and then comparing specific capacitance (C_S) to the double layer capacitance observed. The electrochemical double layer capacitance (C_{DL}) was calculated following Equation (3):

$$i_{DL} = C_{DL} \times \nu \quad (3)$$

where i_{DL} represents the current observed while ν is the scan rate. As can be seen from the Figure 7, C_{DL} calculated from the i vs ν plot resulted in value of 0.5 mF. The ratio of C_{DL} and Cs was used to calculate ECSA as shown in Equation (4).

$$ECSA = C_{DL}/C_S \quad (4)$$

Using the C_S value (40μF cm^{-2}) from reported values and C_{DL} value (0.5 mF) from the plot, ECSA value was calculated to be 12.74 cm^2. The effect of catalyst morphology on the working electrode was also estimated from the roughness factor (RF). RF was calculated to be 159.28 from the ratio between ECSA and geometric electrode area (0.08 cm^2). High value of ECSA and roughness factor depicts that CO_2 dissolved in the electrolyte has more access to the catalytic sites on working electrode, leading to better conversion efficiency. The intrinsic effect of catalyst composite on CO2RR activity was investigated through electrochemical impedance spectroscopy (EIS) to investigate the kinetics of charge transfer on $NiSe_2$ catalytic surface during the CO2RR process. Nyquist plots were measured at different potentials ranging from 0 to -1.3 V in CO_2-saturated 0.3 M $NaHCO_3$ to investigate how the charge transfer kinetics varied as a function of applied potential and stages of CO_2 reduction. These plots also indicate how intermediate

adsorption on the catalyst surface may affect the charge transfer kinetics leading to variation in reduction current density and CO2RR efficiency.

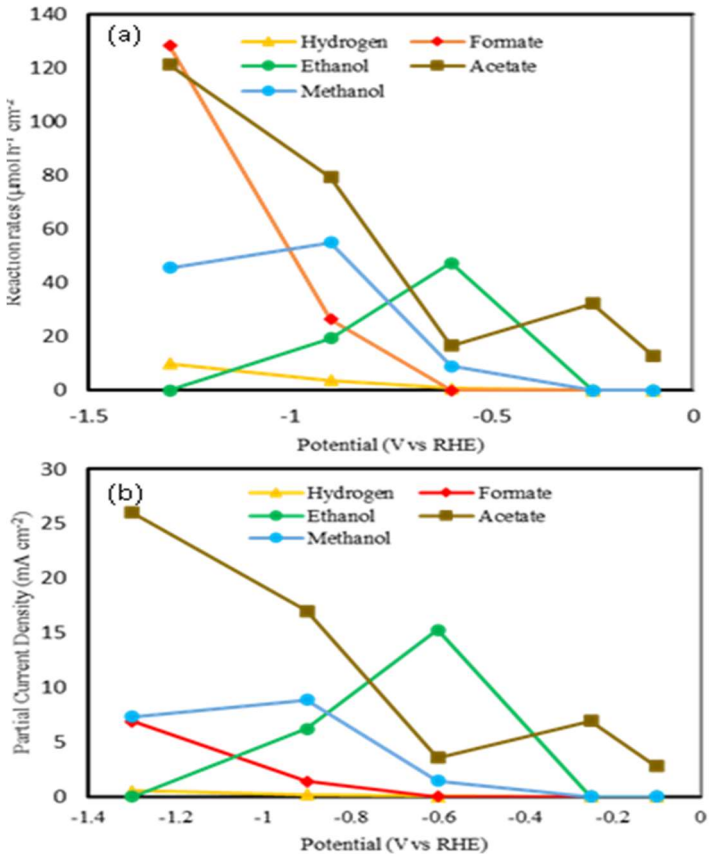

Figure 8. CO_2RR performances of $NiSe_2$ catalyst. (a) Formation rates of Hydrogen, formate, ethanol, acetate and methanol. (b) Partial current density of individual products, hydrogen, formate, ethanol, acetate and methanol.

For instance, at cathode, adsorption of intermediates on catalyst surface can be affected by hydrated Na^+ ions which also functions as buffer in solution. In the proximity of cathode, columbic interactions can also cause the hydrolysis of hydrated Na^+ cations. The Nyquist plots were fitted to equivalent circuits as shown in inset of Figure 8, in which

charge transfer resistance (R_{CT}) refers to the electrode-electrolyte interface and illustrates the barrier that electrons must cross to reach the electroactive species adsorbed on the electrode surface, while R_s represents film resistance of the catalyst composite. It is imperative that lower R_{CT} values will lead to faster charge transfer rate at the interface resulting in facile reduction on the electrode surface. The R_{CT} and R_s estimated at different potentials has been listed in Table 1. It can be clearly seen that the charge-transfer resistance decreases as a function of applied potential explaining how the reduction current density and efficiency increases with potential.

Large ECSA ensures better electrolyte access to catalytically active sites while low charge transfer resistance and film resistance facilitates charge transfer across the electrode electrolyte interface and within the catalyst matrix. Both of these factors can enhance the

Table 1. Fitting parameters obtained from Nyquist plots at various potentials.

Potential (V vs RHE)	Rct	Rs	CPE_{dl}	W
-0.25	36.78	17.8	0.50	0.0000915
-0.6	25.07	3.77	0.91	0.00011
-0.9	10.23	3.6	1.14	0.00012
-1.3	2.80	2.6	1.3	0.00029

reduction current density while lowering the potential required for CO2RR. Another factor that can influence such electrocatalytic activity is the catalyst surface wetting with aqueous electrolyte which maximizes electrolyte access on the surface and enhances intermediate adsorption. Surface wetting can be qualitatively estimated through measuring contact angle of the electrolyte drop on the catalyst-electrode surface.

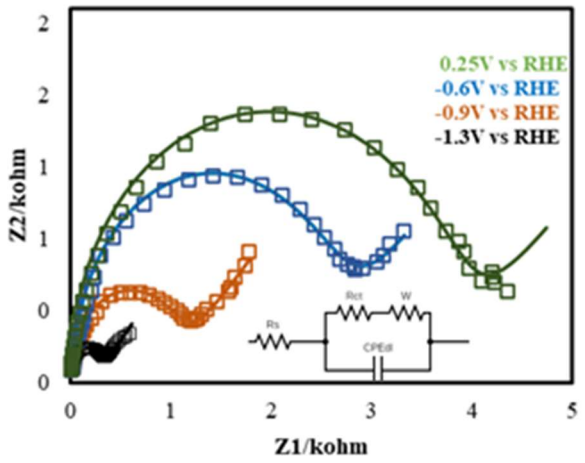

Figure 9. EIS Nyquist plots of $NiSe_2$@CFP in CO_2-saturated 0.3 M $NaHCO_3$ electrolyte (Ph 6.8) from 0 V vs RHE to -1.3 V vs RHE. Inset shows the equivalent circuit fitted to experimental spectra, where R_{CT} corresponds to the charge-transfer resistance on catalyst-electrolyte interface, while R_s indicates film resistance of the catalyst composite.

Difference in the contact angle of the electrolyte with $NiSe_2$ @CFP and CFP was observed as shown in Figure S2. Increased contact angle in $NiSe_2$ @CFP indicates better hydrophilicity and surface wetting which increases the exposure of active sites in catalyst for CO_2 electroreduction. [203]

The product selectivity and composition on the other hand, depends heavily on the nature and energetics of intermediate adsorption on the catalyst surface. Previously we have proposed that carbon monoxide (*CO) formed through initial reduction of the anion radical CO_2^- on catalyst surface plays a significant role as the reactive intermediate. The dwell time of *CO on the catalyst surface is proposed to influence the extent of CO_2 reduction and product composition. A longer dwell time of intermediate *CO will expectedly lead to further reduction of CO_2 to carbon rich (C2 and C3) products, while lesser dwell time will lead to ready release of CO or formic acid as the reduction

products(s). The *CO dwell time on the surface can be inferred from the *CO adsorption energy on the surface. The *CO adsorption energy on $NiSe_2$ surface was calculated through density functional theory (DFT) approach following methodology as described previously.[177] Details of DFT calculations has been provided in supporting information. It was observed that *CO adsorption energy on $NiSe_2$ surface was smaller than that of Ni metal, but higher than that of Cu. Earlier we had proposed that the *CO adsorption energy could be directly correlated to the observed product selectivity with smaller *CO adsorption energy leading to C1 products (CO and formic acid), while higher adsorption energy leads to catalyst poisoning. This hypothesis was based on the plot shown in Figure 9 and comparison with reported literature from various groups. Catalysts such as Au, Ag, and Cu with very low CO adsorption energy traditionally produces CO and formic acid from CO_2, while Pt, Pd, Ru etc. Are easily poisoned by CO_2. In Cu-based system it was shown that intermediate *CO adsorption energy led to preferential formation of C2 products in Cu_2Se.[177] Hence, we had proposed the mid-section of this plot represents optimal *CO adsorption energy which maximizes CO dwell time for subsequent reduction to carbon-rich products without leading to catalyst poisoning. It was observed that CO adsorption energy of $NiSe_2$ is indeed in the middle region illustrating optimal catalyst composition for CO_2 reduction to C2/C3 products. It must also be noted that the CO adsorption energy on $NiSe_2$ surface was lower than that of Ni. This can be attributed to the fact that CO adsorption on transition metal site is influenced by the possibility of forming metal-ligand back bonding involving metal *d*-orbitals and π* orbitals of CO. Such overlap will be affected by the proximity of the *d*- and π* orbitals. In this case, as oxidation state

of the metal site increases in $NiSe_2$ (Ni^{2+}), the *d*-orbital energies become more stabilized leading to a lesser degree of overlap compared to metal in 0 oxidation state (Ni).

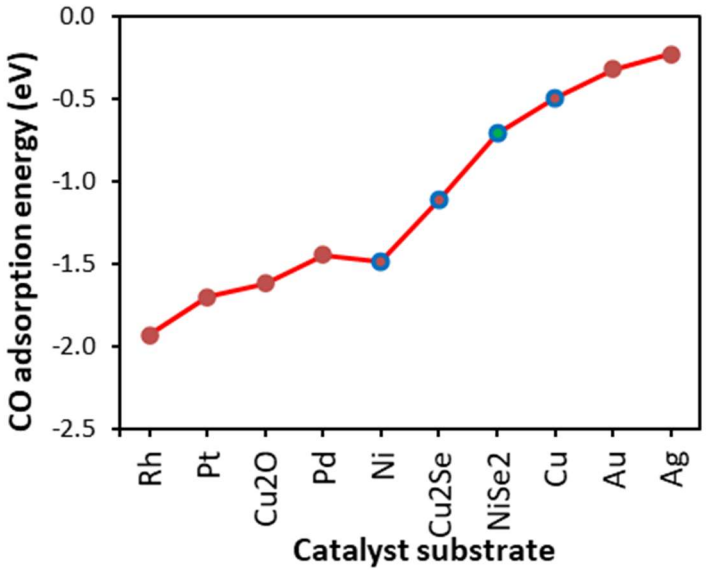

Figure 10. CO adsorption energy on $NiSe_2$ (111) surface compared with other known CO2RR reduction catalysts. All CO adsorption energies were estimated through DFT calculations.

Hence, it can be expected that the metal-to-ligand back bonding in metallic Ni is stronger than that in $NiSe_2$ due to better overlap attributed to closer proximity of the participant orbitals. It should also be noted that this observation is in sharp contrast with Cu and Cu_2Se where Cu has smaller *CO adsorption energy compared to Cu_2Se. This difference can be attributed to the d10 full shell configuration of Cu which imparts extra stability leading to large separation between the d- π^* orbitals. Hence, it becomes important to realize the importance of d-shell occupancy on the extent of metal-to-ligand back bonding and its effect on the CO2RR outcome. Electronegativity of the anion also has a

critical role to play in metal-to-ligand back bonding, wherein, reducing electronegativity is expected to raise energy of the bonding molecular orbitals leading to smaller gap between the metal and ligand group orbitals. This case study with $NiSe_2$ reveals the importance to understand the effect of such intrinsic factors on the CO2RR activity through its effect on metal-to-ligand back bonding that optimizes intermediate *CO adsorption on the surface and further CO2RR activity.

4. CONCLUSION

In summary, $NiSe_2$ was identified as a highly efficient electrocatalyst for CO_2 reduction. The $NiSe_2$ was synthesized through one-pot hydrothermal synthesis method. The novelty of this catalyst lies in the fact that it can lead to preferential formation of value-added C2 products at very low applied potential with minimum energy expense. Acetic acid was formed exclusively between a potential range of 100 to 250 mV vs RHE while at slightly higher potential it showed acetic acid and ethanol as the only products after several hours of CO_2 reduction. Preferential formation of C1 products such as methanol and formic acid was observed at higher applied potential. Interestingly this catalyst showed negligible presence of CO in the reduction products, thereby isolating it from most of the CO2RR catalysts that has been reported till date. It should be also noted that formation of H_2 through HER was observed at much higher potential indicating that at low applied potential CO2RR was more kinetically favored on $NiSe_2$ surface. Low R_{CT} between the catalysts and the substrate in the electrodes, moderate binding energy of intermediates on the $NiSe_2$ catalyst and abundant exposed active sites in the nanoporous catalyst composite enhance

the efficiency of $NiSe_2$ for reduction of CO_2 to C_2 products. According to applied potential, reduction products of CO2RR showed selectivity between C1 and C2 products. At high applied potential (-1.3 V), formic acid was detected along with acetic acid and methanol with a Faradaic efficiency of 43.47%, 54.82% and 15.5 % respectively. At higher anodic potential (<-1.3 V) increased selectivity towards C2 products such as ethanol and acetic acid were obtained. For ethanol, maximum faradaic efficiency was achieved at a low applied potential of -0.6 V vs RHE. Through literature search, it was realized that that these applied potentials are among the lowest applied potential at which C2 products have been obtained with high yield and Faradaic efficiency. The liquid and gaseous reduction products were characterized through NMR and GC-TCD techniques, respectively using time-dependent measurements. H_2 was detected at high cathodic potential (> -0.6 V) reaching its maximum at -1.3 V indicating that $NiSe_2$ has suppressed HER catalytic activity at low overpotentials. Since HER at cathode is a competing reaction and inhibits CO2RR on the catalyst surface, result mentioned above are significant for practical application of this catalyst. Interestingly, there was no CO formed among the reduction products which is different from other catalyst having CO as their major products. The $NiSe_2$ catalyst was further studied for the CO_2 electroreduction by estimating CO adsorption energy on the catalyst site using DFT calculations. Calculations showed moderate CO adsorption energies which indicates adsorbed *CO has longer dwell time on the catalyst surface causing selective reduction to C2 products. In summary, $NiSe_2$ catalyst can reduce CO_2 to methanol, ethanol and ethanoic acid at lowest applied potentials reported till date with high Faradaic efficiency. These experimental results along with the findings of catalytic activity

with CO adsorption energy obtained using DFT study can lead to optimal catalyst design for synthesizing carbon-rich high-value products through CO_2 reduction.

SUPPORTING INFORMATION

1. NMR SPECTROSCOPY

Liquid products formed during CO_2 electrochemical reduction were analyzed with ^{1}H-NMR. Aliquots were collected at regular intervals as mentioned in the manuscript and 2 µL DMSO (internal standard) and 200 µL D_2O was added to 0.5 ml electrolyte. The NMR experiments were performed on a Bruker 400 MHz NMR spectrometer, using a presaturation sequence to suppress the water signal. NMR spectra of reaction mixture was measured before starting any electrochemical reaction to make sure that there was no impurity in the solution which can lead to false results.

Table S1. Chemical shifts and assignments of peaks from different possible products observed in 1H-NMR spectra after CO_2 reduction.

Observed NMR Values			Products		Standard NMR Values[47]
Chemical Shift	1H Splitting	J coupling	Probed Nucleus	Name	Chemical Shift
8.35	s		$CHOO^-$	Formate	8.35
3.64	q	7.08	CH_3CH_2OH	Ethanol	3.64
3.23	s		CH_3OH	Methanol	3.23
1.8	s		$CH_3C(=O)O^-$	Acetate	1.8
1.20	t	7.16	CH_3CH_2OH	Ethanol	1.20

2. QUANTIFICATION OF THE PRODUCTS

Liquid products were quantified from NMR spectra by calibrating it with respect to the internal standard and quantifying the identified products. Gaseous products of CO_2 reduction were collected and transferred to GC using gas-tight syringe. The GC was equipped with thermal conductivity detector (GC- TCD) and Molecular Sieve 5A capillary column. Helium (99.999%) was used as the carrier gas. The GC columns led directly to a TCD detector to quantify hydrogen and carbon monoxide. At ambient conditions, CO_2 was continuously purged through a cathode compartment flow cell at a rate of 20 sccm while a constant potential was applied for designated time. The cell effluent was sampled using 100 µL syringe. The Faradaic efficiency (FEs) calculated by measuring the current and using mole percentages quantified through GC-TCD as well as NMR analysis as follows:

Table S2. Calculated Faradaic Efficiency along with product concentration obtained at -1.3 V vs RHE.

Products	No. of moles of product(mol)	n (number of electrons to form specific product)	C_e (Charge required to form certain product) (C)	$F = \frac{C_e}{C_T} * 100$
H_2	2.83627E-06	2	0.547314379	1.266931432
formate	3.63399E-05	2	7.012509647	16.23266122
ethanol	0	12	0	0
acetate	3.43726E-05	8	26.53154813	61.41562068
Methanol	1.29243E-05	6	7.481982747	17.31940451

Table S3. Calculated Faradaic Efficiency along with product concentration obtained at -0.9 V vs RHE.

Products	No. of moles of product(mol)	n (number of electrons required to form specific product)	C_e (Charge required to form certain product) (C)	$F = \frac{C_e}{C_T} * 100$
H_2	1.0523E-06	2	0.203062331	0.564062031
Formate	7.47992E-06	2	1.443400686	4.009446351
Ethanol	5.46773E-06	12	6.330646802	17.58513
Acetate	2.24623E-05	8	17.33820268	48.16167412
Methanol	1.56143E-05	6	9.039280197	25.10911166

Table S4. Calculated Faradaic Efficiency along with product concentration obtained at -0.6 V vs RHE.

Products	No. of moles of product(mol)	n (number of electrons required to form specific product)	C_e (Charge required to form certain product) (C)	$F = \frac{C_e}{C_T} * 100$
H_2	2.41366E-07	2	0.046576365	0.215631319
Formate	0	2	0	0
Ethanol	1.34583E-05	12	15.58232909	72.14041245
Acetate	4.71388E-06	8	3.638550456	16.845141
Methanol	2.52189E-06	6	1.459946464	6.759011406

Table S5. Calculated Faradaic Efficiency along with product concentration obtained at -0.25 V vs RHE.

Products	No. of moles of product(mol)	*n* (number of electrons required to form specific product)	C_e (Charge required to form certain product) (C)	$F = \frac{C_e}{C_T} * 100$
H_2	0	2	0	0
Formate	0.00E+00	2	0	0
Ethanol	0	12	0	0
Acetate	9.18E-06	8	7.088056034	98.45
Methanol	0	6	0	0

Table S6. Calculated Faradaic Efficiency along with product concentration obtained at -0.1 V vs RHE.

Products	No. of moles of product(mol)	*n* (number of electrons required to form specific product)	C_e (Charge required to form certain product) (C)	$F = \frac{C_e}{C_T} * 100$
H_2	0	2	0	0
Formate	0	2	0	0
Ethanol	0	12	0	0
Acetate	3.67314E-06	8	2.835222414	97.22984958
Methanol	0	6	0	0

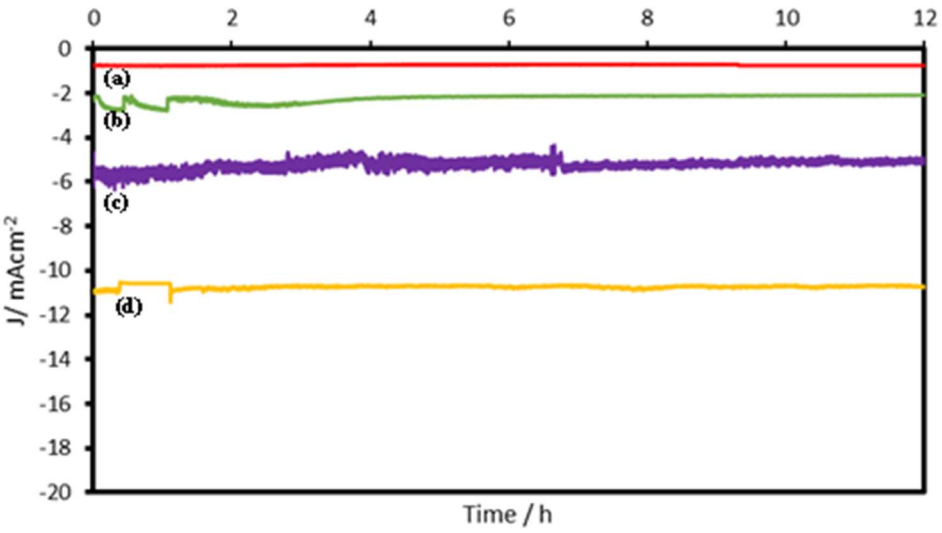

Figure S1. Current density plot for 12 h of chronoamperometry study at different applied potential: (a) -0.1V vs RHE, (b) -0.25V vs RHE, (c) -0.6V vs RHE, (d) -0.9V vs RHE

REFERENCES

1 Y. Hori, K. Kikuchi and S. Suzuki, Production of CO AND CH_4 in electrochemical reduction of CO_2 at metal electrodes in aqueous hydrogencarbonate solution, *Chem. Lett.*, 1985, **14**, 1695–1698.

2 Y. Zheng, A. Vasileff, X. Zhou, Y. Jiao, M. Jaroniec and S.-Z. Qiao, Understanding the Roadmap for Electrochemical Reduction of CO_2 to Multi-Carbon Oxygenates and Hydrocarbons on Copper-Based Catalysts, *J. Am. Chem. Soc.*, 2019, **141**, 7646–7659.

3 A. Saxena, W. Liyanage, J. Masud, S. Kapila and M. Nath, Selective Electroreduction of CO_2 to Carbon-rich Products by Simple Binary Copper Selenide Electrocatalyst, *J. Mater. Chem. A*, 2021, **9**, 7150–7161.

4 K. P. Kuhl, E. R. Cave, D. N. Abram and T. F. Jaramillo, New insights into the electrochemical reduction of carbon dioxide on metallic copper surfaces, *Energy Environ. Sci.*, , DOI:10.1039/c2ee21234j.

5 Z. Yang, F. E. Oropeza and K. H. L. Zhang, P-block metal-based (Sn, In, Bi, Pb) electrocatalysts for selective reduction of CO2to formate, *APL Mater.*, 2020, **8**, 60901.

6 S. Ma, M. Sadakiyo, M. Heim, R. Luo, R. T. Haasch, J. I. Gold, M. Yamauchi and P. J. A. Kenis, Electroreduction of carbon dioxide to hydrocarbons using bimetallic Cu-Pd catalysts with different mixing patterns, *J. Am. Chem. Soc.*, 2017, **139**, 47–50.

7 T. Adit Maark and B. R. K. Nanda, CO and CO_2 Electrochemical Reduction to Methane on Cu, Ni, and Cu_3Ni (211) Surfaces, *J. Phys. Chem. C*, 2016, **120**, 8781–8789.

8 I. Merino-Garcia, J. Albo, P. Krzywda, G. Mul and A. Irabien, Bimetallic Cu-based hollow fibre electrodes for CO_2 electroreduction, *Catal. Today*, 2020, **346**, 34–39.

9 J. Albo, M. Perfecto-Irigaray, G. Beobide and A. Irabien, Cu/Bi metal-organic framework-based systems for an enhanced electrochemical transformation of CO_2 to alcohols, *J. CO2 Util.*, 2019, **33**, 157–165.

10 J. Albo, D. Vallejo, G. Beobide, O. Castillo, P. Castaño and A. Irabien, Copper-Based Metal–Organic Porous Materials for CO_2 Electrocatalytic Reduction to Alcohols, *ChemSusChem*, 2017, **10**, 1100–1109.

11 H. Yang, Y. Wu, G. Li, Q. Lin, Q. Hu, Q. Zhang, J. Liu and C. He, Scalable Production of Efficient Single-Atom Copper Decorated Carbon Membranes for CO_2 Electroreduction to Methanol, *J. Am. Chem. Soc.*, 2019, **141**, 12717–12723.

12 J. Albo and A. Irabien, Cu_2O-loaded gas diffusion electrodes for the continuous electrochemical reduction of CO_2 to methanol, *J. Catal.*, 2016, **343**, 232–239.

13 F. Cheng, X. Zhang, K. Mu, X. Ma, M. Jiao, Z. Wang, P. Limpachanangkul, B. Chalermsinsuwan, Y. Gao, Y. Li, Z. Chen and L. Liu, Recent Progress of Sn-Based Derivative Catalysts for Electrochemical Reduction of CO_2, *Energy Technol.*, 2021, **9**, 2000799.

14 Y. Liu, S. Chen, X. Quan and H. Yu, Efficient Electrochemical Reduction of Carbon Dioxide to Acetate on Nitrogen-Doped Nanodiamond, *J. Am. Chem. Soc.*, 2015, **137**, 11631–11636.

15 S. M. Bashir, S. S. Hossain, S. ur Rahman, S. Ahmed and M. M. Hossain, NiO/MWCNT Catalysts for Electrochemical Reduction of CO_2, *Electrocatalysis*, 2015, **6**, 544–553.

16 X. Shao, X. Zhang, Y. Liu, J. Qiao, X.-D. Zhou, N. Xu, J. L. Malcombe, J. Yi and J. Zhang, Metal chalcogenide-associated catalysts enabling CO_2 electroreduction to produce low-carbon fuels for energy storage and emission reduction: catalyst structure, morphology, performance, and mechanism, *J. Mater. Chem. A*, 2021, **9**, 2526–2559.

17 D. Yang, Q. Zhu, C. Chen, H. Liu, Z. Liu, Z. Zhao, X. Zhang, S. Liu and B. Han, Selective electroreduction of carbon dioxide to methanol on copper selenide nanocatalysts, *Nat. Commun. 2019 101*, 2019, **10**, 1–9.

18 D. Mateo, J. Albero and H. García, Graphene supported NiO/Ni nanoparticles as efficient photocatalyst for gas phase CO_2 reduction with hydrogen, *Appl. Catal. B Environ.*, 2018, **224**, 563–571.

19 H. Singh, J. Bernabe, J. Chern and M. Nath, Copper selenide as multifunctional non-enzymatic glucose and dopamine sensor, *J. Mater. Res. 2021 367*, 2021, **36**, 1413–1424.

20 F. N. Harris, Applications of Acetic Acid to Well Completion, Stimulation and Reconditioning, *J. Pet. Technol.*, 1961, **13**, 637–639.

21 A. T. Swesi, J. Masud, W. P. R. Liyanage, S. Umapathi, E. Bohannan, J. Medvedeva and M. Nath, Textured $NiSe_2$ Film: Bifunctional Electrocatalyst for Full Water Splitting at Remarkably Low Overpotential with High Energy Efficiency /639/638/77/886 /639/301/299/886 /639/301/299/161 /128 /120 /145 /140/146 article, *Sci. Rep.*, 2017, **7**, 1–11.

22 E. L. Clark, J. Resasco, A. Landers, J. Lin, L. T. Chung, A. Walton, C. Hahn, T. F. Jaramillo and A. T. Bell, Standards and Protocols for Data Acquisition and Reporting for Studies of the Electrochemical Reduction of Carbon Dioxide, *ACS Catal.*, 2018, **8**, 6560–6570.

23 Q. Jiang, R. Chen, H. Chen, J. Jiang, X. Yang, Y. Ju, R. Ji and Y. Zhang, Improved performance in dye-sensitized solar cells via controlling crystalline structure of nickel selenide, *J. Mater. Sci.*, 2018, **53**, 7672–7682.

24 Y. Zhao, J. Liang, C. Wang, J. Ma and G. G. Wallace, Tunable and Efficient Tin Modified Nitrogen-Doped Carbon Nanofibers for Electrochemical Reduction of Aqueous Carbon Dioxide, *Adv. Energy Mater.*, 2018, **8**, 1702524.

25 Y. Hori, in *Modern ASpects of Electrochemistry no 42*, 2008.

26 M. Dworkin, S. Falkow, E. Rosenberg, K.-H. Schleifer and E. Stackebrandt, Eds., The Prokaryotes, , DOI:10.1007/0-387-30742-7.

27 The Cativa™ Process for the Manufacture of Acetic Acid | Johnson Matthey Technology Review, https://www.technology.matthey.com/article/44/3/94-105/, (accessed 18 November 2021).

28 D. Tan, C. Cui, J. Shi, Z. Luo, B. Zhang, X. Tan, B. Han, L. Zheng, J. Zhang and J. Zhang, Nitrogen-carbon layer coated nickel nanoparticles for efficient electrocatalytic reduction of carbon dioxide, *Nano Res.*, 2019, **12**, 1167–1172.

29 K. P. Kuhl, E. R. Cave, D. N. Abram and T. F. Jaramillo, New insights into the electrochemical reduction of carbon dioxide on metallic copper surfaces, *Energy Environ. Sci.*, 2012, **5**, 7050–7059.

30 W. Qiu, R. Liang, Y. Luo, G. Cui, J. Qiu and X. Sun, A Br^- anion adsorbed porous Ag nanowire film: in situ electrochemical preparation and application toward efficient CO_2 electroreduction to CO with high selectivity, *Inorg. Chem. Front.*, 2018, **5**, 2238–2241.

31 Y. Yu, N. Zhong, J. Fang, S. Tang, X. Ye, Z. He and S. Song, Comparative Study between Pristine Ag and Ag Foam for Electrochemical Synthesis of Syngas with Carbon Dioxide and Water, *Catal. 2019, Vol. 9, Page 57*, 2019, **9**, 57.

32 W. Zheng, C. Guo, J. Yang, F. He, B. Yang, Z. Li, L. Lei, J. Xiao, G. Wu and Y. Hou, Highly active metallic nickel sites confined in N-doped carbon nanotubes toward significantly enhanced activity of CO_2 electroreduction, *Carbon N. Y.*, 2019, **150**, 52–59.

33 J. Zhou, L. Yuan, J. Wang, L. Song, Y. You, R. Zhou, J. Zhang and J. Xu, Combinational modulations of $NiSe_2$ nanodendrites by phase engineering and iron-doping towards an efficient oxygen evolution reaction, *J. Mater. Chem. A*, 2020, **8**, 8113–8120.

34 H. Yang, Q. Lin, C. Zhang, X. Yu, Z. Cheng, G. Li, Q. Hu, X. Ren, Q. Zhang, J. Liu and C. He, Carbon dioxide electroreduction on single-atom nickel decorated carbon membranes with industry compatible current densities, *Nat. Commun.*, 2020, **11**, 1–8.

35 T. Zhang, L. Lin, Z. Li, X. He, S. Xiao, V. N. Shanov and J. Wu, Nickel-Nitrogen-Carbon Molecular Catalysts for High Rate CO_2 Electro-reduction to CO: On the Role of Carbon Substrate and Reaction Chemistry, *ACS Appl. Energy Mater.*, 2020, **3**, 1617–1626.

36 Z. Wang, P. Hou, Y. Wang, X. Xiang and P. Kang, Acidic Electrochemical Reduction of CO_2 Using Nickel Nitride on Multiwalled Carbon Nanotube as Selective Catalyst, *ACS Sustain. Chem. Eng.*, 2019, **7**, 6106–6112.

37 H. Y. Jeong, M. Balamurugan, V. S. K. Choutipalli, E. S. Jeong, V. Subramanian, U. Sim and K. T. Nam, Achieving highly efficient CO_2 to CO electroreduction exceeding 300 mA cm^{-2} with single-atom nickel electrocatalysts, *J. Mater. Chem. A*, 2019, **7**, 10651–10661.

38 C. Yan, H. Li, Y. Ye, H. Wu, F. Cai, R. Si, J. Xiao, S. Miao, S. Xie, F. Yang, Y. Li, G. Wang and X. Bao, Coordinatively unsaturated nickel-nitrogen sites towards selective and high-rate CO_2 electroreduction, *Energy Environ. Sci.*, 2018, **11**, 1204–1210.

39 S. Pugliese, N. T. Huan, J. Forte, D. Grammatico, S. Zanna, B. L. Su, Y. Li and M. Fontecave, Functionalization of Carbon Nanotubes with Nickel Cyclam for the Electrochemical Reduction of CO_2, *ChemSusChem*, 2020, **13**, 6449–6456.

40 K. Mou, Z. Chen, X. Zhang, M. Jiao, X. Zhang, X. Ge, W. Zhang and L. Liu, Highly Efficient Electroreduction of CO_2 on Nickel Single-Atom Catalysts: Atom Trapping and Nitrogen Anchoring, *Small*, 2019, **15**, 1903668.

41 C. Gao, Z. Peng and X. Wu, Controllable synthesis of hollow $NiSe_2$ spheres as an active electrocatalyst for hydrogen evolution reaction, *https://doi.org/10.1142/S1793604720500332*, , DOI:10.1142/S1793604720500332.

42 L. F. Huang, M. J. Hutchison, R. J. Santucci, J. R. Scully and J. M. Rondinelli, Improved Electrochemical Phase Diagrams from Theory and Experiment: The Ni-Water System and Its Complex Compounds, *J. Phys. Chem. C*, 2017, **121**, 9782–9789.

43 J. Masud, W. P. R. Liyanage, X. Cao, A. Saxena and M. Nath, Copper Selenides as High-Efficiency Electrocatalysts for Oxygen Evolution Reaction, *ACS Appl. Energy Mater.*, 2018, **1**, 4075–4083.

44 R. Shi, J. Guo, X. Zhang, G. I. N. Waterhouse, Z. Han, Y. Zhao, L. Shang, C. Zhou, L. Jiang and T. Zhang, Efficient wettability-controlled electroreduction of CO_2 to CO at Au/C interfaces, *Nat. Commun. 2020 111*, 2020, **11**, 1–10.

III. COBALT TELLURIDE ELECTROCATALYST FOR SELECTIVE ELECTROREDUCTION OF CO_2 TO VALUE-ADDED CHEMICALS

Apurv Saxena[a], Harish Singh[a], Manashi Nath[a]*

[a]Department of Chemistry, Missouri University of Science & Technology, Rolla, MO 65409, USA.

ABSTRACT

Recent emphasis on carbon dioxide utilization has necessitated the exploration of different catalyst compositions other than copper-based systems that can significantly improve the activity and selectivity towards specific products at low applied potential. In this study a binary CoTe has been reported as an efficient electrocatalyst for CO_2 reduction in aqueous medium under ambient conditions at neutral pH. CoTe showed high Faradaic efficiency and selectivity of 86.83 % and 75 % respectively for acetic acid at very low potential of – 0.25 V vs RHE. More intriguingly, C1 products like formic acid was formed preferentially at slightly higher applied potential achieving high formation rate of 547.24 μmol cm^{-2} h^{-1} at -1.1 V vs RHE. CoTe showed better CO2RR activity when compared with Co_3O_4, which can be attributed to the enhanced electrochemical activity of the catalytically active transition metal center as well as improved intermediate adsorption on the catalyst surface. While reduced anion electronegativity and improved lattice covalency in tellurides enhance the electrochemical activity of Co, high d-electron density improves the intermediate CO adsorption on the catalyst site leading to CO_2 reduction at lower applied potential and high selectivity for C2 products. CoTe also shows stable CO2RR catalytic activity for 50 h and low Tafel slope (50.3 mV dec^{-1}) indicating faster reaction

kinetics and robust functionality. Selective formation of value-added C2 products with low energy expense can make this catalyst potentially viable for integration with other CO_2 capture technologies thereby, helping to close the carbon loop.

1. INTRODUCTION

1.1. BACKGROUND

Continuous usage of fossil fuels along with advent of the industrial age has led to catastrophic levels of CO_2 in the atmosphere which has skyrocketed after the industrial revolution, reaching 401.3 parts per million in 2015 from approximately 270 ppm in the pre-Industrial revolution era.[1,2] Unfortunately atmospheric CO_2 levels are expected to rise further and exceed 600 parts per million by the end of the twenty-first century.[1–4] Development of techniques for reducing the level of carbon dioxide has become very crucial given the havoc caused by global warming.[1] These techniques are broadly categorized into CO_2 sequestration, storage and utilization which can be integrated with direct air capture (DAC). Among these electrochemical CO_2 reduction reaction (CO2RR) is one of the most promising CO_2 utilization strategies among CO_2 conversion technologies such as biochemical, photosynthetic, thermo-catalytic, and photocatalytic processes, due to the mild electrolyzer operating conditions, selectivity toward the desired products, and other factors.[5] [6] Inspiration of this technique can be derived from photosynthesis process which meticulously convert CO_2 to maintain proper balance of atmospheric gases. Carbon dioxide has two double bonds with a total bond energy of 750 $kJmol^{-1}$ which makes it extremely challenging to bring it out of the potential well.[7] Hence a catalyst is required

to reduce CO_2 to other products by reducing the activation energy through effective catalyst-mediated charge transfer.[3] Electrochemical conversion is an environment friendly way of supplying that energy due to its mild operation conditions and renewable sources of electricity. Hori et al reported some pioneer research on carbon dioxide electroreduction using various transition metals like Pb, Hg, In, Sn etc. and Cu, Au, Ag, Pt etc. which led to the formation of formate and CO, respectively as the reduction products. However, through subsequent research it was also found that lot of these metal catalysts had poor selectivity towards specific reduction products, were environmentally toxic and frequently underwent poisoning.[8] Intense research activities over the last several years has led to identification of catalysts with better selectivity and activity achieved through modulating catalyst morphology and dimensionality[9][10], vacancy creation[11], and doping.[12–14][15] However, it must also be noted that majority of the catalysts reported for CO2RR were Cu-based compositions.[ref] There has been very few reports of electrocatalysts for CO2RR based on Fe, Co, and/or Ni based compositions. Among these Co-based catalysts have already been used in industry for various processes like Fisher–Tropsh synthesis,[16,17] and electrocatalytic water splitting.[ref] Co–based catalysts exhibit unique properties like enhanced conductivity and electrochemical tunability which makes them suitable for CO_2 electroreduction. Indeed Co-based catalysts have been reported for CO2RR, specifically as Co SACs (single atom catalyst),[18–23] Co-MOFs,[24–27] Co-coordination complexes, cobalt based nitrides,[28,29][30] and oxides.[23,31][32][33][34] Cobalt exhibits better CO2RR activity due to factors like optimum CO_2 adsorption energy and low energy difference between d-band and Fermi level.[35] Also, it has been observed that during the CO_2 reduction Co^{2+} converts into Co^{+}.

This transition happens during the rate determining step which results in selectivity towards products and enhances activity and stability of the product.[36,37]. Co SAC has been found to be highly selective towards CO with faradaic efficiency 95% with current density towards CO production being 86.4 $mAcm^{-2}$. This is significant improvement from the Cobalt metal based catalyst.[22] Cobalt nanoparticles dispersed on NrGO developed through a one-step synthesis was found to be selective towards methanol with high faradaic efficiency of 71.4% at -0.9V vs SCE.[38] Tellurium nanosheet modified Co single atoms showed strong interaction between the N from Te Ns and Cobalt atoms leading to efficient CO_2 Conversion.[39] Co_3O_4 nanofiber modified electrodes has been found to have good activity towards CO2RR having high faradaic efficiency for both CO and formate (90%).[40] Ultrathin Co_3O_4 layers of 1.72 and 3.51 nm thickness exhibited 64.3% Faradaic Efficiency at -0.88V vs. SCE with superior structural stability.[33] cobalt phthalocyanine exhibited very high activity towards CO_2 conversion when phthalocyanine was modified by trimethyl ammonium. This catalyst reduces CO_2 to CO with selectivity of 95% over a wide range of pH (4-14).[41] A hydrothermally synthesized core–shell structured Co_3S_4@Co_3O_4 catalyst show high selectivity towards formic acid with FE= 85.3%.[42]

In all these electrocatalysts, transition metal serves as the catalytic center for CO2RR where the reaction progress via intermediate steps involving adsorption of O-containing intermediates.[43] Hence, it can be expected that tuning the electron density around the transition metal center will influence adsorption of reaction intermediates and resulting charge transfer rate, leading to reduction of overpotential for electrocatalytic CO2RR. Previously we have shown that changing anion electronegativity leads to modulation of d-electron density around transition metal center.[ref] More specifically, we

have shown that reducing anion electronegativity leads to better electrocatalytic activity making selenides and tellurides as better electrocatalysts with lower overpotential.[ref] Similar observation was made in Cu-based systems, where Cu_2Se was observed to exhibit lower overpotential for CO2RR compared to Cu or CuO.[44] While lower overpotential is a measure for enhanced catalytic activity, for CO2RR, the additional criteria for improved activity is selectivity for formation of specific reduction products and the ability to form carbon-rich value-added products in with high Faradaic efficiency. We have proposed that selectivity towards C2+ reduction products depend critically on the adsorption energy and dwell time of intermediate CO on the catalyst site, which in turn depends on the *d*-electron density of the transition metal as well as electronegativity of the coordinated anions. In this article, we have described CoTe nanostructures as a new family of metal chalcogenide electrocatalysts for the CO2RR with high selectivity for forming C2+ reduction products at low applied potential and neutral pH. Apart from enhanced catalytic activity, these CoTe nanostructures also showed high faradaic efficiency, and long-term functional stability. Also, because of the extensive stoichiometry alterations that are possible in metal-rich chalcogenides, these materials are highly efficient, inexpensive, and robust electrocatalysts for a variety of electrochemical sensors, energy conversion, and storage applications.[45–48]

2. EXPERIMENTAL PROCEDURE

2.1. MATERIALS

All the reagents were of analytical grade and used as received. Deionized water (resistivity 18 MΩ cm) was used to prepare all solutions. Cobalt sulfate ($CoSO_4 \cdot 6H_2O$)

was purchased from Sigma-Aldrich; hydrazine hydrate ($N_2H_4 \cdot H_2O$, 100%) and tellurium dioxide (TeO_2) were purchased from Acros Organics. Nafion and carbon cloth (CC) substrate were obtained from Fuel Cells Etc., in College Station, Texas.

2.2. SYNTHESIS OF COTE

CoTe was prepared by hydrothermal technique as reported previously.[23] Specifically, an equimolar ratio (1:1) of cobalt sulfate ($CoSO_4.6H_2O$) and tellurium dioxide (TeO_2) powder was used for the synthesis. Initially the $CoSO_4.6H_2O$ was dissolved in 9 mL of deionized water in a Teflon-lined stainless-steel autoclave with a capacity of 23 mL. After vigorous stirring for 20 minutes, TeO_2 was added to the mixture. Finally, 3 mL of $N_2H_4H_2O$ were added to the mixture, which was continually stirred for another 30 minutes. The resultant solution was placed in a teflon lined stainless-steel autoclave. The autoclave was sealed and kept at 145 °C for 24 hours before being allowed to cool naturally to room temperature. The resulting product was centrifuged and rinsed several times with an ethanol/deionized water mixture. The final product was dried at 60°C in a vacuum oven.

2.3. CHARACTERIZATION

Powder X-ray diffraction (PXRD) patterns were obtained using a Philip X-Pert powder X-ray diffractometer using Ni-filtered Cu-K radiation with a wavelength of1.5406, within the 20°–90° range. The morphology of the as-prepared sample was examined using an FEI Helios Nanolab 600 scanning electron microscope with a working distance of 10 mm and a 15 kV acceleration voltage. A Tecnai F20 was used to acquire TEM images of the synthesized samples directly on the formvar-coated Cu grid. Additionally, the surface

chemical composition was analyzed using X-ray Photoelectron Spectroscopy (XPS) with a KRATOS AXIS 165 spectrometer equipped with an Al X-ray source. To examine the true surface chemistry, all XPS data were acquired without sputtering.

2.4. ELECTROCHEMICAL MEASUREMENTS

In order to conduct the electrochemical measurements, we used an IviumStat potentiostat with graphite rod, Ag|AgCl (KCl-saturated) and carbon cloth as counter, reference and working electrode, respectively. All electrochemical experiments were performed in a H Cell at ambient temperature. Nafion membrane 117 proton exchange membrane was used to separate the anodic and cathodic compartments of H Cell. The electrochemical activity of catalyst was measured by using a 3-electrode system where CoTe-modified carbon cloth was used as the working electrode. The Ag|AgCl reference electrode was calibrated with a Pt wire in H_2-saturated H_2SO_4 and an open circuit potential was obtained as −0.199 V. The potential reported vs Ag|AgCl was changed to reversible hydrogen electrode (RHE) using the Equation (1):

$$E_{RHE} = E_{Ag|AgCl} + 0.059\,\text{pH} + E^0_{Ag|AgCl} \quad (1)$$

where E_{RHE} is the transformed potential vs RHE. $E_{Ag|AgCl}$ is the experimentally obtained potential. $E^0_{Ag|AgCl}$ is the standard potential of Ag|AgCl (0.199 V). The pH of CO_2 saturated 0.3 M $NaHCO_3$ was estimated to be 6.8. Catalyst ink was made by sonicating 5 mg of hydrothermally synthesized CoTe in 500 µL of 1% Nafion in isopropanol. The ink was then drop-casted on carbon fiber paper to make working electrode. Measured potentials vs Ag|AgCl were converted to RHE for accurate comparison and data interpretation. Before starting the electrochemical reduction, the electrolyte was purged vigorously with CO_2 for

20 minutes and the flow was then tuned down to ~10 mL min^{-1} during CO_2RR. To gauge CO_2 electrochemical reduction capability of electrocatalysts, different electrochemical experiments were performed on drop-casted working electrodes. The working electrode consist of catalyst and Nafion binder mixture deposited on one side of the carbon cloth (CC). Carbon cloth is a microporous substrate having pores of size between 1–100 μm. This type of substrate improves mechanical strength, electrical conductivity, and mass transport during CO_2 electroreduction. The Nafion helps in the catalyst utilization by increasing the ionic connection and increases water content in the pores because of its hydrophilic nature. Hence, catalyst mixture in form of microporous layer improves the interfacial electrical conductivity and inhibits electrolyte flooding.[52]

3. RESULTS

The phase purity and crystallinity of the hydrothermally synthesized samples were confirmed using PXRD patterns. Figure 1a shows the PXRD pattern of the hydrothermally synthesized product, which confirms crystallinity of the as-synthesized product and is well matched with the CoTe standard diffraction pattern (PDF No.00–034-0420), demonstrating that the product was pure cobalt telluride.

SEM and TEM were used to examine the morphology of the as-synthesized material. SEM and TEM images of hydrothermally produced CoTe are shown in Figure 1 (b–c) which shows that short nanorods with an average length of around 400 nm were formed in hydrothermally synthesized CoTe. To achieve high catalytic activity, it is desirable to use nanostructured morphology, because they have a large surface area and mass to volume

ratio. Hence, the nanostructured morphology for CoTe seems to be for CO2RR catalytic activity. XPS studies were also used to confirm the catalyst's bulk and surface composition.

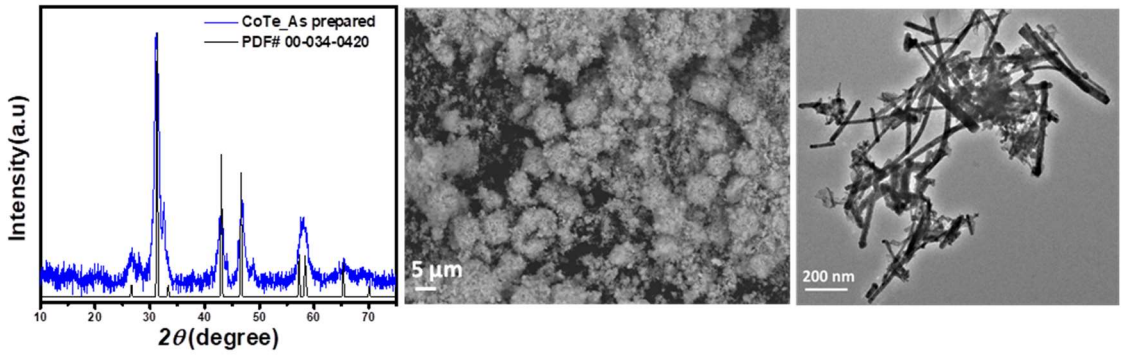

Figure 1. Characterization (a) Powder X-ray diffraction patterns (b)SEM (c) TEM of hydrothermally synthesized CoTe.

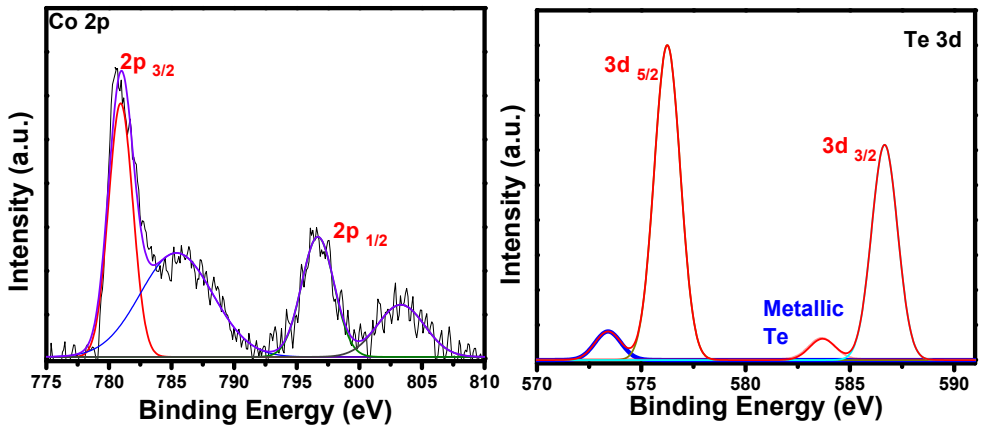

Figure 2. XPS spectra of (a) Co 2p and (b) Te 3d in CoTe.

The XPS spectra of hydrothermally produced CoTe are shown in Figure 2. The Co 2p and Te 3d spectra are shown in Figure 2 (a, b). Co 2p spectra exhibits two peaks at 780.4 and 795.8 eV, which correspond to $2p_{3/2}$ and $2p_{1/2}$, respectively, and are comparable to

Co^{2+}.[23] The satellite peaks were found at 786.6 and 803.0 eV, which are consistent with the existing literature.[53][23] Metallic Te was present in the Te XPS spectra at 572.8 and 583.3 eV. The XPS spectra also confirmed formation of CoTe in pure phase.

3.1. ELECTROCATALYTIC CO2RR PERFORMANCE OF COTE CATALYST

In this study, all electrochemical measurements for studying CO2RR along with product detection and quantification has been performed by following standard protocol as has been reported previously including design of experimental set-up and measurement techniques.[54,55] Moreover, performance of our electrochemical set-up was calibrated and verified by measuring the CO2RR activity of standard polycrystalline Ag electrode and comparing it with previous reports. Products of CO2RR was found to be formic acid and CO at -0.9 V (vs RHE) on Ag electrode as shown in Figure S1, which is similar to that reported by previous researchers,[8][56] confirming the reliability of our electrochemical set-up for CO2RR studies. Observed current density from the LSV polarization curves were also similar to the reported studies which further confirms the validity of the experiments.[57,58] Comparison of the CoTe-modified electrode with the polycrystalline Ag, shows that different CO_2 reduction products were identified with CoTe-modified electrode under similar conditions, further corroborating the novelty of this catalyst. Details of CO2RR studies with CoTe-modified electrode has been discussed in the following sections.

Linear scan voltammetry (LSV) was carried out in CO_2 or N_2 saturated 0.3 M $NaHCO_3$ at a 10 mV/s scan rate. On applying negative potential in N_2 saturated electrolyte

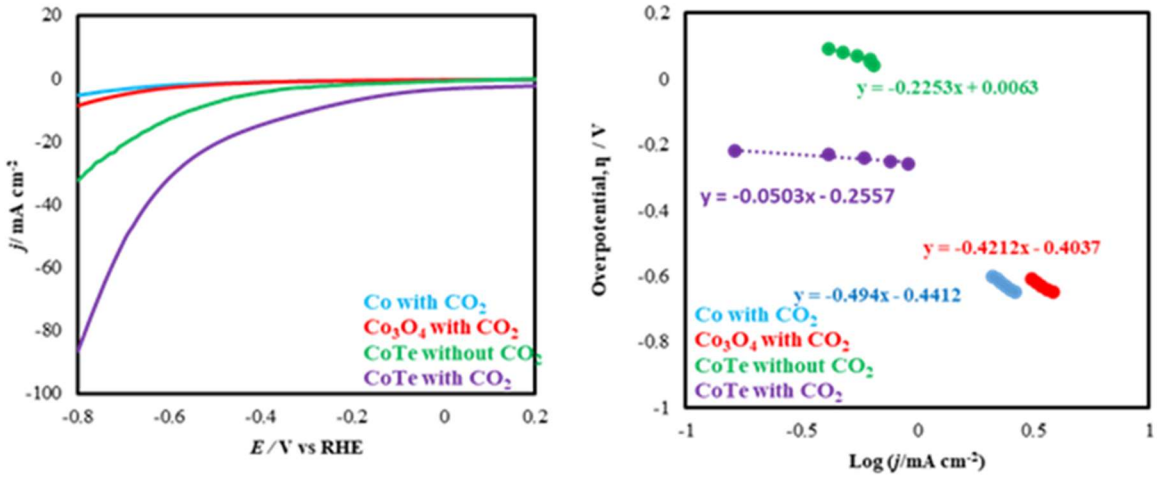

Figure 3. Electrocatalytic activity (a) LSVs measured in 0.3 M $NaHCO_3$ at a scan rate of 10 mV s^{-1} in presence and absence of CO_2 with CoTe modified GC and bare GC electrodes. (b) Tafel plots measured in 0.3 M $NaHCO_3$.

only hydrogen evolution (HER) takes place, however, in CO_2-saturated electrolyte CO2RR and HER both occur simultaneously. As shown in Figure 3, CoTe exhibited higher current density in CO_2-saturated electrolyte than in N_2-saturated electrolyte at the same potentials, confirming that the CoTe electrodes is active for CO2RR. CoTe achieved a CO2RR reduction current density of 62.8 mA cm^{-2} at -1.1 V vs RHE which is significantly higher than the current density exhibited by bulk Co, Co_3O_4 and the partially oxidized bulk Co.[27][44]

3.1.1. Tafel Plot. The Tafel analysis can be an effective tool for explaining the electrokinetic activity of the electrocatalysts for CO2RR via Tafel slopes. The Tafel equation illustrates the relation between overpotential η with the current density j as shown in Equation (2):

$$\eta = \alpha + (2.3\,RT)\,\log j\,/\alpha nF \qquad (2)$$

where α represents the transfer coefficient, n is the number of electrons passed during the reaction, and F is the Faraday constant. The Tafel slope is calculated by 2.3RT/αnF. The Tafel plots in this work were calculated from the reverse scan of CV collected at a scan rate of 2 mV s^{-1} in a non-stirred N_2-saturated 1.0 M KOH solution. Data for the Tafel equation is obtained from the kinetically controlled range of CO_2 electrochemical reduction which determines the relation between of overpotential η and current density j. The Tafel slope is crucial in measuring electrochemical performances, and it gives insights about the kinetics in the electrochemical reduction. Typically, lower Tafel slopes for a catalyst indicates faster CO2RR kinetics in a bicarbonate electrolyte. Tafel slope polarization curves were measured in continuously purged and stirred electrolyte solution at a lower scan rate of 2 mV s^{-1} to minimize mass transfer limitations. The Tafel plots of CoTe are shown in Figure 3 (b). Tafel slope of CoTe was estimated to be 50.3 mV dec^{-1} in presence of CO_2 while in absence of CO_2 it showed a much higher Tafel slope of 225.3 mV dec^{-1}. The very low Tafel slope indicates faster kinetics for the reduction of CO_2 in a bicarbonate electrolyte. The Tafel slope for CoTe is near to the theoretical value of 118 mV dec^{-1}, which is expected for the chemical rate-determining step (RDS) of initial single-electron transfer step for formation of adsorbed radical intermediate ($CO_2^{\cdot-}$) on the catalyst surface which initiates the catalytic CO_2 reduction.[59,60] Lower Tafel slope values indicating faster intermediate adsorption kinetics on CoTe-modified electrode at lower applied potential also corroborates well with formation of CO_2 reduction products at lower applied potential including selective formation of carboxylic acids such as acetic acid as discussed below. The standard reduction potential of CO_2 to acetic acid is 290 mV.[61] The low Tafel slope (50.3 mV dec^{-1}) measured near low overpotential of 290 mV indicates faster kinetics

for acetic acid generation illustrating high selectivity and efficiency of the catalyst. However, given the complexity of CO2RR on the catalyst surface and multitude of steps, more studies are needed to correctly ascertain the proper RDS as well as accurate mechanism for CO2RR on the surface of CoTe. The Tafel slope for CoTe@CFP was observed to be smaller than that of bare Co and Co_3O_4 which confirms the contribution of chalcogenides in fast transfer of electrons.

3.2. CO2RR PRODUCTS IDENTIFICATION AND QUANTIFICATION

The carbon dioxide reduction products were identified and quantified by performing chronoamperometric studies at constant applied potentials of -0.25 V, -0.6 V, -0.9 V, -1.1 V vs RHE in CO_2 purged $NaHCO_3$ to study the effect of applied potential on product composition and selectivity, if any.

The products were collected from the cathodic chamber after 1 h of chronoamperometry at each fixed applied potential while the catholyte was subjected to constant purging with CO2 gas at low flow rate (20 sccm). Identification and quantification of liquid products were done by 1H NMR while gaseous products were detected and quantified using GC-TCD. From NMR plots as shown in Figure 4a, it was observed that the product composition was very dependent on the applied potential and showed selectivity towards specific products at each potential. The Faradaic efficiency for formation of specific product was estimated from absolute product quantity obtained through NMR and GC-TCD measurements, and using standard procedure as described previously.[54][16] Interestingly, reduction products generated at low applied potentials (-0.25 V to -0.6 V vs RHE) included carbon rich compounds like acetic acid, while at higher

applied potential, C1 products such as formic acid were obtained predominantly. At -0.25 V vs RHE, yield of formic acid yield was low probably due to low current density.

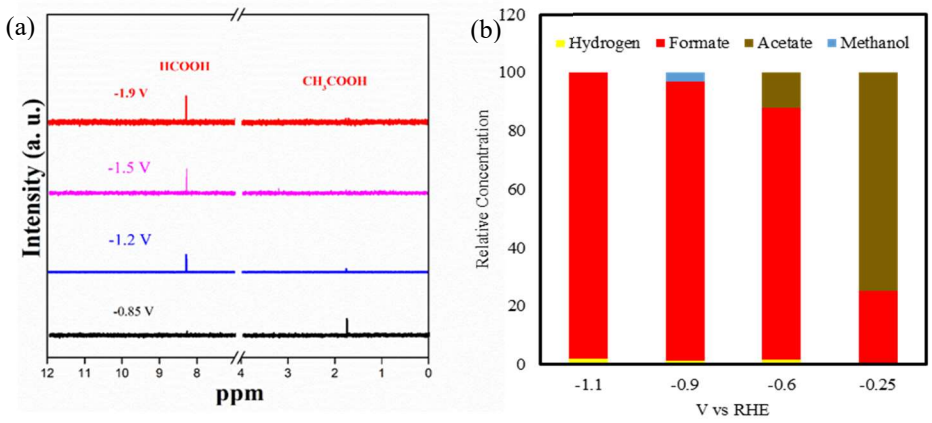

Figure 4. Product quantification (a) NMR spectra identifying CO_2 reduction products in reaction aliquots collected at different potentials. (b) Bar plot illustrating relative concentrations of liquid products quantified from NMR at different stationary applied potentials.

Previous studies has reported that when pH decreases in the vicinity of the electrode surface due to continuous hydrogen evolution,[62] in situ conversion of CO_2 to HCO_3^- occurs. However, this spontaneous change happens at higher concentration of nascent hydrogen which also leads to formation of formic acid at higher applied potential. Formic acid becomes a major product at -0.6 V with relative concentration of 86.25 % and FE = 58.34%. When the applied potential was increased further, FE of formic acid reached maximum (93.39%) at -1.1 V vs RHE. Due to high HER activity and more hydrogen generation, Faradaic efficiency of formic acid formation was found to decrease at further negative potential (> -1.1V).[64] CoTe exhibited high faradaic efficiency of formate production over 90% under a broad range from −0.6 to −1.1 V vs RHE and acetate

production at -0.25V vs RHE. This observation confirms the enhanced efficiency of CoTe catalyst which requires lower potential for CO2RR and exhibits a higher FE than any other Co-based catalyst at similar applied potential. It must be noted here that the product composition was exclusively acetic acid for potential range near 0.25V vs RHE. Such high selectivity towards formation of acetic acid with low energy expense has been rarely observed with CO2RR catalyst. Acetic acid is an industrially important chemical, and the selectivity towards its production at lower applied potential highlights the novelty of this catalyst. Specifically, this catalyst paves the way for high-selectivity direct acetic acid synthesis from CO_2 replacing the conventional multi-step industrial process which typically begins with synthesis of syngas and ends with the generation of methanol followed by its carbonylation.[63] Hydrogen evolved during the reaction when quantified contributed to FE of 1.71%, 1.23% and 1.03% at -1.1 V, -0.9 V and -0.6 V vs RHE, respectively. The observed product selectivity also suggests that at lower applied potential intermediate adsorption and kinetics of CO2RR on the catalyst surface is more favorable than rate of water reduction. Moreover, absence of CoTe catalyst very unique as almost all copper-based and other conventional CO2RR CO in the product composition and preferential formation of exclusive C2 products , makes electrocatalyst are known to produce CO as their main product.[64] Cobalt is known to yield formic acid as the major product after CO2RR as has been reported previously. In this study, we have observed that when the catalytically active Co2+ is placed in the covalently bonded network of Te ions, electrochemical CO_2 reduction tends to yield more C2 products at lower potential. The results from our study will help to improve the existing and future catalyst compositions.

Especially, once the influence of CoTe dense packed structures and effect of telluride on covalency is mechanistically studied.

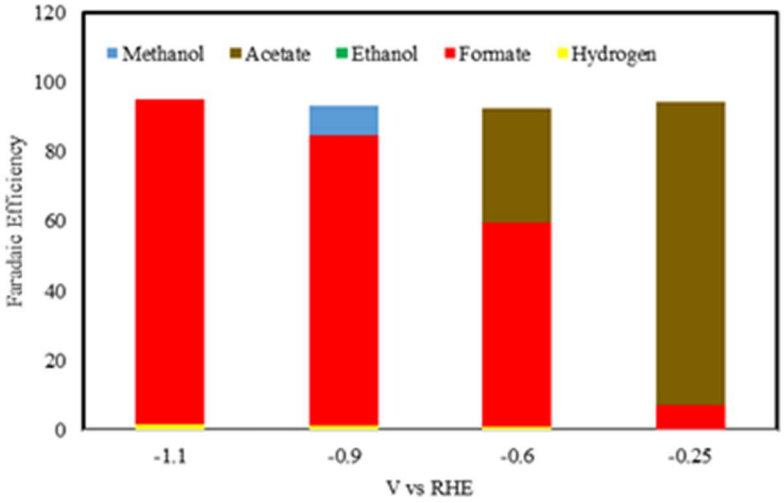

Figure 5. Bar plots depicting relative faradaic efficiency of cumulative liquid and gas phase CO_2 reduction products at different applied potentials quantified through NMR and GC-TCD.

The functional stability of the CoTe electrocatalyst for long term hydrocarbon generation is also a critical factor in evaluating catalyst performance, applicability, and performance. Operational stability of CoTe for CO2RR was investigated by performing chronoamperometric study at different applied potentials for long time. It should be noted that no change in the current density and Faradaic Efficiency was observed at -0.25 V, -0.6 V, -0.9 V, and -1.1V as shown in Figure S2 and CoTe exhibited exceptional functional stability for over 50 h of electrolysis. Moreover, NMR analysis of the aliquots collected every 10 h during the 50h period showed that there was no change in product composition during this time confirming high degree of operation stability and minimal catalyst surface

poisoning with adsorbed intermediates which is a common occurrence in noble metal based CO2RR electrocatalysts. Typically, CO_2 electroreduction activity decreases rapidly during high rate reactions because of catalysis agglomeration[65] change of active-phase composition,[9][66] and element dissolution.[12][67] There has been very few studies where catalyst has been shown to be stable at commercially relevant current densities. To our knowledge, such extended functional stability for CO_2 electroreduction with continuous product formation for more than 50 h, has not been demonstrated by other electrocatalysts. Hence, the CoTe has exhibited an unprecedented activity and stability compared not only to the Co-based catalysts, but also to the noble metal-based catalysts (Table S4). To achieve formate and acetic acid production from CO_2 with the help of renewable power sources in a practical scale, it is critically necessary to develop catalysts that are not only active but also stable. Various surface and bulk characterization techniques (morphological, structural and compositional) were employed for tracking the integrity of the catalyst during CO2RR at different current densities and at different points of time. Analysis of the catalyst surface after prolonged CO2RR activity showed that the composition of CoTe (101) was retained as observed from the pxrd pattern which showed similarity with the as-synthesized sample. SEM images also confirmed structural integrity after prolonged activity within potential range of -0.25V to -1.1 V vs RHE (Figure S3 & S4, respectively).

The reaction rates for different products at specific voltages has been estimated from NMR data and chronoamperometry measurement, as shown in Figure 7(a) above. To understand better about the selectivity and reaction kinetics, we estimated the production rates and partial current density for each product at different potentials. As shown in Figure

7(a), formic acid was major product at higher negative potentials contributing towards the CO2RR activity. Partial current density of the products was calculated from total current density and faradaic efficiency of that product which was plotted as function of potential. Faradaic efficiency of formic acid in particular is affected by two factors: (i) concentration of protons in the vicinity of electrode; (ii) the electric field near the electrode.[68] The high current density observed resulted in improved proton concentration near the electrodes, thereby increasing the rate of formate production. The formic acid partial current density has been used as a key parameter to determine the CO_2 -to-formate reduction activity and is calculated from FE of formate and total current density at different potentials on each sample (Figure 7(b)). The formic acid partial current density of CoTe sample is higher than those of the bare Co and Cobalt oxide reported in other studies[27][44], and reaches to the highest value of 58.6 $mAcm^{-2}$ at an applied potential of -1.1 V vs RHE. This value is 11% and 93% higher than those of reported Co_3O_4 and Co sample, respectively.[69] At low negative potential, acetic acid achieved high production rate. Acetic acid also exhibited higher current density at lower applied potential. Trends in current density and production rate plots confirms the selectivity towards specific products and also the uniqueness of this catalyst when compared with other Co-based CO_2 electroreduction catalysts which yields only C1 products. This CO2RR activity can be attributed towards different rate of *CO conversion on the surface, which is affected by the (*CO) [intermediate] dwell time on the surface. Also, rate of decarboxylation and dehydroxylation at specific potentials can play a major role in CO2RR activity. The CO2RR activity achieved with CoTe indicates that this catalyst is capable of promoting CO_2 electrochemical conversion to yield significant quantities of value-added products with higher production rates over long period of time.

3.2.1. Electrochemical Capacitance Measurements. Enhanced electrocatalytic activity can typically be assigned to intrinsic factors which includes facile catalyst activation through intermediate adsorption and enhanced charge transport, as well as extrinsic factors such as catalyst morphology and surface roughness which influences electrolyte and analyte access to the catalytically active sites. The extrinsic factors affecting CO2RR electrocatalytic activity of CoTe was investigated by estimating the electrochemically active surface area (ECSA) by following previously reported experimental procedure.[70] The ECSA was calculated by plotting electrochemical double layer capacitance in the non-Faradaic region as a function of scan rate and then comparing specific capacitance (CS) to the double layer capacitance. The electrochemical double layer capacitance (CDL) was calculated following Equation (3):

$$i_{DL} = C_{DL} \times \nu \tag{3}$$

where i_{DL} represents the current observed while ν is the scan rate. As can be seen from the Figure 7, C_{DL} calculated from the i vs ν plot resulted in value of 0.5 mF. The ratio of C_{DL} and Cs was used to calculate ECSA as shown in Equation (4).

$$ECSA = C_{DL}/C_S \tag{4}$$

Cyclic voltammetry (CV) was used for the ECSA and roughness factor (RF) measurements. The cyclic voltammograms in CO_2 saturated 0.3 M $NaHCO_3$ were collected at scan rates from 5 mV/s to 400 mV/s. Polarization curves were obtained in potential range of 32 mV according to OCP of CoTe electrode. Current density from cyclic voltammograms was plotted as a function of scan rate. The surface roughness factor was calculated from the capacitance data. Using the Cs value (40μF cm^{-2}) from reported values and C_{DL} value (0.5 mF) from the plot, ECSA value was calculated to be 12.74 cm^2. The

effect of catalyst morphology on the working electrode was also estimated from the RF which was calculated to be 159.28 from the ratio between ECSA and geometric electrode area (0.08 cm^2). High value of ECSA and RF depicts that CO_2 dissolved in the electrolyte has more access to the catalytic sites on working electrode, leading to better conversion efficiency.

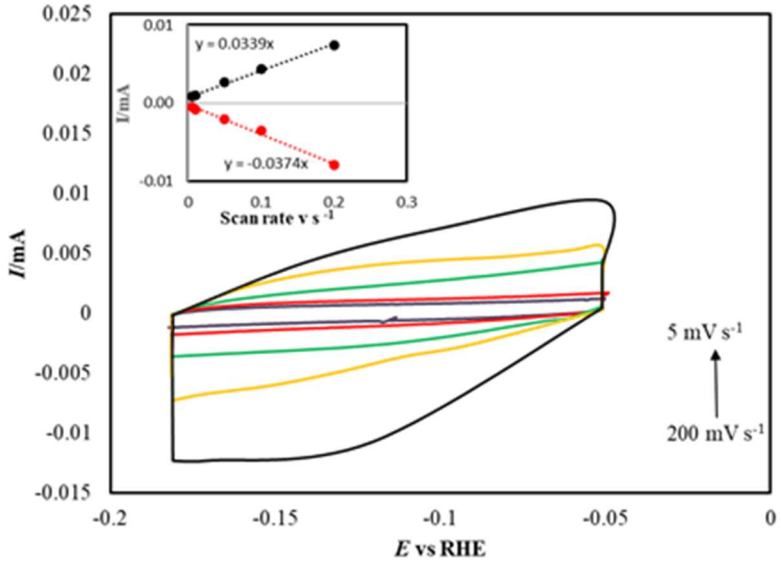

Figure 6. CV scans of CoTe@CC from scan rate 5 to 200 mV/s. Data obtained over a potential range of 32 mV around the open circuit potential in 0.3M $NaHCO_3$.

Few studies have claimed that CO_2 mass transfer is less in H-cell because of less solubility of CO_2 in electrolyte. This results in current density in the range of 0-50 $mAcm^{-2}$ for CO_2 reduction. [2,17] The CO_2 mass transfer is expected to improve in flow cell set-up, and is can be use of such flow cell for CoTe will lead to suppression of H_2 evolution resulting in higher faradaic efficiency for formic acid at higher negative potential along with higher current density (>300 $mAcm^{-2}$).

3.2.2. Electrochemical Impedance Spectroscopy Measurements. Electrochemical Impedance (EIS) was measured for CoTe-modified electrode in CO_2 saturated 0.3 M $NaHCO_3$ electrolyte to estimate the charge transfer resistance at the catalyst-analyte(electrolyte) interface and study its variance as a function of applied potential.

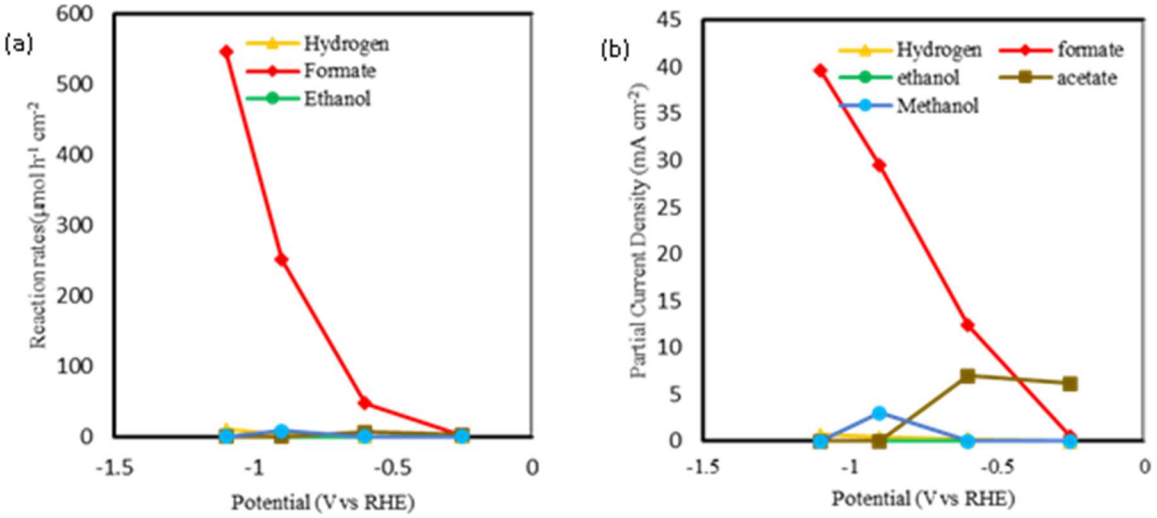

Figure. 7. CO2RR performances of CoTe catalyst. (a) Formation rates of Hydrogen, formate, ethanol, acetate and methanol. (b) Partial current density of individual products, hydrogen, formate, ethanol, acetate and methanol.

Nyquist plots were measured at different negative potentials from -0.2 to -1.1 V vs RHE in frequency range of 1–105 Hz in CO_2 purged $NaHCO_3$ solution as shown in Figure 8. As the potential is decreased towards more negative potentials, modular values of the impedance decreased indicating that rate of electrochemical reaction increased on the electrode surface. EIS study was also conducted (Figure. 8(a)) with and without CO_2 purging (N_2 saturated) at a specific potential (-1.1V) to show the difference in reaction

kinetics between CO2RR and HER. CoTe was found to have lower impedance in CO_2 purged solution in comparison to N_2 purged solution which proves that CO2RR process is better facilitated than HER at this potential. The Nyquist plots were fitted using the equivalent circuit which consisted of electrode film resistance (Rf), charge transfer resistance at electrode-electrolyte interface (RCT), and Warburg resistance.

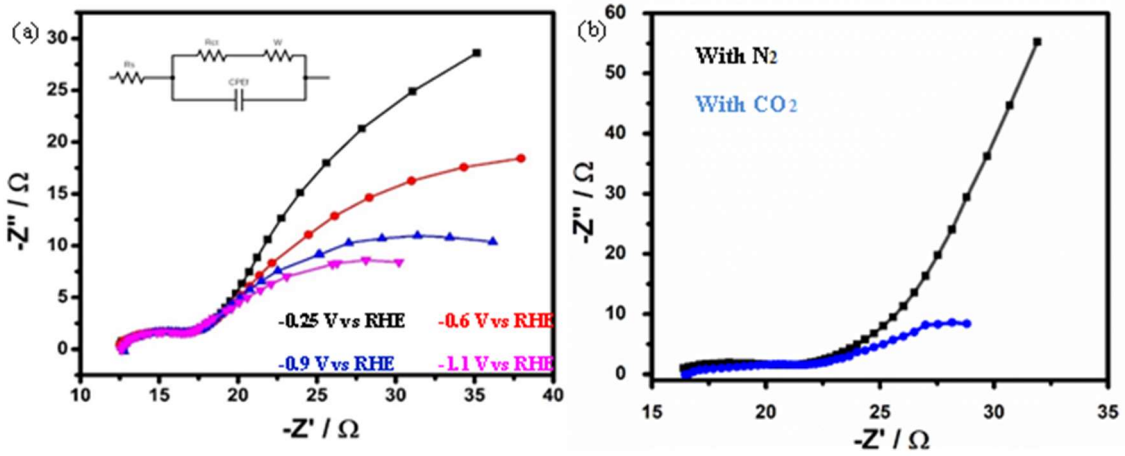

Figure. 8. EIS Nyquist plots of CoTe@CFP in CO_2-saturated 0.3 M $NaHCO_3$ electrolyte (pH 6.8) from 0 V vs RHE to -1.1 V vs RHE. Inset shows the equivalent circuit fitted to experimental spectra, where RCT corresponds to the charge-transfer resistance on catalyst-electrolyte interface, while Rs indicates film resistance of the catalyst composite.

Table 1 shows the variation of Rf and RCT at different applied potentials. It was observed that RCT increased at lower applied potential indicating faster charge transfer and higher reaction rates for C2 product formation. Warburg impedance (W) associated with Rct was also reported in Table 1. For efficient fitting of of Nyquist plot. Lower values of Warburg resistance at higher negative potential implies that the diffusion is more which played an important role in enhancing CO2RR activity. Moreover, in CO_2-saturated

electrolyte, both HER and CO2RR occur competitively at potentials lower than -0.4 V. The R_{CT} for the CoTe in the CO_2-staurated electrolyte is smaller than that in the N_2-saturated medium, which indicates that CoTe is significantly more active for CO2RR compared to HER.

Table 1. Fitting parameters obtained from Nyquist plots at various potentials.

Potential (V vs RHE)	-1.1	-0.9	-0.6	-0.25
Parameters	Value	Value	Value	Value
Rs	1.26E+01	1.38E+01	1.31E+01	1.33E+01
RCT	2.24E+00	2.33E+00	2.76E+00	3.20E+00
C1	1.84E-05	1.04E-05	2.77E-05	1.79E-05
W1	1.44E-02	1.45E-02	1.87E-02	1.95E-02

Therefore, detailed EIS analysis confirms that the CoTe modified electrode can exhibit significant improvement in selectivity for CO2RR supporting higher reaction rates and faster charge transfer. Impedance spectroscopy was used to gain insight into charge transfer kinetics on the working electrode during the electrochemical reaction. In our previous work, we have demonstrated that CoTe forms a more compact lattice by linking chains of edge-shared CoTe6 octahedra in three dimensions. [23] As a result of this lattice structure, the Co-terminated lattice planes of CoTe exhibit greater anion deficiency with substantial unsaturation at the Co site. Anion deficit in the lattice has previously been attributed to greater catalytic activity.[71]

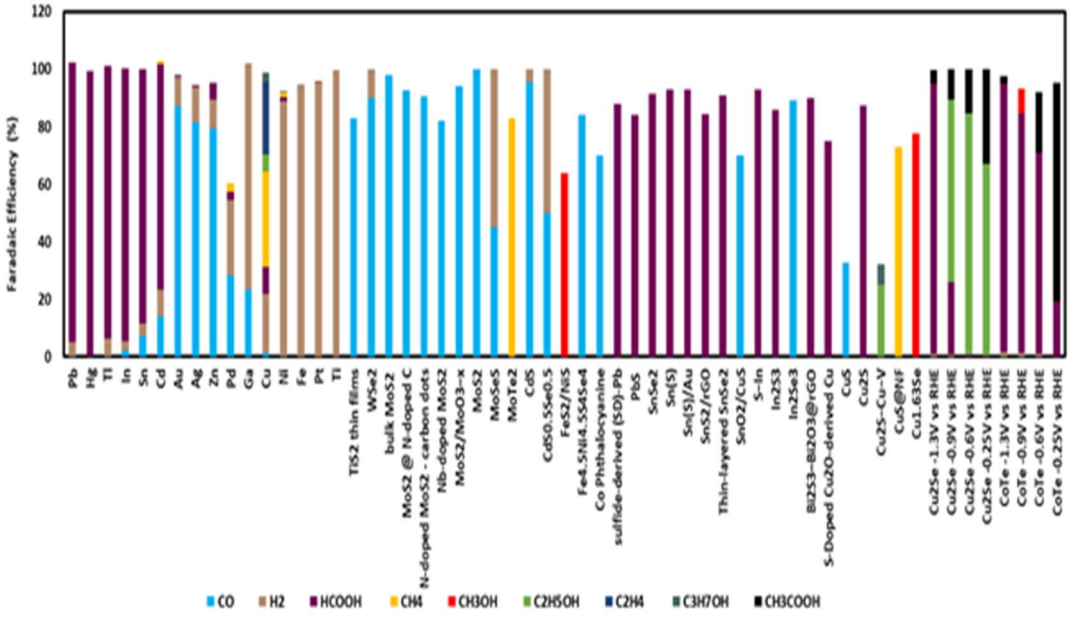

Figure 9. Comprehensive comparison of products obtained through electrocatalytic CO2RR with CoTe and other catalysts as assembled from various reports published from different research groups.

4. CONCLUSIONS

4.1. CONCLUSIONS AND FUTURE WORK

CO2RR gives us a hope to develop a carbon neutral way of living where electrochemical reduction can store the CO_2 into valuable chemicals by converting renewable energy to reduction can store the CO_2 into valuable chemicals by converting renewable energy to chemical energy. Due to technical simplicity and upscaling capacity at potential of choosing makes the CO_2 reduction to Acetic acid easy to commercialization process of CO_2. In this study, we have reported successful one step synthesis of CoTe. The as-prepared CoTe catalyst showed enhanced catalytic performance for electroreduction

CO_2 to Acetic acid with high FE of 87% at low potential of -0.25 V vs RHE. Also, at higher negative potentials which is lower in comparison to other Cobalt catalysts we obtained formic acid with high FE and high partial current density of 40 mA cm^{-2} at - 0.6 V vs RHE. The formation rate of formic acid reached to 547.24 μmol $cm^{-2}h^{-1}$, which was comparable to other excellent electrocatalysts from previous studies. This enhanced performance can be due to various factors like the high ECSA and plenty catalytically active sites, faster charge transfer, high covalency resulting in optimum stabilization of the CO*- intermediate and better interaction between the active sites and the OCHO• intermediate.

In summary, the CoTe electrocatalyst deposited on carbon fiber paper is first cobalt based catalyst which have produced acetic acid from CO_2 reduction. This catalyst show high current density of 62.8 mA cm^{-2} for extended period of time. Sturdiness of this catalyst is due to increase of Co-Te covalency which results in less dissolution of tellurium during CO2RR. This catalyst is uniquely selective and energy efficient because it is selective towards Acetic acid at very low potential (-0.25 V) with FE = 87% and towards formic acid at higher negative potential (-1.1 V) with FE = 93.39 % with high formation rate (547.24 μmol cm^{-2} h^{-1}) for formate. These results will contribute to development of stable and active catalysts for industrial scale.

SUPPORTING INFORMATION

1. USE OF WIDELY ACCEPTED EXPERIMENTAL PROCEDURES

We followed data collections methods and protocol as outlined in, "Standards and Protocols for Data Acquisition and Reporting for Studies of the Electrochemical Reduction of Carbon Dioxide" [1] (referred to as Standards paper, hereafter). All our measurements, data collection protocols and reporting follow the guidelines provided in the above-mentioned paper very closely. All our electrochemical experiments have been performed in magnetically stirred solution under rapid bubbling with CO_2 gas to reduce the limitations of mass transfer, as has been suggested in the Standards paper. Limitations to mass transfer can also be reduced by reducing surface roughness of the electrodes and using flat surfaces. All our electrocatalytic experiments have been performed on flat carbon fiber paper electrodes with minimal surface roughness.

As recommended in the Standards paper, we refrained from using Pt as counter electrode to minimize leaching and eventual impurity enrichment in the electrolyte and near the electrode which can lead to unexpected conversions and erroneous data. All our electrocatalytic reactions has been performed with glassy carbon as counter electrode. Additionally, we have characterized the electrodes and electrolyte with XRD and ICP-MS which shows the presence of only Co, and Te, and no other impurity atoms confirming purity of the system.

The Standards paper suggested benchmarking of the catalysts by comparing with systems polycrystalline Ag. We calibrated our electrochemical setup by measuring CO2RR activity with polycrystalline silver electrode.

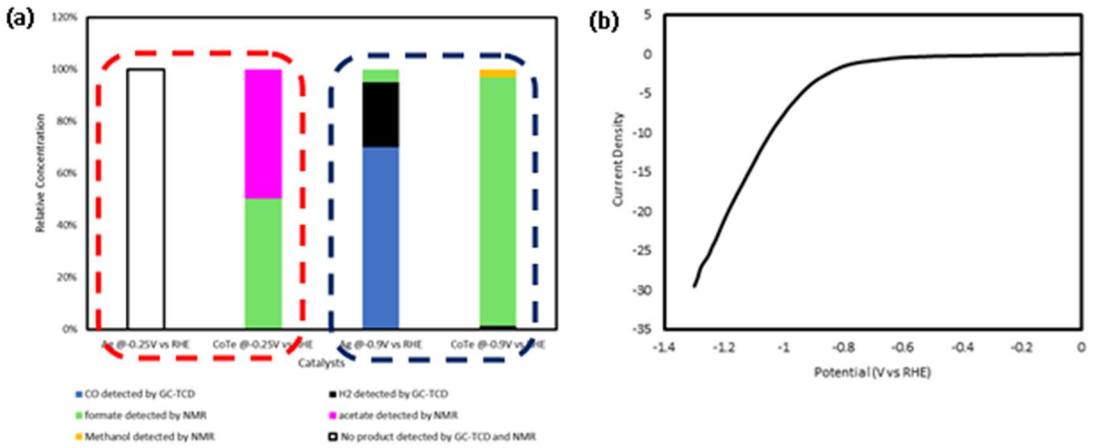

Figure S1. Comparison of CO2RR activity with (a) polycrystalline Ag film synthesized in the authors' lab with CoTe. The polycrystalline Ag tested in the authors laboratory showed formation of CO, HCOOH, and H_2 at -0.9 V vs RHE, while no product was detected with NMR and GC-TCD at -0.25 V (after 2-6 h). The CoTe sample on the other hand, showed distinct presence of acetic acid, ethanol, methanol, and formic acid at -0.9 V, while at -0.25 V it shows exclusive formation of acetic acid. (b) LSV plots of polycrystalline Ag measured in the author's laboratory which matched with that of reported literature

Polycrystalline silver electrode in our experimental setup shows similar performance (formation of CO, H_2, and formic acid, at -0.9 V vs RHE applied potential) as has been reported in various studies,[1–3] validating the accuracy of our electrochemical setup. The NMR analysis for products formed from polycrystalline Ag and CoTe electrode confirms the presence of methanol, ethanol and acetic acid for $NiSe_2$ electrode. Also, the current-density plot of Ag@carbon cloth in presence of CO_2 matches with already done

studies (Figure S2 below)[2,3] All our CO2RR experiments were performed in $NaHCO_3$ electrolyte without presence of any other alkali metal ions, which may lead to erroneous data as has been indicated in the Standards paper. We have also reported ECSA and product-specific current density as has been suggested in the Standards paper.

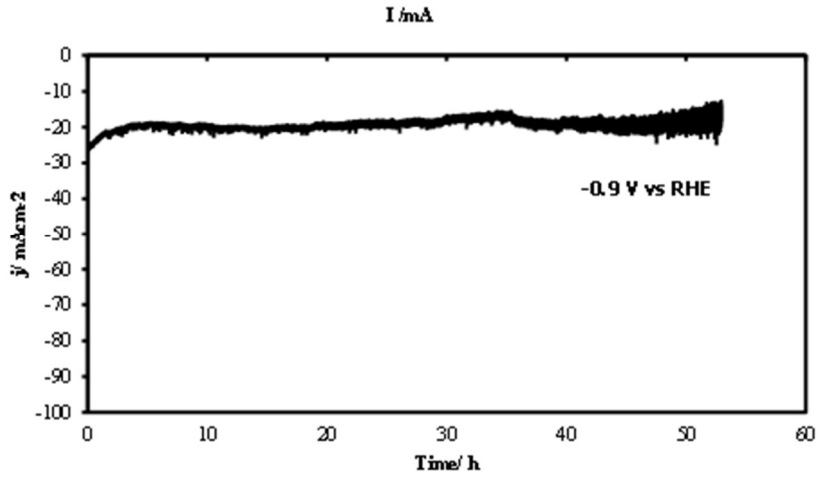

Figure S2. Chronoamperometry study of catalyst for CO2RR

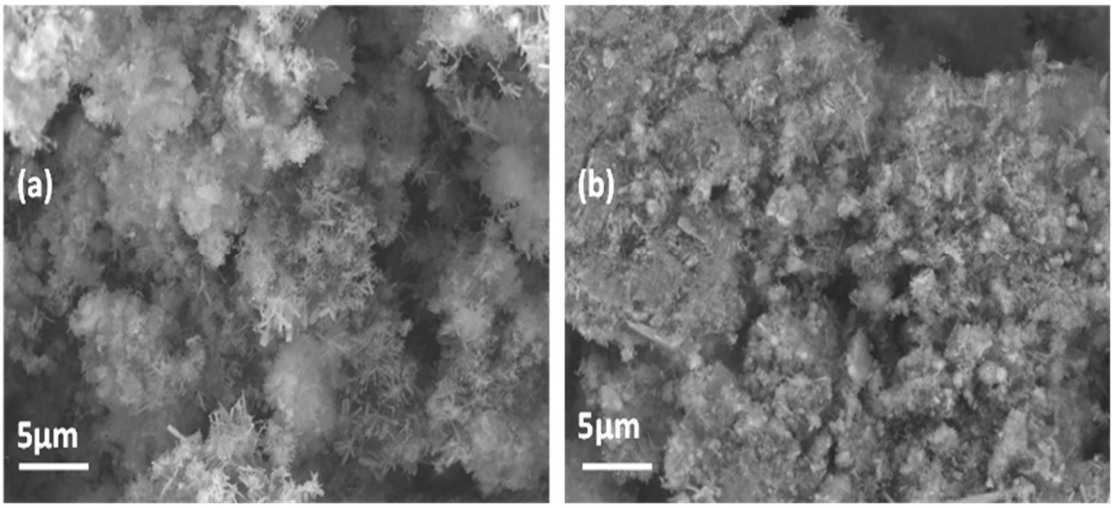

Figure S3. (a) SEM before (b)after CO2RR of hydrothermally synthesized CoTe.

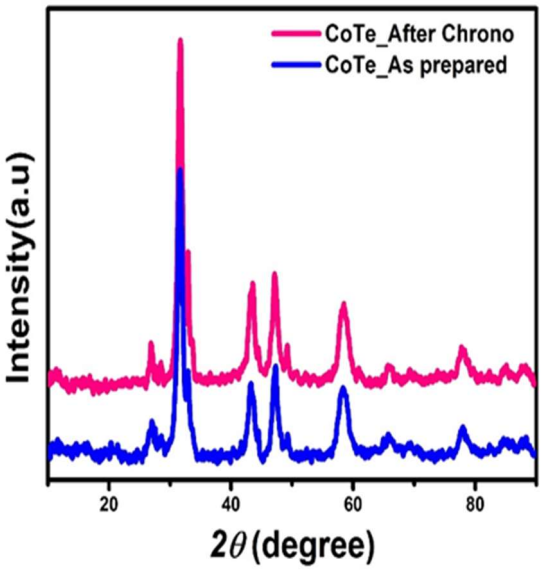

Figure S4. (a) XRD before (b)after CO2RR of hydrothermally synthesized CoTe.

Table S1. ICP-MS results from $NaHCO_3$ electrolyte collected at different stages of CO2RR with CoTe

Sample	Co 59 (ppb)	Te 125 (ppb)
Purified $NaHCO_3$ after 12h CO2RR chronoamperometry with CoTe	<DL	<DL

REFERENCES

1 M. Mikkelsen, M. Jørgensen and F. C. Krebs, The teraton challenge. A review of fixation and transformation of carbon dioxide, *Energy Environ. Sci.*, 2010, **3**, 43–81.

2 N. S. Spinner, J. A. Vega and W. E. Mustain, Recent progress in the electrochemical conversion and utilization of CO_2, *Catal. Sci. Technol.*, 2011, **2**, 19–28.

3 D. D. Zhu, J. L. Liu and S. Z. Qiao, Recent Advances in Inorganic Heterogeneous Electrocatalysts for Reduction of Carbon Dioxide, *Adv. Mater.*, 2016, **28**, 3423–3452.

4 C. W. Li, J. Ciston and M. W. Kanan, Electroreduction of carbon monoxide to liquid fuel on oxide-derived nanocrystalline copper, *Nat. 2014 5087497*, 2014, **508**, 504–507.

5 E. Boutin, L. Merakeb, B. Ma, B. Boudy, M. Wang, J. Bonin, E. Anxolabéhère-Mallart and M. Robert, Molecular catalysis of CO_2 reduction: recent advances and perspectives in electrochemical and light-driven processes with selected Fe, Ni and Co aza macrocyclic and polypyridine complexes, *Chem. Soc. Rev.*, 2020, **49**, 5772–5809.

6 M. Nath, H. Singh and A. Saxena, Progress of Transition Metal Chalcogenides as Efficient Electrocatalysts for Energy Conversion, *Curr. Opin. Electrochem.*, 2022, 100993.

7 K. Li, B. Peng and T. Peng, Recent Advances in Heterogeneous Photocatalytic CO_2 Conversion to Solar Fuels, *ACS Catal.*, 2016, **6**, 7485–7527.

8 Y. Hori, H. Wakebe, T. Tsukamoto and O. Koga, Electrocatalytic process of CO selectivity in electrochemical reduction of CO_2 at metal electrodes in aqueous media, *Electrochim. Acta*, 1994, **39**, 1833–1839.

9 K. Ye, Z. Zhou, J. Shao, L. Lin, D. Gao, N. Ta, R. Si, G. Wang and X. Bao, In Situ Reconstruction of a Hierarchical Sn-Cu/SnOx Core/Shell Catalyst for High-Performance CO_2 Electroreduction, *Angew. Chemie Int. Ed.*, 2020, **59**, 4814–4821.

10 N. Han, Y. Wang, H. Yang, J. Deng, J. Wu, Y. Li and Y. Li, Ultrathin bismuth nanosheets from in situ topotactic transformation for selective electrocatalytic CO_2 reduction to formate, *Nat. Commun. 2018 91*, 2018, **9**, 1–8.

11 Z. Wang, R. Qi, D. Liu, X. Zhao, L. Huang, S. Chen, Z. Chen, M. Li, B. You, Y. Pang and B. Yu Xia, Exfoliated Ultrathin $ZnIn_2S_4$ Nanosheets with Abundant Zinc Vacancies for Enhanced CO_2 Electroreduction to Formate, *ChemSusChem*, 2021, **14**, 852–859.

12 J. H. Zhou, K. Yuan, L. Zhou, Y. Guo, M. Y. Luo, X. Y. Guo, Q. Y. Meng and Y. W. Zhang, Boosting Electrochemical Reduction of CO_2 at a Low Overpotential by Amorphous Ag-Bi-S-O Decorated Bi0 Nanocrystals, *Angew. Chemie Int. Ed.*, 2019, **58**, 14197–14201.

13 W. Ma, S. Xie, X. G. Zhang, F. Sun, J. Kang, Z. Jiang, Q. Zhang, D. Y. Wu and Y. Wang, Promoting electrocatalytic CO_2 reduction to formate via sulfur-boosting water activation on indium surfaces, *Nat. Commun. 2019 101*, 2019, **10**, 1–10.

14 I. Grigioni, L. K. Sagar, Y. C. Li, G. Lee, Y. Yan, K. Bertens, R. K. Miao, X. Wang, J. Abed, D. H. Won, F. P. Garciá De Arquer, A. H. Ip, D. Sinton and E. H. Sargent, CO_2 Electroreduction to Formate at a Partial Current Density of 930 mA cm^{-2} with InP Colloidal Quantum Dot Derived Catalysts, *ACS Energy Lett.*, 2021, **6**, 79–84.

15 X. Zheng, P. De Luna, F. P. García de Arquer, B. Zhang, N. Becknell, M. B. Ross, Y. Li, M. N. Banis, Y. Li, M. Liu, O. Voznyy, C. T. Dinh, T. Zhuang, P. Stadler, Y. Cui, X. Du, P. Yang and E. H. Sargent, Sulfur-Modulated Tin Sites Enable Highly Selective Electrochemical Reduction of CO_2 to Formate, *Joule*, 2017, **1**, 794–805.

16 K. P. Kuhl, E. R. Cave, D. N. Abram and T. F. Jaramillo, New insights into the electrochemical reduction of carbon dioxide on metallic copper surfaces, *Energy Environ. Sci.*, 2012, **5**, 7050–7059.

17 A. Saxena, W. Liyanage, J. Masud, S. Kapila and M. Nath, Selective electroreduction of CO_2 to carbon-rich products with a simple binary copper selenide electrocatalyst, *J. Mater. Chem. A*, 2021, **9**, 7150–7161.

18 M. Abdinejad, Z. Mirza, X. A. Zhang and H. B. Kraatz, Enhanced Electrocatalytic Activity of Primary Amines for CO_2 Reduction Using Copper Electrodes in Aqueous Solution, *ACS Sustain. Chem. Eng.*, 2020, **8**, 1715–1720.

19 M. Bernal, A. Bagger, F. Scholten, I. Sinev, A. Bergmann, M. Ahmadi, J. Rossmeisl and B. R. Cuenya, CO_2 electroreduction on copper-cobalt nanoparticles: Size and composition effect, *Nano Energy*, 2018, **53**, 27–36.

20 L. A. Richard, P. Moreau, S. Rugmini and F. Daly, Fischer-Tropsch performance correlated to catalyst structure: Trends in activity and stability for a silica-supported cobalt catalyst, *Appl. Catal. A Gen.*, 2013, **464**–**465**, 200–206.

21 N. Fischer, E. Van Steen and M. Claeys, Structure sensitivity of the Fischer–Tropsch activity and selectivity on alumina supported cobalt catalysts, *J. Catal.*, 2013, **299**, 67–80.

22 P. Arde, B. T. Ramanjaneyulu, V. Reddy, A. Saxena and R. V. Anand, N-Heterocyclic carbene catalysed aerobic oxidation of aromatic aldehydes to aryl esters using boronic acids, *Org. Biomol. Chem.*, 2012, **10**, 848–851.

23 M. Nath, U. De Silva, H. Singh, M. Perkins, W. P. R. Liyanage, S. Umapathi, S. Chakravarty and J. Masud, Cobalt Telluride: A Highly Efficient Trifunctional Electrocatalyst for Water Splitting and Oxygen Reduction, *ACS Appl. Energy Mater.*, 2021, **4**, 8158–8174.

24 Y. Guo, Y. Wang, Y. Shen, Z. Cai, Z. Li, J. Liu, J. Chen, C. Xiao, H. Liu, W. Lin and C. Wang, Tunable Cobalt-Polypyridyl Catalysts Supported on Metal-Organic Layers for Electrochemical CO_2 Reduction at Low Overpotentials, *J. Am. Chem. Soc.*, 020, **142**, 21493–21501.

25 Z. Geng, Y. Cao, W. Chen, X. Kong, Y. Liu, T. Yao and Y. Lin, Regulating the coordination environment of Co single atoms for achieving efficient electrocatalytic activity in CO_2 reduction, *Appl. Catal. B Environ.*, 2019, **240**, 234–240.

26 P. Hou, W. Song, X. Wang, Z. Hu and P. Kang, Well-Defined Single-Atom Cobalt Catalyst for Electrocatalytic Flue Gas CO_2 Reduction, *Small*, 2020, **16**, 2001896.

27 S. Gao, Y. Lin, X. Jiao, Y. Sun, Q. Luo, W. Zhang, D. Li, J. Yang and Y. Xie, Partially oxidized atomic cobalt layers for carbon dioxide electroreduction to liquid fuel, *Nat. 2016 5297584*, 2016, **529**, 68–71.

28 S. Y. Zhang, Y. Y. Yang, Y. Q. Zheng and H. L. Zhu, Ag-doped Co3O4 catalyst derived from heterometallic MOF for syngas production by electrocatalytic reduction of CO2 in water, *J. Solid State Chem.*, 2018, **263**, 44–51.

29 R. Matheu, E. Gutierrez-Puebla, M. Á. Monge, C. S. Diercks, J. Kang, M. S. Prévot, X. Pei, N. Hanikel, B. Zhang, P. Yang and O. M. Yaghi, Three-Dimensional Phthalocyanine Metal-Catecholates for High Electrochemical Carbon Dioxide Reduction, *J. Am. Chem. Soc.*, 2019, **141**, 17081–17085.

30 D. Long, X. Li, Z. Yin, S. Fan, P. Wang, F. Xu, L. Wei, M. O. Tadé and S. Liu, Novel Co_3O4 @ $CoFe_2O_4$ double-shelled nanoboxes derived from Metal–Organic Framework for CO_2 reduction, *J. Alloys Compd.*, 2021, **854**, 156942.

31 S. Lin, C. S. Diercks, Y. B. Zhang, N. Kornienko, E. M. Nichols, Y. Zhao, A. R. Paris, D. Kim, P. Yang, O. M. Yaghi and C. J. Chang, Covalent organic frameworks comprising cobalt porphyrins for catalytic CO2 reduction in water, *Science (80-.).*, 2015, **349**, 1208–1213.

32 P. Huang, J. Huang, S. A. Pantovich, A. D. Carl, T. G. Fenton, C. A. Caputo, R. L. Grimm, A. I. Frenkel and G. Li, Selective CO_2 Reduction Catalyzed by Single Cobalt Sites on Carbon Nitride under Visible-Light Irradiation, *J. Am. Chem. Soc.*, 2018, **140**, 16042–16047.

33 J. Fu, L. Zhu, K. Jiang, K. Liu, Z. Wang, X. Qiu, H. Li, J. Hu, H. Pan, Y. R. Lu, T. S. Chan and M. Liu, Activation of CO_2 on graphitic carbon nitride supported single-atom cobalt sites, *Chem. Eng. J.*, 2021, **415**, 128982.

34 J. Di, C. Chen, C. Zhu, P. Song, M. Duan, J. Xiong, R. Long, M. Xu, L. Kang, S. Guo, S. Chen, H. Chen, Z. Chi, Y. X. Weng, H. Li, L. Song, M. Wu, Q. Yan, S. Li and Z. Liu, Cobalt nitride as a novel cocatalyst to boost photocatalytic CO_2 reduction, *Nano Energy*, 2021, **79**, 105429.

35 S. Gao, X. Jiao, Z. Sun, W. Zhang, Y. Sun, C. Wang, Q. Hu, X. Zu, F. Yang, S. Yang, L. Liang, J. Wu and Y. Xie, Ultrathin Co_3O_4 Layers Realizing Optimized CO_2 Electroreduction to Formate , *Angew. Chemie*, 2016, **128**, 708–712.

36 Y. Cheng, J. P. Veder, L. Thomsen, S. Zhao, M. Saunders, R. Demichelis, C. Liu, R. De Marco and S. P. Jiang, Electrochemically substituted metal phthalocyanines, e-MPc (M = Co, Ni), as highly active and selective catalysts for CO_2 reduction, *J. Mater. Chem. A*, 2018, **6**, 1370–1375.

37 V. S. K. Yadav and M. K. Purkait, Electrochemical Studies for CO_2 Reduction Using Synthesized Co3O4 (Anode) and Cu2O (Cathode) as Electrocatalysts, *Energy and Fuels*, 2015, **29**, 6670–6677.

38 S. Guo, S. Zhao, X. Wu, H. Li, Y. Zhou, C. Zhu, N. Yang, X. Jiang, J. Gao, L. Bai, Y. Liu, Y. Lifshitz, S. T. Lee and Z. Kang, A Co_3O_4-CDots-C_3N_4 three component electrocatalyst design concept for efficient and tunable CO_2 reduction to syngas, *Nat. Commun. 2017 81*, 2017, **8**, 1–9.

39 D. T. Nguyen, C. C. Nguyen and T. O. Do, Rational one-step synthesis of cobalt clusters embedded-graphitic carbon nitrides for the efficient photocatalytic CO_2 reduction under ambient conditions, *J. Catal.*, 2020, **392**, 88–96.

40 C. Li, X. Tong, P. Yu, W. Du, J. Wu, H. Rao and Z. M. Wang, Carbon dioxide photo/electroreduction with cobalt, *J. Mater. Chem. A*, 2019, **7**, 16622–16642.

41 P. Yang, R. Wang, H. Tao, Y. Zhang, M. M. Titirici and X. Wang, Cobalt Nitride Anchored on Nitrogen-Rich Carbons for Efficient Carbon Dioxide Reduction with Visible Light, *Appl. Catal. B Environ.*, 2021, **280**, 119454.

42 J. Huang, X. Guo, G. Yue, Q. Hu and L. Wang, Boosting CH $_3$ OH Production in Electrocatalytic CO $_2$ Reduction over Partially Oxidized 5 nm Cobalt Nanoparticles Dispersed on Single-Layer Nitrogen-Doped Graphene, *ACS Appl. Mater. Interfaces*, 2018, **10**, 44403–44414.

43 L. Shi, X. Ren, Q. Wang, Y. Li, F. Ichihara, H. Zhang, Y. Izumi, L. Ren, W. Zhou, Y. Yang and J. Ye, Stabilizing Atomically Dispersed Catalytic Sites on Tellurium Nanosheets with Strong Metal–Support Interaction Boosts Photocatalysis, *Small*, 2020, **16**, 2002356.

44 A. Aljabour, H. Coskun, D. H. Apaydin, F. Ozel, A. W. Hassel, P. Stadler, N. S. Sariciftci and M. Kus, Nanofibrous cobalt oxide for electrocatalysis of CO_2 reduction to carbon monoxide and formate in an acetonitrile-water electrolyte solution, *Appl. Catal. B Environ.*, 2018, **229**, 163–170.

45 M. Wang, K. Torbensen, D. Salvatore, S. Ren, D. Joulié, F. Dumoulin, D. Mendoza, B. Lassalle-Kaiser, U. Işci, C. P. Berlinguette and M. Robert, CO_2 electrochemical catalytic reduction with a highly active cobalt phthalocyanine, *Nat. Commun. 2019 101*, 2019, **10**, 1–8.

46 Y. Yan, K. Li, X. Chen, Y. Yang and J. M. Lee, Heterojunction-Assisted Co_3S_4@Co_3O_4 Core–Shell Octahedrons for Supercapacitors and Both Oxygen and Carbon Dioxide Reduction Reactions, *Small*, 2017, **13**, 1701724.

47 I. V. Chernyshova, P. Somasundaran and S. Ponnurangam, On the origin of the elusive first intermediate of CO2 electroreduction, *Proc. Natl. Acad. Sci. U. S. A.*, 2018, **115**, E9261–E9270.

48 H. Singh, J. Bernabe, J. Chern and M. Nath, Copper selenide as multifunctional non-enzymatic glucose and dopamine sensor, *J. Mater. Res. 2021 367*, 2021, **36**, 1413–1424.

49 H. Singh, M. Marley-Hines, S. Chakravarty and M. Nath, Multi-walled carbon nanotube supported Manganese Selenide as Highly Active Bifunctional OER and ORR electrocatalyst, *J. Mater. Chem. A*, 2022, **6**, 4883–5230.

50 S. Umapathi, H. Singh, J. Masud and M. Nath, Nanostructured copper selenide as an ultrasensitive and selective non - enzymatic glucose sensor, *Mater. Adv.*, , DOI:10.1039/D0MA00890G.

51 B. G. Amin, J. Masud and M. Nath, Facile one-pot synthesis of NiCo2Se4-rGO on Ni foam for high performance hybrid supercapacitors, *RSC Adv.*, 2019, **9**, 37939–37946.

52 B. Kim, F. Hillman, M. Ariyoshi, S. Fujikawa and P. J. A. Kenis, Effects of composition of the micro porous layer and the substrate on performance in the electrochemical reduction of CO2 to CO, *J. Power Sources*, 2016, **312**, 192–198.

53 Y. X. Lei, N. X. Miao, J. P. Zhou, Q. U. Hassan and J. Z. Wang, Novel magnetic properties of CoTe nanorods and diversified CoTe2 nanostructures obtained at different NaOH concentrations, *http://www.tandfonline.com/action/journalInformation?show=aimsScope&journalCode=tsta20#.VmBmuzZFCUk*, 2017, **18**, 325–333.

54 E. L. Clark, J. Resasco, A. Landers, J. Lin, L. T. Chung, A. Walton, C. Hahn, T. F. Jaramillo and A. T. Bell, Standards and Protocols for Data Acquisition and Reporting for Studies of the Electrochemical Reduction of Carbon Dioxide, *ACS Catal.*, 2018, **8**, 6560–6570.

55 K. P. Kuhl, E. R. Cave, D. N. Abram and T. F. Jaramillo, New insights into the electrochemical reduction of carbon dioxide on metallic copper surfaces, *Energy Environ. Sci.*, 2012, **5**, 7050–7059.

56 T. Kottakkat, K. Klingan, S. Jiang, Z. P. Jovanov, V. H. Davies, G. A. M. El-Nagar, H. Dau and C. Roth, Electrodeposited AgCu Foam Catalysts for Enhanced Reduction of CO 2 to CO, *ACS Appl. Mater. Interfaces*, 2019, **11**, 14734–14744.

57 W. Qiu, R. Liang, Y. Luo, G. Cui, J. Qiu and X. Sun, A Br− anion adsorbed porous Ag nanowire film: in situ electrochemical preparation and application toward efficient CO2 electroreduction to CO with high selectivity, *Inorg. Chem. Front.*, 2018, **5**, 2238–2241.

58 Y. Yu, N. Zhong, J. Fang, S. Tang, X. Ye, Z. He and S. Song, Comparative Study between Pristine Ag and Ag Foam for Electrochemical Synthesis of Syngas with Carbon Dioxide and Water, *Catal. 2019, Vol. 9, Page 57*, 2019, **9**, 57.

59 Y. Zhao, J. Liang, C. Wang, J. Ma and G. G. Wallace, Tunable and Efficient Tin Modified Nitrogen-Doped Carbon Nanofibers for Electrochemical Reduction of Aqueous Carbon Dioxide, *Adv. Energy Mater.*, 2018, **8**, 1702524.

60 Y. Hori, in *Modern ASpects of Electrochemistry no 42*, 2008.

61 M. Dworkin, S. Falkow, E. Rosenberg, K.-H. Schleifer and E. Stackebrandt, Eds., The Prokaryotes, , DOI:10.1007/0-387-30742-7.

62 D. Tan, C. Cui, J. Shi, Z. Luo, B. Zhang, X. Tan, B. Han, L. Zheng, J. Zhang and J. Zhang, Nitrogen-carbon layer coated nickel nanoparticles for efficient electrocatalytic reduction of carbon dioxide, *Nano Res.*, 2019, **12**, 1167–1172.

63 The Cativa™ Process for the Manufacture of Acetic Acid | Johnson Matthey Technology Review, https://www.technology.matthey.com/article/44/3/94-105/, (accessed 18 November 2021).

64 H. Yang, Q. Lin, C. Zhang, X. Yu, Z. Cheng, G. Li, Q. Hu, X. Ren, Q. Zhang, J. Liu and C. He, Carbon dioxide electroreduction on single-atom nickel decorated carbon membranes with industry compatible current densities, *Nat. Commun.*, 2020, **11**, 1–8.

65 J. Wu, S. G. Sun and X. D. Zhou, Origin of the performance degradation and implementation of stable tin electrodes for the conversion of CO2 to fuels, *Nano Energy*, 2016, **27**, 225–229.

66 Y. Shi, Y. Ji, J. Long, Y. Liang, Y. Liu, Y. Yu, J. Xiao and B. Zhang, Unveiling hydrocerussite as an electrochemically stable active phase for efficient carbon dioxide electroreduction to formate, *Nat. Commun. 2020 111*, 2020, **11**, 1–10.

67 H. Cheng, S. Liu, J. Zhang, T. Zhou, N. Zhang, X. S. Zheng, W. Chu, Z. Hu, C. Wu and Y. Xie, Surface Nitrogen-Injection Engineering for High Formation Rate of CO2Reduction to Formate, *Nano Lett.*, 2020, **20**, 6097–6103.

68 J. Wu, P. P. Sharma, B. H. Harris and X. D. Zhou, Electrochemical reduction of carbon dioxide: IV dependence of the Faradaic efficiency and current density on the microstructure and thickness of tin electrode, *J. Power Sources*, 2014, **258**, 189–194.

69 M. Usman, M. Humayun, M. D. Garba, L. Ullah, Z. Zeb, A. Helal, M. H. Suliman, B. Y. Alfaifi, N. Iqbal, M. Abdinejad, A. A. Tahir and H. Ullah, Electrochemical Reduction of CO2: A Review of Cobalt Based Catalysts for Carbon Dioxide Conversion to Fuels, *Nanomater. 2021, Vol. 11, Page 2029*, 2021, **11**, 2029.

70 J. Masud, W. P. R. Liyanage, X. Cao, A. Saxena and M. Nath, Copper Selenides as High-Efficiency Electrocatalysts for Oxygen Evolution Reaction, *ACS Appl. Energy Mater.*, , DOI:10.1021/acsaem.8b00746.

71 J. Suntivich, K. J. May, H. A. Gasteiger, J. B. Goodenough and Y. Shao-Horn, A perovskite oxide optimized for oxygen evolution catalysis from molecular orbital principles, *Science (80-.).*, 2011, **334**, 1383–1385.

IV. COPPER COBALT SELENIDE AS EFFICIENT ELECTROCATALYST FOR SELECTIVE REDUCTION OF CO2 TO CARBON-RICH PRODUCTS

Apurv Saxena[a], Shubhender Kapila[a], Julia Medvedeva[b], Manashi Nath

Deparment of Chemistry, Missouri University of Science and Technology, Rolla, MO 65409

1. INTRODUCTION

Increased usage of fossil fuels and other non-renewable resources to power this planet over the last several decades has caused environmental pollution leading major energy crisis. One of the primary by-products of fossil combustion and resulting greenhouse gas is carbon dioxide. Rising levels of CO_2 in the atmosphere has led to severe catastrophic effects including erratic climatic changes and global warming. While carbon dioxide capture and sequestration can provide some solution to this rising CO_2 level in the atmosphere, however, these technologies need to be complemented by the chemical conversion of atmospheric CO_2 to other carbonaceous products. Such processes can effectively reduce CO_2 levels in the atmosphere, and at the same time close the carbon loop. Studies has been done using both heterogeneous and homogenous routes for catalytic carbon dioxide reduction reaction (CO2RR)[1,2] and other catalytic proceses[3,4].The homogenous route for CO2RR lacks scalability and leads toa low yield of product formation. heterogeneous catalysis for CO2RR, different type of catalysts has been used like organometallic complexes[5–7], metal electrodes[8,9] and metal chalcogenides[10]. Among different methods for heterogeneous catalysis, electrochemical reduction of CO_2 has

become a critical research problem over the last few decades. One of the primary challenges for the advent of CO_2 electroreduction is the discovery of efficient CO2RR electrocatalysts, that can not only reduce the reaction energy barrier leading to the facile transformation of CO_2, but also lead to high selectivity in product formation.

Among various catalysts that has been studied for CO_2 conversion, copper-based catalysts has been established to be very efficient in CO_2 electrochemical reduction as different reduction products can be generated using different conditions with high selectivity.[11] Different aspects such as change in crystal faces[12], morphology of the catalyst[13], size of the catalyst particles[14] and the valence state of central metal atom[15,16] on the CO2RR catalytic activity has been investigated by various groups. However, although Cu-based catalysts have shown significant advances for CO2RR, the need to investigate effect of transition metal doping in the Cu-based compounds and more importantly development of Cu-free catalysts has become imminent for gaining fundamental insight into structure-property correlation and formation of hydrocarbon and oxygenates product for these electrocatalysts.

One of the primary considerations for electrocatalyst is the availability of accessible variable oxidation states of the catalytically active site. Cobalt is one such transit n group element which exhibits oxidation states from 0 to +4 which are readily accessible through facile electrochemical tuning.[17] Co-based compositions has already proven to be efficient electrocatalyst in many other processes like water splitting.[18] However, during CO_2 electroreduction only the active site changes from Co^{2+} to Co^{1+}.[19] Metallic cobalt[20], cobalt-based bimetallic compounds[21,22], and cobalt oxide[23] has been studied for CO_2

electrochemical conversion. Cobalt porphyrin-based electrocatalyst have also been reported to achieve the conversion of carbon dioxide to CO.[24,25]

Regulation of the activity and product selectivity has been achieved by varying the catalyst size in cobalt based catalysts.[20,21,26,27] According to a study by Wannakao et al., Co metal has moderate CO binding strength as compared to other metals and thus has better catalytic performance for CO_2 electrochemical reduction. Presence of cobalt center decreases the possibility of catalyst poisoning which happens in metals like Pt, Rh and also decreases the potential applied compared to the metals with weak binding strength like Zn.[28] Also the presence of loosely held d electrons in the Co metal centers increases electrical conductivity which enhances the activity towards CO2RR.[23] Thus, cobalt-based catalysts have started gaining considerable attention for CO2RR due to their enhanced performance.

In this study, we have synthesized mixed transitional metal selenide $CuCo_2Se_4$ through efficient one pot solvothermal synthesis method, and studies reactivity of this copper cobalt selenide for carbon dioxide reduction under ambient conditions. It was observed that simultaneous presence of Cu and Co in the catalyst enhances the activity of towards CO2RR in comparison of binary selenides. In addition, $CuCo_2Se_4$ exhibited high degree of product selectivity forming carbon-rich products such as acetic acid and ethanol exclusively at low applied potential. We have also investigated the adsorption energy of intermediate CO on the catalyst surface through density functional theory (DFT) calculations, which showed that the CO adsorption energy was in the optimal range and better than that in binary Cu selenides. Such facile adsorption of intermediate CO in the

catalyst surface along with better electronic conductivity of the $CuCo_2Se_4$ matrix possibly leads to higher product selectivity at low applied potential.

2. EXPERIMENTAL AND COMPUTATIONAL METHODS

All chemicals were of analytical grade and used as purchased, $CoCl_2 \cdot 6H_2O$, $CuCl_2 \cdot 2H_2O$, SeO_2, $N_2H_4 \cdot H_2O$ and KOH was purchased from Sigma Aldrich. Carbon fiber paper (CFP) was used as the electrode and purchased from MSE supplies,

2.1. SYNTHESIS OF $CUCO_2SE_4$ AND ELECTRODE PREPARATION

$CuCo_2Se_4$ was synthesized using hydrothermal synthesis. 20 mmol of $CuCl_2 \cdot 2H_2O$, 40 mmol of $CoCl_2 \cdot 6H_2O$, and 40 mmol of SeO_2 were stirred together for 15 minutes in 15 mL of distilled water. 1.5 mL of $N_2H_4 \cdot H_2O$ (hydrazine) was added dropwise while stirring to form a brown colloidal solution. This solution then transferred into a Teflon-lined stainless-steel autoclave and heated at 145 °C for 24, following which it was cooled to room temperature under ambient conditions. The final product was obtained using centrifugation. The crude powder was washed using absolute ethanol and then vacuum dried overnight.

Catalyst ink was made by uniformly dispersing 5 mg of catalyst in 0.25 mL of 1 % Nafion ethanol solution using sonication for 15 min. The $CuCo_2Se_4$ electrode was prepared by uniformly dropcasting the catalyst ink on confined area. The area on the CFP substate was confined using Teflon tape and geometric area of 0.283 cm^2 was left exposed for drop casting of catalyst ink. The prepared electrode was dried overnight at room temperature.

2.2. CHARACTERIZATION OF CATALYST

2.2.1. Powder X-ray Diffraction. Powder X-ray diffraction (PXRD) was used to identify the crystalline phase of the as-synthesized catalyst powder using a Philips X-Pert diffractometer utilizing CuKα (1.5418 Å) radiation. Scanning Electron Microscopy (SEM) and X-ray Photoelectron Spectroscopy (XPS). FEI Helios NanoLab 600 FIB/FESEM was used to observe the Morphology of the product at an acceleration voltage of 10 kV and a working distance of 5 mm. To identify the composition via identifying the relative atomic ratio of elements present in the catalyst, EDS (Energy dispersive spectroscopy) was done from the same SEM. X-ray photoelectron spectroscopy (XPS) was used to observe the oxidation states of the elements in the $CuCo_2Se_4$ catalyst using a KRATOS AXIS X-ray Photoelectron Spectrometer. Specific correction of Co, Cu, and Se binding energies was carried out by employing the C 1s binding energy of 284.5 eV. All XPS signals were measured from the pristine catalyst surface without any sputtering.

2.2.2. Electrochemical Activity for CO_2 Conversion. The test of the electrochemical activity was performed in a two compartment H Cell with CO2 saturated 0.3 M $NaHCO_3$ solution. Both the compartments were separated by a Nafion anion exchange membrane. KCl saturated Ag|AgCl was used as reference electrode and was put in cathodic compartment with the working electrode. The carbon rod as counter electrode placed in the anodic compartment of the H-Cell. $CuCo_2Se_4$ coated CFP prepared by method described above was used as the working electrode. A catalyst loading of 1 mg cm^{-2} was used for these studies.

2.3. DENSITY FUNCTIONAL THEORY CALCULATIONS

First-principles density functional theory calculations were done using Vienna ab initio simulation package (VASP).[29–32] These calculations were done to gauge the electronic properties of surface and bulk geometries of $CuCo_2Se_4$. To calculate the adsorption energies of CO molecules int the surface of the catalyst, exchange-correlation functional Perdew−Burke−Ernzerhof (PBE) [6] within the generalized gradient approximation (GGA)[7] with an on-site Coulomb U term was used. This method illustrates the cohesive energy, electronic structure, and mechanical and magnetic properties of bulk and surfaces of 3d-metal-based materials.

To gain more insight into the electronic structure and magnetic properties of bulk and slabs of $CuCo_2Se_4$ as well as the adsorption energy of CO at the surfaces GGA+U method,[33] was used. For this method, Co *d* states $U = 0$ and 6 eV and for Cu *d* states $U = 0$ and 6 eV was used. Force and total energy reduction were used to optimize the internal atomic locations of all structures till the Hellmann–Feynman force on every atom was less than 0.01 eV/atom. The calculations used Brillouin-zone sampling which was done with Γ-centered Monkhorst–Pack[34] with k-mesh of at least 11x8x3 grid for $CuCo_2Se_4$ (100) surface the cutoff energy of 500 eV was used for bulk and slab geometries. 2x2x2 and 2x3x3 unit cells with a vacuum region along z direction of 15 Å were used as surface models. To the orbital occupation, Methfessel−Paxton smearing was applied with smearing parameter σ of 0.2 eV. the cutoff energy of 500 eV was used for bulk and slab geometries applied with the convergence criteria of 1.0 × 10−6 eV for electronic self-consistent iterations. For calculating CO adsorption energies, first clean surface energy was calculated by relaxing free surfaces, and after that CO ions were attached over the active sites of the

catalyst at a distance of ~ 1.80 Å taken from the bond lengths of Metal carbonyl complexes. After this the system was relaxed and E_{sys}., the total formation energy of the system was calculated. The adsorption energy of CO, $E_{ad} = E_{sys} – E_{clean} – E_{CO}$, E_{CO} being the energy of free CO.

3. RESULTS AND DISCUSSION

3.1. CHARACTERIZATION

Powder X-ray diffraction (PXRD) pattern collected from the as-synthesized powder showed a good match with the standard pattern of $CuCo_2Se_4$ (PDF No. 04-019-0997) confirming the formation of pure $CuCo_2Se_4$ as shown in Figure 1. No other crystalline impurity phases were detected in the PXRD pattern. The diffraction peaks showed considerable broadening indicating the formation of nanostructured grains. Scherrer equation was used to calculate the size of such grains and crystalline domain following standard procedure.[35] From the line broadening of the diffraction peaks, the approximate size of the particles was calculated to be 2.67 nm. $CuCo_2Se_4$ exhibits a spinel structure-type AB_2X_4 (X = chalcogen atom)., where A is a divalent cation occupying the tetrahedral layer and B is a trivalent cation occupying the fully occupied octahedral metal layer. As shown in the Figure 1 inset, the crystal structure of $CuCo_2Se_4$ shows that Co atoms were in the octahedral coordination sites and Cu atoms in the tetrahedral sites where the unit cell have similar geometries for each of the Co/Cu atom. Also the bond length between Co–Se and Cu–Se was found out to be ~2.38 and 2.37 Å, respectively.

Morphology of the hydrothermally synthesized powder was observed using SEM. In Fig. 2, SEM images depicted porous nanostructures having a size range of 100 nm - 200

nm. Such nanostructured morphology provides large number of accessible active sites for CO_2 and intermediate CO adsorption, which can get further reduced to desirable products.

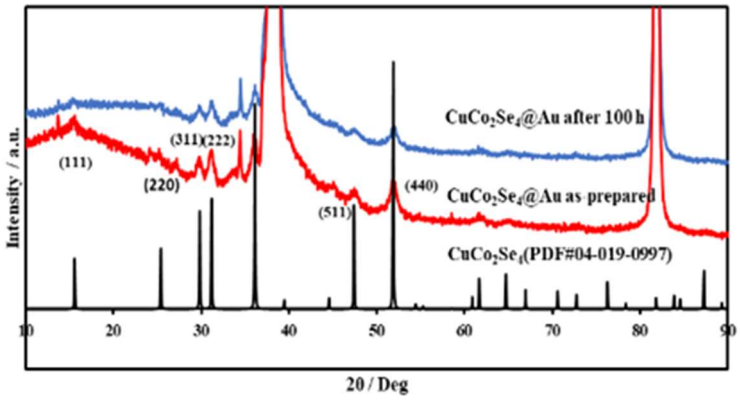

Figure 1. PXRD pattern of hydrothermally synthesized $CuCo_2Se_4$ compared with the standard $CuCo_2Se_4$ reference pattern (PDF# 04-019-0997)

The oxidation states and chemical composition of the as-synthesized powder was further investigated through X-ray photoelectron spectroscopy (XPS). XPS peaks at 778 eV and 793 eV, indicated the presence of Co in a Co-selenide bonding atmosphere,[36] while peaks at 934 and 954 eV indicated the presence of copper selenide bonding.[37] Deconvoluted spectra of Co and Cu XPS peaks showed presence of multiple oxidation states. As shown in Fig 2c, deconvoluted Cu spectra shows peaks at 931.5 and 952.5 eV corresponding to Cu^+ $2p_{3/2}$ and Cu^+ $2p_{1/2}$, and at 933.8 and 954.1 eV were assigned to Cu^{2+} $2p_{3/2}$ and Cu^{2+} $2p_{1/2}$ including the satellite peaks at 941.8 and 961.7 eV.[38] Similarly in Co 2p XPS spectrum, peaks at 780.5 and 796.8 eV reflect to Co^{2+} $2p_{3/2}$ and Co^{2+} 2p1/2 and 777.8 and 793.3 eV peaks correspond to Co^{3+} $2p_{3/2}$ and Co^{3+} $2p_{1/2}$, respectively.[39] satellite peaks of Co 2p were detected at 787 and 803 eV.[39]. The satellite peaks observed can be

explained as due to overlapping of antibonding orbitals between the Cu, Co and Se as has been reported previously.[3437] XPS peaks corresponding to Se 3d states were observed at 54.1 and 55 eV corresponding to Se $3d_{5/2}$ and Se $3d_{3/2}$, respectively, demonstrating the existence of Se^{2-}.[36] The peak at 59.2 eV shows the existence of minute amount of SeO_x species on the surface which can happen due to the surface oxidation of pristine selenide. However, it must be noted that there was no metal oxide detected on the catalyst surface. The relative percentages of the various cations present in the composition was estimated as 7% Co^{3+}, 44% Co^{2+}, 8.5 % Cu^{+}, and 38.5 % Cu^{2+}.

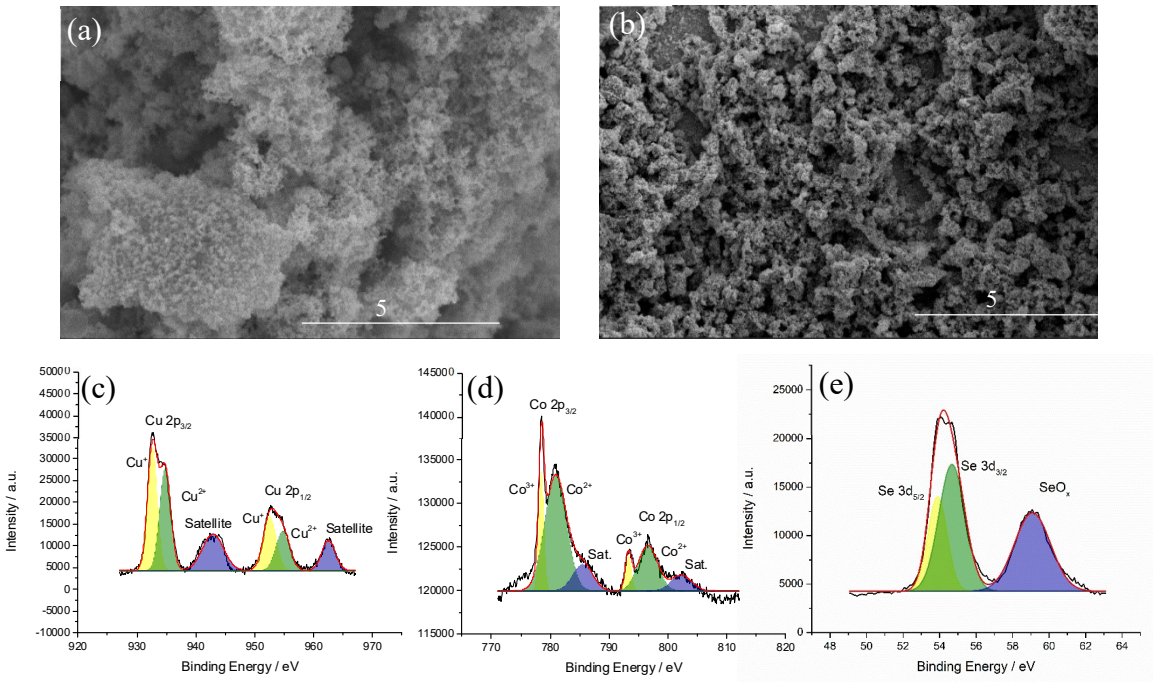

Figure 2. SEM images of the $CuCo_2Se_4$ nanoparticles at (a) high and (b) low magnification showing formation of nanostructures and surface roughness, respectively. (c) Cu 2p and (d) Co 2p and (e) Se 3d XPS spectra of as-synthesized $CuCo_2Se_4$.

3.2. ELECTROCATALYTIC PERFORMANCE FOR CO_2RR

The CO_2 electrochemical reduction activity of $CuCo_2Se_4$ was investigated through linear sweep voltammetry (LSV) at a scan speed of 10 mV s^{-1} in Argon and CO_2-saturated 0.3 M $NaHCO_3$ electrolyte solution. Electrochemical experiments were performed in two compartment H-cell where both catholyte and anolyte were 0.3 M $NaHCO_3$ solution.

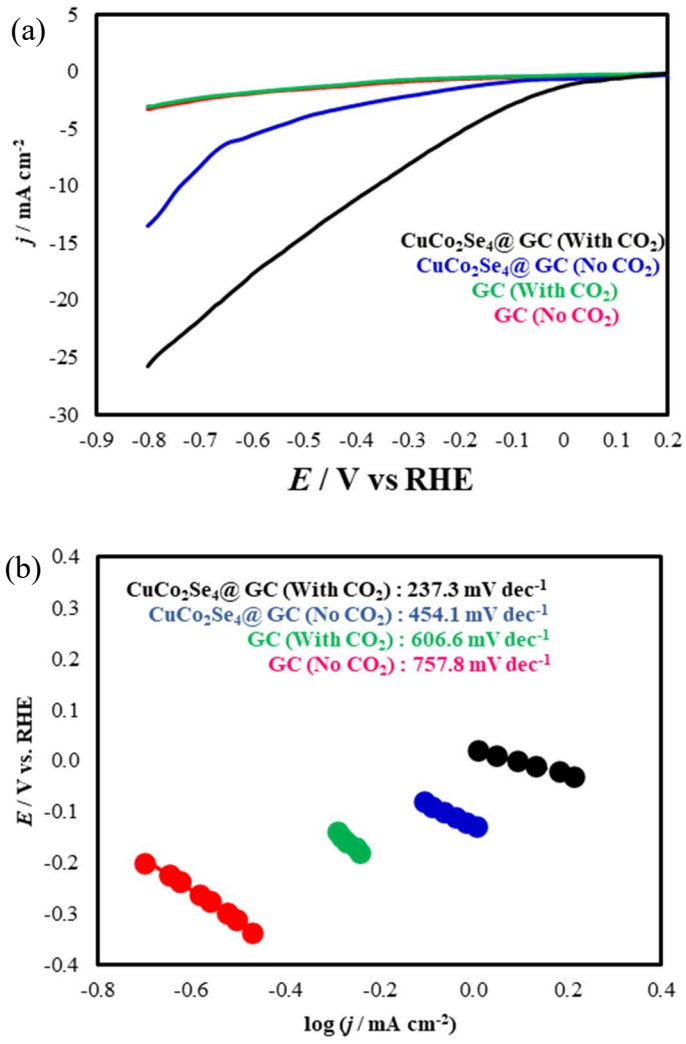

Figure 3. (a) LSVs measured in 0.3 M $NaHCO_3$ at a scan rate of 10 mV s^{-1} in presence and absence of CO_2 with different electrodes. (b) Tafel plots measured in 0.3 M $NaHCO_3$.

In keeping with modern techniques, carbon rod was used as the counter electrode instead of Pt, to minimize impurity enrichment in the electrolyte. Using a Pt wire in H_2-saturated H_2SO_4 solution, the Ag|AgCl reference electrode was standardized utilizing open circuit potential (OCP, 0.199 V). All the reduction potentials measured with Ag|AgCl reference electrode were converted to the RHE using equation (1) and reported current densities were calculated taking geometric area of electrode into consideration.

$$E_{RHE} = E_{Ag|AgCl} + 0.059\,\text{pH} + E^0_{Ag|AgCl} \quad (1)$$

where E_{RHE} = converted potential vs RHE, $E_{Ag|AgCl}$ = experimentally obtained potential, $E^0_{Ag|AgCl}$ = standard potential of Ag|AgCl (0.199 V).

The LSVs were measured in a stirred solution under continuous purging of CO_2 to minimize mass transfer limitations. The control experiment (without CO_2) involved purging with Ar under similar conditions. The LSV plots of $CuCo_2Se_4$ modified electrodes were compared with that of bare carbon cloth measured under similar conditions to confirm the catalytic effect of $CuCo_2Se_4$ for CO2RR. $CuCo_2Se_4$@CFP showed increased reduction current when CO_2 purged electrolyte was used compared to Ar purged electrolyte which confirmed that $CuCo_2Se_4$@CFP was indeed more active towards CO2RR and suppresses the competing HER reaction under these conditions. Bare CFP on the other hand, did not show any significant activity towards CO2RR which confirmed the catalytic activity of $CuCo_2Se_4$ and no substrate effect. $CuCo_2Se_4$ catalyst also exhibited high current density reaching upto 26 mA cm^{-2} at low applied potential of 800 mV.

Tafel slopes of the catalyst was estimated to explore the chemical kinetics of CO_2 electrochemical reduction. Tafel slope can be calculated using the Equation(2):

$$\eta = \alpha + (2.3\,RT)\,\frac{log\,j}{\alpha nF} \quad (2)$$

where η = overpotential, a = transfer coefficient, n = number of electrons involved in the reaction, F = Faraday constant, j = current density and the slope = 2.3RT/ αnF

With a scan speed of 10 mV s^{-1}, the Tafel slope was determined in the kinetically controlled area of CO2RR. It was observed that the $CuCo_2Se_4$@CFP electrode exhibited lowest value of Tafel slope with value of 237 mV dec^{-1} in CO_2 purged electrolyte. This suggests that mechanism of CO2RR over $CuCo_2Se_4$@CFP is similar to the chemical rate-determining step (RDS) of initial single-electron transfer step for adsorbed radical intermediate (CO_2^-) formation which has theoretical value of Tafel slope to be 118 mV dec^{-1}. A much lower Tafel slope closer to 59 mVdec^{-1} indicates rapid one-electron transfer step followed by the formation of formate as RDS.[40] Moreover, Tafel slope of bare CFP was higher than that of $CuCo_2Se_4$ indicating that electron transfer at $CuCo_2Se_4$@CFP electrode surface was much faster.

Chronoamperometry studies were used for detecting and quantifying the product composition generated by electrochemical reduction of CO_2 at different applied potentials from -0.9 V to -0.1 V vs RHE for the time period of 1 hour. Initially, these electrochemical experiments were started after purging CO_2 vigorously for 30 minutes. The electrolyte (0.3M $NaHCO_3$ aqueous) was then constantly purged with CO_2 at a rate of (20 sccm) during the chronoamperometry studies. Quantification for liquid and gaseous products were done using NMR and GC-TCD. 0.1 µL DMSO was used as an internal standard mixed with 500 µL of aliquot (reaction solution) and 100 µL D_2O. Water suppression technique was used to suppress the water peak in NMR spectra. Gaseous products were detected and quantified using GC-TCD technique and using calibration curves of standards.

It was observed that composition and selectivity of CO2RR products at $CuCo_2Se_4$@CFP electrode varied with the applied potential. Specifically, at lower negative potentials, C2 products such as ethanol and acetate were obtained preferentially, while C1 products formed at high negative potentials. Acetate was the major product formed till -0.6V vs RHE. This is drastically different from other catalyst systems known for CO2RR which produce formic acid and other C1 products at these potentials. Also, such high selectivity indicates high production rate due to the fact that all the energy is getting used to form the C2 product.

Advent of formic acid in the product composition was observed at -0.6 V (vs RHE) in addition to carbon rich C2 products. As reported in a study that with decreasing potential, given the rapid hydrogen production, pH drops around the electrode surfacepH decreases near the electrode surface due to continuous hydrogen evolution,[24] leading to spontaneous conversion of CO_2 to HCO_3^- in situ leading to facile formation of formic acid at higher applied potential.

Relative product yield was calculated by quantifying of products at different potentials using calculations in Table S1. Figure 4(b) shows the product selectivity at various applied potentials. Lower applied potential favors the formation of C2 products exclusively rather than producing C1 products which predominantly forms at higher negative potential. These results illustrate the potential for application of this catalyst for industrial application as energy input is less and selectivity is high for specific products.

GC-TCD was used for characterization and quantification of the gaseous products. The head-space gas was collected after 1 hour of CO2RR at different applied potentials (-0.1 V, -0.25 V, -0.6 V, -0.9 V vs RHE), wherein hydrogen was detected with FE = 0 %,

0.51%, 0.90 %, and 2.7 % respectively as shown in figure 5. It should be noted that no other hydrocarbon gas was observed during these measurements. Hydrogen evolution is a competing reaction which restricts the faradaic efficiency of hydrocarbon products. The LSV plot of the experiment done on $CuCo_2Se_4$@CFP in an Ar-purged electrolyte also suggests that HER becomes more prominent at higher negative potentials as shown in figure 3a. Hydrogen formation during CO2RR can be observed from the -0.25V vs RHE. Interestingly, no CO was detected in the head-space gas at any applied potential. Such absence of CO in product composition yields further confirmation that preferential formation of C2 products follows longer dwell time and further reduction of adsorbed intermediate CO on the catalyst surface inhibiting its ready desorption. We have investigated the formation rates and partial current density for every product over a series of potentials to gain a better understanding of the specificity of the CO_2 reduction reaction and to comprehend reaction dynamics. This type of examination for various products can yield critical mechanistic insights. The analyses of reaction rates (Figure 6 (a)) and partial current density (Figure 6 (b)) revealed that acetic acid was the most important factor in increased activity throughout a broad array of potential. Formic acid formed at a level proportional to acetic acid at greater applied voltage. Acetic acid and ethanol, on the other hand, formed at significantly larger rates when the applied potential was low. These performance patterns validated the catalyst's product selectivity and novelty when compared to conventional CO2RR catalysts that have greater formation constants for primarily C1 products.

Because of the varied rates *CO conversion on the surface, such a variation in electrochemical activity can be derived. Such difference in electrochemical activity can be deduced because of different rate of *CO conversion on the surface as described below.

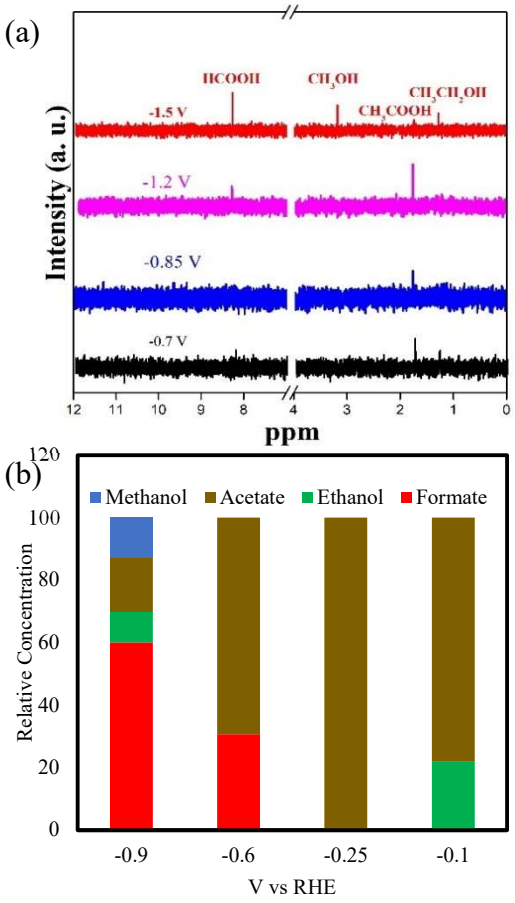

Figure 4 (a) NMR spectra identifying CO_2 reduction products in reaction aliquots collected at different potentials. (b) Plots illustrating relative concentrations of liquid products quantified from NMR at different stationary applied potentials.

Dehydroxylation and decarbonylation of chemical intermediates can also occur at varying rates depending on the applied voltage. Such findings also show that $CuCo_2Se_4$ is

catalytically active for CO2 reduction and generates considerable amounts of carbon-rich compounds at high rates over longer durations.

Intrinsic characteristics such as rapid catalyst activation via intermediate adsorption and improved charge transfer are often attributed to increased catalytic performance. Whereas electrolyte and reagent exposure to the active sites is influenced by extrinsic variables like catalyst's morphology and surface roughness. External parameters influencing electrocatalytic activity were estimated using a previously described experimental technique[41] By measuring double layer capacitance as shown in Fig. 6 with in non-Faradaic zone as a variable of scan speed and comparing specific capacitance (CS) to the double layer capacitance measured, electrochemically active surface area was calculated. The electrochemical double layer capacitance (C_{DL}) was calculated following Equation. (3).

$$i_{DL} = C_{DL} \times \nu \tag{3}$$

where i_{DL} represents the current observed while ν is the scan rate. As can be seen from the Figure 7, C_{DL} calculated from the i vs ν plot resulted in value of 0.02 mF. The ratio of C_{DL} and Cs was used to calculate ECSA as shown in Equation. (4).

$$ECSA = C_{DL}/C_S \tag{4}$$

The cyclic voltammograms were recorded at scan speeds ranging between 5 mV/s to 200 mV/s in CO_2 purged 0.3 M $NaHCO_3$. Polarization curves was done in potential range of 15 mV according to OCP of $CuCo_2Se_4$ electrode. Current density was displayed as a function of scan rate using cyclic voltammograms.

The capacitance values were used to derive the surface roughness factor. The ECSA ratio was derived from the Cs number (40 μF cm^{-2}) obtained from the reported data and the

CDL (0.071 mF) from the plot. ECSA value was calculated to be 1.76 cm^2. The effect of catalyst morphology on the working electrode was also estimated from the roughness factor (RF). RF was calculated to be 6.24 from the ratio between ECSA and geometric electrode area (0.283 cm^2). High value of ECSA and roughness factor depicts that CO_2 dissolved in the electrolyte has more access to the catalytic sites on working electrode, leading to better conversion efficiency.

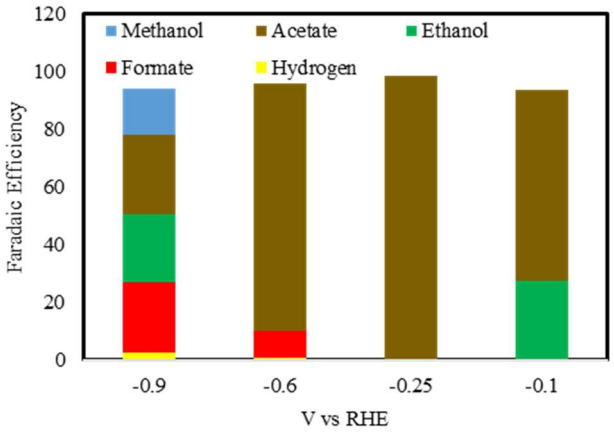

Figure 5. Bar plots depicting relative faradaic efficiency of cumulative liquid and gas phase CO_2 reduction products at different applied potentials quantified through NMR and GC-TCD.

For further investigation of electrochemical performance of $CuCo_2Se_4$@CFP towards CO2RR, EIS (electrochemical impedance spectroscopy) was performed as shown in Fig. 8. Internal resistance of the catalyst composite and the charge-transfer resistance at the (electrode)–electrolyte interface of the catalyst was calculated by performing EIS and investigating Nyquist plot. At the potential -0.1 V vs RHE, Nyquist plot was observed in CO_2 saturated 0.3 M $NaHCO_3$. This plot was fitted with the equivalent circuit and

electrolyte resistance (R_s), resistance of the catalytic composite (R_f), and charge-transfer resistance (R_{ct}) was calculated from the circuit.

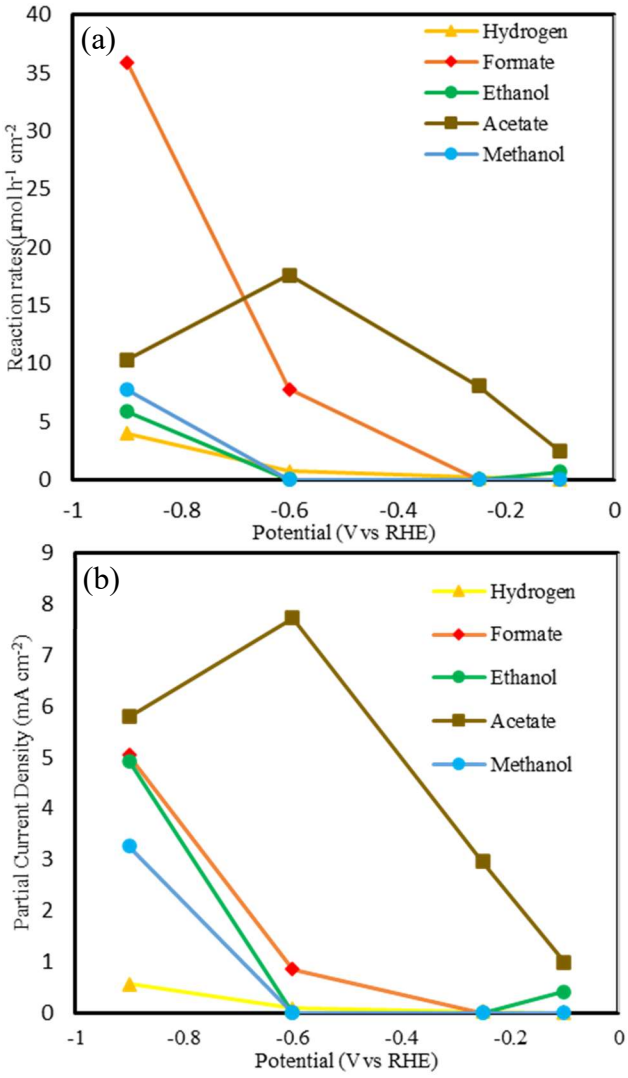

Figure 6. CO_2RR performances of $CuCo_2Se_4$ catalyst. (a) Reaction rates of Hydrogen, formate, ethanol, acetate and methanol. (b) ECSA normalised Partial current density of individual products, hydrogen, formate, ethanol, acetate and methanol.

The uncompensated electrolyte resistance R_s, R_{ct} and R_f of catalyst composite were 1.69 Ω, 40 Ω and 230 Ω respectively was obtained from the fitting of the equivalent circuit.

Using Rct, charge-transfer resistance which is calculated from the lower frequency region we can get an idea of CO2RR process going on the catalyst surface. Lower Rct value means that electron transfer is efficient at the catalyst–electrolyte interface resulting in faster CO_2 reduction rate, better catalytic activity and lower overpotential which can be seen from electrocatalytic measurements mentioned above. R_f catalyst resistance influences the charge transport within the catalyst composite. Lower R_f can result in high current density and faster kinetics at low potentials.

Table 1. Fitting parameters obtained from Nyquist plots at various potentials.

Resistor and Capacitance	value
Rs/Ω	1.69
R_f /Ω	230
Rct/Ω	40
CPEdl/F	0.002
CPEf/F	0.0023

3.3. ELECTROCHEMICAL PERFORMANCE OF $CUCO_2SE_4$ FOR ALCOHOL OXIDATION REACTION (AOR)

To evaluate the electrocatalytic performance of catalytic materials that have been produced for use in alcohol electrooxidation, a 3 electrode H-Cell setup was used to carry out a series of electrochemical experiments. LSV polarization plots showed activity in the absence and presence of 1 mol L^{-1} methanol and ethanol in 1M KOH.

The results from LSVs (Fig. 9(a)) demonstrate a moderate level of OER activity, with an anodic current density of 15 mA cm^{-2} at the potential of 1.45 V vs. RHE. When Methanol was added to make solution 1 M methanol, the polarization curve recorded showed enhanced activity. Also, it was observed from the polarization curves that the overpotentials changed by 250 mV, 300 mV at 15 and 50 mA cm^{-2} respectively when compared to water splitting potentials. When Ethanol was added, overpotentials got reduced by 230 mV, 260 mV at 15 and 50 mA cm^{-2} respectively This means that for industrial applications very less amount of cell potential has to be applied and at that cell potential CO2RR will produce the same product in both compartments of H-Cell. Also using the Tafel slopes (Fig. 9(b)) calculated from the polarization curves, more insights into the underlying kinetics were produced.

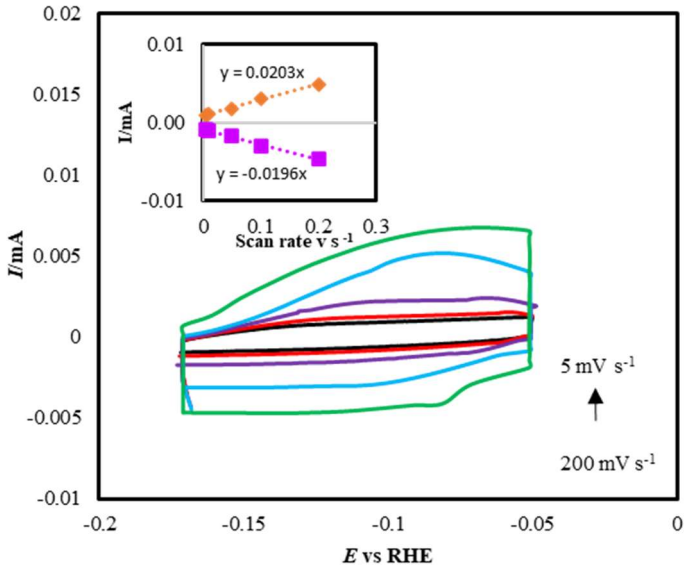

Figure 7. Cyclic voltammograms measured for $CuCo_2Se_4$ catalyst in 0.3 M $NaHCO_3$ under continuous Ar purging at different scan rates from 5 to 200 mV s^{-1}. Inset shows plot of anodic and cathodic current measured at -0.12 V vs RHE as function of scan rate.

Tafel slope is lower in the case of methanol oxidation and ethanol oxidation of value 78.6 mV dec^{-1} and 52.7 mV dec^{-1} respectively when compared to the water splitting. This proves that the kinetics improve when the methanol and ethanol are present in the solution. Also, it proves that mass transfer is enhanced, and a larger number of catalytic sites present in the electrode surface are available. For identification of the products in the anodic compartment, ^{1}H NMR was used. Formic acid was detected at the chemical shift of 8.3 ppm in the anodic compartment when methanol was added, and Acetic acid was observed at the chemical shift of 1.7 ppm when ethanol was added.

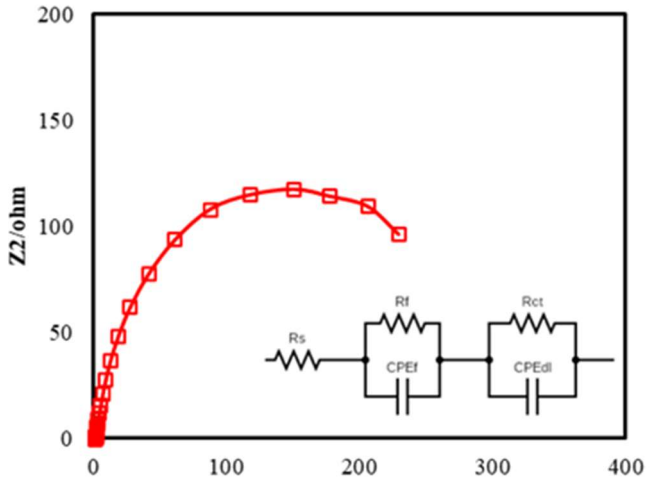

Figure 8. EIS Nyquist plots of $CuCo_2Se_4$@CFP in CO_2-saturated 0.3 M $NaHCO_3$ electrolyte (pH 6.8) from 0 V vs RHE to -1.3 V vs RHE. Inset shows the equivalent circuit fitted to experimental spectra, where R_{CT} corresponds to the charge-transfer resistance on catalyst-electrolyte interface, while R_s indicates film resistance of the catalyst composite

Long-period chromatography experiments were also conducted at a fixed potential of 1.5 V vs RHE to detect the rate of methanol oxidation and to determine the rate of formic

acid production. The rate of reaction stagnates over time which can be revitalized by adding more methanol hence improving the mass transfer kinetics. The current density of $CuCo_2Se_4$ goes through little change over a long period (100 h) signifying its applicability to industry.

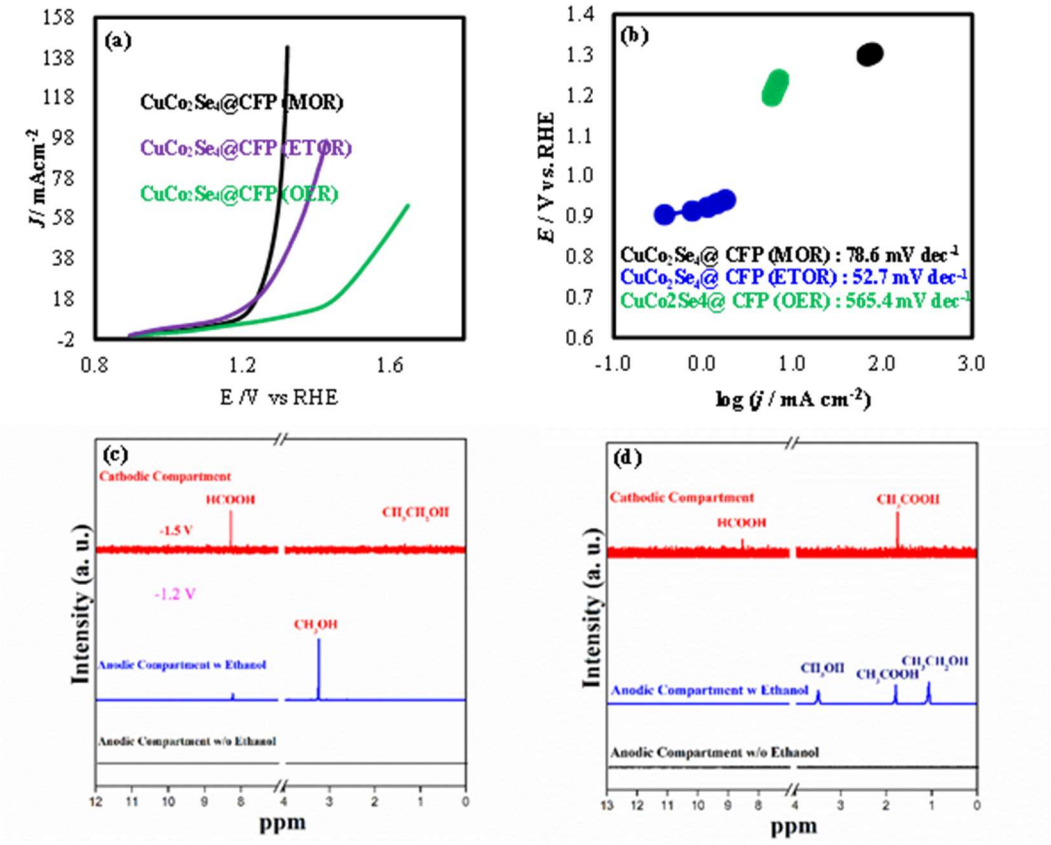

Figure 9. Electrocatalytic performances of $CuCo_2Se_4$/CFP a) Polarization curves of $CuCo_2Se_4$/CFP in absence (red) presence of 1M ethanol (green), 1M methanol (black) in 1 M KOH solution. (b) Tafel plots of above polarization curves (c) 1H-NMR of anodic and cathodic compartment of Ethanol oxidation (EtOR) (d) 1H-NMR of anodic and cathodic compartment of methanol oxidation (MOR)

3.4. ELECTROCHEMICAL CATALYTIC ACTIVITY OF $CUCO_2SE_4$ FOR CO2RR-AOR COMBINED REACTION ($CUCO_2SE_4$/CF|| $CUCO_2SE_4$/CF)

Because of the enhanced activity of the catalyst for CO2RR in cathodic compartment and Alcohol oxidation in the anodic compartment, a two-electrode H-cell was setup with catalyst loaded working electrode as an anode having 1 M CH_3OH or 1M C_2H_5OH in electrolyte 1 M KOH and catalyst loaded on the counter electrode as the cathode in 0.3 M $NaHCO_3$ solution. This electrolyzer operated at ambient temperature and pressure producing the same product in both compartments. Polarization curves from linear scan voltammetry showed that a standard current density of 15 mA cm^{-2} was obtained in CO2RR- methanol oxidation and CO2RR- ethanol oxidation at 0.67V and 0.73V vs RHE respectively. Most importantly, these cell potentials are 280 mV and 220 mV less than what is required when no alcohol is added under the same setup. The voltages were found to be significantly smaller than the theoretical voltage [1.299 V in Eq. (3)] for overall CO2RR (no alcohol present). When methanol was reactant in the anodic compartment formic acid is produced in the electrolyzer at a potential of 0.7V vs RHE. When Ethanol was present in the anodic chamber Acetic acid was produced at the 0.75 V vs RHE.

Also, at 50 mA cm^{-2} current densities were obtained at 0.77 V and 0.78 V, respectively. The Faraday efficiency obtained for acetate production in the anodic and cathodic compartment was 71.35 % and 92.20 % respectively at an overall cell potential of 0.7 V. For formate production, FE was 84.35 % and 92.50 % in the anodic and cathodic compartment, respectively, at the cell voltage of 0.75 V.

To understand the interactions of intermediates on the catalyst surface, enhanced performance of the catalyst and selectivity towards C2 reduction products, the catalyst surface was investigated further through Density functional theory (DFT). CO adsorption

energies on Cu and Co sites of $CuCo_2Se_4$ (100) surface was estimated, as shown in Figure 11. This material was earlier discovered and investigated by the PIs as highly efficient electrocatalyst for water splitting.70 Our preliminary results suggest that Co has higher *CO binding energy by about 450 meV (Eads = -1.37 eV (Co site with CO attached) and

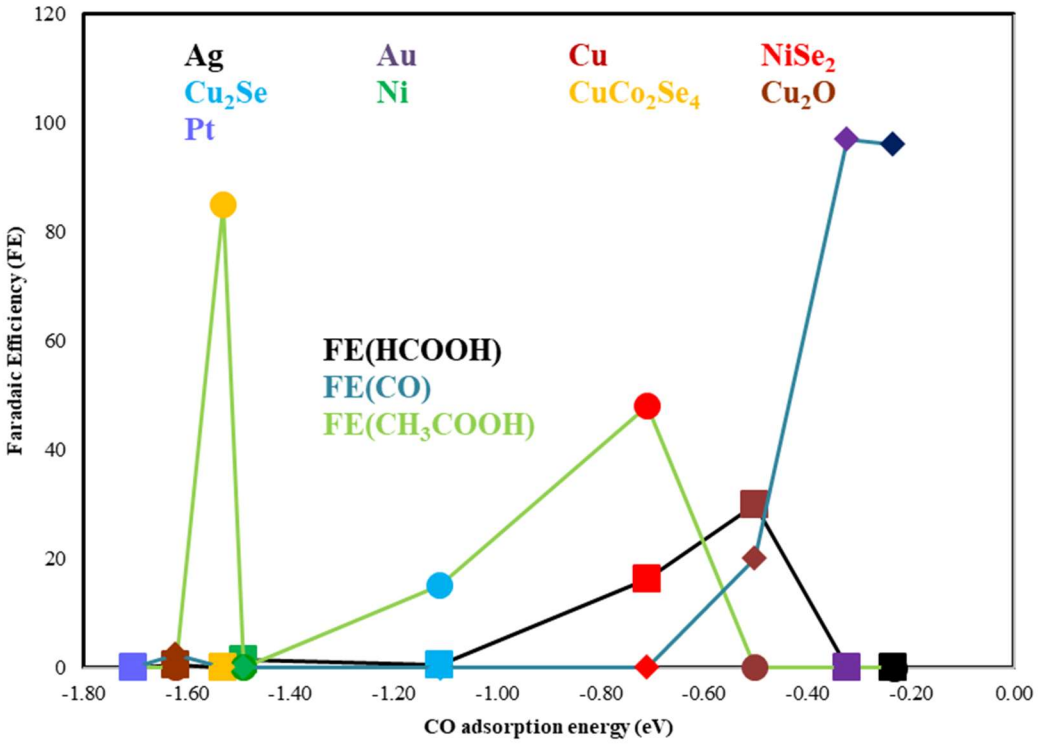

Figure 10. Faradaic efficiencies of Formic acid and Carbon monoxide and Acetic acid varying with different metallic surfaces and reported catalysts

-0.92 eV (Cu site with CO attached)) indicating that the Co site will lead to a preferable formation of higher reduction products. Moreover, the optimized distances between M-CO and C-O reveal strengthening of the Co-CO bond and weakening of the C≡O to partial double bond character: the Co(Cu)-CO distances are 1.75 Å (1.83 Å), whereas the C-O

distances are 1.16 Å and 1.15 Å for the CO attached to Co and Cu sites, respectively, both being longer as compared to the distance in a free-standing C-O, 1.14 Å, calculated using the same methods. Currently, authors are investigating the role of magnetic interactions on bonding, charge distribution and electronic properties of the surface structure, following earlier findings by the PIs that the magnetic moment on Co is enhanced from 0.8 mB in bulk to 2.1 mB for (100) surface and further to 2.3 mB for (111) surface of $CuCo_2Se_4$. It must be noted here that there have been very few reports of Co-based CO2RR electrocatalysts besides, metallic Co, Co-oxide and porphyrin based organometallic complexes.71-74 Even in such cases, the major product formed has been CO(g) and HCO2H.

The CO adsorption energy on Cu and Co sites in $CuCo_2Se_4$ was compared with other CO2RR different catalysts to correlate it with preferential formation of C1/C2 product based on the hypothesis that larger CO adsorption energy led to longer CO dwell time on the surface. More specifically, the CO adsorption energy was compared with Faradaic efficiency for formation of CO, HCOOH (C1 products) and acetic acid (C2 products) as shown in Figure 10. For metal catalysts like Au, Ag, low CO adsorption energy was observed and have been reported to produce CO as a main product. While for metal catalysts like Pt, Pd and Ni high CO adsorption energy was observed. However, these catalysts also show a high binding energy for *H leading to electron consumption that are utilized for hydrogen evolution rather than electrochemically reduction of CO_2 in aqueous medium. With high CO adsorption energy, catalysts can also get poisoned due to CO passivation by the small amounts of CO produced during continuous electroreduction of CO_2. Cu and Co metal have showed higher larger CO adsorption energy compared to

metals like Au and Ag but lesser then the catalysts like Pt, Pd and Ni, as shown in Figure 10. Co metal catalyst has been reported to produce hydrocarbons like CH_4, CO and Cu produces wide range of hydrocarbons which relates to the moderate CO adsorption energy on these metal catalysts. $CuCo_2Se_4$ shows slightly higher CO adsorption energy than that of Co and Cu but lower than the passivation level observed with Pt, Pd and Ni catalysts, which favors further reduction of CO adsorbed on the surface to produce carbon rich products like acetic acid.

CO adsorption on the catalyst surface proceed through two possible pathways using coordinate bond: first is through σ donation from CO to metal through Highest Occupied Molecular Orbitals located on C and second is through back donation from metal (d-) to CO (π*) which can be observed from the low intensity peak near -3.7 eV energy which is due to contribution of CO pDOS, similar to previously reported results.[42]

While the DFT study should involve all of the reaction pathways of mechanism and explore all the possible lattice planes of the $CuCo_2Se_4$ for understanding selectivity exhibited by catalyst towards formation of specific reduction products, DFT results in this study prove that $CuCo_2Se_4$ catalyst surface facilitates the selectivity towards carbon-rich products by enhancing intermediate CO adsorption. These DFT results are synchronous with the experimental observations achieved in this study.

To understand the interactions of intermediates on the catalyst surface the catalyst surface was investigated further through Density functional theory (DFT) with GGA+U (U = 6 eV) approximation. Density of states (DOS) were calculated for Co *d* states and for Cu *d* states before and after CO adsorption on surface active site (Co and Cu, respectively). DOS was also estimated for the bulk $CuCo_2Se_4$, which showed that hybridization of Se p

orbitals and Cu-Co d orbitals constituted the valence band, whereas vacant d orbitals of Co and anti-bonding p orbitals of Se formed conduction band as shown in Figure 11 & 12. These observations suggest that the possibility of d-d electron transfer/overlap among Co and Cu. The DOS of bulk $CuCo_2Se_4$ also suggest present of metal-to-ligand (Se) charge transfer. Also, the continuity in DOS in the vicinity of Fermi level suggest that $CuCo_2Se_4$ has enhanced conductivity,[1]which is also evident from the EIS data that shows low resistance (Rct) of bulk $CuCo_2Se_4$. To understand the differences in electronic and magnetic properties of the bulk $CuCo_2Se_4$, the combined PDOS of all Co atoms from each layer of (100) Co/Cu slab have been plotted and presented in Figure 11 & 12.

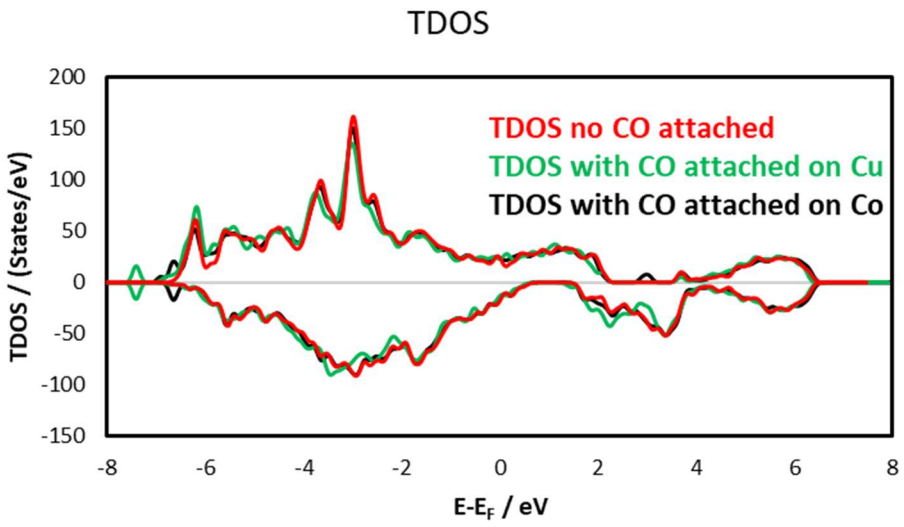

Figure 11. Total density of states (TDOS) of bulk $CuCo_2Se_4$ compared with CO attached on Co and Cu atoms

To investigate which metal atom on the surface is more likely to be the catalytically active site for CO2RR, the adsorption of CO on (100) Co/Cu terminated slabs was modeled

by placing CO radical in the vicinity of the active metal site (Co or Cu) of the relaxed free surface at an initial distance of about 2.2 Å from the metal atom. The GGA+U total energy of the fully optimized structure with CO bonded to the surface Cu atom is -1.53 eV which is higher than that bonded to the Co atom (-0.91 eV) for the (100) surface. The large energy difference of 620 mV suggests that Cu atom is the highly preferred catalytically active site, however, the presence of magnetically active Co in the vicinity of Cu influences the CO adsorption energy. Moreover, the optimized distances between M-CO and C-O reveal strengthening of the Co-CO bond and weakening of the C≡O to partial double bond character: the Co(Cu)-CO distances are 1.75 Å (1.83 Å), whereas the C-O distances are 1.16 Å and 1.15 Å for the CO attached to Co and Cu sites, respectively, both being longer as compared to the distance in a free-standing C-O, 1.14 Å, calculated using the same methods.

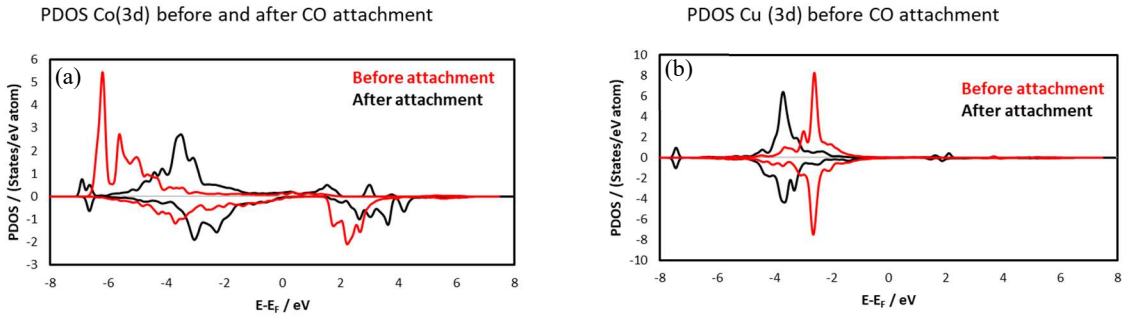

Figure 12. Partial density of states (PDOS) and it's parts (a) Co atom in (100) surface before and after CO^- attachment (b), and OH^- ions after attachment on Co atom (c). Cu atom in (100) surface before and after CO^- attachment

It was also observed that the magnetic order on Co changes in each layer of the slab when CO is bonded to Co, and does not change when it bonds to Cu. This suggests that

magnetism plays a crucial role in favoring the CO adsorption on Co. The comparison of PDOS of Co and Cu atoms with and without CO attachment is shown in Figure 12. For both Co and Cu with CO ion attached, there is a significant orbital splitting of the occupied metal states associated with rearranged electron cloud. Upon bonding to the CO, local magnetic moment on the Co atom increases from 1.066 μB to 2.011 μ_B for (100) slab and the Co–Se distances increase from 2.42 Å to 2.5 Å. Accordingly, the calculated PDOS of Co (Figure 3) shows that the occupied spin-up Co states become more localized upon bonding with CO due to the weaker Co–Se interactions and are shifted to the lower negative energy because of the stronger magnetic exchange splitting. On the other hand, PDOS exhibit opposite trends in the empty spin-down states of Co, namely, the shift to the lower and higher energies, respectively, as shown in Figure 4.

From the DFT studies of the electronic properties and the CO adsorption energy calculations on the surface of $CuCo_2Se_4$, it can be concluded that Cu atom is the active catalytic site for the $CuCo_2Se_4$ system. However, the presence of magnetic Co on the neighboring sites influences the electronic density around the Cu ions as well as intermediate adsorption energy.

4. CONCLUSION

In conclusion, the $CuCo_2Se_4$ electrocatalyst placed on carbon fiber paper is the first cobalt-based catalyst to create acetic acid as a result of CO_2 reduction. For a lengthy period of time, this catalyst showed a high current density of 29.9 mA cm^2. The increased Cu-Se covalency of this catalyst translates in reduced tellurium dissolution under CO2RR, making

it more durable. Because it is selective towards acetic acid at extremely low potential (-0.25 V) with FE = 65 percent and towards formic acid and methanol at greater negative potential (-0.9 V) with FE = 24 % and 16 % and a high formation rate (35.8 mol cm^{-2} h^{-1}) for formate, this catalyst is exceptionally selective and energy efficient. These discoveries will lead to creation of stable and active catalysts for industrial scale. The electrocatalyst surface was further investigated using DFT simulations to determine CO adsorption energy on the catalytic site, which revealed a moderate adsorption energy, implying a prolonged dwell time of adsorbed CO on the catalyst surface, resulting in preferential reduction to C2 products. As noted above, this $CuCo_2Se_4$ catalyst surface can successfully convert CO_2 to ethanol and acetic acid with excellent Faradaic efficiency at one of the lowest applied potentials known until date. This finding, together with the relationship between catalytic activity and CO adsorption energy, will lead to the best catalyst design for generating carbon-rich, high-value products by reducing CO_2.

REFERENCES

(1) Whipple, D. T.; Kenis, P. J. A. Prospects of CO2 Utilization via Direct Heterogeneous Electrochemical Reduction. *J. Phys. Chem. Lett.* **2010**, *1* (24), 3451–3458. https://doi.org/10.1021/JZ1012627/ASSET/IMAGES/MEDIUM/JZ-2010-012627_0004.GIF.

(2) Duan, X.; Xu, J.; Wei, Z.; Ma, J.; Guo, S.; Wang, S.; Liu, H.; Dou, S. Metal-Free Carbon Materials for CO2 Electrochemical Reduction. *Adv. Mater.* **2017**, *29* (41), 1701784. https://doi.org/10.1002/ADMA.201701784.

(3) Singh, H.; Bernabe, J.; Chern, J.; Nath, M. Copper Selenide as Multifunctional Non-Enzymatic Glucose and Dopamine Sensor. *J. Mater. Res. 2021 367* **2021**, *36* (7), 1413–1424. https://doi.org/10.1557/S43578-021-00227-0.

(4) Singh, H.; Marley-Hines, M.; Chakravarty, S.; Nath, M. Multi-Walled Carbon Nanotube Supported Manganese Selenide as Highly Active Bifunctional OER and ORR Electrocatalyst. *J. Mater. Chem. A* **2022**, *6*, 4883–5230. https://doi.org/10.1039/D1TA09864K.

(5) Gonglach, S.; Paul, S.; Haas, M.; Pillwein, F.; Sreejith, S. S.; Barman, S.; De, R.; Müllegger, S.; Gerschel, P.; Apfel, U. P.; Coskun, H.; Aljabour, A.; Stadler, P.; Schöfberger, W.; Roy, S. Molecular Cobalt Corrole Complex for the Heterogeneous Electrocatalytic Reduction of Carbon Dioxide. *Nat. Commun.* **2019**, *10* (1), 1–10. https://doi.org/10.1038/s41467-019-11868-5.

(6) Su, P.; Iwase, K.; Harada, T.; Kamiya, K.; Nakanishi, S. Covalent Triazine Framework Modified with Coordinatively-Unsaturated Co or Ni Atoms for CO2 Electrochemical Reduction. *Chem. Sci.* **2018**, *9* (16), 3941–3947. https://doi.org/10.1039/c8sc00604k.

(7) Sonoyama, N.; Kirii, M.; Sakata, T. Electrochemical Reduction of CO2 at Metal-Porphyrin Supported Gas Diffusion Electrodes under High Pressure CO2. *Electrochem. commun.* **1999**, *1* (6), 213–216. https://doi.org/10.1016/S1388-2481(99)00041-7.

(8) Mistry, H.; Varela, A. S.; Bonifacio, C. S.; Zegkinoglou, I.; Sinev, I.; Choi, Y. W.; Kisslinger, K.; Stach, E. A.; Yang, J. C.; Strasser, P.; Cuenya, B. R. Highly Selective Plasma-Activated Copper Catalysts for Carbon Dioxide Reduction to Ethylene. *Nat. Commun.* **2016**, *7* (1), 1–9. https://doi.org/10.1038/ncomms12123.

(9) Hori, Y.; Kikuchi, K.; Suzuki, S. PRODUCTION OF CO AND CH 4 IN ELECTROCHEMICAL REDUCTION OF CO 2 AT METAL ELECTRODES IN AQUEOUS HYDROGENCARBONATE SOLUTION . *Chem. Lett.* **1985**, *14* (11), 1695–1698. https://doi.org/10.1246/cl.1985.1695.

(10) Saxena, A.; Liyanage, W.; Masud, J.; Kapila, S.; Nath, M. Selective Electroreduction of CO2 to Carbon-Rich Products by Simple Binary Copper Selenide Electrocatalyst. *J. Mater. Chem. A* **2021**. https://doi.org/10.1039/d0ta11518e.

(11) Nath, M.; Singh, H.; Saxena, A. Progress of Transition Metal Chalcogenides as Efficient Electrocatalysts for Energy Conversion. *Curr. Opin. Electrochem.* **2022**, 100993. https://doi.org/10.1016/J.COELEC.2022.100993.

(12) De Gregorio, G. L.; Burdyny, T.; Loiudice, A.; Iyengar, P.; Smith, W. A.; Buonsanti, R. Facet-Dependent Selectivity of Cu Catalysts in Electrochemical CO2 Reduction at Commercially Viable Current Densities. *ACS Catal.* **2020**, *10* (9), 4854–4862. https://doi.org/10.1021/acscatal.0c00297.

(13) Li, Y.; Cui, F.; Ross, M. B.; Kim, D.; Sun, Y.; Yang, P. Structure-Sensitive CO2 Electroreduction to Hydrocarbons on Ultrathin 5-Fold Twinned Copper Nanowires. *Nano Lett.* **2017**, *17* (2), 1312–1317. https://doi.org/10.1021/acs.nanolett.6b05287.

(14) Liu, S.; Huang, S. Size Effects and Active Sites of Cu Nanoparticle Catalysts for CO 2 Electroreduction. *Appl. Surf. Sci.* **2019**, *475*, 20–27. https://doi.org/10.1016/j.apsusc.2018.12.251.

(15) Chen, K.; Ling, J.; Wu, C. In Situ Generation and Stabilization of Accessible Cu/Cu $_2$ O Heterojunctions inside Organic Frameworks for Highly Efficient Catalysis. *Angew. Chemie Int. Ed.* **2020**, *59* (5), 1925–1931. https://doi.org/10.1002/anie.201913811.

(16) Lin, S. C.; Chang, C. C.; Chiu, S. Y.; Pai, H. T.; Liao, T. Y.; Hsu, C. S.; Chiang, W. H.; Tsai, M. K.; Chen, H. M. Operando Time-Resolved X-Ray Absorption Spectroscopy Reveals the Chemical Nature Enabling Highly Selective CO_2 Reduction. *Nat. Commun.* **2020**, *11* (1), 1–12. https://doi.org/10.1038/s41467-020-17231-3.

(17) Singh, A. K.; Mukherjee, R. Cobalt(Ii) and Cobalt(Iii) Complexes of Thioether-Containing Hexadentate Pyrazine Amide Ligands: C–S Bond Cleavage and Cyclometallation Reaction. *J. Chem. Soc. Dalt. Trans.* **2008**, No. 2, 260–270. https://doi.org/10.1039/b709901k.

(18) Nath, M.; De Silva, U.; Singh, H.; Perkins, M.; Liyanage, W. P. R.; Umapathi, S.; Chakravarty, S.; Masud, J. Cobalt Telluride: A Highly Efficient Trifunctional Electrocatalyst for Water Splitting and Oxygen Reduction. *ACS Appl. Energy Mater.* **2021**, *4* (8), 8158–8174. https://doi.org/10.1021/ACSAEM.1C01438/SUPPL_FILE/AE1C01438_SI_001.PDF.

(19) Sheng, H.; Frei, H. Direct Observation by Rapid-Scan FT-IR Spectroscopy of Two-Electron-Reduced Intermediate of Tetraaza Catalyst [CoIIN4H(MeCN)]2+ Converting CO2 to CO. *J. Am. Chem. Soc.* **2016**, *138* (31), 9959–9967. https://doi.org/10.1021/jacs.6b05248.

(20) Iablokov, V.; Beaumont, S. K.; Alayoglu, S.; Pushkarev, V. V.; Specht, C.; Gao, J.; Alivisatos, A. P.; Kruse, N.; Somorjai, G. A. Size-Controlled Model Co Nanoparticle Catalysts for CO 2 Hydrogenation: Synthesis, Characterization, and Catalytic Reactions. *Nano Lett.* **2012**, *12* (6), 3091–3096. https://doi.org/10.1021/nl300973b.

(21) Bernal, M.; Bagger, A.; Scholten, F.; Sinev, I.; Bergmann, A.; Ahmadi, M.; Rossmeisl, J.; Cuenya, B. R. CO2 Electroreduction on Copper-Cobalt Nanoparticles: Size and Composition Effect. *Nano Energy* **2018**, *53*, 27–36. https://doi.org/10.1016/j.nanoen.2018.08.027.

(22) Nafria, R.; Genç, A.; Ibáñez, M.; Arbiol, J.; Ramírez De La Piscina, P.; Homs, N.; Cabot, A. Co-Cu Nanoparticles: Synthesis by Galvanic Replacement and Phase Rearrangement during Catalytic Activation. *Langmuir* **2016**, *32* (9), 2267–2276. https://doi.org/10.1021/acs.langmuir.5b04622.

(23) Gao, S.; Lin, Y.; Jiao, X.; Sun, Y.; Luo, Q.; Zhang, W.; Li, D.; Yang, J.; Xie, Y. Partially Oxidized Atomic Cobalt Layers for Carbon Dioxide Electroreduction to Liquid Fuel. *Nature* **2016**, *529* (7584), 68–71. https://doi.org/10.1038/nature16455.

(24) Hu, X.-M.; Rønne, M. H.; Pedersen, S. U.; Skrydstrup, T.; Daasbjerg, K. Enhanced Catalytic Activity of Cobalt Porphyrin in CO_2 Electroreduction upon Immobilization on Carbon Materials. *Angew. Chemie Int. Ed.* **2017**, *56* (23), 6468–6472. https://doi.org/10.1002/anie.201701104.

(25) Marianov, A. N.; Kochubei, A. S.; Roman, T.; Conquest, O. J.; Stampfl, C.; Jiang, Y. Resolving Deactivation Pathways of Co Porphyrin-Based Electrocatalysts for CO_2 Reduction in Aqueous Medium. *ACS Catal.* **2021**, *11* (6), 3715–3729. https://doi.org/10.1021/acscatal.0c05092.

(26) Yu, H.; Cao, D.; Fisher, A.; Johnston, R. L.; Cheng, D. Size Effect on the Adsorption and Dissociation of CO 2 on Co Nanoclusters. *Appl. Surf. Sci.* **2017**, *396*, 539–546. https://doi.org/10.1016/j.apsusc.2016.10.192.

(27) Mu, Q.; Zhu, W.; Yan, G.; Lian, Y.; Yao, Y.; Li, Q.; Tian, Y.; Zhang, P.; Deng, Z.; Peng, Y. Activity and Selectivity Regulation through Varying the Size of Cobalt Active Sites in Photocatalytic CO2 Reduction. *J. Mater. Chem. A* **2018**, *6* (42), 21110–21119. https://doi.org/10.1039/c8ta06151c.

(28) Wannakao, S.; Jumpathong, W.; Kongpatpanich, K. Tailoring Metalloporphyrin Frameworks for an Efficient Carbon Dioxide Electroreduction: Selectively Stabilizing Key Intermediates with H-Bonding Pockets. *Inorg. Chem.* **2017**, *56* (12), 7200–7209. https://doi.org/10.1021/acs.inorgchem.7b00839.

(29) Kresse, G.; Furthmüller, J. Efficient Iterative Schemes for Ab Initio Total-Energy Calculations Using a Plane-Wave Basis Set. *Phys. Rev. B - Condens. Matter Mater. Phys.* **1996**, *54* (16), 11169–11186. https://doi.org/10.1103/PhysRevB.54.11169.

(30) Kresse, G.; Furthmüller, J. Efficiency of Ab-Initio Total Energy Calculations for Metals and Semiconductors Using a Plane-Wave Basis Set. *Comput. Mater. Sci.* **1996**, *6* (1), 15–50. https://doi.org/10.1016/0927-0256(96)00008-0.

(31) Kresse, G.; Hafner, J. Ab Initio Molecular-Dynamics Simulation of the Liquid-Metalamorphous- Semiconductor Transition in Germanium. *Phys. Rev. B* **1994**, *49* (20), 14251–14269. https://doi.org/10.1103/PhysRevB.49.14251.

(32) Kresse, G.; Hafner, J. Ab Initio Molecular Dynamics for Liquid Metals. *Phys. Rev. B* **1993**, *47* (1), 558–561. https://doi.org/10.1103/PhysRevB.47.558.

(33) Dudarev, S. L.; Botton, G. A.; Savrasov, S. Y.; Humphreys, C. J.; Sutton, A. P. Electron-Energy-Loss Spectra and the Structural Stability of Nickel Oxide: An LSDA+U Study. *Phys. Rev. B* **1998**, *57* (3), 1505. https://doi.org/10.1103/PhysRevB.57.1505.

(34) Cao, X.; Medvedeva, J. E.; Nath, M. Copper Cobalt Selenide as a High-Efficiency Bifunctional Electrocatalyst for Overall Water Splitting: Combined Experimental and Theoretical Study. *ACS Appl. Energy Mater.* **2020**, *3* (3), 3092–3103. https://doi.org/10.1021/ACSAEM.0C00262/ASSET/IMAGES/LARGE/AE0C00262_0009.JPEG.

(35) Holzwarth, U.; Gibson, N. The Scherrer Equation versus the "Debye-Scherrer Equation." *Nature Nanotechnology*. Nature Publishing Group August 28, 2011, p 534. https://doi.org/10.1038/nnano.2011.145.

(36) Masud, J.; Swesi, A. T.; Liyanage, W. P. R.; Nath, M. Cobalt Selenide Nanostructures: An Efficient Bifunctional Catalyst with High Current Density at Low Coverage. *ACS Appl. Mater. Interfaces* **2016**, *8* (27), 17292–17302. https://doi.org/10.1021/ACSAMI.6B04862.

(37) Masud, J.; Liyanage, W. P. R.; Cao, X.; Saxena, A.; Nath, M. Copper Selenides as High-Efficiency Electrocatalysts for Oxygen Evolution Reaction. *ACS Appl. Energy Mater.* **2018**, *1* (8), 4075–4083. https://doi.org/10.1021/acsaem.8b00746.

(38) Chauhan, M.; Reddy, K. P.; Gopinath, C. S.; Deka, S. Copper Cobalt Sulfide Nanosheets Realizing a Promising Electrocatalytic Oxygen Evolution Reaction. *ACS Catal.* **2017**, *7* (9), 5871–5879. https://doi.org/10.1021/ACSCATAL.7B01831.

(39) Chen, H.; Chen, S.; Fan, M.; Li, C.; Chen, D.; Tian, G.; Shu, K. Bimetallic Nickel Cobalt Selenides: A New Kind of Electroactive Material for High-Power Energy Storage. *J. Mater. Chem. A* **2015**, *3* (47), 23653–23659. https://doi.org/10.1039/C5TA08366D.

(40) Sun, Z.; Ma, T.; Tao, H.; Fan, Q.; Han, B. Fundamentals and Challenges of Electrochemical CO2 Reduction Using Two-Dimensional Materials. *Chem*. Elsevier Inc October 12, 2017, pp 560–587. https://doi.org/10.1016/j.chempr.2017.09.009.

(41) Dong, X.; Yu, Y.; Jing, X.; Jiang, H.; Hu, T.; Meng, C.; Huang, C.; Zhang, Y. Sandwich-like Honeycomb Co2SiO4/RGO/Honeycomb Co2SiO4 Structures with Enhanced Electrochemical Properties for High-Performance Hybrid Supercapacitor. *J. Power Sources* **2021**, *492*, 229643. https://doi.org/10.1016/J.JPOWSOUR.2021.229643.

(42) Yang, D.; Zhu, Q.; Chen, C.; Liu, H.; Liu, Z.; Zhao, Z.; Zhang, X.; Liu, S.; Han, B. Selective Electroreduction of Carbon Dioxide to Methanol on Copper Selenide Nanocatalysts. *Nat. Commun.* **2019**, *10* (1), 1–9. https://doi.org/10.1038/s41467-019-08653-9.

(43) Hansen, H. A.; Varley, J. B.; Peterson, A. A.; Nørskov, J. K. Understanding Trends in the Electrocatalytic Activity of Metals and Enzymes for CO2 Reduction to CO. *J. Phys. Chem. Lett.* **2013**, *4* (3), 388–392. https://doi.org/10.1021/jz3021155.

V. PROGRESS OF TRANSITION METAL CHALCOGENIDES AS EFFICIENT ELECTROCATALYSTS FOR ENERGY CONVERSION

Manashi Nath[a]*, Harish Singh[a#] Apurv Saxena[a#]

[a]Department of Chemistry, Missouri University of Science & Technology, Rolla, MO 65409, USA.

[#]Equal contribution.

ABSTRACT

The continuous excessive usage of fossil fuels has resulted in its fast depletion leading to an escalating energy crisis as well as several environmental issues leading to increased research towards sustainable energy conversion. Electrocatalysts play crucial role in the development of numerous novel energy conversion devices including fuel cells and solar fuel generators. In particular, high-efficiency and cost-effective catalysts are required for large-scale implementation of these new devices. Over the last few years transition metal chalcogenides have emerged as highly efficient electrocatalysts for several electrochemical devices such as water splitting, carbon dioxide electroreduction and, solar energy converters. These transition metal chalcogenides exhibit high electrochemical tunability, abundant active sites and superior electrical conductivity. Hence, they have been actively explored for various electrocatalytic activities. Herein, we have provided comprehensive review of transition-metal chalcogenide electrocatalysts for hydrogen evolution, oxygen evolution, and carbon dioxide reduction and illustrated structure-property correlation that increases their catalytic activity.

1. INTRODUCTION

The family of transition metal chalcogenides has attracted tremendous attention in the materials community due to its promising future in sensors, energy conversion and energy storage among other applications.[1–5] In addition, transition metal based electrocatalysts for electrochemical energy conversion has attracted significant attention during last several years owing to their high activity, low cost and facile tunability. Among these electrocatalytic water splitting which includes hydrogen evolution and oxygen evolution reactions (HER and OER, respectively) has been the focus of major research activity.[1,6] The challenge for practical implementation of water splitting technology, however, depends on identification of suitable and stable catalysts which can lower reaction energy barrier and increase Faraday efficiency for both reactions. Traditionally, Pt metal is most active as HER catalyst, whereas oxides of iridium (Ir), and ruthenium (Ru), exhibit higher OER performance. However, high price and low stability of these precious metal-based catalysts make commercialization difficult. Transition metal-based chalcogenides (TMCs) have recently shown unprecedented high efficiency for HER and OER in wide range of pH. Apart from water splitting, recently TMCs have also shown tremendous success in electrocatalytic CO_2 reduction (CO2RR). Continuous dependence on fossil fuels for several decades had led to accumulation of high levels of CO_2 which has led to several catastrophic environmental effects threatening well-being of mankind. One of the prime objectives of researchers is to develop technologies that can convert CO_2 to useful products thereby closing the carbon loop. Transition metal based compounds have been specially attractive for such CO_2 utilization technologies, among which the

chalcogenides offer special advantage owing to their selectivity towards forming value-added carbon-rich reduction products.[7–11]

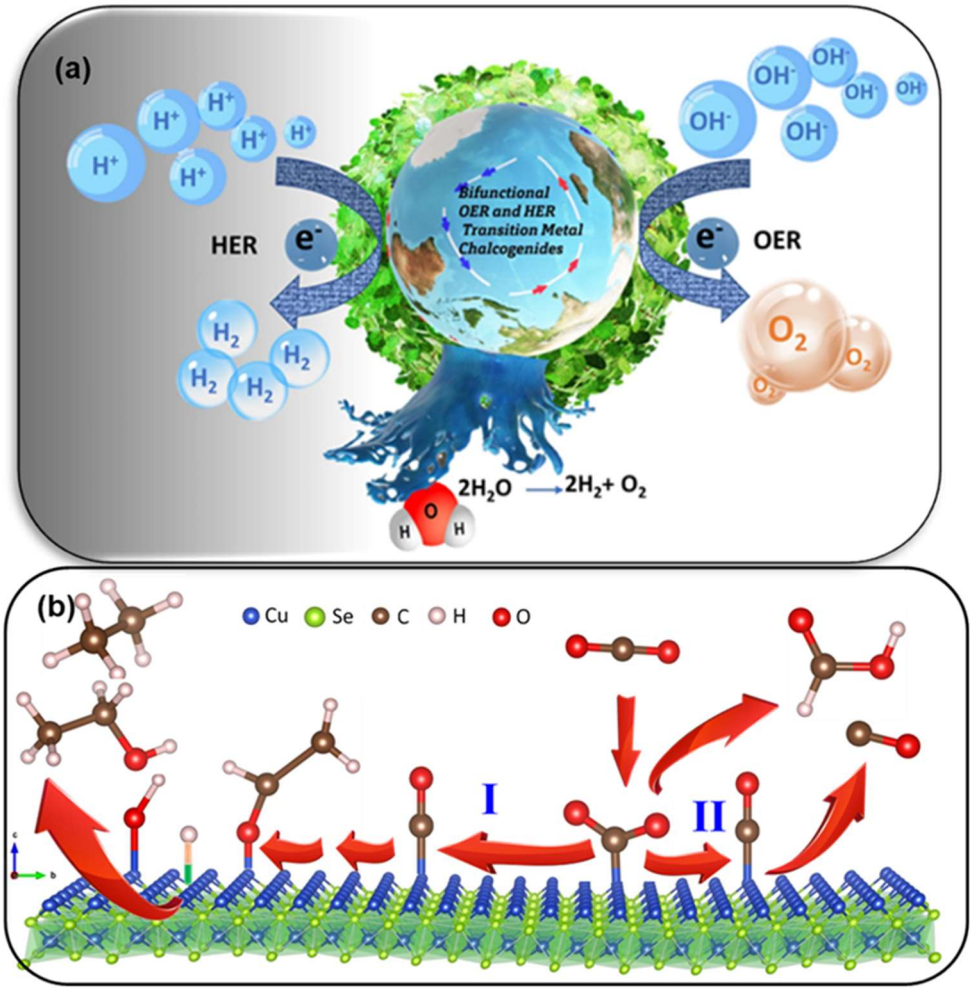

Figure 1. Schematic Illustration of the TMC electrocatalysts (a). for overall water splitting reaction (HER and OER). (b). for CO_2 reduction on catalyst surface proceeding via multi-step electron transfer reaction pathways. The catalyst surface modeled after Cu_2Se also illustrates the importance of catalyst design, whereby increasing intermediate *CO dwell time on the surface (strong adsorption) can lead to Pathway I being more predominant resulting in carbon-rich reduction products. Weak adsorption of *CO on the other hand leads to predominance of Pathway II and ready desorption of CO and HCOOH as products.

In this perspective we will highlight recent progress made in transition metal chalcogenides based electrocatalysts for water splitting and CO2RR and discuss the reasons behind their high activity (Figure 1).

2. TRANSITION METAL CHALCOGENIDES FOR CO_2 ELECTROREDUCTION

Research on electrocatalytic conversion of CO2 has evolved over past few years with respect to developing catalyst composition with special emphasis on achieving selectivity for the reduction products.[7–11] In the following section we will discuss first about Cu- and other transition metal based catalyst and then focus on transition metal chalcogenides. We will highlight new CO2RR catalysts which will provide fundamental understanding of catalytic processes to achieve product selectivity, that can be helpful for development of efficient CO2RR catalysts in future. From early on transition-based electrocatalysts have been proved as efficient candidates for CO2RR in commercial devices.[80] They have the ability to convert CO2 into variety of hydrocarbons with good faradaic efficiency. While CO2 conversion is of utmost importance to reduce atmospheric levels of this greenhouse gas, production of carbon monoxide, i.e., CO as the reduction product does not really mitigate the problem, since CO itself is a toxic gas. The produced CO, hence, needs to be further processed to other carbonaceous product with higher value. Ongoing research is based on improving selectivity for value-added carbon-rich products. It was hypothesized that adsorption energy of intermediate *CO on the transition metal site played a critical role in influencing product composition and selectivity.[7] Specifically, catalysts with smaller adsorption *CO adsorption energy led to preferential formation of

CO and formic acid as the reduction product (Figure 3(a)). Catalysts with significantly larger *CO adsorption energy, on the other hand, exhibited surface poisoning with CO. Hence, recent efforts have been guided towards designing catalyst compositions that will have *CO adsorption energy in the moderate range as shown in Figure 3(a). Since metal-to-ligand back bonding plays a major role in deciding binding of intermediate *CO to the transition metal site, optimizing *CO adsorption energy has been attempted by modulating d-electron density near the transition metal site through investigating different transition metals and changing anion coordination. The following sections compile various CO2RR catalysts that has been reported based on their d-electron density, and also highlights the correlation of *CO adsorption energy with product selectivity as has been studied in chalcogenide-based catalysts.

2.1. COPPER AND OTHER TRANSITION METAL CATALYSTS

Copper was found to have enhanced activity towards CO2RR producing at least 16 different C1–C3 hydrocarbon/oxygenate products which is better than other metals but the selectivity was not attained towards a specific product.[81] Other transition metals such as Au,[82][83–86] Ag, [81][87,88] Pd,[89] Co,[90][11] Zn,[11][91][92] led to formation of CO as the major product of CO2 reduction. Similarly, other metal catalysts like Pb,[93] In,[94] Sn,[89][95] and Bi,[96,97] also led to formation of CO predominantly. Polycrystalline Ag is known for producing CO with Faradaic efficiency (FE) of 22.4% at −0.8 VRHE.[11] DFT based studies revealed that most of these metal catalysts had a weak binding energy towards CO, which led to weaker adsorption and formation of CO as major

product. Therefore, there was a need to modify transition metals like Cu and other metals to get better selectivity for C2+ products.

2.2. TRANSITION METAL CHALCOGENIDES

2.2.1. Copper Chalcogenides and Other Transition Metals with d^5-d^{10} Electrons. It has been proposed that chalcogenide anions increased lattice covalency owing to their decreased electronegativity, which led to enrichment of d-electron density near the transition metal site.[16] Hence, it was expected that chalcogenides will show better *CO adsorption energy leading to better selectivity of C2 products.[7,98][91] Indeed DFT calculation revealed that Cu-selenides showed better *CO adsorption energy compared to the base metal and its oxide as shown in Figure 3(a). Experimental studies also confirms that chalcogens favors the formation of C2 products and deters the formation of C1 products because of decrease in surface concentration of CO.[11][91] Investigation of various Cu-based catalysts such as Cu, Cu-oxide, Cu-sulfide and Cu-selenide catalysts, revealed that selectivity towards certain carbon products increased with Cu-chalcogenides compared to Cu. This fact can be proven by comparing polycrystalline Cu,[99][91] and CuS having HCOOH product with FE= 80% at −0.8 VRHE[91], 3D- Cu_2S showing improved performance with a FE=87.3% at −0.9 VRHE,[100] while, Cu_2Se nanocubes,[7] and $Cu_{1.63}Se$ nanowires,[101] $Cu_{1.8}Se$ nanowires,[11] showed a high C2 product selectivity. In case of other transition metals also chalcogenides showed improved activity and selectivity.

FeS_2/NiS showed very good performance in reduction of CO_2 to form CH_3OH with overpotential of 280 mV and Faradaic efficiency of 64%.[102] Using molecular

engineering, iron porphyrin was synthesized which showed good activity achieving 98% Faradaic efficiency for CO production.[11] Cobalt Phthalocyanine with pyridyl moieties as axial ligands achieved 70% FE towards CO production.[82] This study showed that upon axial coordination to CoPc, catalytic activity towards CO2RR improved due to energy level rise of dz^2 orbital.[103]

When Ag was modified by sulfur to form Ag_2S, selectivity improved to 92.0% at very low overpotential (−0.754 V).[82][104] Zn has shown limited activity towards CO2RR.[105] Zn nanosheets exhibit Faradaic efficiency of 70.9% when producing CO from CO_2 electrochemical reduction. Upon modification with sulfur to make ZnS/Zn, the FE increased to 94.2%.[106] ZnTe is also an efficient catalyst to photochemically convert CO_2.[107] Similarly Cd also changes selectivity from formic acid to CO when it is converted to CdS.[74] CdS showed good stability of 40+ hours and 95% FE towards CO during CO2RR.[11] Sn is also known to be an active metal towards CO2RR often modulated by surface structure. Modifications like change in particle size,[108] oxide layer thickness,[109] morphology,[110] and electrolyte's pH have improved the activity, selectivity, energetic efficiency, and robustness of tin-based catalysts.[111,112] As reported in the study, tin oxide (SnOx) layer was found to be active because $CO_2^{\bullet-}$ intermediate adheres better to the catalyst surface, and oxide layer suppresses the competing hydrogen evolution reaction.[113,114] The catalytic efficiency was improved further by converting SnOx to $SnSe_2$ which balances the binding strength of $CO_2^{\bullet-}$ intermediates and also improves conductivity as compared to oxide layer.[115] The electronic conductivity of metal selenides was found to be better due to higher electronegativity of oxygen than selenium. This also leads to the fast charge transfer during

catalytic activity.[115] Hence, $SnSe_2$ showed high current density (12.0 mA cm^{-2}) and high FE (88.4%) at very low potential (−0.76 V vs RHE) for CO2RR.[115]

2.3. TRANSITION METAL WITH D1-D3 ELECTRONS

Liu et al. showed that ultrathin $MoTe_2$ layers can reduce CO_2 to CH_4 with faradaic efficiency of 83 % with extended stability of 45 hours. Ultrathin layers lead to highly efficient mass transport due to layered structure which makes active sites available and improves CO_2 electrochemical reduction.[116] To improve conductivity and number of active sites two-dimensional (2D) $MoSe_2$ doped transition metals (Fe, Co, Ni and Cu) were explored using density functional theory (DFT) calculations. Cu doped $MoSe_2$ was found to potentially have great activity for methane production.[117] WSe_2 nanoflakes show activity towards CO2RR at very low overpotential of 0.054 V forming CO as main product (FE=24%).[82]

3. PERSPECTIVE AND FUTURE OUTLOOK

Transition metal chalcogenides have gained considerable attraction in the last few years as electrocatalysts for various electrochemical energy conversion processes owing to their tunable electrochemical properties, structural richness, enhanced charge transfer ability, and possibility of tuning electron density at the catalytic center through doing and vacancy ordering. In this review we have highlighted their high activity for electrocatalytic water splitting and CO_2 electroreduction. Various binary and multinary metal

chalcogenides catalysts have been reported for OER with significantly improved catalytic performance compared to the state-of-the-art precious metal based oxides.

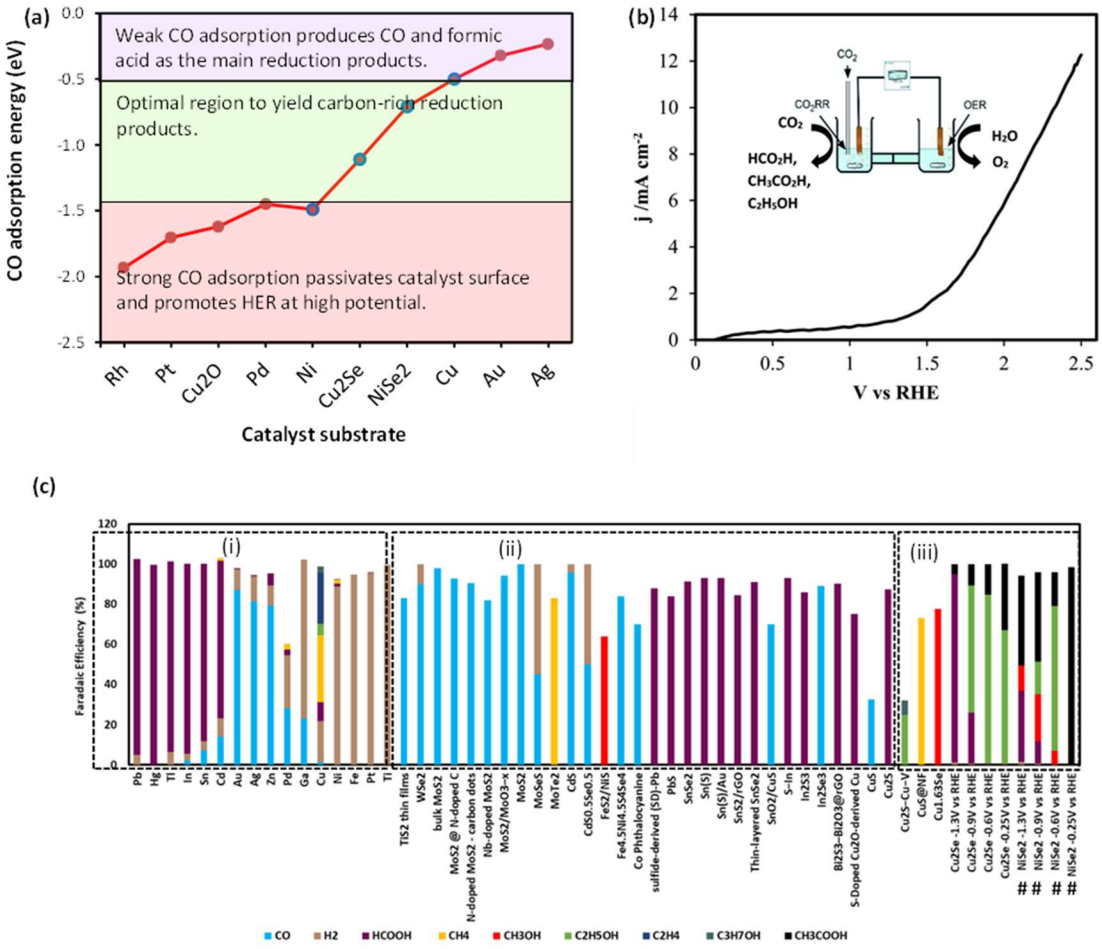

Figure 2. Experimental and theoretical studies (a) Comparison of the *CO adsorption energy calculated on various catalyst surfaces estimated from DFT calculations. (b) Experimental setup for comprehensive CO2RR-OER electrochemical cell comprising cathodic CO2RR and anodic OER with Cu_2Se as both the cathodic and the anodic electrocatalyst. (c) Benchmarking of CO2RR activity of various metal chalcogenide electrocatalysts highlighting the various reduction products formed.

In particular, these catalysts exhibited low η10 overpotentials primarily due to facile catalyst activation through enhanced electrochemical tunability of the transition metal center, which is facilitated by the lower electronegativity and higher covalency of the chalcogenide anions. These semiconducting TMCs also have a high potential for use in solar water splitting due to their ideal band gap and acceptable band-edge positions that aligns well with both water reduction and oxidation potentials. Transition metal dichalcogenides (TMDCs) were previously investigated as potential candidates for photoelectrodes with efficiencies of up to 17% when illuminated in acidic solutions utilizing n-type single crystals.[28–30] Coupling these transition metal chalcogenide electrocatalysts with efficient photoabsorbers to create a hybrid module will lead to significant advances in solar water splitting, by combining low overpotential and functional stability of the electrocatalysts with efficient solar energy capture.

Interestingly, the transition metal chalcogenides function as highly efficient electrocatalysts for CO_2 electroreduction, producing carbon-rich products with high selectivity. Such capability makes these TMS highly applicable for CO_2 utilization which has become an issue of prime interest to reduce carbon footprint of industrial processes. In this review, we have discussed the fundamental issues related to formation of carbon-rich product from CO_2 electroreduction and its relationship with the underlying chemical reactions on the catalyst surface. By comparing the product formation on various catalyst surfaces it was observed that *CO dwell time on the surface can be used as an appropriate descriptor for tuning the product composition. The *CO dwell time depends on the CO adsorption energy on the catalytic site. Comparison of the CO adsorption energy on various catalyst surfaces showed that weak adsorption energy (leading to less *CO dwell time)

resulted in C1 products, whereas very high adsorption energy leads to indefinite stay of *CO on the surface and catalyst poisoning as seen in Ni, Pd and Pt. This observation offers insight into designing an optimal catalyst surface where the CO adsorption energy should be in the middle range as shown in Figure 3(a) to yield predominantly C2+ products. Tuning anion electronegativity and changing the transition metal center can lead to such optimal *CO adsorption energy as is shown in the benchmark Figure 3(c). The section marked as (i) and (ii) in Figure 3(c) shows catalysts producing mainly C1 products and H_2, wherein, (i) represents the base metals, while (ii) contains the binary and ternary compounds. This can be attributed to lower *CO adsorption energy. Section (iii) represents catalysts that can produce C2+ products. Hence, future outlook for effective CO_2 reduction electrocatalysts with high selectivity for carbon-rich product involves designing the catalyst surface that can facilitate metal-ligand (CO) back-bonding by aligning the metal d-orbitals with the ligand (CO) π^* orbitals, leading to better CO dwell time on the surface and optimal *CO adsorption energy. Such catalysts can have significant effect on CO_2 utilization by forming value-added chemicals and fuels from waste CO_2.

Several of these TMCs have shown efficient catalytic activity for both anodic and cathodic processes such as OER-HER and OER-CO2RR, respectively, making them suitable as bifunctional electrocatalyst. Among these, the OER-CO2RR bifunctional activity is useful, since such electrocatalytic cell (as shown in Figure 3 (b)), can essentially reduce atmospheric CO_2 to value-added carbon-rich products while enriching O_2 in the atmosphere.[7] Such electrochemical setup has also been used to carry out more economical oxidation processes such as methanol oxidation, ethanol oxidation, urea oxidation etc. [125][126] It will be interesting to explore such electrocatalytic activity for

TMCs. Such bifunctional activity can be lucrative for practical industrial applications since it has minimum energy expense and the total cell potential for this Methanol oxidation/OER-CO2RR electrolytic cell is lower than combination of individual processes.

REFERENCES

[1] M. Nath, U. De Silva, H. Singh, M. Perkins, W.P.R. Liyanage, S. Umapathi, S. Chakravarty, J. Masud, Cobalt Telluride: A Highly Efficient Trifunctional Electrocatalyst for Water Splitting and Oxygen Reduction, ACS Appl. Energy Mater. (2021) acsaem.1c01438. https://doi.org/10.1021/ACSAEM.1C01438.

[2] H. Singh, J. Bernabe, J. Chern, M. Nath, Copper selenide as multifunctional non-enzymatic glucose and dopamine sensor, J. Mater. Res. 36 (2021) 1413–1424. https://doi.org/10.1557/s43578-021-00227-0.

[3] S. Umapathi, H. Singh, J. Masud, M. Nath, Nanostructured copper selenide as an ultrasensitive and selective non - enzymatic glucose sensor, Mater. Adv. (2020). https://doi.org/10.1039/D0MA00890G.

[4] B.G. Amin, J. Masud, M. Nath, Facile one-pot synthesis of $NiCo_2Se_4$-rGO on Ni foam for high performance hybrid supercapacitors, RSC Adv. 9 (2019) 37939–37946. https://doi.org/10.1039/c9ra06439g.

[5] J. Masud, W.P.R. Liyanage, X. Cao, A. Saxena, M. Nath, Copper Selenides as High-Efficiency Electrocatalysts for Oxygen Evolution Reaction, ACS Appl. Energy Mater. 1 (2018) 4075–4083. https://doi.org/10.1021/acsaem.8b00746.

[6] X. Cao, J.E. Medvedeva, M. Nath, Copper Cobalt Selenide as a High-Efficiency Bifunctional Electrocatalyst for Overall Water Splitting: Combined Experimental and Theoretical Study, ACS Appl. Energy Mater. 3 (2020) 3092–3103. https://doi.org/10.1021/ACSAEM.0C00262/SUPPL_FILE/AE0C00262_SI_001.PDF.

[7] A. Saxena, W. Liyanage, J. Masud, S. Kapila, M. Nath, Selective electroreduction of CO_2 to carbon-rich products with a simple binary copper selenide electrocatalyst, J. Mater. Chem. A. 9 (2021) 7150–7161. https://doi.org/10.1039/D0TA11518E.

[8] G. Wang, J. Chen, Y. Ding, P. Cai, L. Yi, Y. Li, C. Tu, Y. Hou, Z. Wen, L. Dai, Electrocatalysis for CO2 conversion: from fundamentals to value-added products, Chem. Soc. Rev. 50 (2021) 4993–5061. https://doi.org/10.1039/D0CS00071J.

[9] C. Zhu, D. Gao, J. Ding, D. Chao, J. Wang, TMD-based highly efficient electrocatalysts developed by combined computational and experimental approaches, Chem. Soc. Rev. 47 (2018) 4332–4356. https://doi.org/10.1039/C7CS00705A.

[10] H. Xie, T. Wang, J. Liang, Q. Li, S. Sun, Cu-based nanocatalysts for electrochemical reduction of CO_2, Nano Today. 21 (2018) 41–54. https://doi.org/10.1016/J.NANTOD.2018.05.001.

[11] X. Shao, X. Zhang, Y. Liu, J. Qiao, X.D. Zhou, N. Xu, J.L. Malcombe, J. Yi, J. Zhang, Metal chalcogenide-associated catalysts enabling CO_2 electroreduction to produce low-carbon fuels for energy storage and emission reduction: catalyst structure, morphology, performance, and mechanism, J. Mater. Chem. A. 9 (2021) 2526–2559. https://doi.org/10.1039/D0TA09232K.

[12] Z. Kang, H. Guo, J. Wu, X. Sun, Z. Zhang, Q. Liao, S. Zhang, H. Si, P. Wu, L. Wang, Y. Zhang, Z. Kang, H. Guo, J. Wu, X. Sun, Z. Zhang, Q. Liao, S. Zhang, H. Si, P. Wu, Y. Zhang, L. Wang, Engineering an Earth-Abundant Element-Based Bifunctional Electrocatalyst for Highly Efficient and Durable Overall Water Splitting, Adv. Funct. Mater. 29 (2019) 1807031. https://doi.org/10.1002/ADFM.201807031.

[13] K.S. Bhat, H.S. Nagaraja, Recent trends and insights in nickel chalcogenide nanostructures for water-splitting reactions, Https://Doi.Org/10.1080/14328917.2019.1703523. 25 (2019) 29–52. https://doi.org/10.1080/14328917.2019.1703523.

[14] H. Singh, M. Marley-Hines, S. Chakravarty, M. Nath, Multi-walled carbon nanotube supported Manganese Selenide as Highly Active Bifunctional OER and ORR electrocatalyst, J. Mater. Chem. A. 6 (2022) 4883–5230. https://doi.org/10.1039/D1TA09864K.

[15] K. Xu, H. Ding, H. Lv, S. Tao, P. Chen, X. Wu, W. Chu, C. Wu, Y. Xie, Understanding Structure-Dependent Catalytic Performance of Nickel Selenides for Electrochemical Water Oxidation, ACS Catal. 7 (2017) 310–315. https://doi.org/10.1021/ACSCATAL.6B02884/SUPPL_FILE/CS6B02884_SI_001.PDF.

[16] U. De Silva, J. Masud, N. Zhang, Y. Hong, W.P.R. Liyanage, M. Asle Zaeem, M. Nath, Nickel telluride as a bifunctional electrocatalyst for efficient water splitting in alkaline medium, J. Mater. Chem. A. 6 (2018) 7608–7622. https://doi.org/10.1039/c8ta01760c.

[17] C. Panda, P.W. Menezes, C. Walter, S. Yao, M.E. Miehlich, V. Gutkin, K. Meyer, M. Driess, From a Molecular 2Fe-2Se Precursor to a Highly Efficient Iron Diselenide Electrocatalyst for Overall Water Splitting, Angew. Chemie - Int. Ed. 56 (2017) 10506–10510. https://doi.org/10.1002/ANIE.201706196.

[18] S. Wan, W. Jin, X. Guo, J. Mao, L. Zheng, J. Zhao, J. Zhang, H. Liu, C. Tang, Self-Templating Construction of Porous $CoSe_2$ Nanosheet Arrays as Efficient Bifunctional Electrocatalysts for Overall Water Splitting, ACS Sustain. Chem. Eng. 6(2018)15374–15382. https://doi.org/10.1021/ACSSUSCHEMENG.8B03804/SUPPL_FILE/SC8B03804_SI_001.PDF.

[19] B. Chakraborty, R. Beltrán-Suito, V. Hlukhyy, J. Schmidt, P.W. Menezes, M. Driess, Crystalline Copper Selenide as a Reliable Non-Noble Electro(pre)catalyst for Overall Water Splitting, ChemSusChem. 13 (2020) 3222–3229. https://doi.org/10.1002/CSSC.202000445.

[20] L. Tao, M. Huang, S. Guo, Q. Wang, M. Li, X. Xiao, G. Cao, Y. Shao, Y. Shen, Y. Fu, M. Wang, Surface modification of $NiCo_2Te_4$ nanoclusters: a highly efficient electrocatalyst for overall water-splitting in neutral solution, Appl. Catal. B Environ. 254 (2019) 424–431. https://doi.org/10.1016/J.APCATB.2019.05.010.

[21] S. Poorahong, D.J. Harding, S. Keawmorakot, M. Siaj, Free standing bimetallic nickel cobalt selenide nanosheets as three-dimensional electrocatalyst for water splitting, J. Electroanal. Chem. 897 (2021) 115568. https://doi.org/10.1016/J.JELECHEM.2021.115568.

[22] X. Hu, Q. Zhou, P. Cheng, S. Su, X. Wang, X. Gao, G. Zhou, Z. Zhang, J. Liu, Nickel-iron selenide polyhedral nanocrystal with optimized surface morphology as a high-performance bifunctional electrocatalyst for overall water splitting, Appl. Surf. Sci. 488 (2019) 326–334. https://doi.org/10.1016/j.apsusc.2019.05.220.

[23] X. Cao, Y. Hong, N. Zhang, Q. Chen, J. Masud, M.A. Zaeem, M. Nath, Phase Exploration and Identification of Multinary Transition-Metal Selenides as High-Efficiency Oxygen Evolution Electrocatalysts through Combinatorial Electrodeposition, ACS Catal. 8 (2018) 8273–8289. https://doi.org/10.1021/ACSCATAL.8B01977/SUPPL_FILE/CS8B01977_SI_001.PDF.

[24] X. Cao, E. Johnson, M. Nath, Expanding Multinary Selenide Based High-Efficiency Oxygen Evolution Electrocatalysts through Combinatorial Electrodeposition: Case Study with Fe-Cu-Co Selenides, ACS Sustain. Chem. Eng. 7 (2019) 9588–9600. https://doi.org/10.1021/acssuschemeng.9b01095.

[25] X. Cao, E. Johnson, M. Nath, identifying high-efficiency oxygen evolution electrocatalysts from Co–Ni–Cu based selenides through combinatorial electrodeposition, J. Mater. Chem. A. 7 (2019) 9877–9889. https://doi.org/10.1039/C9TA00863B.

[26] M. Cao, H. Wang, P. Kannan, S. Ji, X. Wang, Q. Zhao, V. Linkov, R. Wang, Highly efficient non-enzymatic glucose sensor based on CuxS hollow nanospheres, Appl. Surf. Sci. 492 (2019) 407–416. https://doi.org/10.1016/j.apsusc.2019.06.248.

[27] X. Du, G. Ma, X. Zhang, Experimental and Theoretical Understanding on Electrochemical Activation Processes of Nickel Selenide for Excellent Water-Splitting Performance: Comparing the Electrochemical Performances with M-NiSe (M = Co, Cu, and V), ACS Sustain. Chem. Eng. 7 (2019) 19257–19267. https://doi.org/10.1021/ACSSUSCHEMENG.9B05514/SUPPL_FILE/SC9B05514_SI_001.PDF.

[28] F. Bozheyev, F. Xi, P. Plate, T. Dittrich, S. Fiechter, K. Ellmer, Efficient charge transfer at a homogeneously distributed $(NH_4)_2Mo_3S_{13}/WSe_2$ heterojunction for solar hydrogen evolution, J. Mater. Chem. A. 7 (2019) 10769–10780. https://doi.org/10.1039/C9TA01220F.

[29] F. Bozheyev, M. Rengachari, S.P. Berglund, D. Abou-Ras, K. Ellmer, Passivation of recombination active PdSex centers in (001)-textured photoactive WSe_2 films, Mater. Sci. Semicond. Process. 93 (2019) 284–289. https://doi.org/10.1016/J.MSSP.2018.12.020.

[30] F. Bozheyev, F. Xi, I. Ahmet, C. Höhn, K. Ellmer, Evaluation of Pt, Rh, SnO_2, $(NH4)_2Mo_3S_{13}$, $BaSO_4$ protection coatings on WSe_2 photocathodes for solar hydrogen evolution, Int. J. Hydrogen Energy. 45 (2020) 19112–19120. https://doi.org/10.1016/J.IJHYDENE.2020.04.251.

[31] L. Nisar, M. Sadaqat, A. Hassan, N.U.A. Babar, A. Shah, M. Najam-Ul-Haq, M.N. Ashiq, M.F. Ehsan, K.S. Joya, Ultrathin CoTe nanoflakes electrode demonstrating low overpotential for overall water splitting, Fuel. 280 (2020) 118666. https://doi.org/10.1016/J.FUEL.2020.118666.

[32] T.A. Ho, C. Bae, H. Nam, E. Kim, S.Y. Lee, J.H. Park, H. Shin, Metallic Ni_3S_2 Films Grown by Atomic Layer Deposition as an Efficient and Stable Electrocatalyst for Overall Water Splitting, ACS Appl. Mater. Interfaces. 10 (2018) 12807–12815. https://doi.org/10.1021/ACSAMI.8B00813/SUPPL_FILE/AM8B00813_SI_001.PDF.

[33] G. Liu, C. Shuai, Z. Mo, R. Guo, N. Liu, X. Niu, Q. Dong, J. Wang, Q. Gao, Y. Chen, W. Liu, The one-pot synthesis of porous Ni 0.85 Se nanospheres on graphene as an efficient and durable electrocatalyst for overall water splitting, New J. Chem. 44 (2020) 17313–17322. https://doi.org/10.1039/D0NJ04197A.

[34] H. Lu, Y. Zhang, Y. Huang, C. Zhang, T. Liu, Reaction Packaging $CoSe_2$ Nanoparticles in N-Doped Carbon Polyhedra with Bifunctionality for Overall Water Splitting, ACS Appl. Mater. Interfaces. 11 (2019) 3372–3381. https://doi.org/10.1021/ACSAMI.8B20184/SUPPL_FILE/AM8B20184_SI_001.PDF.

[35] X. Wu, D. He, H. Zhang, H. Li, Z. Li, B. Yang, Z. Lin, L. Lei, X. Zhang, Ni0.85Se as an efficient non-noble bifunctional electrocatalyst for full water splitting, Int. J. Hydrogen Energy. 41 (2016) 10688–10694. https://doi.org/10.1016/J.IJHYDENE.2016.05.010.

[36] H. Li, S. Chen, H. Lin, X. Xu, H. Yang, L. Song, X. Wang, Nickel Diselenide Ultrathin Nanowires Decorated with Amorphous Nickel Oxide Nanoparticles for Enhanced Water Splitting Electrocatalysis, Small. 13 (2017) 1701487. https://doi.org/10.1002/SMLL.201701487.

[37] Y. Yin, J. Xu, W. Guo, Z. Wang, X. Du, C. Chen, Z. Zheng, D. Liu, D. Qu, Z. Xie, H. Tang, J. Li, A single-step fabrication of $CoTe_2$ nanofilm electrode toward efficient overall water splitting, Electrochim. Acta. 307 (2019) 451–458. https://doi.org/10.1016/J.ELECTACTA.2019.03.213.

[38] Z. Wu, J. Li, Z. Zou, X. Wang, Folded nanosheet-like $Co_{0.85}Se$ array for overall water splitting, J. Solid State Electrochem. 22 (2018) 1785–1794. https://doi.org/10.1007/S10008-018-3885-3/FIGURES/6.

[39] J. Zhang, Y. Wang, C. Zhang, H. Gao, L. Lv, L. Han, Z. Zhang, Self-Supported Porous $NiSe_2$ Nanowrinkles as Efficient Bifunctional Electrocatalysts for Overall Water Splitting, ACS Sustain. Chem. Eng. 6 (2018) 2231–2239. https://doi.org/10.1021/ACSSUSCHEMENG.7B03657/SUPPL_FILE/SC7B03657_SI_001.PDF.

[40] K. Lan, J. Li, Y. Zhu, L. Gong, F. Li, P. Jiang, F. Niu, R. Li, Morphology engineering of $CoSe_2$ as efficient electrocatalyst for water splitting, J. Colloid Interface Sci. 539 (2019) 646–653. https://doi.org/10.1016/J.JCIS.2018.12.044.

[41] Y. Wang, X. Li, M. Zhang, Y. Zhou, D. Rao, C. Zhong, J. Zhang, X. Han, W. Hu, Y. Zhang, K. Zaghib, Y. Wang, Y. Deng, Lattice-Strain Engineering of Homogeneous NiS0.5Se0.5 Core–Shell Nanostructure as a Highly Efficient and Robust Electrocatalyst for Overall Water Splitting, Adv. Mater. 32 (2020) 2000231. https://doi.org/10.1002/ADMA.202000231.

[42] S. Chakrabartty, S. Karmakar, C.R. Raj, An Electrocatalytically Active Nanoflake-Like Co_9S_8-$CoSe_2$ Heterostructure for Overall Water Splitting, ACS Appl. Nano Mater. 3 (2020) 11326–11334. https://doi.org/10.1021/ACSANM.0C02431/SUPPL_FILE/AN0C02431_SI_001.PDF.

[43] H. Bian, T. Chen, Z. Chen, J. Liu, Z. Li, P. Du, B. Zhou, X. Zeng, J. Tang, C. Liu, One-step synthesis of mesoporous Cobalt sulfides (CoSx) on the metal substrate as an efficient bifunctional electrode for overall water splitting, Electrochim. Acta. 389 (2021) 138786. https://doi.org/10.1016/J.ELECTACTA.2021.138786.

[44] Y. Chen, S. Xu, S. Zhu, R. Jiji Jacob, G. Pastel, Y. Wang, Y. Li, J. Dai, F. Chen, H. Xie, B. Liu, Y. Yao, L.G. Salamanca-Riba, M.R. Zachariah, T. Li, L. Hu, Millisecond synthesis of CoS nanoparticles for highly efficient overall water splitting, (n.d.). https://doi.org/10.1007/s12274-019-2304-0.

[45] G. Janani, S. Yuvaraj, S. Surendran, Y. Chae, Y. Sim, S.J. Song, W. Park, M.J. Kim, U. Sim, Enhanced bifunctional electrocatalytic activity of Ni-Co bimetallic chalcogenides for efficient water-splitting application, J. Alloys Compd. 846 (2020) 156389. https://doi.org/10.1016/J.JALLCOM.2020.156389.

[46] L. He, B. Cui, B. Hu, J. Liu, K. Tian, M. Wang, Y. Song, S. Fang, Z. Zhang, Q. Jia, Mesoporous Nanostructured CoFe-Se-P Composite Derived from a Prussian Blue Analogue as a Superior Electrocatalyst for Efficient Overall Water Splitting, ACS Appl. Energy Mater. 1 (2018) 3915–3928. https://doi.org/10.1021/ACSAEM.8B00663/SUPPL_FILE/AE8B00663_SI_001.PDF.

[47] J. Li, M. Wan, T. Li, H. Zhu, Z. Zhao, Z. Wang, W. Wu, M. Du, $NiCoSe_{2-x}$/N-doped C mushroom-like core/shell nanorods on N-doped carbon fiber for efficiently electrocatalyzed overall water splitting, Electrochim. Acta. 272 (2018) 161–168. https://doi.org/10.1016/J.ELECTACTA.2018.04.032.

[48] G. Mei, H. Liang, B. Wei, H. Shi, F. Ming, X. Xu, Z. Wang, Bimetallic MnCo selenide yolk shell structures for efficient overall water splitting, Electrochim. Acta. 290 (2018) 82–89. https://doi.org/10.1016/J.ELECTACTA.2018.09.062.

[49] K.C. Majhi, M. Yadav, Bimetallic chalcogenide nanocrystallites as efficient electrocatalyst for overall water splitting, J. Alloys Compd. 852 (2021) 156736. https://doi.org/10.1016/J.JALLCOM.2020.156736.

[50] C. Zhang, Y. Zhang, S. Zhou, C. Li, Self-supported iron-doping $NiSe_2$ nanowrinkles as bifunctional electrocatalysts for electrochemical water splitting, J. Alloys Compd. 818 (2020) 152833. https://doi.org/10.1016/J.JALLCOM.2019.152833.

[51] Y. Sun, K. Xu, Z. Wei, H. Li, T. Zhang, X. Li, W. Cai, J. Ma, H. Jin Fan, Y. Li, Y.Q. Sun, H.L. Li, T. Zhang, X.Y. Li, W.P. Cai, Y. Li, K. Xu, H.J. Fan, Z.X. Wei, J.M. Ma, Strong Electronic Interaction in Dual-Cation-Incorporated $NiSe_2$ Nanosheets with Lattice Distortion for Highly Efficient Overall Water Splitting, Adv. Mater. 30 (2018) 1802121. https://doi.org/10.1002/ADMA.201802121.

[52] J. Huang, S. Wang, J. Nie, C. Huang, X. Zhang, B. Wang, J. Tang, C. Du, Z. Liu, J. Chen, Active site and intermediate modulation of 3D $CoSe_2$ nanosheet array on Ni foam by Mo doping for high-efficiency overall water splitting in alkaline media, Chem. Eng. J. 417 (2021) 128055. https://doi.org/10.1016/J.CEJ.2020.128055.

[53] G. Song, Z. Wang, J. Sun, J. Sun, D. Yuan, L. Zhang, $ZnCo_2S_4$ nanosheet array anchored on nickel foam as electrocatalyst for electrochemical water splitting, Electrochem. Commun. 105 (2019) 106487. https://doi.org/10.1016/J.ELECOM.2019.106487.

[54] G. Liu, C. Shuai, Z. Mo, R. Guo, N. Liu, Q. Dong, J. Wang, H. Pei, W. Liu, X. Guo, Fe-doped Ni0.85Se nanospheres interspersed into carbon nanotubes as efficient and stable electrocatalyst for overall water splitting, Electrochim. Acta. 385 (2021) 138452. https://doi.org/10.1016/J.ELECTACTA.2021.138452.

[55] C. Liu, D. Jia, Q. Hao, X. Zheng, Y. Li, C. Tang, H. Liu, J. Zhang, X. Zheng, P-Doped Iron-Nickel Sulfide Nanosheet Arrays for Highly Efficient Overall Water Splitting, ACS Appl. Mater. Interfaces. 11 (2019) 27667–27676. https://doi.org/10.1021/ACSAMI.9B04528/SUPPL_FILE/AM9B04528_SI_002.AVI.

[56] D. Li, Z. Liu, J. Wang, B. Liu, Y. Qin, W. Yang, J. Liu, Hierarchical trimetallic sulfide $FeCo_2S_4$–$NiCo_2S_4$ nanosheet arrays supported on a Ti mesh: An efficient 3D bifunctional electrocatalyst for full water splitting, Electrochim. Acta. 340 (2020) 135957. https://doi.org/10.1016/J.ELECTACTA.2020.135957.

[57] J.Y. Xue, F.L. Li, Z.Y. Zhao, C. Li, C.Y. Ni, H.W. Gu, D.J. Young, J.P. Lang, In Situ Generation of Bifunctional Fe-Doped MoS_2 Nanocanopies for Efficient Electrocatalytic Water Splitting, Inorg. Chem. 58 (2019) 11202–11209. https://doi.org/10.1021/ACS.INORGCHEM.9B01814/SUPPL_FILE/IC9B01814_SI_001.PDF.

[58] Y. Guo, X. Zhou, J. Tang, S. Tanaka, Y.V. Kaneti, J. Na, B. Jiang, Y. Yamauchi, Y. Bando, Y. Sugahara, Multiscale structural optimization: Highly efficient hollow iron-doped metal sulfide heterostructures as bifunctional electrocatalysts for water splitting, Nano Energy. 75 (2020) 104913. https://doi.org/10.1016/J.NANOEN.2020.104913.

[59] R. V. Digraskar, V.S. Sapner, A. V. Ghule, B.R. Sathe, Enhanced Overall Water-Splitting Performance: Oleylamine-Functionalized GO/Cu_2ZnSnS_4 Composite as a Nobel Metal-Free and NonPrecious Electrocatalyst, ACS Omega. (2019). https://doi.org/10.1021/ACSOMEGA.9B01680/SUPPL_FILE/AO9B01680_SI_001.PDF.

[60] X. Du, H. Su, X. Zhang, Cr doped-Co9S8 nanoarrays as high-efficiency electrocatalysts for water splitting, J. Alloys Compd. 824 (2020) 153965. https://doi.org/10.1016/J.JALLCOM.2020.153965.

[61] C. Zhang, S. Zhou, X. Dong, Y. Han, J. Li, W. Yin, Three-dimensional self-supported iron-doped nickel sulfides for sustainable overall water splitting, Vacuum. 181 (2020) 109661. https://doi.org/10.1016/J.VACUUM.2020.109661.

[62] T. Chen, Y. Tan, Hierarchical $CoNiSe_2$ nano-architecture as a high-performance electrocatalyst for water splitting, Nano Res. 2018 113. 11 (2018) 1331–1344. https://doi.org/10.1007/S12274-017-1748-3.

[63] X. Zhao, H. Liu, Y. Rao, X. Li, J. Wang, G. Xia, M. Wu, Carbon Dots Decorated Hierarchical $NiCo_2S_4/Ni_3S_2$ Composite for Efficient Water Splitting, ACS Sustain. Chem. Eng. 7 (2019) 2610–2618. https://doi.org/10.1021/ACSSUSCHEMENG.8B05611/SUPPL_FILE/SC8B05611_SI_001.PDF.

[64] S. Czioska, J. Wang, X. Teng, Z. Chen, Hierarchically Structured $CuCo_2S_4$ Nanowire Arrays as Efficient Bifunctional Electrocatalyst for Overall Water Splitting, ACS Sustain. Chem. Eng. 6 (2018) 11877–11883. https://doi.org/10.1021/ACSSUSCHEMENG.8B02155/SUPPL_FILE/SC8B02155_SI_001.PDF.

[65] J. Hu, Y. Ou, Y. Li, D. Gao, Y. Zhang, P. Xiao, $FeCo_2S_4$ Nanosheet Arrays Supported on Ni Foam: An Efficient and Durable Bifunctional Electrocatalyst for Overall Water-Splitting, ACS Sustain. Chem. Eng. 6 (2018) 11724–11733. https://doi.org/10.1021/ACSSUSCHEMENG.8B01978/SUPPL_FILE/SC8B01978_SI_001.PDF.

[66] Q. Zhang, C. Ye, X.L. Li, Y.H. Deng, B.X. Tao, W. Xiao, L.J. Li, N.B. Li, H.Q. Luo, Self-Interconnected Porous Networks of NiCo Disulfide as Efficient Bifunctional Electrocatalysts for Overall Water Splitting, ACS Appl. Mater. Interfaces. 10 (2018) 27723–27733. https://doi.org/10.1021/ACSAMI.8B04386/SUPPL_FILE/AM8B04386_SI_002.AVI.

[67] X. Du, W. Lian, X. Zhang, Homogeneous core–shell $NiCo_2S_4$ nanorods as flexible electrode for overall water splitting, Int. J. Hydrogen Energy. 43 (2018) 20627–20635. https://doi.org/10.1016/J.IJHYDENE.2018.09.123.

[68] F. Li, R. Xu, Y. Li, F. Liang, D. Zhang, W.F. Fu, X.J. Lv, N-doped carbon coated $NiCo_2S_4$ hollow nanotube as bifunctional electrocatalyst for overall water splitting, Carbon N. Y. 145 (2019) 521–528. https://doi.org/10.1016/J.CARBON.2019.01.065.

[69] X. Zheng, X. Han, Y. Zhang, J. Wang, C. Zhong, Y. Deng, W. Hu, Controllable synthesis of nickel sulfide nanocatalysts and their phase-dependent performance for overall water splitting, Nanoscale. 11 (2019) 5646–5654. https://doi.org/10.1039/C8NR09902B.

[70] D. Chen, Y. Chen, W. Zhang, R. Cao, Nickel selenide from single-molecule electrodeposition for efficient electrocatalytic overall water splitting, New J. Chem. 45 (2021) 351–357. https://doi.org/10.1039/D0NJ04966B.

[71] A.T. Swesi, J. Masud, W.P.R. Liyanage, S. Umapathi, E. Bohannan, J. Medvedeva, M. Nath, Textured $NiSe_2$ Film: Bifunctional Electrocatalyst for Full Water Splitting at Remarkably Low Overpotential with High Energy Efficiency /639/638/77/886 /639/301/299/886 /639/301/299/161 /128 /120 /145 /140/146 article, Sci. Rep. 7 (2017) 1–11. https://doi.org/10.1038/s41598-017-02285-z.

[72] B.G. Amin, A.T. Swesi, J. Masud, M. Nath, R. Li, / Chemcomm, C. Communication, $CoNi_2Se_4$ as an efficient bifunctional electrocatalyst for overall water splitting, Chem. Commun. 53 (2017) 5412–5415. https://doi.org/10.1039/C7CC01489A.

[73] X. Xu, F. Song, X. Hu, ARTICLE A nickel iron diselenide-derived efficient oxygen-evolution catalyst, Nat. Publ. Gr. (2016). https://doi.org/10.1038/ncomms12324.

[74] C. Wang, M. Cao, X. Jiang, M. Wang, Y. Shen, A catalyst based on copper-cadmium bimetal for electrochemical reduction of CO_2 to CO with high faradaic efficiency, Electrochim. Acta. 271 (2018) 544–550. https://doi.org/10.1016/J.ELECTACTA.2018.03.156.

[75] M. Sun, R.-T. Gao, X. Liu, R. Gao, L. Wang, Manganese-based oxygen evolution catalysts boosting stable solar-driven water splitting: MnSe as an intermetallic phase, J. Mater. Chem. A. 8 (2020) 25298–25305. https://doi.org/10.1039/D0TA09946E.

[76] J. Masud, M. Nath, Co_7Se_8 Nanostructures as Catalysts for Oxygen Reduction Reaction with High Methanol Tolerance, ACS Energy Lett. 1 (2016) 27–31. https://doi.org/10.1021/acsenergylett.6b00006.

[77] A.T. Swesi, J. Masud, M. Nath, Nickel selenide as a high-efficiency catalyst for oxygen evolution reaction, Energy Environ. Sci. 9 (2016) 1771–1782. https://doi.org/10.1039/C5EE02463C.

[78] K. Wan, J. Luo, C. Zhou, T. Zhang, J. Arbiol, X. Lu, B.W. Mao, X. Zhang, J. Fransaer, Hierarchical Porous Ni3S4 with Enriched High-Valence Ni Sites as a Robust Electrocatalyst for Efficient Oxygen Evolution Reaction, Adv. Funct. Mater. 29 (2019) 1900315. https://doi.org/10.1002/ADFM.201900315.

[79] A.T. Swesi, J. Masud, M. Nath, Enhancing electrocatalytic activity of bifunctional Ni_3Se_2 for overall water splitting through etching-induced surface nanostructuring, J. Mater. Res. 31 (2016) 2888–2896. https://doi.org/10.1557/jmr.2016.301.

[80] D. Johnson, Z. Qiao, A. Djire, Progress and Challenges of Carbon Dioxide Reduction Reaction on Transition Metal Based Electrocatalysts, ACS Appl. Energy Mater. 4 (2021) 8661–8684. https://doi.org/10.1021/ACSAEM.1C01624.

[81] S. Nitopi, E. Bertheussen, S.B. Scott, X. Liu, A.K. Engstfeld, S. Horch, B. Seger, I.E.L. Stephens, K. Chan, C. Hahn, J.K. Nørskov, T.F. Jaramillo, I. Chorkendorff, Progress and Perspectives of Electrochemical CO_2 Reduction on Copper in Aqueous Electrolyte, Chem. Rev. 119 (2019) 7610–7672. https://doi.org/10.1021/ACS.CHEMREV.8B00705/SUPPL_FILE/CR8B00705_SI_001.PDF.

[82] F.Y. Gao, Z.Z. Wu, M.R. Gao, Electrochemical CO_2 Reduction on Transition-Metal Chalcogenide Catalysts: Recent Advances and Future Perspectives, Energy and Fuels. 35 (2021) 12869–12883. https://doi.org/10.1021/ACS.ENERGYFUELS.1C01650.

[83] W. Zhu, Y.J. Zhang, H. Zhang, H. Lv, Q. Li, R. Michalsky, A.A. Peterson, S. Sun, Active and selective conversion of CO_2 to CO on ultrathin Au nanowires, J. Am. Chem. Soc. 136 (2014) 16132–16135. https://doi.org/10.1021/JA5095099/SUPPL_FILE/JA5095099_SI_001.PDF.

[84] H.E. Lee, K.D. Yang, S.M. Yoon, H.Y. Ahn, Y.Y. Lee, H. Chang, D.H. Jeong, Y.S. Lee, M.Y. Kim, K.T. Nam, Concave Rhombic Dodecahedral Au Nanocatalyst with Multiple High-Index Facets for CO_2 Reduction, ACS Nano. 9 (2015) 8384–8393. https://doi.org/10.1021/ACSNANO.5B03065/SUPPL_FILE/NN5B03065_SI_001.PDF.

[85] Y. Chen, C.W. Li, M.W. Kanan, Aqueous CO_2 reduction at very low overpotential on oxide-derived au nanoparticles, J. Am. Chem. Soc. 134 (2012) 19969–19972. https://doi.org/10.1021/JA309317U/SUPPL_FILE/JA309317U_SI_001.PDF.

[86] W. Zhu, R. Michalsky, Ö. Metin, H. Lv, S. Guo, C.J. Wright, X. Sun, A.A. Peterson, S. Sun, Monodisperse Au nanoparticles for selective electrocatalytic reduction of CO_2 to CO, J. Am. Chem. Soc. 135 (2013) 16833–16836. https://doi.org/10.1021/JA409445P/SUPPL_FILE/JA409445P_SI_001.PDF.

[87] Y.S. Ham, S. Choe, M.J. Kim, T. Lim, S.K. Kim, J.J. Kim, Electrodeposited Ag catalysts for the electrochemical reduction of CO_2 to CO, Appl. Catal. B Environ. 208 (2017) 35–43. https://doi.org/10.1016/J.APCATB.2017.02.040.

[88] W. Luc, C. Collins, S. Wang, H. Xin, K. He, Y. Kang, F. Jiao, Ag-sn bimetallic catalyst with a core-shell structure for CO_2 reduction, J. Am. Chem. Soc. 139 (2017) 1885–1893. https://doi.org/10.1021/JACS.6B10435/SUPPL_FILE/JA6B10435_SI_001.PDF.

[89] X. Zhang, S.X. Guo, K.A. Gandionco, A.M. Bond, J. Zhang, Electrocatalytic carbon dioxide reduction: from fundamental principles to catalyst design, Mater. Today Adv. 7 (2020) 100074. https://doi.org/10.1016/J.MTADV.2020.100074.

[90] A. Abdelwahab, J. Castelo-Quibén, M. Pérez-Cadenas, A. Elmouwahidi, F.J. Maldonado-Hódar, F. Carrasco-Marín, A.F. Pérez-Cadenas, Cobalt-Doped Carbon Gels as Electro-Catalysts for the Reduction of CO_2 to Hydrocarbons, Catal. 2017, Vol. 7, Page 25. 7 (2017) 25. https://doi.org/10.3390/CATAL7010025.

[91] J. Zhao, S. Xue, J. Barber, Y. Zhou, J. Meng, X. Ke, An overview of Cu-based heterogeneous electrocatalysts for CO_2 reduction, J. Mater. Chem. A. 8 (2020) 4700–4734. https://doi.org/10.1039/C9TA11778D.

[92] J. Albo, A. Sáez, J. Solla-Gullón, V. Montiel, A. Irabien, Production of methanol from CO_2 electroreduction at Cu_2O and Cu_2O/ZnO-based electrodes in aqueous solution, Appl. Catal. B Environ. 176–177 (2015) 709–717. https://doi.org/10.1016/J.APCATB.2015.04.055.

[93] C.X. Zhao, Y.F. Bu, W. Gao, Q. Jiang, CO_2 Reduction Mechanism on the Pb(111) Surface: Effect of Solvent and Cations, J. Phys. Chem. C. 121 (2017) 19767–19773. https://doi.org/10.1021/ACS.JPCC.7B04375/SUPPL_FILE/JP7B04375_SI_001.PDF.

[94] F. Ye, J. Gao, Y. Chen, Y. Fang, Oxidized indium with transformable dimensions for CO_2 electroreduction toward formate aided by oxygen vacancies, Sustain. Energy Fuels. 4 (2020) 3726–3731. https://doi.org/10.1039/D0SE00498G.

[95] X. Zheng, P. De Luna, F.P. García de Arquer, B. Zhang, N. Becknell, M.B. Ross, Y.Y. Li, M.N. Banis, Y.Y. Li, M. Liu, O. Voznyy, C.T. Dinh, T. Zhuang, P. Stadler, Y. Cui, X. Du, P. Yang, E.H. Sargent, P. De Luna, F.P.G. de Arquer, B. Zhang, N. Becknell, M.B. Ross, Y.Y. Li, M.N. Banis, Y.Y. Li, M. Liu, O. Voznyy, C.T. Dinh, T. Zhuang, P. Stadler, Y. Cui, X. Du, P. Yang, E.H. Sargent, Sulfur-Modulated Tin Sites Enable Highly Selective Electrochemical Reduction of CO_2 to Formate, Joule. 1 (2017) 794–805.

[96] P. Deng, H. Wang, R. Qi, J. Zhu, S. Chen, F. Yang, L. Zhou, K. Qi, H. Liu, B.Y. Xia, Bismuth Oxides with Enhanced Bismuth-Oxygen Structure for Efficient Electrochemical Reduction of Carbon Dioxide to Formate, ACS Catal. 10 (2020) 743–750. https://doi.org/10.1021/ACSCATAL.9B04043/SUPPL_FILE/CS9B04043_SI_001.PDF.

[97] A. Atifi, T.P. Keane, J.L. Dimeglio, R.C. Pupillo, D.R. Mullins, D.A. Lutterman, J. Rosenthal, Insights into the Composition and Function of a Bismuth-Based Catalyst for Reduction of CO_2 to CO, J. Phys. Chem. C. 123 (2019) 9087–9095. https://doi.org/10.1021/ACS.JPCC.9B00504/SUPPL_FILE/JP9B00504_SI_001.PDF.

[98] K.U.D. Calvinho, A.W. Alherz, K.M.K. Yap, A.B. Laursen, S. Hwang, Z.J.L. Bare, Z. Clifford, C.B. Musgrave, G.C. Dismukes, Surface Hydrides on Fe_2P Electrocatalyst Reduce CO_2 at Low Overpotential: Steering Selectivity to Ethylene Glycol, J. Am. Chem. Soc. 143 (2021) 21275–21285. https://doi.org/10.1021/JACS.1C03428.

[99] HoriYoshio, KikuchiKatsuhei, SuzukiShin, PRODUCTION OF CO AND CH_4 IN ELECTROCHEMICAL REDUCTION OF CO_2 AT METAL ELECTRODES IN AQUEOUS HYDROGENCARBONATE SOLUTION, Http://Dx.Doi.Org/10.1246/Cl.1985.1695. 14 (2006) 1695–1698. https://doi.org/10.1246/CL.1985.1695.

[100] W. He, I. Liberman, I. Rozenberg, R. Ifraemov, I. Hod, Electrochemically Driven Cation Exchange Enables the Rational Design of Active CO_2 Reduction Electrocatalysts , Angew. Chemie. 132 (2020) 8339–8346. https://doi.org/10.1002/ANGE.202000545.

[101] D. Yang, Q. Zhu, C. Chen, H. Liu, Z. Liu, Z. Zhao, X. Zhang, S. Liu, B. Han, Selective electroreduction of carbon dioxide to methanol on copper selenide nanocatalysts, Nat. Commun. 2019 101. 10 (2019) 1–9. https://doi.org/10.1038/s41467-019-08653-9.

[102] S. Zhao, S. Guo, C. Zhu, J. Gao, H. Li, H. Huang, Y. Liu, Z. Kang, Achieving electroreduction of CO_2 to CH_3OH with high selectivity using a pyrite–nickel sulfide nanocomposite, RSC Adv. 7 (2017) 1376–1381. https://doi.org/10.1039/C6RA26868D.

[103] P.M. Zimmerman, C.C.L. McCrory, K.E. Rivera Cruz, Y. Liu, T.L. Soucy, Increasing the CO_2 reduction activity of cobalt phthalocyanine by modulating the σ-donor strength of axially coordinating ligands, ACS Catal. 11 (2021) 13203–13216. https://doi.org/10.1021/ACSCATAL.1C02379/SUPPL_FILE/CS1C02379_SI_002.PDF.

[104] L. Zeng, J. Shi, J. Luo, H. Chen, Silver sulfide anchored on reduced graphene oxide as a high -performance catalyst for CO_2 electroreduction, J. Power Sources. 398 (2018) 83–90. https://doi.org/10.1016/J.JPOWSOUR.2018.07.049.

[105] Y. Hori, Electrochemical CO_2 Reduction on Metal Electrodes, Mod. Asp. Electrochem. (2008) 89–189. https://doi.org/10.1007/978-0-387-49489-0_3.

[106] J.Z. Zhen, J.X. Liu, T.Y. Chen, F. Shi, Y.N. Dai, B. Yang, Y.F. Li, X. Wang, T.G. Nong, Y.Q. Hu, J. Shi, Fabrication of ZnS/Zn electrode using sulphur infiltration method for CO_2 reduction into CO in organic media, J. Alloys Compd. 771 (2019) 994–999. https://doi.org/10.1016/J.JALLCOM.2018.08.318.

[107] J.-W.W. Jang, S. Cho, G. Magesh, Y.J. Jang, J.Y. Kim, W.Y. Kim, J.K. Seo, S. Kim, K.-H.H. Lee, J.S. Lee, Aqueous-Solution Route to Zinc Telluride Films for Application to CO_2 Reduction, Angew. Chemie Int. Ed. 53 (2014) 5852–5857. https://doi.org/10.1002/ANIE.201310461.

[108] S. Zhang, P. Kang, T.J. Meyer, Nanostructured tin catalysts for selective electrochemical reduction of carbon dioxide to formate, J. Am. Chem. Soc. 136 (2014) 1734–1737. https://doi.org/10.1021/JA4113885/SUPPL_FILE/JA4113885_SI_001.PDF.

[109] J. Wu, F.G. Risalvato, S. Ma, X.D. Zhou, Electrochemical reduction of carbon dioxide III. The role of oxide layer thickness on the performance of Sn electrode in a full electrochemical cell, J. Mater. Chem. A. 2 (2014) 1647–1651. https://doi.org/10.1039/C3TA13544F.

[110] D.H. Won, C.H. Choi, J. Chung, M.W. Chung, E.H. Kim, S.I. Woo, Rational Design of a Hierarchical Tin Dendrite Electrode for Efficient Electrochemical Reduction of CO_2, ChemSusChem. 8 (2015) 3092–3098. https://doi.org/10.1002/CSSC.201500694.

[111] J. Wu, F.G. Risalvato, F.-S. Ke, P.J. Pellechia, X.-D. Zhou, Electrochemical Reduction of Carbon Dioxide I. Effects of the Electrolyte on the Selectivity and Activity with Sn Electrode, J. Electrochem. Soc. 159 (2012) F353–F359. https://doi.org/10.1149/2.049207JES/XML.

[112] W. Lv, R. Zhang, P. Gao, L. Lei, Studies on the faradaic efficiency for electrochemical reduction of carbon dioxide to formate on tin electrode, J. Power Sources. 253 (2014) 276–281. https://doi.org/10.1016/J.JPOWSOUR.2013.12.063.

[113] Y. Chen, M.W. Kanan, Tin oxide dependence of the CO_2 reduction efficiency on tin electrodes and enhanced activity for tin/tin oxide thin-film catalysts, J. Am. Chem. Soc. 134 (2012) 1986–1989. https://doi.org/10.1021/JA2108799/SUPPL_FILE/JA2108799_SI_001.PDF.

[114] J.E. Pander, M.F. Baruch, A.B. Bocarsly, Probing the Mechanism of Aqueous CO_2 Reduction on Post-Transition-Metal Electrodes using ATR-IR Spectroelectrochemistry, ACS Catal. 6 (2016) 7824–7833. https://doi.org/10.1021/ACSCATAL.6B01879.

[115] B. He, L. Jia, Y. Cui, W. Zhou, J. Sun, J. Xu, Q. Wang, L. Zhao, SnSe2 Nanorods on Carbon Cloth as a Highly Selective, Active, and Flexible Electrocatalyst for Electrochemical Reduction of CO_2 into Formate, ACS Appl. Energy Mater. 2 (2019) 7655–7662. https://doi.org/10.1021/ACSAEM.9B01643/SUPPL_FILE/AE9B01643_SI_001.PDF.

[116] X. Liu, H. Yang, J. He, H. Liu, L. Song, L. Li, J. Luo, X.J. Liu, J. He, H.X. Liu, L.D. Song, J. Luo, H. Yang, L. Li, Highly Active, Durable Ultrathin $MoTe_2$ Layers for the Electroreduction of CO_2 to CH_4, Small. 14 (2018) 1704049. https://doi.org/10.1002/SMLL.201704049.

[117] J. Ye, D. Rao, X. Yan, Regulating the electronic properties of $MoSe_2$ to improve its CO_2 electrocatalytic reduction performance via atomic doping, New J. Chem. 45 (2021) 5350–5356. https://doi.org/10.1039/D0NJ05993E.

[118] X. Yang, P. Deng, D. Liu, S. Zhao, D. Li, H. Wu, Y. Ma, B.Y. Xia, M. Li, C. Xiao, S. Ding, Partial sulfuration-induced defect and interface tailoring on bismuth oxide for promoting electrocatalytic CO_2 reduction, J. Mater. Chem. A. 8 (2020) 2472–2480. https://doi.org/10.1039/C9TA11363K.

[119] Y. Wang, C. Niu, Y. Zhu, D. He, W. Huang, Tunable syngas formation from electrochemical CO_2 reduction on copper nanowire arrays, ACS Appl. Energy Mater. 3 (2020) 9841–9847. https://doi.org/10.1021/ACSAEM.0C01504/SUPPL_FILE/AE0C01504_SI_001.PDF.

[120] W. Ma, S. Xie, X.G. Zhang, F. Sun, J. Kang, Z. Jiang, Q. Zhang, D.Y. Wu, Y. Wang, Promoting electrocatalytic CO_2 reduction to formate via sulfur-boosting water activation on indium surfaces, Nat. Commun. 2019 101. 10 (2019) 1–10. https://doi.org/10.1038/s41467-019-08805-x.

[121] A. Aljabour, H. Coskun, X. Zheng, M.G. Kibria, M. Strobel, S. Hild, M. Kehrer, D. Stifter, E.H. Sargent, P. Stadler, Active sulfur sites in semimetallic titanium disulfide enable CO_2 electroreduction, ACS Catal. 10 (2020) 66–72. https://doi.org/10.1021/ACSCATAL.9B02872/SUPPL_FILE/CS9B02872_SI_001.PDF.

[122] H. Li, X. Liu, S. Chen, D. Yang, Q. Zhang, L. Song, H. Xiao, Q. Zhang, L. Gu, X. Wang, Edge-Exposed Molybdenum Disulfide with N-Doped Carbon Hybridization: A Hierarchical Hollow Electrocatalyst for Carbon Dioxide Reduction, Adv. Energy Mater. 9 (2019) 1900072. https://doi.org/10.1002/AENM.201900072.

[123] J. Li, X. Xu, B. Huang, Z. Lou, B. Li, Light-Induced in Situ Formation of a Nonmetallic Plasmonic MoS_2/MoO_{3-x} Heterostructure with Efficient Charge Transfer for CO_2 Reduction and SERS Detection, ACS Appl. Mater. Interfaces. 13 (2021) 10047–10053. https://doi.org/10.1021/ACSAMI.0C21401/SUPPL_FILE/AM0C21401_SI_001.PDF.

[124] K. Pellumbi, M. Smialkowski, D. Siegmund, U.P. Apfel, Enhancing the CO_2 Electroreduction of Fe/Ni-Pentlandite Catalysts by S/Se Exchange, Chemistry. 26 (2020) 9938. https://doi.org/10.1002/CHEM.202001289.

[125] X. Wei, Y. Li, L. Chen, J. Shi, Formic Acid Electro-Synthesis by Concurrent Cathodic CO_2 Reduction and Anodic CH3OH Oxidation, Angew. Chemie Int. Ed. 60 (2021) 3148–3155. https://doi.org/10.1002/ANIE.202012066.

[126] Vass, B. Endrődi, C. Janáky, Coupling electrochemical carbon dioxide conversion with value-added anode processes: An emerging paradigm, Curr. Opin. Electrochem. 25 (2021) 100621. https://doi.org/10.1016/J.COELEC.2020.08.003.

SECTION

2. CONCLUSIONS

Catalyst selection through viable techniques have been established for catalyst innovation. Catalyst selection do provide faster testing of large number of materials, but it does not provide the mechanism or formula to make future discoveries more efficient. We utilize the method of making and testing new catalysts, understanding or preparing hypothesis about the activities or reason behind the activity. And then we use this hypothesis in predicting new materials that would eradicate the limitations present in the old catalysts.

First step was prediction and according to our hypothesis we decided to synthesize the materials. Second step was to synthesize the materials and characterize them for their correct composition. Third the materials were tested in the H-Cell for this activity towards the CO_2 electroreduction to determine what products have been produced and at what rate. After we narrowed down for the most active materials, we did further experiments in different conditions to find out the optimal conditions for the optimal results from these catalysts. We performed both experimental and theoretical studies on the copper selenide to understand the mechanism on the catalyst and to find out path for further improvement.

BIBLIOGRAPHY

1 Earth's CO_2 Home Page, https://www.co2.earth/, (accessed 7 September 2020).

2 N. Abas, A. Kalair and N. Khan, Review of fossil fuels and future energy technologies, *Futures*, 2015, **69**, 31–49.

3 J. Conti, P. Holtberg, J. Diefenderfer, A. LaRose, J. T. Turnure and L. Westfall, *International Energy Outlook 2016 With Projections to 2040*, 2016.

4 Homepage -U.S. Energy Information Administration (EIA), https://www.eia.gov/, (accessed 7 September 2020).

5 Renewable Energy |Center for Climate and Energy Solutions, https://www.c2es.org/content/renewable-energy/, (accessed 7 September 2020).

6 A. Demirbaş, Biomass resource facilities and biomass conversion processing for fuels and chemicals, *Energy Convers. Manag.*, 2001, **42**, 1357–1378.

7 Breaking the chemical and engineering barriers to lignocellulosic biofuels., https://www.cabdirect.org/cabdirect/abstract/20083142634,(accessed 7 September 2020).

8 N. S. Lewis, *Energy Environ. Sci.*, 2016, 9, 2172–2176.

9 IPCC, Climate Change 2014 Synthesis Report Summary Chapter for Policymakers, *Ipcc*, 2014, 31.

10 A Degree of Concern: Why Global Temperatures Matter – Climate Change: Vital Signs of the Planet, https://climate.nasa.gov/news/2865/a-degree-of-concern-why-global-temperatures-matter/, (accessed 7 September 2020).

11 Ocean acidification | National Oceanic and Atmospheric Administration, https://www.noaa.gov/education/resource-collections/ocean-coasts/ocean-acidification, (accessed 7 September 2020).

12 N. S. Lewis and D. G. Nocera, *Proc. Natl. Acad. Sci. U. S. A.*, 2006, 103, 15729–15735.

13 J. Barber, Photosynthetic energy conversion: Natural and artificial, *Chem. Soc. Rev.*, 2009, **38**, 185–196.

14 D. P. Clarke, Y. M. Al-Abdeli and G. Kothapalli, The impact of renewable energy intermittency on the operational characteristics of a stand-alone hydrogen generation system with on-site water production, *Int. J. Hydrogen Energy*, 2013, **38**, 12253–12265.

15 Z. Yan, J. L. Hitt, J. A. Turner and T. E. Mallouk, Renewable electricity storage using electrolysis, *Proc. Natl. Acad. Sci. U. S. A.*, 2020, **117**, 12558–12563.

16 S. D. Ebbesen and M. Mogensen, Electrolysis of carbon dioxide in Solid Oxide Electrolysis Cells, *J. Power Sources*, , DOI:10.1016/j.jpowsour.2009.02.093.

17 C. Delacourt, P. L. Ridgway, J. B. Kerr and J. Newman, Design of an Electrochemical Cell Making Syngas ($CO+H_2$) from CO_2 and H_2O Reduction at Room Temperature, *J. Electrochem. Soc.*, 2008, **155**, B42.

18 K. P. Kuhl, E. R. Cave, D. N. Abram and T. F. Jaramillo, New insights into the electrochemical reduction of carbon dioxide on metallic copper surfaces, *Energy Environ. Sci.*, , DOI:10.1039/c2ee21234j.

19 J. Wu, F. G. Risalvato, P. P. Sharma, P. J. Pellechia, F. S. Ke and X. D. Zhou, Electrochemical reduction of carbon dioxide: II. Design, assembly, and performance of low temperature full electrochemical cells, *J. Electrochem. Soc.*, , DOI:10.1149/2.030309jes.

20 C. W. Li and M. W. Kanan, CO_2 reduction at low overpotential on Cu electrodes resulting from the reduction of thick Cu_2O films, *J. Am. Chem. Soc.*, 2012, **134**, 7231–7234.

21 Y. Chen, C. W. Li and M. W. Kanan, Aqueous CO_2 reduction at very low overpotential on oxide-derived au nanoparticles, *J. Am. Chem. Soc.*, , DOI:10.1021/ja309317u.

22 Y. Chen and M. W. Kanan, Tin oxide dependence of the CO_2 reduction efficiency on tin electrodes and enhanced activity for tin/tin oxide thin-film catalysts, *J. Am. Chem. Soc.*, , DOI:10.1021/ja2108799.

23 A. Goyal, G. Marcandalli, V. A. Mints and M. T. M. Koper, Competition between CO_2 Reduction and Hydrogen Evolution on a Gold Electrode under Well-Defined Mass Transport Conditions, *J. Am. Chem. Soc.*, 2020, **142**, 4154–4161.

24 D. Du, R. Lan, J. Humphreys and S. Tao, Progress in inorganic cathode catalysts for electrochemical conversion of carbon dioxide into formate or formic acid, *J. Appl. Electrochem.*, 2017, **47**, 661–678.

25 Y. Hori, K. Kikuchi and S. Suzuki, PRODUCTION OF CO AND CH 4 IN ELECTROCHEMICAL REDUCTION OF CO 2 AT METAL ELECTRODES IN AQUEOUS HYDROGENCARBONATE SOLUTION , *Chem. Lett.*, 1985, **14**, 1695–1698.

26 Y. Hori, in *Modern ASpects of Electrochemistry no 42*, 2008.

27 H. Yano, T. Tanaka, M. Nakayama and K. Ogura, Selective electrochemical reduction of CO_2 to ethylene at a three-phase interface on copper(I) halide-confined Cu-mesh electrodes in acidic solutions of potassium halides, *J. Electroanal. Chem.*, 2004, **565**, 287–293.

28 M. R. Gonçalves, A. Gomes, J. Condeço, T. R. C. Fernandes, T. Pardal, C. A. C. Sequeira and J. B. Branco, Electrochemical conversion of CO_2 to C2 hydrocarbons using different ex situ copper electrodeposits, *Electrochim. Acta*, 2013, **102**, 388–392.

29 C. W. Li, J. Ciston and M. W. Kanan, Electroreduction of carbon monoxide to liquid fuel on oxide-derived nanocrystalline copper, *Nature*, 2014, **508**, 504–507.

30 A. Saxena, W. Liyanage, J. Masud, S. Kapila and M. Nath, Selective electroreduction of CO_2 to carbon-rich products with a simple binary copper selenide electrocatalyst, *J. Mater. Chem. A*, 2021, **9**, 7150–7161.

31 G. Wang, J. Chen, Y. Ding, P. Cai, L. Yi, Y. Li, C. Tu, Y. Hou, Z. Wen and L. Dai, Electrocatalysis for CO_2 conversion: from fundamentals to value-added products, *Chem. Soc. Rev.*, 2021, **50**, 4993–5061.

32 C. Zhu, D. Gao, J. Ding, D. Chao and J. Wang, TMD-based highly efficient electrocatalysts developed by combined computational and experimental approaches, *Chem. Soc. Rev.*, 2018, **47**, 4332–4356.

33 H. Xie, T. Wang, J. Liang, Q. Li and S. Sun, Cu-based nanocatalysts for electrochemical reduction of CO_2, *Nano Today*, 2018, **21**, 41–54.

34 X. Shao, X. Zhang, Y. Liu, J. Qiao, X. D. Zhou, N. Xu, J. L. Malcombe, J. Yi and J. Zhang, Metal chalcogenide-associated catalysts enabling CO 2 electroreduction to produce low-carbon fuels for energy storage and emission reduction: catalyst structure, morphology, performance, and mechanism, *J. Mater. Chem. A*, 2021, **9**, 2526–2559.

35 D. Johnson, Z. Qiao and A. Djire, Progress and Challenges of Carbon Dioxide Reduction Reaction on Transition Metal Based Electrocatalysts, *ACS Appl. Energy Mater.*, 2021, **4**, 8661–8684.

36 S. Nitopi, E. Bertheussen, S. B. Scott, X. Liu, A. K. Engstfeld, S. Horch, B. Seger, I. E. L. Stephens, K. Chan, C. Hahn, J. K. Nørskov, T. F. Jaramillo and I. Chorkendorff, Progress and Perspectives of Electrochemical CO_2 Reduction on Copper in Aqueous Electrolyte, *Chem. Rev.*, 2019, **119**, 7610–7672.

37 F. Y. Gao, Z. Z. Wu and M. R. Gao, Electrochemical CO_2 Reduction on Transition-Metal Chalcogenide Catalysts: Recent Advances and Future Perspectives, *Energy and Fuels*, 2021, **35**, 12869–12883.

38 W. Zhu, Y. J. Zhang, H. Zhang, H. Lv, Q. Li, R. Michalsky, A. A. Peterson and S. Sun, Active and selective conversion of CO_2 to CO on ultrathin Au nanowires, *J. Am. Chem. Soc.*, 2014, **136**, 16132–16135.

39 H. E. Lee, K. D. Yang, S. M. Yoon, H. Y. Ahn, Y. Y. Lee, H. Chang, D. H. Jeong, Y. S. Lee, M. Y. Kim and K. T. Nam, Concave Rhombic Dodecahedral Au Nanocatalyst with Multiple High-Index Facets for CO_2 Reduction, *ACS Nano*, 2015, **9**, 8384–8393.

40 Y. Chen, C. W. Li and M. W. Kanan, Aqueous CO_2 reduction at very low overpotential on oxide-derived au nanoparticles, *J. Am. Chem. Soc.*, 2012, **134**, 19969–19972.

41 W. Zhu, R. Michalsky, Ö. Metin, H. Lv, S. Guo, C. J. Wright, X. Sun, A. A. Peterson and S. Sun, Monodisperse Au nanoparticles for selective electrocatalytic reduction of CO_2 to CO, *J. Am. Chem. Soc.*, 2013, **135**, 16833–16836.

42 Y. S. Ham, S. Choe, M. J. Kim, T. Lim, S. K. Kim and J. J. Kim, Electrodeposited Ag catalysts for the electrochemical reduction of CO_2 to CO, *Appl. Catal. B Environ.*, 2017, **208**, 35–43.

43 W. Luc, C. Collins, S. Wang, H. Xin, K. He, Y. Kang and F. Jiao, Ag-sn bimetallic catalyst with a core-shell structure for CO_2 reduction, *J. Am. Chem. Soc.*, 2017, **139**, 1885–1893.

44 X. Zhang, S. X. Guo, K. A. Gandionco, A. M. Bond and J. Zhang, Electrocatalytic carbon dioxide reduction: from fundamental principles to catalyst design, *Mater. Today Adv.*, 2020, **7**, 100074.

45 A. Abdelwahab, J. Castelo-Quibén, M. Pérez-Cadenas, A. Elmouwahidi, F. J. Maldonado-Hódar, F. Carrasco-Marín and A. F. Pérez-Cadenas, Cobalt-Doped Carbon Gels as Electro-Catalysts for the Reduction of CO_2 to Hydrocarbons, *Catal. 2017, Vol. 7, Page 25*, 2017, **7**, 25.

46 J. Zhao, S. Xue, J. Barber, Y. Zhou, J. Meng and X. Ke, An overview of Cu-based heterogeneous electrocatalysts for CO_2 reduction, *J. Mater. Chem. A*, 2020, **8**, 4700–4734.

47 J. Albo, A. Sáez, J. Solla-Gullón, V. Montiel and A. Irabien, Production of methanol from CO_2 electroreduction at Cu_2O and Cu_2O/ZnO-based electrodes in aqueous solution, *Appl. Catal. B Environ.*, 2015, **176**–**177**, 709–717.

48 C. X. Zhao, Y. F. Bu, W. Gao and Q. Jiang, CO_2 Reduction Mechanism on the Pb(111) Surface: Effect of Solvent and Cations, *J. Phys. Chem. C*, 2017, **121**, 19767–19773.

49 F. Ye, J. Gao, Y. Chen and Y. Fang, Oxidized indium with transformable dimensions for CO_2 electroreduction toward formate aided by oxygen vacancies, *Sustain. Energy Fuels*, 2020, **4**, 3726–3731.

50 X. Zheng, P. De Luna, F. P. García de Arquer, B. Zhang, N. Becknell, M. B. Ross, Y. Y. Li, M. N. Banis, Y. Y. Li, M. Liu, O. Voznyy, C. T. Dinh, T. Zhuang, P. Stadler, Y. Cui, X. Du, P. Yang, E. H. Sargent, P. De Luna, F. P. G. de Arquer, B. Zhang, N. Becknell, M. B. Ross, Y. Y. Li, M. N. Banis, Y. Y. Li, M. Liu, O. Voznyy, C. T. Dinh, T. Zhuang, P. Stadler, Y. Cui, X. Du, P. Yang and E. H. Sargent, Sulfur-Modulated Tin Sites Enable Highly Selective Electrochemical Reduction of CO_2 to Formate, *Joule*, 2017, **1**, 794–805.

51 P. Deng, H. Wang, R. Qi, J. Zhu, S. Chen, F. Yang, L. Zhou, K. Qi, H. Liu and B. Y. Xia, Bismuth Oxides with Enhanced Bismuth-Oxygen Structure for Efficient Electrochemical Reduction of Carbon Dioxide to Formate, *ACS Catal.*, 2020, **10**, 743–750.

52 A. Atifi, T. P. Keane, J. L. Dimeglio, R. C. Pupillo, D. R. Mullins, D. A. Lutterman and J. Rosenthal, Insights into the Composition and Function of a Bismuth-Based Catalyst for Reduction of CO_2 to CO, *J. Phys. Chem. C*, 2019, **123**, 9087–9095.

53 U. De Silva, J. Masud, N. Zhang, Y. Hong, W. P. R. Liyanage, M. Asle Zaeem and M. Nath, Nickel telluride as a bifunctional electrocatalyst for efficient water splitting in alkaline medium, *J. Mater. Chem. A*, , DOI:10.1039/c8ta01760c.

54 K. U. D. Calvinho, A. W. Alherz, K. M. K. Yap, A. B. Laursen, S. Hwang, Z. J. L. Bare, Z. Clifford, C. B. Musgrave and G. C. Dismukes, Surface Hydrides on Fe_2P Electrocatalyst Reduce CO_2 at Low Overpotential: Steering Selectivity to Ethylene Glycol, *J. Am. Chem. Soc.*, 2021, **143**, 21275–21285.

55 HoriYoshio, KikuchiKatsuhei and SuzukiShin, PRODUCTION OF CO AND CH4 IN ELECTROCHEMICAL REDUCTION OF CO_2 AT METAL ELECTRODES IN AQUEOUS HYDROGENCARBONATE SOLUTION, *http://dx.doi.org/10.1246/cl.1985.1695*, 2006, **14**, 1695–1698.

56 W. He, I. Liberman, I. Rozenberg, R. Ifraemov and I. Hod, Electrochemically Driven Cation Exchange Enables the Rational Design of Active CO_2 Reduction Electrocatalysts , *Angew. Chemie*, 2020, **132**, 8339–8346.

57 D. Yang, Q. Zhu, C. Chen, H. Liu, Z. Liu, Z. Zhao, X. Zhang, S. Liu and B. Han, Selective electroreduction of carbon dioxide to methanol on copper selenide nanocatalysts, *Nat. Commun. 2019 101*, 2019, **10**, 1–9.

58 S. Zhao, S. Guo, C. Zhu, J. Gao, H. Li, H. Huang, Y. Liu and Z. Kang, Achieving electroreduction of CO_2 to CH_3OH with high selectivity using a pyrite–nickel sulfide nanocomposite, *RSC Adv.*, 2017, **7**, 1376–1381.

59 P. M. Zimmerman, C. C. L. McCrory, K. E. Rivera Cruz, Y. Liu and T. L. Soucy, Increasing the CO_2 reduction activity of cobalt phthalocyanine by modulating the σ-donor strength of axially coordinating ligands, *ACS Catal.*, 2021, **11**, 13203–13216.

60 L. Zeng, J. Shi, J. Luo and H. Chen, Silver sulfide anchored on reduced graphene oxide as a high -performance catalyst for CO_2 electroreduction, *J. Power Sources*, 2018, **398**, 83–90.

61 Y. Hori, Electrochemical CO_2 Reduction on Metal Electrodes, *Mod. Asp. Electrochem.*, 2008, 89–189.

62 J. Z. Zhen, J. X. Liu, T. Y. Chen, F. Shi, Y. N. Dai, B. Yang, Y. F. Li, X. Wang, T. G. Nong, Y. Q. Hu and J. Shi, Fabrication of ZnS/Zn electrode using sulphur infiltration method for CO_2 reduction into CO in organic media, *J. Alloys Compd.*, 2019, **771**, 994–999.

63 J.-W. W. Jang, S. Cho, G. Magesh, Y. J. Jang, J. Y. Kim, W. Y. Kim, J. K. Seo, S. Kim, K.-H. H. Lee and J. S. Lee, Aqueous-Solution Route to Zinc Telluride Films for Application to CO_2 Reduction, *Angew. Chemie Int. Ed.*, 2014, **53**, 5852–5857.

64 C. Wang, M. Cao, X. Jiang, M. Wang and Y. Shen, A catalyst based on copper-cadmium bimetal for electrochemical reduction of CO_2 to CO with high faradaic efficiency, *Electrochim. Acta*, 2018, **271**, 544–550.

65 S. Zhang, P. Kang and T. J. Meyer, Nanostructured tin catalysts for selective electrochemical reduction of carbon dioxide to formate, *J. Am. Chem. Soc.*, 2014, **136**, 1734–1737.

66 J. Wu, F. G. Risalvato, S. Ma and X. D. Zhou, Electrochemical reduction of carbon dioxide III. The role of oxide layer thickness on the performance of Sn electrode in a full electrochemical cell, *J. Mater. Chem. A*, 2014, **2**, 1647–1651.

67 D. H. Won, C. H. Choi, J. Chung, M. W. Chung, E. H. Kim and S. I. Woo, Rational Design of a Hierarchical Tin Dendrite Electrode for Efficient Electrochemical Reduction of CO_2, *ChemSusChem*, 2015, **8**, 3092–3098.

68 J. Wu, F. G. Risalvato, F.-S. Ke, P. J. Pellechia and X.-D. Zhou, Electrochemical Reduction of Carbon Dioxide I. Effects of the Electrolyte on the Selectivity and Activity with Sn Electrode, *J. Electrochem. Soc.*, 2012, **159**, F353–F359.

69 W. Lv, R. Zhang, P. Gao and L. Lei, Studies on the faradaic efficiency for electrochemical reduction of carbon dioxide to formate on tin electrode, *J. Power Sources*, 2014, **253**, 276–281.

70 Y. Chen and M. W. Kanan, Tin oxide dependence of the CO_2 reduction efficiency on tin electrodes and enhanced activity for tin/tin oxide thin-film catalysts, *J. Am. Chem. Soc.*, 2012, **134**, 1986–1989.

71 J. E. Pander, M. F. Baruch and A. B. Bocarsly, Probing the Mechanism of Aqueous CO_2 Reduction on Post-Transition-Metal Electrodes using ATR-IR Spectroelectrochemistry, *ACS Catal.*, 2016, **6**, 7824–7833.

72 B. He, L. Jia, Y. Cui, W. Zhou, J. Sun, J. Xu, Q. Wang and L. Zhao, $SnSe_2$ Nanorods on Carbon Cloth as a Highly Selective, Active, and Flexible Electrocatalyst for Electrochemical Reduction of CO_2 into Formate, *ACS Appl. Energy Mater.*, 2019, **2**, 7655–7662.

73 X. Liu, H. Yang, J. He, H. Liu, L. Song, L. Li, J. Luo, X. J. Liu, J. He, H. X. Liu, L. D. Song, J. Luo, H. Yang and L. Li, Highly Active, Durable Ultrathin $MoTe_2$ Layers for the Electroreduction of CO_2 to CH_4, *Small*, 2018, **14**, 1704049.

74 J. Ye, D. Rao and X. Yan, Regulating the electronic properties of $MoSe_2$ to improve its CO_2 electrocatalytic reduction performance via atomic doping, *New J. Chem.*, 2021, **45**, 5350–5356.

75 J. Masud, W. P. R. Liyanage, X. Cao, A. Saxena and M. Nath, Copper Selenides as High-Efficiency Electrocatalysts for Oxygen Evolution Reaction, *ACS Appl. Energy Mater.*, 2018, **1**, 4075–4083.

76 Hydrogen Transport & Distribution | Hydrogen, https://hydrogeneurope.eu/hydrogen-transport-distribution, (accessed 7 September 2020).

77 Methane Steam Reforming - an overview | ScienceDirect Topics, https://www.sciencedirect.com/topics/engineering/methane-steam-reforming, (accessed 7 September 2020).

78 M. Balat, Potential importance of hydrogen as a future solution to environmental and transportation problems, *Int. J. Hydrogen Energy*, 2008, **33**, 4013–4029.

79 P. A. Pilavachi, A. I. Chatzipanagi and A. I. Spyropoulou, Evaluation of hydrogen production methods using the Analytic Hierarchy Process, *Int. J. Hydrogen Energy*, 2009, **34**, 5294–5303.

80 K. S. Whiteley, T. G. Heggs, H. Koch, R. L. Mawer and W. Immel, in *Ullmann's Encyclopedia of Industrial Chemistry*, Wiley-VCH Verlag GmbH & Co. KGaA, Weinheim, Germany, 2000, pp. 1–103.

81 J. A. Turner, *Science (80-.).*, 1999, 285, 687–689.

82 G. Glenk and S. Reichelstein, Economics of converting renewable power to hydrogen, *Nat. Energy*, 2019, **4**, 216–222.

83 J. Tollefson, *Nature*, 2010, 464, 1262–1264.

84 F. Barbir, PEM electrolysis for production of hydrogen from renewable energy sources, *Sol. Energy*, 2005, **78**, 661–669.

85 T. Reier, H. N. Nong, D. Teschner, R. Schlögl and P. Strasser, *Adv. Energy Mater.*, 2017, 7.

86 D. M. F. Santos, C. A. C. Sequeira and J. L. Figueiredo, Hydrogen production by alkaline water electrolysis, *Quim. Nova*, 2013, **36**, 1176–1193.

87 K. Zeng and D. Zhang, *Prog. Energy Combust. Sci.*, 2010, 36, 307–326.

88 J. D. Holladay, J. Hu, D. L. King and Y. Wang, *Catal. Today*, 2009, 139, 244–260.

89 M. Schalenbach, G. Tjarks, M. Carmo, W. Lueke, M. Mueller and D. Stolten, Acidic or Alkaline? Towards a New Perspective on the Efficiency of Water Electrolysis, *J. Electrochem. Soc.*, 2016, **163**, F3197–F3208.

90 Y. Shi and B. Zhang, *Chem. Soc. Rev.*, 2016, 45.

91 J. O. M. Bockris, Kinetics of activation controlled consecutive electrochemical reactions: Anodic evolution of oxygen, *J. Chem. Phys.*, , DOI:10.1063/1.1742616.

92 S. Anantharaj, S. R. Ede, K. Sakthikumar, K. Karthick, S. Mishra and S. Kundu, *ACS Catal.*, 2016, 6.

93 M. Nath, U. De Silva, H. Singh, M. Perkins, W. P. R. Liyanage, S. Umapathi, S. Chakravarty and J. Masud, Cobalt Telluride: A Highly Efficient Trifunctional Electrocatalyst for Water Splitting and Oxygen Reduction, *ACS Appl. Energy Mater.*, , DOI:10.1021/ACSAEM.1C01438.

94 H. Singh, J. Bernabe, J. Chern and M. Nath, Copper selenide as multifunctional non-enzymatic glucose and dopamine sensor, *J. Mater. Res. 2021 367*, 2021, **36**, 1413–1424.

95 S. Umapathi, H. Singh, J. Masud and M. Nath, Nanostructured copper selenide as an ultrasensitive and selective non - enzymatic glucose sensor, *Mater. Adv.*, , DOI:10.1039/D0MA00890G.

96 B. G. Amin, J. Masud and M. Nath, Facile one-pot synthesis of $NiCo_2Se_4$-rGO on Ni foam for high performance hybrid supercapacitors, *RSC Adv.*, 2019, **9**, 37939–37946.

97 J. Masud, W. P. R. Liyanage, X. Cao, A. Saxena and M. Nath, Copper Selenides as High-Efficiency Electrocatalysts for Oxygen Evolution Reaction, *ACS Appl. Energy Mater.*, , DOI:10.1021/acsaem.8b00746.

98 X. Cao, J. E. Medvedeva and M. Nath, Copper Cobalt Selenide as a High-Efficiency Bifunctional Electrocatalyst for Overall Water Splitting: Combined Experimental and Theoretical Study, *ACS Appl. Energy Mater.*, 2020, **3**, 3092–3103.

99 Z. Kang, H. Guo, J. Wu, X. Sun, Z. Zhang, Q. Liao, S. Zhang, H. Si, P. Wu, L. Wang, Y. Zhang, Z. Kang, H. Guo, J. Wu, X. Sun, Z. Zhang, Q. Liao, S. Zhang, H. Si, P. Wu, Y. Zhang and L. Wang, Engineering an Earth-Abundant Element-Based Bifunctional Electrocatalyst for Highly Efficient and Durable Overall Water Splitting, *Adv. Funct. Mater.*, 2019, **29**, 1807031.

100 K. S. Bhat and H. S. Nagaraja, Recent trends and insights in nickel chalcogenide nanostructures for water-splitting reactions, *https://doi.org/10.1080/14328917.2019.1703523*, 2019, **25**, 29–52.

101 H. Singh, M. Marley-Hines, S. Chakravarty and M. Nath, Multi-walled carbon nanotube supported Manganese Selenide as Highly Active Bifunctional OER and ORR electrocatalyst, *J. Mater. Chem. A*, 2022, **6**, 4883–5230.

102 K. Xu, H. Ding, H. Lv, S. Tao, P. Chen, X. Wu, W. Chu, C. Wu and Y. Xie, Understanding Structure-Dependent Catalytic Performance of Nickel Selenides for Electrochemical Water Oxidation, *ACS Catal.*, 2017, **7**, 310–315.

103 C. Panda, P. W. Menezes, C. Walter, S. Yao, M. E. Miehlich, V. Gutkin, K. Meyer and M. Driess, From a Molecular 2Fe-2Se Precursor to a Highly Efficient Iron Diselenide Electrocatalyst for Overall Water Splitting, *Angew. Chemie - Int. Ed.*, 2017, **56**, 10506–10510.

104 S. Wan, W. Jin, X. Guo, J. Mao, L. Zheng, J. Zhao, J. Zhang, H. Liu and C. Tang, Self-Templating Construction of Porous CoSe2 Nanosheet Arrays as Efficient Bifunctional Electrocatalysts for Overall Water Splitting, *ACS Sustain. Chem. Eng.*, 2018, **6**, 15374–15382.

105 B. Chakraborty, R. Beltrán-Suito, V. Hlukhyy, J. Schmidt, P. W. Menezes and M. Driess, Crystalline Copper Selenide as a Reliable Non-Noble Electro(pre)catalyst for Overall Water Splitting, *ChemSusChem*, 2020, **13**, 3222–3229.

106 L. Tao, M. Huang, S. Guo, Q. Wang, M. Li, X. Xiao, G. Cao, Y. Shao, Y. Shen, Y. Fu and M. Wang, Surface modification of NiCo2Te4 nanoclusters: a highly efficient electrocatalyst for overall water-splitting in neutral solution, *Appl. Catal. B Environ.*, 2019, **254**, 424–431.

107 S. Poorahong, D. J. Harding, S. Keawmorakot and M. Siaj, Free standing bimetallic nickel cobalt selenide nanosheets as three-dimensional electrocatalyst for water splitting, *J. Electroanal. Chem.*, 2021, **897**, 115568.

108 X. Hu, Q. Zhou, P. Cheng, S. Su, X. Wang, X. Gao, G. Zhou, Z. Zhang and J. Liu, Nickel-iron selenide polyhedral nanocrystal with optimized surface morphology as a high-performance bifunctional electrocatalyst for overall water splitting, *Appl. Surf. Sci.*, 2019, **488**, 326–334.

109 X. Cao, Y. Hong, N. Zhang, Q. Chen, J. Masud, M. A. Zaeem and M. Nath, Phase Exploration and Identification of Multinary Transition-Metal Selenides as High-Efficiency Oxygen Evolution Electrocatalysts through Combinatorial Electrodeposition, *ACS Catal.*, 2018, **8**, 8273–8289.

110 X. Cao, E. Johnson and M. Nath, Expanding Multinary Selenide Based High-Efficiency Oxygen Evolution Electrocatalysts through Combinatorial Electrodeposition: Case Study with Fe-Cu-Co Selenides, *ACS Sustain. Chem. Eng.*, 2019, **7**, 9588–9600.

111 X. Cao, E. Johnson and M. Nath, Identifying high-efficiency oxygen evolution electrocatalysts from Co–Ni–Cu based selenides through combinatorial electrodeposition, *J. Mater. Chem. A*, 2019, **7**, 9877–9889.

112 M. Cao, H. Wang, P. Kannan, S. Ji, X. Wang, Q. Zhao, V. Linkov and R. Wang, Highly efficient non-enzymatic glucose sensor based on CuxS hollow nanospheres, *Appl. Surf. Sci.*, 2019, **492**, 407–416.

113 X. Du, G. Ma and X. Zhang, Experimental and Theoretical Understanding on Electrochemical Activation Processes of Nickel Selenide for Excellent Water-Splitting Performance: Comparing the Electrochemical Performances with M-NiSe (M = Co, Cu, and V), *ACS Sustain. Chem. Eng.*, 2019, **7**, 19257–19267.

114 F. Bozheyev, F. Xi, P. Plate, T. Dittrich, S. Fiechter and K. Ellmer, Efficient charge transfer at a homogeneously distributed (NH4)2Mo3S13/WSe2 heterojunction for solar hydrogen evolution, *J. Mater. Chem. A*, 2019, **7**, 10769–10780.

115 F. Bozheyev, M. Rengachari, S. P. Berglund, D. Abou-Ras and K. Ellmer, Passivation of recombination active PdSex centers in (001)-textured photoactive WSe2 films, *Mater. Sci. Semicond. Process.*, 2019, **93**, 284–289.

116 F. Bozheyev, F. Xi, I. Ahmet, C. Höhn and K. Ellmer, Evaluation of Pt, Rh, SnO2, (NH4)2Mo3S13, BaSO4 protection coatings on WSe2 photocathodes for solar hydrogen evolution, *Int. J. Hydrogen Energy*, 2020, **45**, 19112–19120.

117 X. Zheng, X. Han, Y. Zhang, J. Wang, C. Zhong, Y. Deng and W. Hu, Controllable synthesis of nickel sulfide nanocatalysts and their phase-dependent performance for overall water splitting, *Nanoscale*, 2019, **11**, 5646–5654.

118 D. Chen, Y. Chen, W. Zhang and R. Cao, Nickel selenide from single-molecule electrodeposition for efficient electrocatalytic overall water splitting, *New J. Chem.*, 2021, **45**, 351–357.

119 C. Zhang, Y. Zhang, S. Zhou and C. Li, Self-supported iron-doping NiSe2 nanowrinkles as bifunctional electrocatalysts for electrochemical water splitting, *J. Alloys Compd.*, 2020, **818**, 152833.

120 A. T. Swesi, J. Masud, W. P. R. Liyanage, S. Umapathi, E. Bohannan, J. Medvedeva and M. Nath, Textured NiSe2 Film: Bifunctional Electrocatalyst for Full Water Splitting at Remarkably Low Overpotential with High Energy Efficiency /639/638/77/886 /639/301/299/886 /639/301/299/161 /128 /120 /145 /140/146 article, *Sci. Rep.*, 2017, **7**, 1–11.

121 B. G. Amin, A. T. Swesi, J. Masud, M. Nath, R. Li, / Chemcomm and C. Communication, CoNi 2 Se 4 as an efficient bifunctional electrocatalyst for overall water splitting, *Chem. Commun.*, 2017, **53**, 5412–5415.

122 X. Xu, F. Song and X. Hu, ARTICLE A nickel iron diselenide-derived efficient oxygen-evolution catalyst, *Nat. Publ. Gr.*, , DOI:10.1038/ncomms12324.

123 M. Sun, R.-T. Gao, X. Liu, R. Gao and L. Wang, Manganese-based oxygen evolution catalysts boosting stable solar-driven water splitting: MnSe as an intermetallic phase, *J. Mater. Chem. A*, 2020, **8**, 25298–25305.

124 Y. Sun, K. Xu, Z. Wei, H. Li, T. Zhang, X. Li, W. Cai, J. Ma, H. Jin Fan, Y. Li, Y. Q. Sun, H. L. Li, T. Zhang, X. Y. Li, W. P. Cai, Y. Li, K. Xu, H. J. Fan, Z. X. Wei and J. M. Ma, Strong Electronic Interaction in Dual-Cation-Incorporated NiSe2 Nanosheets with Lattice Distortion for Highly Efficient Overall Water Splitting, *Adv. Mater.*, 2018, **30**, 1802121.

125 J. Masud and M. Nath, Co7Se8 Nanostructures as Catalysts for Oxygen Reduction Reaction with High Methanol Tolerance, *ACS Energy Lett.*, 2016, **1**, 27–31.

126 H. Li, S. Chen, H. Lin, X. Xu, H. Yang, L. Song and X. Wang, Nickel Diselenide Ultrathin Nanowires Decorated with Amorphous Nickel Oxide Nanoparticles for Enhanced Water Splitting Electrocatalysis, *Small*, 2017, **13**, 1701487.

127 H. Bian, T. Chen, Z. Chen, J. Liu, Z. Li, P. Du, B. Zhou, X. Zeng, J. Tang and C. Liu, One-step synthesis of mesoporous Cobalt sulfides (CoSx) on the metal substrate as an efficient bifunctional electrode for overall water splitting, *Electrochim. Acta*, 2021, **389**, 138786.

128 A. T. Swesi, J. Masud and M. Nath, Nickel selenide as a high-efficiency catalyst for oxygen evolution reaction, *Energy Environ. Sci.*, 2016, **9**, 1771–1782.

129 X. Wu, D. He, H. Zhang, H. Li, Z. Li, B. Yang, Z. Lin, L. Lei and X. Zhang, Ni0.85Se as an efficient non-noble bifunctional electrocatalyst for full water splitting, *Int. J. Hydrogen Energy*, 2016, **41**, 10688–10694.

130 Y. Yin, J. Xu, W. Guo, Z. Wang, X. Du, C. Chen, Z. Zheng, D. Liu, D. Qu, Z. Xie, H. Tang and J. Li, A single-step fabrication of CoTe2 nanofilm electrode toward efficient overall water splitting, *Electrochim. Acta*, 2019, **307**, 451–458.

131 K. Wan, J. Luo, C. Zhou, T. Zhang, J. Arbiol, X. Lu, B. W. Mao, X. Zhang and J. Fransaer, Hierarchical Porous Ni3S4 with Enriched High-Valence Ni Sites as a Robust Electrocatalyst for Efficient Oxygen Evolution Reaction, *Adv. Funct. Mater.*, 2019, **29**, 1900315.

132 K. Lan, J. Li, Y. Zhu, L. Gong, F. Li, P. Jiang, F. Niu and R. Li, Morphology engineering of CoSe2 as efficient electrocatalyst for water splitting, *J. Colloid Interface Sci.*, 2019, **539**, 646–653.

133 S. Chakrabartty, S. Karmakar and C. R. Raj, An Electrocatalytically Active Nanoflake-Like Co9S8-CoSe2Heterostructure for Overall Water Splitting, *ACS Appl. Nano Mater.*, 2020, **3**, 11326–11334.

134 Y. Chen, S. Xu, S. Zhu, R. Jiji Jacob, G. Pastel, Y. Wang, Y. Li, J. Dai, F. Chen, H. Xie, B. Liu, Y. Yao, L. G. Salamanca-Riba, M. R. Zachariah, T. Li and L. Hu, Millisecond synthesis of CoS nanoparticles for highly efficient overall water splitting, , DOI:10.1007/s12274-019-2304-0.

135 A. T. Swesi, J. Masud and M. Nath, Enhancing electrocatalytic activity of bifunctional Ni3Se2 for overall water splitting through etching-induced surface nanostructuring, *J. Mater. Res.*, 2016, **31**, 2888–2896.

136 G. Janani, S. Yuvaraj, S. Surendran, Y. Chae, Y. Sim, S. J. Song, W. Park, M. J. Kim and U. Sim, Enhanced bifunctional electrocatalytic activity of Ni-Co bimetallic chalcogenides for efficient water-splitting application, *J. Alloys Compd.*, 2020, **846**, 156389.

137 L. Nisar, M. Sadaqat, A. Hassan, N. U. A. Babar, A. Shah, M. Najam-Ul-Haq, M. N. Ashiq, M. F. Ehsan and K. S. Joya, Ultrathin CoTe nanoflakes electrode demonstrating low overpotential for overall water splitting, *Fuel*, 2020, **280**, 118666.

138 T. A. Ho, C. Bae, H. Nam, E. Kim, S. Y. Lee, J. H. Park and H. Shin, Metallic Ni3S2 Films Grown by Atomic Layer Deposition as an Efficient and Stable Electrocatalyst for Overall Water Splitting, *ACS Appl. Mater. Interfaces*, 2018, **10**, 12807–12815.

139 G. Liu, C. Shuai, Z. Mo, R. Guo, N. Liu, X. Niu, Q. Dong, J. Wang, Q. Gao, Y. Chen and W. Liu, The one-pot synthesis of porous Ni 0.85 Se nanospheres on graphene as an efficient and durable electrocatalyst for overall water splitting, *New J. Chem.*, 2020, **44**, 17313–17322.

140 H. Lu, Y. Zhang, Y. Huang, C. Zhang and T. Liu, Reaction Packaging CoSe 2 Nanoparticles in N-Doped Carbon Polyhedra with Bifunctionality for Overall Water Splitting, *ACS Appl. Mater. Interfaces*, 2019, **11**, 3372–3381.

141 Z. Wu, J. Li, Z. Zou and X. Wang, Folded nanosheet-like Co0.85Se array for overall water splitting, *J. Solid State Electrochem.*, 2018, **22**, 1785–1794.

142 J. Zhang, Y. Wang, C. Zhang, H. Gao, L. Lv, L. Han and Z. Zhang, Self-Supported Porous NiSe2 Nanowrinkles as Efficient Bifunctional Electrocatalysts for Overall Water Splitting, *ACS Sustain. Chem. Eng.*, 2018, **6**, 2231–2239.

143 Y. Wang, X. Li, M. Zhang, Y. Zhou, D. Rao, C. Zhong, J. Zhang, X. Han, W. Hu, Y. Zhang, K. Zaghib, Y. Wang and Y. Deng, Lattice-Strain Engineering of Homogeneous NiS0.5Se0.5 Core–Shell Nanostructure as a Highly Efficient and Robust Electrocatalyst for Overall Water Splitting, *Adv. Mater.*, 2020, **32**, 2000231.

144 L. He, B. Cui, B. Hu, J. Liu, K. Tian, M. Wang, Y. Song, S. Fang, Z. Zhang and Q. Jia, Mesoporous Nanostructured CoFe-Se-P Composite Derived from a Prussian Blue Analogue as a Superior Electrocatalyst for Efficient Overall Water Splitting, *ACS Appl. Energy Mater.*, 2018, **1**, 3915–3928.

145 J. Li, M. Wan, T. Li, H. Zhu, Z. Zhao, Z. Wang, W. Wu and M. Du, NiCoSe2-x/N-doped C mushroom-like core/shell nanorods on N-doped carbon fiber for efficiently electrocatalyzed overall water splitting, *Electrochim. Acta*, 2018, **272**, 161–168.

146 G. Mei, H. Liang, B. Wei, H. Shi, F. Ming, X. Xu and Z. Wang, Bimetallic MnCo selenide yolk shell structures for efficient overall water splitting, *Electrochim. Acta*, 2018, **290**, 82–89.

147 K. C. Majhi and M. Yadav, Bimetallic chalcogenide nanocrystallites as efficient electrocatalyst for overall water splitting, *J. Alloys Compd.*, 2021, **852**, 156736.

148 J. Huang, S. Wang, J. Nie, C. Huang, X. Zhang, B. Wang, J. Tang, C. Du, Z. Liu and J. Chen, Active site and intermediate modulation of 3D CoSe2 nanosheet array on Ni foam by Mo doping for high-efficiency overall water splitting in alkaline media, *Chem. Eng. J.*, 2021, **417**, 128055.

149 G. Song, Z. Wang, J. Sun, J. Sun, D. Yuan and L. Zhang, ZnCo2S4 nanosheet array anchored on nickel foam as electrocatalyst for electrochemical water splitting, *Electrochem. commun.*, 2019, **105**, 106487.

150 G. Liu, C. Shuai, Z. Mo, R. Guo, N. Liu, Q. Dong, J. Wang, H. Pei, W. Liu and X. Guo, Fe-doped Ni0.85Se nanospheres interspersed into carbon nanotubes as efficient and stable electrocatalyst for overall water splitting, *Electrochim. Acta*, 2021, **385**, 138452.

151 C. Liu, D. Jia, Q. Hao, X. Zheng, Y. Li, C. Tang, H. Liu, J. Zhang and X. Zheng, P-Doped Iron-Nickel Sulfide Nanosheet Arrays for Highly Efficient Overall Water Splitting, *ACS Appl. Mater. Interfaces*, 2019, **11**, 27667–27676.

152 D. Li, Z. Liu, J. Wang, B. Liu, Y. Qin, W. Yang and J. Liu, Hierarchical trimetallic sulfide FeCo2S4–NiCo2S4 nanosheet arrays supported on a Ti mesh: An efficient 3D bifunctional electrocatalyst for full water splitting, *Electrochim. Acta*, 2020, **340**, 135957.

153 J. Y. Xue, F. L. Li, Z. Y. Zhao, C. Li, C. Y. Ni, H. W. Gu, D. J. Young and J. P. Lang, In Situ Generation of Bifunctional Fe-Doped MoS2 Nanocanopies for Efficient Electrocatalytic Water Splitting, *Inorg. Chem.*, 2019, **58**, 11202–11209.

154 Y. Guo, X. Zhou, J. Tang, S. Tanaka, Y. V. Kaneti, J. Na, B. Jiang, Y. Yamauchi, Y. Bando and Y. Sugahara, Multiscale structural optimization: Highly efficient hollow iron-doped metal sulfide heterostructures as bifunctional electrocatalysts for water splitting, *Nano Energy*, 2020, **75**, 104913.

155 R. V. Digraskar, V. S. Sapner, A. V. Ghule and B. R. Sathe, Enhanced Overall Water-Splitting Performance: Oleylamine-Functionalized GO/Cu2ZnSnS4 Composite as a Nobel Metal-Free and NonPrecious Electrocatalyst, *ACS Omega*, , DOI:10.1021/ACSOMEGA.9B01680/SUPPL_FILE/AO9B01680_SI_001.PDF.

156 X. Du, H. Su and X. Zhang, Cr doped-Co9S8 nanoarrays as high-efficiency electrocatalysts for water splitting, *J. Alloys Compd.*, 2020, **824**, 153965.

157 C. Zhang, S. Zhou, X. Dong, Y. Han, J. Li and W. Yin, Three-dimensional self-supported iron-doped nickel sulfides for sustainable overall water splitting, *Vacuum*, 2020, **181**, 109661.

158 T. Chen and Y. Tan, Hierarchical CoNiSe2 nano-architecture as a high-performance electrocatalyst for water splitting, *Nano Res. 2018 113*, 2018, **11**, 1331–1344.

159 X. Zhao, H. Liu, Y. Rao, X. Li, J. Wang, G. Xia and M. Wu, Carbon Dots Decorated Hierarchical NiCo 2 S 4 /Ni 3 S 2 Composite for Efficient Water Splitting, *ACS Sustain. Chem. Eng.*, 2019, **7**, 2610–2618.

160 S. Czioska, J. Wang, X. Teng and Z. Chen, Hierarchically Structured CuCo2S4 Nanowire Arrays as Efficient Bifunctional Electrocatalyst for Overall Water Splitting, *ACS Sustain. Chem. Eng.*, 2018, **6**, 11877–11883.

161 J. Hu, Y. Ou, Y. Li, D. Gao, Y. Zhang and P. Xiao, FeCo2S4 Nanosheet Arrays Supported on Ni Foam: An Efficient and Durable Bifunctional Electrocatalyst for Overall Water-Splitting, *ACS Sustain. Chem. Eng.*, 2018, **6**, 11724–11733.

162 Q. Zhang, C. Ye, X. L. Li, Y. H. Deng, B. X. Tao, W. Xiao, L. J. Li, N. B. Li and H. Q. Luo, Self-Interconnected Porous Networks of NiCo Disulfide as Efficient Bifunctional Electrocatalysts for Overall Water Splitting, *ACS Appl. Mater. Interfaces*, 2018, **10**, 27723–27733.

163 X. Du, W. Lian and X. Zhang, Homogeneous core–shell NiCo2S4 nanorods as flexible electrode for overall water splitting, *Int. J. Hydrogen Energy*, 2018, **43**, 20627–20635.

164 F. Li, R. Xu, Y. Li, F. Liang, D. Zhang, W. F. Fu and X. J. Lv, N-doped carbon coated NiCo2S4 hollow nanotube as bifunctional electrocatalyst for overall water splitting, *Carbon N. Y.*, 2019, **145**, 521–528.

165 Y. Wang, C. Niu, Y. Zhu, D. He and W. Huang, Tunable syngas formation from electrochemical CO_2 reduction on copper nanowire arrays, *ACS Appl. Energy Mater.*, 2020, **3**, 9841–9847.

166 W. Ma, S. Xie, X. G. Zhang, F. Sun, J. Kang, Z. Jiang, Q. Zhang, D. Y. Wu and Y. Wang, Promoting electrocatalytic CO_2 reduction to formate via sulfur-boosting water activation on indium surfaces, *Nat. Commun. 2019 101*, 2019, **10**, 1–10.

167 A. Aljabour, H. Coskun, X. Zheng, M. G. Kibria, M. Strobel, S. Hild, M. Kehrer, D. Stifter, E. H. Sargent and P. Stadler, Active sulfur sites in semimetallic titanium disulfide enable CO_2 electroreduction, *ACS Catal.*, 2020, **10**, 66–72.

168 H. Li, X. Liu, S. Chen, D. Yang, Q. Zhang, L. Song, H. Xiao, Q. Zhang, L. Gu and X. Wang, Edge-Exposed Molybdenum Disulfide with N-Doped Carbon Hybridization: A Hierarchical Hollow Electrocatalyst for Carbon Dioxide Reduction, *Adv. Energy Mater.*, 2019, **9**, 1900072.

169 J. Li, X. Xu, B. Huang, Z. Lou and B. Li, Light-Induced in Situ Formation of a Nonmetallic Plasmonic MoS_2/MoO_{3-x} Heterostructure with Efficient Charge Transfer for CO_2Reduction and SERS Detection, *ACS Appl. Mater. Interfaces*, 2021, **13**, 10047–10053.

170 K. Pellumbi, M. Smialkowski, D. Siegmund and U. P. Apfel, Enhancing the CO_2 Electroreduction of Fe/Ni-Pentlandite Catalysts by S/Se Exchange, *Chemistry*, 2020, **26**, 9938.

171 D. Yang, Q. Zhu, C. Chen, H. Liu, Z. Liu, Z. Zhao, X. Zhang, S. Liu and B. Han, Selective electroreduction of carbon dioxide to methanol on copper selenide nanocatalysts, *Nat. Commun. 2019 101*, 2019, **10**, 1–9.

172 X. Yang, P. Deng, D. Liu, S. Zhao, D. Li, H. Wu, Y. Ma, B. Y. Xia, M. Li, C. Xiao and S. Ding, Partial sulfuration-induced defect and interface tailoring on bismuth oxide for promoting electrocatalytic CO_2 reduction, *J. Mater. Chem. A*, 2020, **8**, 2472–2480.

173 X. Wei, Y. Li, L. Chen and J. Shi, Formic Acid Electro-Synthesis by Concurrent Cathodic CO_2 Reduction and Anodic CH_3OH Oxidation, *Angew. Chemie Int. Ed.*, 2021, **60**, 3148–3155.

174 Vass, B. Endrődi and C. Janáky, Coupling electrochemical carbon dioxide conversion with value-added anode processes: An emerging paradigm, *Curr. Opin. Electrochem.*, 2021, **25**, 100621.

VITA

Apurv Saxena was born and raised in Kota, Rajasthan, India. In May 2012, he obtained his Bachelor of Science and Master of Science dual degree in Chemistry from Indian Institute of Science Education and Research, Mohali, India. In the Fall of 2016, he began working in the Department of Chemistry at Missouri S&T, where he was mentored by Dr. Manashi Nath. His research focused on the carbon dioxide electrochemical conversion and electrochemical water splitting. He has published three research articles. He received a Doctor of Philospohy in Chemistry from Missouri University of Science and Technology, Rolla, Missouri in July 2022.